TRANSVERSE EMITTANCE MEASUREMENT AND PRESERVATION AT THE LHC

Dissertation

with the aim of achieving a doctoral degree
at the Faculty of Mathematics, Informatics
and Natural Sciences

Department of Physics
University of Hamburg, Germany

submitted by

Maria Kuhn

2016 in Hamburg

Evaluators of the dissertation:	Prof. Dr. Jörg Rossbach
	Dr. Ralph W. Aßmann
Members of the examination commission:	Prof. Dr. Jan Louis
	Dr. Bernhard Schmidt
	Prof. Dr. Peter Schleper
Date of the oral defense:	20 June 2016

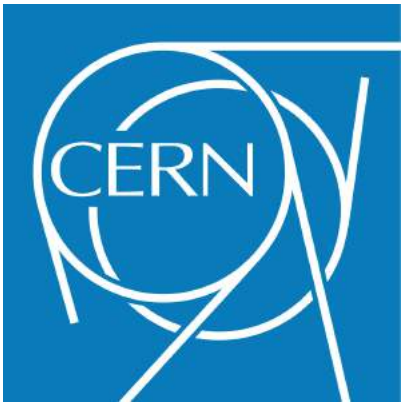

This work has been carried out through the Wolfgang-Gentner-Program at the European Center for Nuclear Research (CERN), Geneva, Switzerland, sponsored by the German Federal Ministry of Education and Research (BMBF).

Abstract

The Large Hadron Collider (LHC) at CERN is a high energy storage ring that provides proton and heavy ion collisions to study fundamental particle physics. The luminosity production is closely linked to emittance preservation in the accelerator. The transverse emittance is the phase space density of the beam and should be conserved when the particle beam is transformed through the accelerator. Perturbing effects, however, can lead to emittance increase and hence luminosity degradation. Measuring the emittance growth is a complex task with high intensity beams and changing energies. The machine optics and the transverse beam size have to be measured as accurately as possible.

Beta function measurements with k-modulation will be discussed. With this method the quadrupole focussing strength is varied and the resulting tune change is traced to determine the beta function at the quadrupole. A new k-modulation measurement tool was developed for the LHC. The fully automatic and online measurement system takes constraints of various systems such as tune measurement precision and powering limitations of the LHC superconducting circuits into account. With sinusoidal k-modulation record low beta function measurement uncertainties in the LHC have been reached. 2015 LHC beta function and β^*, which is the beta function at the collision point, measurements with k-modulation will be presented.

Wire scanners and synchrotron light monitors are presently used in the LHC to measure the transverse beam size. Accuracy and limitations of the LHC transverse profile monitors will be discussed. During the 2012 LHC proton run it was found that wire scanner photomultiplier saturation added significant uncertainty on all measurements. A large discrepancy between emittances from wire scanners and luminosity was discovered but not solved. During Long Shutdown 1 the wire scanner system was upgraded with new photomultipliers. A thorough study of LHC wire scanner measurement precision in 2015 will be presented.

During LHC Run 1 significant transverse emittance growth throughout the LHC cycle was observed. About 30 % of the potential luminosity performance was lost through the different phases of the LHC cycle. At the LHC design stage the total allowed emittance increase through the cycle was set to 7 %. Measurements indicated that most of the blow-up occurred during the injection plateau and the ramp. Intra-beam scattering was one of the main drivers for emittance growth.

In April 2015 the LHC re-started with a collision energy of 6.5 TeV per beam. This thesis presents the first transverse emittance preservation studies in LHC Run 2 with 25 ns beams. A breakdown of the growth throughout the various phases in the LHC cycle is given for low intensity beams measured with wire scanners. Also presented is data collected from synchrotron light monitors and the LHC experiments. Finally, the emittance growth results will be compared to intra-beam scattering simulations. A theory on emittance growth due to noise from the LHC transverse damper and other external sources will be discussed. The results of the investigations are summarized and an outlook in terms of emittance blow-up for future LHC upgrade scenarios with low emittance beams will be given.

Kurzfassung

Der Large Hadron Collider (LHC) am CERN ist ein Hochenergie-Speicherring, in dem Protonen und Schwerionen kollidieren, um Elementarteilchen zu studieren. Die Luminositätsproduktion ist eng mit der Emittanzerhaltung in dem Beschleuniger verbunden. Die transversale Emittanz ist die Phasenraumdichte des Strahls und sollte konstant bleiben, wenn der Strahl durch den Bechleuniger transformiert wird. Allerdings können stöhrende Effekte zum Anwachsen der Emittanz führen. Das Messen des Emittanzwachstums ist eine schwierige Aufgabe bei hohen Strahlintensitäten und sich ändernder Energie. Die Beschleunigeroptik und die transversale Strahlgröße müssen so genau wie möglich gemessen werden.

Es werden Messungen der Beta-Funktion mit k-Modulation diskutiert. Mit dieser Methode wird die Quadrupol-Fokussierungsstärke variiert und die resultierende Tune-Änderung gemessen, um die Beta-Funktion an dem Quadrupol zu bestimmen. Ein neues Werkzeug für k-Modulationsmessungen im LHC wurde entwickelt. Das vollautomatische online Messsystem berücksichtigt Einschränkungen wie Tune-Messgenauigkeit und Stromversorgungsgrenzen der LHC supraleitenden Schaltkreise. Mit sinusförmiger k-Modulation wurden rekordgenaue Beta-Funktionsmessergebnisse im LHC erreicht. Es werden 2015 LHC k-Modulations- und β*, welches die Beta-Funktion am Kollisionspunkt ist, Messresultate präsentiert.

Zurzeit werden Wire-Scanner und Synchrotron-Lichtmonitore im LHC zur transversalen Strahlgrößenmessung verwendet. Genauigkeit und Beschränkungen der transversalen Profilmonitore im LHC werden diskutiert. Während des LHC Protonen-Runs 2012 verursachte Wire-Scanner-Photomultiplier-Sättigung eine zusätzliche Messunsicherheit. Emittanzen, gemessen mit Wire-Scannern und abgeleitet von der Luminosität wiesen eine große Diskrepanz auf. Die Ursache konnte nicht gefunden werden. Während des langen Shutdowns (LS1) wurden die Wire-Scanner-Systeme mit neuen Photomultipliern verbessert. Eine Untersuchung der LHC Wire-Scanner Messgenauigkeit in 2015 wird präsentiert.

Während des ersten LHC Protonen-Runs (LHC Run 1) wurde signifikantes Emittanzwachstum durch den LHC Zyklus beobachtet. Ungefähr 30 % der potenziellen Luminositätsleistung ging in den verschiedenen Phasen des LHC Zyklus verloren. Der Designwert für den maximalen erlaubten Emittanzanstieg durch den Zyklus ist 7 %. Messungen zeigten, dass die Emittanzen hauptsächlich während des Injektionsplateaus und der Energierampe anwachsen. Intra-Beam-Scattering gilt als einer der Hauptgründe für das Emittanzwachstum.

Der LHC wurde im April 2015 mit einer Kollisionsenergie von 6.5 TeV pro Strahl wieder gestartet. Diese Arbeit präsentiert die ersten transversalen Emittanzmessungen von 25 ns Strahlen im zweiten LHC Run (LHC Run 2). Eine Aufschlüsselung des Wachstums von Strahlen mit geringer Strahlintensität, gemessen mit Wire-Scannern durch die verschiedenen Phasen des LHC Zyklus, wird dargelegt. Die Emittanzwerte werden verglichen mit Daten des Synchrotron-Lichtmonitors und aus den LHC Experimenten. Eine Theorie für Emittanzwachstum basierend auf Rauschen vom LHC transversalen Dämpfers und anderen externen Quellen wird besprochen. Die

Untersuchungsergebnisse sind in dieser Arbeit zusammengefasst. Außerdem wird ein Ausblick auf Emittanzerhaltung von zukünftige LHC Upgrade-Szenarien mit kleinen Strahlemittanzen gegeben.

Acknowledgements

The measurements presented in this thesis would not have been possible without the help and advice from many colleagues. I am very grateful for our collaboration.

First and foremost, I would like to thank my supervisor at CERN, Verena Kain, for her support and encouragement. Her determination and competence carried this thesis. I appreciate her suggestions and contributions to every part of this work.

I extend my gratitude to Jörg Rossbach and Ralph Assmann, my supervisors at the University of Hamburg and DESY, for their wisdom and support. I am very thankful that they encourage my personal and professional development and that they share their knowledge with me. Their guidance is outstanding.

I thank Jorg Wenninger, Mike Lamont and the entire LHC Operations team for a wonderful collaboration during my four years at CERN. I appreciate the input and training opportunities and I am grateful for the experience and the support from the group.

Special thanks are dedicated to Enrico Bravin, Guillaume Baud, Bernd Dehning, Jonathan Emery, Ana Guerrero, Emiliano Piselli, Federico Roncarolo and George Trad for their effort to improve the LHC transverse profile monitors. Their support during measurements and for the analysis is priceless.

The assistance from Fabio Follin, Kajetan Fuchsberger, Delphine Jacquet concerning Java questions is very much acknowledged.

The project k-modulation in the LHC was only possible with the help from Rogelio Garcia, Andy Langner, and Ralph Steinhagen. I would like to thank all of them for their input to the automated k-modulation tool and the optics measurements and analysis.

I would also like to express my gratitude to Gerd Kotzian, Wolfgang Hofle and Daniel Valuch who are responsible for the LHC transverse damper system. They supported many emittance growth investigations.

I am thankful for the collaboration with Michaela Schaumann and Fanouria Antoniou for IBS simulations.

Furthermore I would like to acknowledge the support from Witold Kozanecki with his expertise in luminosity.

I would also like to thank Gianluigi Arduini and Yannis Papaphilippou for many fruitful discussions.

The help from everybody who proofread this thesis is gratefully acknowledged.

Last but not least, I thank my family and friends for personal and emotional support in all circumstances.


CERN

Contents

Part I.

Introduction: Particle Collider and Emittance

1. Introduction

The Large Hadron Collider (LHC) [1] is the world's largest particle accelerator. It is part of the CERN (European Center for Nuclear Research) accelerator complex and provides proton and heavy ion beam collisions at high design energies of 7 TeV per charge. In the circular accelerator's collision points the LHC experiments ATLAS,CMS, LHCb and Alice[1] are located to record the product of the collisions. The main purpose of the LHC experiments is to find answers for unresolved questions in fundamental particle physics [2], such as the origin of particles' masses and constituents of dark matter and energy. The Higgs Field is the key mechanism to the concept of mass in the Standard Model of particle physics. The LHC was built to find the associated interaction particle, the Higgs Boson, and other new fundamental particles and forces.

The LHC was designed to achieve higher collision energies than any previous collider, with a high collision rate to produce rare particle reactions with a statistical significance. The accelerator's performance parameter that defines the event rate for a given interaction cross section is called luminosity.

The LHC's first run, called LHC Run 1, started at the end of 2009 followed by three years of operations. The first proton beam collisions were realized on 30 March 2010 with the record beam collision energy at that time of 3.5 TeV per beam. In 2012 the collision energy was increased to 4 TeV per beam. The outstanding performance of the high luminosity runs 2011 and 2012 was due to embarking on 50 ns bunch spacing, instead of the nominal 25 ns, with high bunch intensity [3]. At the end of Run 1, on 4 July 2012, the LHC had delivered enough integrated luminosity to enable ATLAS and CMS to announce the discovery of a Higgs-like boson [4]. In March 2013 it was confirmed as the Standard Model Higgs Boson and later that year the Nobel Prize in physics was awarded to Francois Englert and Peter W. Higgs "for the theoretical discovery of a mechanism that contributes to our understanding of the origin of mass of subatomic particles, and which recently was confirmed through the discovery of the predicted fundamental particle, by the ATLAS and CMS experiments at CERN's Large Hadron Collider" [5].

Before LHC Run 2 started in the beginning of 2015 with a higher collision energy, the LHC underwent intensive maintenance and upgrade works during Long Shutdown 1 (LS1) in 2013 and 2014 to allow operation at 6.5 TeV per beam. During the first year of Run 2, the LHC was already able to provide enough proton beam collisions at 6.5 TeV for the experiments to record useful data in this new energy regime.

The focus of this work is the measurement and preservation of one of the key parameters in a collider, the transverse beam emittance. The collider performance, the luminosity production, is tightly linked to it. The transverse beam emittance normalized to the beam energy should be conserved in proton accelerators. Many effects can, however, lead to emittance growth and hence luminosity degradation. During the 2012 LHC proton run about 30 % of the potential luminosity performance

[1] The LHC experiments will be explained in chapter 2.

was lost throughout the different phases of the LHC cycle, mainly due to blow-up of the normalized transverse emittance. At the LHC design stage the total allowed emittance increase through the cycle was set to only 7 % [1].

Finding sources and solutions for transverse emittance growth in the LHC is crucial for luminosity production. In 2012 a number of possible causes of emittance blow-up in the LHC were studied. The measurements and conclusions were thoroughly analysed in [6]. This thesis continues the quest for highly accurate emittance measurements in the LHC and normalized transverse emittance preservation of LHC proton beams. Emittance measurements during the 2015 LHC cycle will be presented and compared to the 2012 findings. Some of the open questions such as causes of emittance blow-up during the LHC energy ramp could finally be tackled. In addition, emittance measurement uncertainty was greatly improved for LHC Run 2.

Outline

In this thesis emittance measurement and preservation of the LHC proton beams will be investigated, LHC operation with ion beams will not be considered. The first part of this thesis gives an introduction to the LHC at the CERN accelerator complex and the concept of emittance. The LHC cycle is explained in detail and important machine and proton beam parameters are summarized. In chapter 3 the dependency of high luminosity on small transverse beam emittance is derived. Chapter 4 gives an overview of typical causes for emittance growth and emittance damping in the LHC.

As part II of this thesis, the 2012 emittance measurement results and possible sources of emittance growth are presented in chapter 5. These findings established the foundation for emittance measurements and preservation studies during LHC Run 2.

The third part of this work focuses on the emittance measurement techniques and resolution. Measuring the emittance growth precisely is a challenging task with high intensity beams and changing energies. An important ingredient to obtain emittance from beam size measurements is the beta function defined by the focusing magnets of the accelerator. Optics measurement methods and uncertainties are presented in chapter 6. In chapter 7 the measurement of the transverse beam size with wire scanners and other instruments is explained. Accuracy and limitations of the LHC transverse profile monitors are discussed. The transverse emittance can also be derived from luminosity. Luminosity measurement and the measurement of related beam parameters as well as associated limitations are explained in chapter 8.

The 2015 emittance measurement results are presented in part IV of this thesis. A breakdown of the growth through the various phases in the LHC cycle is given for low intensity beams, as well as a comparison with the luminosity data from the LHC experiments. Possible sources and solutions for transverse emittance blow-up in the LHC are analysed.

Finally, an outlook for future LHC upgrade scenarios with low emittance beams and even higher beam intensities will be given in chapter 10.

2. The Large Hadron Collider (LHC) at the CERN Accelerator Complex

CERN (from French: "Conseil Européen pour la Recherche Nucléaire") is the European Center for Nuclear Research. The laboratory is located at the Franco-Swiss boarder in Geneva, Switzerland. Founded in 1954, after the Second World War, the organization's goal was to unite European scientists and build a nuclear physics research center. CERN has now 21 member states and focuses on fundamental particle research [2].

2.1. The LHC Experiments

To probe the fundamental structure of the Universe, particle beam collisions at the high energy frontier are created with accelerators. The Large Hadron Collider (LHC) [1] is the last accelerator in the CERN accelerator chain and it collides two hadron beams at unprecedented high energies to find answers for unresolved questions in particle physics [2].

Four large experiments are situated in the LHC interaction points to benefit from the proton and heavy ion collisions, see Fig. 2.1:

- ATLAS: A Toroidal LHC ApparatuS
- CMS: Compact Muon Solenoid
- LHCb: Large Hadron Collider beauty
- ALICE: A Large Ion Collider Experiment

The Standard Model of particle physics describes the fundamental particles and interactions that form the Universe. Some theories of the Standard Model and beyond still need to be proven experimentally. The LHC and its experiments were able to achieve outstanding milestones in fundamental particle physics during the first LHC running years, for instance with the discovery of the Higgs Boson by ATLAS [7] and CMS [8]. In 2015 the LHC embarked on new physics quests to explore observed phenomena such as the accelerated expansion of the Universe or gravitational interaction. One of the theories that these experiments are testing is Supersymmetry, which could possibly explain dark matter and dark energy that make up 96 % of the Universe and cannot be described by the Standard Model.

The LHCb experiment [9] investigates the properties of antimatter to explore the question of the Universe's existence, for instance why there is more matter than antimatter in the Universe. Finally, the ALICE experiment [10] uses the LHC ion beam collisions to detect the creation of a quark-gluon plasma as it is believed to have existed just after the Big Bang, a state of matter where no nuclei or nuclear particles exist. Moreover, all experiments look for clues of hidden dimensions of space as proposed in the String Theory.

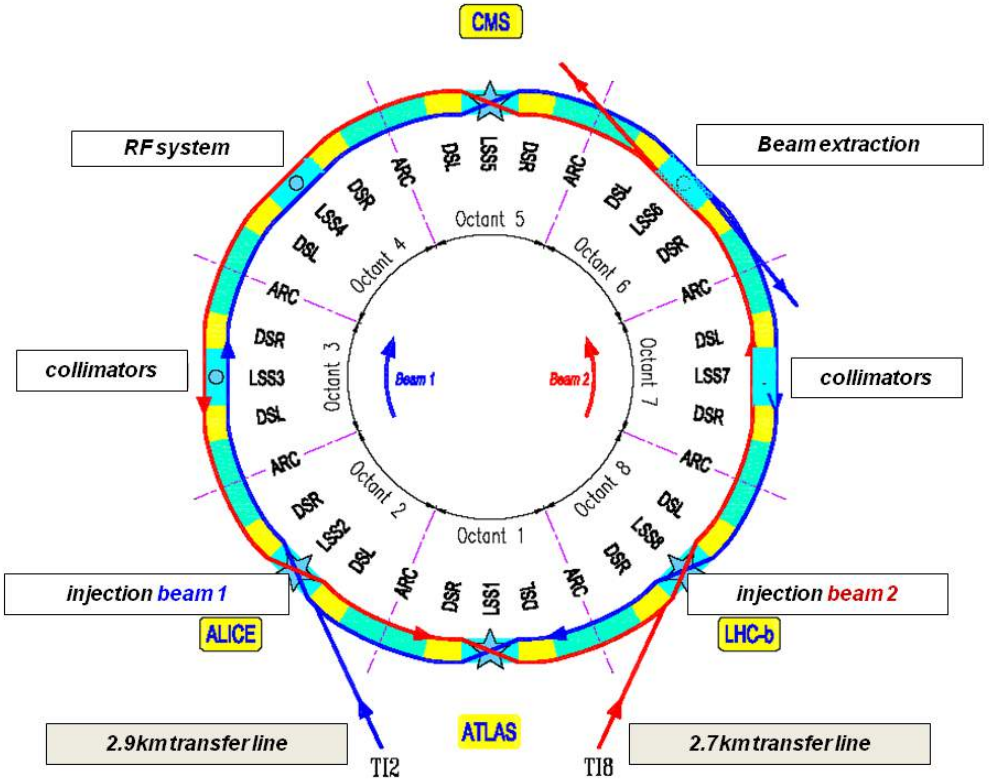

Figure 2.1.: LHC schematic layout [1]. Beam 1 circulates clockwise and Beam 2 counter-clockwise. The beams are injected through the transfer lines (TI) from the SPS. The four interaction points with detectors are ATLAS, ALICE, CMS and LHCb. The LHC is designed with eight identical arcs consisting in total of about 8000 superconducting magnets.

2.2. LHC Design Parameters

The LHC has a circumference of about 27 km which makes it the world's largest accelerator. It is installed in the former LEP (Large Electron-Positron Collider) tunnel which is located 70 to 140 m below the earth's surface. The LHC is a hadron collider with a design energy of 7 TeV per charge [1]. The maximum possible collision energy is defined by the radius of the circular accelerator and the achievable maximum magnet field strength of the main dipole magnets that define the geometry. For a collision energy of 7 TeV per beam a magnet field strength of 8.3 T is needed, which can only be reached with superconducting electromagnets [1]. A picture of an LHC dipole magnet inside the tunnel is shown in Fig. 2.2.

Superconducting magnets and accelerating cavities are installed in the LHC surrounded by a cryogenic system that makes the LHC the largest refrigerator in the world. Superfluid Helium at 1.9 K is used as coolant [1]. Inside the LHC beam pipes ultra-high vacuum with an internal pressure of 10^{-8} Pa has to be established to avoid residual gas interactions of the beam [1].

The RF superconducting cavity system in the LHC has a frequency of 400.8 MHz [1]. It captures the beam at injection into the LHC with minimal losses and then accelerates and finally stores the beam at top energy. For LHC design parameters

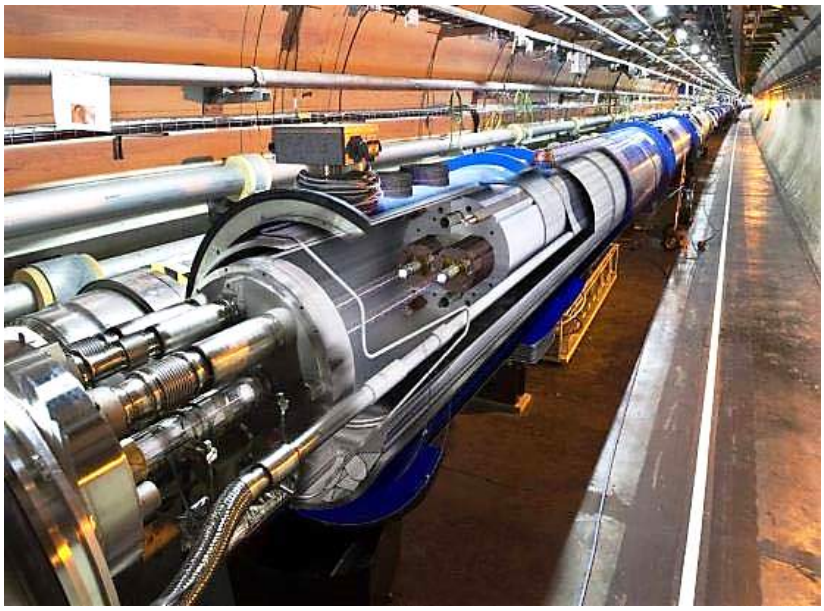

Figure 2.2.: LHC magnets [11]. A view of the main superconducting dipole magnets in the LHC tunnel. The magnets have a twin aperture, which is enclosed in ultra-high vacuum. The beam pipe is surrounded by a cryogenic system. Superconducting interconnections build the link between the dipole magnets.

a total operating RF voltage of the cavities of 8 MV at injection energy and 16 MV at 7 TeV per beam is foreseen. The maximum number of RF buckets that can be filled with bunches is defined by the RF frequency and the revolution frequency ($f_{\text{rev}} = 11.245$ kHz). In the LHC the number of RF buckets is 35640 [1]. However, not all them are filled with bunches.

The two rings of the LHC are designed to be filled with protons (p) or ions (Pb). So far p-p, Pb-Pb and also p-Pb collisions have been produced in the LHC.

In a collider the highest possible collision rate in the experiments, which is equal to the physics production rate, is desired. In the design case the LHC is filled with 2808 bunches per ring with a bunch intensity of 1.15×10^{11} protons. This results in a stored beam energy of 360 MJ at 7 TeV. The operation of superconducting magnets with high beam current is delicate. Small beam losses can lead to magnet quenches, where the magnet looses its superconducting state and releases the stored magnetic energy. The concerned magnetic circuits need to be switched off quickly in such a case and the beam is extracted from the LHC. Beam loss control and restriction with collimators is one of the major challenges in the LHC.

2.3. LHC Layout

Figure 2.1 shows the LHC ring with the location of the experiments ATLAS, CMS, LHCb and ALICE. The schematic displays the two counter-rotating beams and their four interaction points (IP). The LHC is divided into eight sectors with eight long straight sections, called insertion regions (IRs), connected by eight arcs. Beam 1 and beam 2 are injected in IR2 and IR8, respectively. Beam 1 is circulating clockwise

and beam 2 counter-clockwise. The LHC collimation[1] system is installed in IR3 and IR7. The accelerating RF cavities and beam instrumentation are located in IR4. The beams are extracted to the beam dump system in IR6. The LHC and its sub-systems are discussed in [1].

In the LHC arcs the main dipoles and quadrupoles are arranged in a FODO lattice. A FODO lattice describes an optics scheme to focus the beam using quadrupole magnets. The LHC FODO cell consists of three dipoles (O), which are alternately separated by a focusing (F) or a defocusing (D) quadrupole magnet, achieving an overall transverse focusing of the beam[2]. A schematic of an LHC FODO cell is given in Fig. 2.3. Additional magnets to correct the orbit, the tune and higher order field errors are available in each cell in the LHC rings.

The focusing strengths and distribution of quadrupole magnets define the local transverse expansion of a particle beam in the accelerator, called beta function (β). Typical beta functions in the LHC FODO lattice are several 10 m up to about 200 m. Together with the beam emittance ε, the beta function at each point in the accelerator is related to the maximum space the beam can occupy in the transverse planes, the transverse beam size σ. The transverse emittance is the phase space density of the beam. Normalized to the beam energy, it is a constant of motion of the beam around the ring of a circular accelerator, which will be explained in chapter 3.

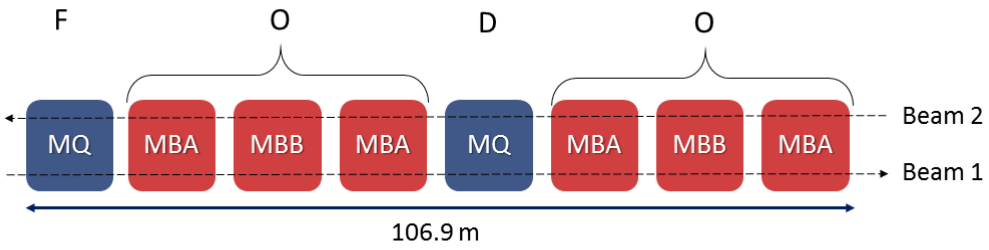

Figure 2.3.: Schematic layout of a LHC FODO cell. MQ are the focusing (F) and defocusing (D) quadrupoles. MBA and MBB are the arc dipoles (O). An LHC FODO cell has a length of 106.9 m. It is equipped with additional corrector coils and beam diagnostics not displayed in this block diagram.

In the four LHC interaction points, where the particle detectors are located, the beams are focused to very small beam sizes to increase the collision rate. For this purpose all IPs in the LHC are equipped with superconducting final focus triplet quadrupole magnets. The beta function in the IP (β^*) can be squeezed to a few cm. In the design case β^* is 55 cm to achieve a nominal transverse rms beam size in the IP of about 17 µm.

[1]The LHC collimation system protects the accelerator against beam loss. Movable two-sided absorbers are placed near the beam trajectory at two locations in the LHC.

[2]The overall focusing is achieved when the quadrupoles are separated by 90° betatron phase advance.

2.4. LHC Timeline

Motivated by the search for the Standard Model Higgs Boson, the LHC was proposed as a high energy hadron collider in 1984 [12]. Ten years later, in 1994, the CERN council approved the construction of the LHC [2]. In 2008 the accelerator was ready for the first beam, but was shut down shortly afterwards for a year due to an electric fault in an interconnect between two superconducting magnets [13]. A large amount of energy was dissipated, which resulted in severe mechanical and electrical damage, see Fig. 2.4. Over 50 superconducting magnets had to be replaced.

Figure 2.4.: 2008 incident [14]. An electrical fault occurred in an interconnect between two superconducting magnets in the LHC. The photo is taken after the incident. Large amounts of energy were accidentally released and caused severe damage such as displacement of the superconducting magnets as shown in the picture.

LHC operation finally started at the end of 2009 after the repairs had been finished. The first three running years of the LHC are called LHC Run 1. The first proton beam collisions were realized on 30 March 2010 with a reduced beam collision energy of 3.5 TeV. 2010 was devoted to commissioning the LHC and laying the foundation for high intensity operation. In 2011 the beam intensity was increased to exploit and explore the LHC performance limits at 3.5 TeV. 2012 was devoted to luminosity[3] production at a higher energy of 4 TeV with further increased beam intensity. Trains of 50 ns bunch spacing were used in 2011 and 2012 with high bunch intensity leading to high instantaneous luminosity [3].

For maintenance and upgrade works the LHC was paused for two years in 2013/14 during the first LHC long shutdown (LS1). Due to the 2008 incident the maximum collision energy was limited during LHC Run 1. During LS1 over 12'000 interconnects between the superconducting magnets were renewed and improved [15]. In 2015, the beginning of LHC Run 2, the LHC was restarted with a collision energy of 6.5 TeV per beam to allow fundamental discoveries in an unprecedented energy regime.

[3]The accelerator's performance parameter to measure the event rate for a given interaction cross section is called luminosity. The luminosity will be introduced in detail in chapter 3.

The integrated luminosity performance over the three years of LHC Run 1 and the start of Run 2 is summarized in Table 2.1 and in Fig. 2.5. A total integrated luminosity of about 4 fb^{-1} (ATLAS 4.1 fb^{-1}, CMS 3.88 fb^{-1}) was reached in 2015, similar to 2011. The best running year in terms of LHC performance so far was in 2012.

Year	Overview	Collision energy per beam [TeV]	ATLAS/CMS integrated luminosity [fb^{-1}]
2010	Commissioning	3.5 TeV	0.04
2011	Exploring limits	3.5 TeV	6.1
2012	Production	4 TeV	23.1
2013/14	Shutdown		
2015	Commissioning	6.5 TeV	4.3/4.1

Table 2.1.: Overview of LHC operation from 2010 to 2015 with collision energy per beam and achieved integrated luminosity in ATLAS and CMS.

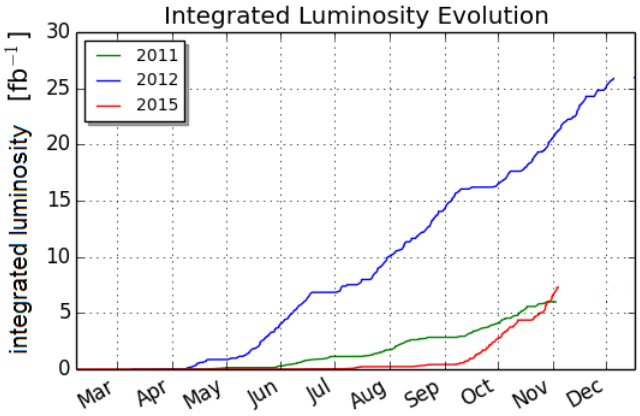

Figure 2.5.: LHC integrated luminosity evolution. Total integrated luminosity delivered to the ATLAS experiment during years 2011, 2012 and 2015. 2012 was the year with the highest luminosity performance of the LHC. After Long Shutdown 1 in 2013/14 the integrated luminosity was slowly increased, comparable to the 2011 run. At the end of 2015 the slope of integrated luminosity is slightly steeper than in 2012 promising high luminosity performance in the coming years.

LHC Run 2 will end in 2018. The coming years will be devoted to luminosity production. For the LHC proton runs in 2016, 2017 and 2018 a goal of about 30 fb^{-1} per year was set. Part of Run 2 will also be dedicated to machine development periods, where beams for the high luminosity upgrade of the LHC (HL LHC) will be tested.

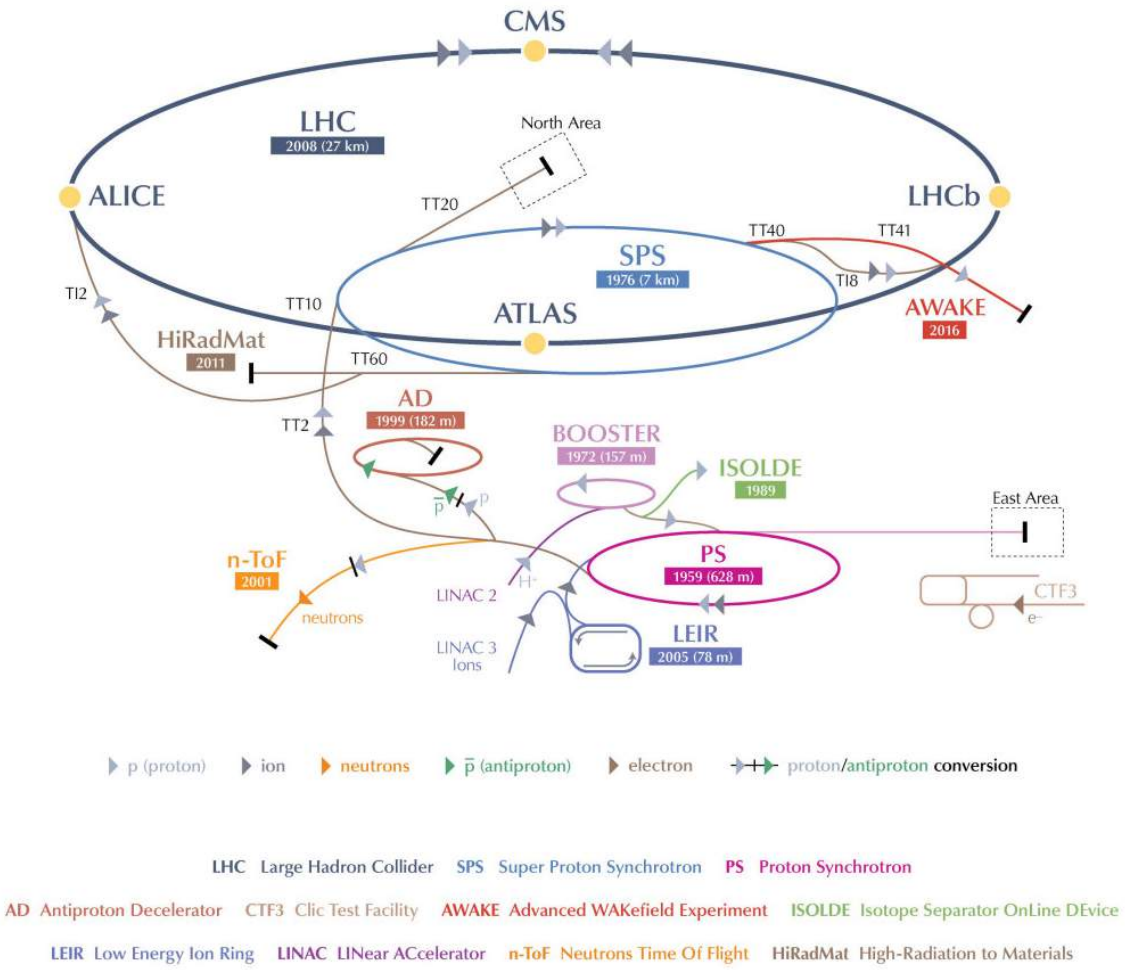

Figure 2.6.: The CERN accelerator complex [2]. All CERN accelerators and experiments with beam are shown. The acceleration chain of the protons to the LHC is: Linac2 $\longrightarrow$ Booster $\longrightarrow$ PS $\longrightarrow$ SPS $\longrightarrow$ LHC.

2.5. The LHC Injector Chain

The LHC is part of the CERN accelerator complex as shown in Fig. 2.6. Most of the other CERN accelerators form the LHC injector chain producing the beams for the LHC. The LHC pre-accelerators are explained in detail in [6].

The proton bunches for the LHC are produced and pre-accelerated in the linear accelerator Linac2. Afterwards they enter the LHC injector chain with only circular accelerators. An overview is given in Table 2.2. From Linac2 the protons are transferred to the Booster with an energy of 50 MeV. A maximum of eight very high brightness bunches can be accelerated in the Booster to an extraction energy of 1.4 GeV. The bunches are injected into the Proton Synchrotron (PS). The different radio frequency (RF) systems in the PS are used to split the bunches from the Booster. The protons in the PS reach an extraction energy of about 26 GeV before they are injected into the Super Proton Synchrotron (SPS).

The final bunch spacing and the maximum bunch brightness desired in the LHC is defined by the Booster and the PS. The brightness B is the ratio of bunch intensity N

	Extraction energy [GeV]	Number of bunches
Booster	1.4	6
PS	26	72
SPS	450	288
LHC	7000	2808

Table 2.2.: Nominal LHC beam production scheme from the Booster to the LHC. The extraction energy (in the LHC: collision energy) and number of bunches for every circular accelerator in the LHC injection chain are listed.

over normalized transverse emittance ε [16]:

$$B = \frac{N}{\varepsilon}. \tag{2.5.1}$$

In the design case six bunches extracted from the Booster are split in the PS into 72 bunches with 25 ns bunch spacing. Several injections are needed to fill the SPS, the last stage of the LHC pre-acceleration chain. Before the proton bunches are injected into the LHC, they are accelerated to the 450 GeV LHC injection energy in the SPS. Then the protons are extracted towards the LHC into two transfer lines (TI2 and TI8). The nominal SPS batch consists of 216 or 288 bunches with an intensity of 1.15×10^{11} protons per bunch (ppb) and a normalized transverse emittance of 3.5 µm at 450 GeV injection energy.

For the nominal filling scheme 12 injections per ring are necessary to fill the LHC with 25 ns bunch spacing to get a total number of 2808 bunches per ring[4]. For the most commonly used filling scheme in Run 1, 12 injections with up to 144 bunches per injection were required per ring. Due to limitations created by electron cloud effects[5] the bunch spacing in LHC Run 1 was increased to 50 ns [17]. The larger bunch spacing allowed higher bunch intensities beyond the design value. The final number of bunches in the LHC for the filling scheme in 2012 was 1374.

At the start of LHC Run 2 in 2015, LHC filling with the design bunch spacing of 25 ns was accomplished. The maximum number of bunches per ring was 2244, achieved in October 2015. However, the maximum number of bunches per batch was limited to 144, as during Run 1, requiring up to 16 injections per ring. A protection device against injection failures (TDI) was limited due to a weakness of the material (Boron Nitride) [18]. TDIs are vertical absorbers that are located downstream of the LHC injection kickers. An exchange of the TDIs was foreseen for the year end technical stop after the 2015 run so that injections with 288 bunches per batch are possible in the 2016 proton run.

[4]The nominal bunch train pattern is 333 334 334 334, with 3 or 4 batches of 72 bunches per SPS extraction, making up a total of 12 injections per ring.

[5]Electron cloud effects are explained in the section 2.7.

2.6. The 2015 LHC Cycle

Once the injection process into the LHC is completed, the proton bunches are accelerated to 7 TeV top energy in the nominal case and afterwards the beta functions at the experiments are squeezed to a minimum. Then the beams are brought into collisions and the LHC becomes a high energy storage ring. The protons collide at four points in the ring, where the LHC experiments are located. A more detailed view of the LHC cycle is given in Fig. 2.7 and will be explained in the following.

The operational cycle of the LHC is divided into distinct phases linked to the main accelerator activities. They are called beam modes. The operational LHC modes with beam during proton physics are "injection", "ramp", "squeeze", and "stable beams" [19]. At the end of each fill the beams are dumped and the LHC magnets are ramped down. In preparation for the next injection, the LHC injection plateau at 450 GeV is set up.

Once the LHC is ready for beam, the proton bunches are injected from the SPS. The injection process takes minimum 30 minutes. When injection is finished, the machine is prepared for the energy ramp. Different machine components are loaded with the ramp functions. Then the beam energy is increased. The ramp from injection energy of 450 GeV to collision energy in 2011 (3.5 TeV) and 2012 (4 TeV) took about 15 minutes. With a collision energy of 6.5 TeV, the ramp in 2015 took

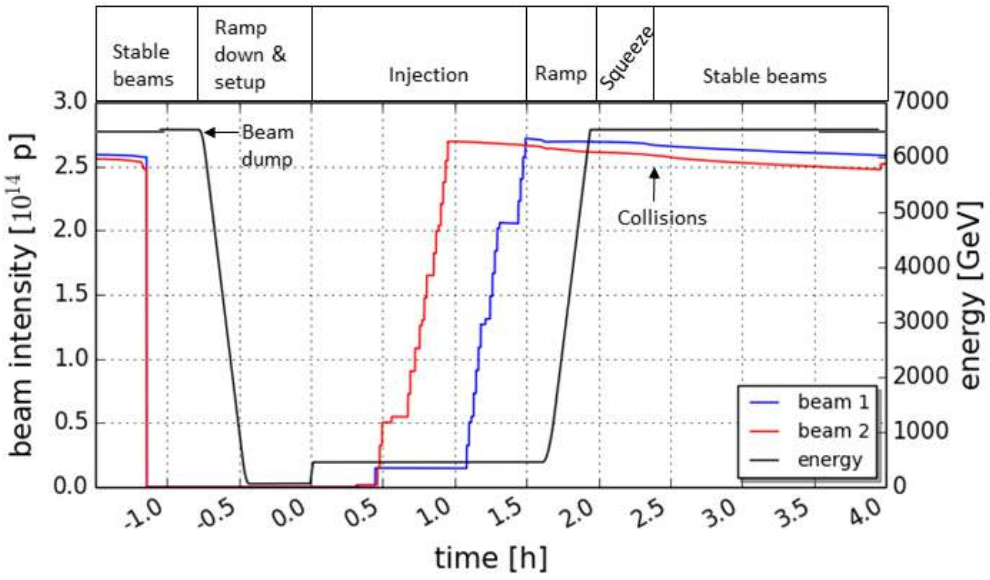

Figure 2.7.: The 2015 LHC cycle. The energy (black), or magnet field strength, during the cycle and the total beam 1 (blue) and beam 2 (red) intensity are shown. The injection process from the SPS to the LHC takes minimum 30 minutes. The injection plateau is followed by the energy ramp (approximately 22 minutes), from 450 GeV to 6.5 TeV in 2015. After reaching the flattop energy, the β^* is squeezed from 11 m to 0.8 m at ATLAS and CMS (approximately 13 minutes) and, finally, the beams are brought into collision. In "stable beams" the experiments take data.

about 22 minutes.

When the flattop energy is reached, the horizontal and vertical LHC tunes are changed from injection tunes to collision tunes for best collision performance[6]. After the pre-squeeze checks are completed, the squeeze is initiated. The beta function at the collision points (β^*) is minimized to reduce the transverse beam size at the interaction point and thus achieve high luminosities.

When β^* is squeezed to only several cm, the beta functions in the LHC triplet quadrupoles reach a local maximum of about 4.5 km resulting in beam sizes of 1.5 mm in that location. Due to aperture limitations in the LHC triplet magnets, the squeeze cannot be executed at 450 GeV. The transverse beam size would be too large for the aperture in the triplet. With higher energies, however, the beam size decreases due to adiabatic reduction of the emittance.

The squeeze to 0.8 m takes about 13 minutes. In 2012 the β^* at the two main experiments in IP1 (ATLAS) and IP5 (CMS) was squeezed from 11 m to 0.6 m. For the start of LHC Run 2 a more relaxed β^* of 0.8 m in ATLAS and CMS was chosen. It will be gradually decreased throughout Run 2.

The squeeze is followed by collapsing the separation orbit bumps at the interaction points. The beams are brought into collision and are aligned to collide head on. The experiments switch on their detectors as soon as the mode "stable beams" is declared. In general, the machine stays in "stable beams" as long as possible.

Each pass through the cycle with its different modes is allocated a number, the fillnumber. The record time in "stable beams" in 2012 was 22.8 hours (Fill 2692). In 2015 an even longer fill could be achieved: 24.3 hours in "stable beams" (Fill 4538).

2.7. The 2015 LHC Beam Parameters

The collider peak performance depends on the beam parameters, such as transverse emittance and bunch intensity, as well as machine configurations. The LHC proton run configurations in 2012 (end of LHC Run 1), 2015 (start of LHC Run 2) and for the design case [1] are summarized in Table 2.3. The resulting peak luminosity is also given. For the LHC running years 2011, 2012 and 2015 the evolution of the ATLAS peak luminosity is shown in Fig. 2.8 and explained in the following.

With the LHC design proton beam parameters a peak luminosity of 10^{34} cm^{-2}s^{-1} can be reached. In that case bunches with intensities of 1.15 $\times 10^{11}$ ppb and a normalized transverse emittance of 3.75 µm at 7 TeV per beam are required. In the design case the LHC is filled with 2808 bunches with a bunch spacing of 25 ns. The machine configuration in this case is $\beta^* = 55$ cm and a crossing angle[7] of 285 µrad. The concept of crossing angle will be explained in chapter 3.

To achieve high luminosities in the LHC, the injectors have to produce high brightness beams, which need to be conserved through the LHC cycle. One of the reasons for the remarkable achievements of the LHC in its first running years was the excellent performance of the LHC injector chain. Beams beyond the design brightness could be produced in the injectors with bunch intensities of 1.7×10^{11} protons and a normalized transverse emittance of 1.5 µm during LHC Run 1. Despite the lower

[6] LHC injection tunes are chosen for optimized dynamic aperture of separated beams. When the beams are colliding the tune working point has to be changed to take into account resonances from beam-beam effects.

[7] In the LHC there are many circulating bunches with short bunch spacing. To prevent unwanted head-on interactions, the two beams collide at an angle of ϕ =285 µrad by design.

	Design	2012	2015
Beam injection energy [TeV]	0.45	0.45	0.45
Collision energy per beam [TeV]	7	4	6.5
Total number of bunches per beam	2808	1374	2244
Maximum number of bunches injected	288	144	144
Number of injections per fill and beam	12	12	16
Bunch spacing [ns]	25	50	25
Bunch length at injection (4σ rms) [ns]	1.3	1.2	1.3
Bunch intensity at injection [ppb]	1.15×10^{11}	$1.1 - 1.7 \times 10^{11}$	$1.0 - 1.3 \times 10^{11}$
Normalized transverse emittance at injection (1σ rms) [µm]	3.5	1.4 - 1.9	2.2 - 2.5
Normalized transverse emittance at collision (1σ rms) [µm]	3.75	2.4	3.0
β^* at IP1/IP5 [cm]	55	60	80
Crossing angle [µrad]	285	290	290
Number of collisions (IP1+IP5/IP2/IP8)	2808/2736/2622	1368/0/1262	2232/1731/1866
Maximum luminosity achieved [$\mathrm{cm^{-2}s^{-1}}$]	10^{34}	7.7×10^{33}	5.1×10^{33}

Table 2.3.: LHC proton run configuration in 2012, 2015 and for design LHC parameters. Beam energy, β^*, crossing angle and number of collisions are given by the machine characteristics. Number of injections, bunch spacing, bunch length, bunch intensity and transverse emittance are beam parameters defined by the injectors' performance. How the peak luminosity is linked to the above mentioned parameters will be explained in chapter 3.

collision energy of 4 TeV per beam instead of the design value of 7 TeV, peak luminosities of 7.7×10^{33} $\mathrm{cm^{-2}s^{-1}}$ were reached in the LHC in 2012. 1368 bunches per beam were colliding in IP1 and IP5 with a bunch spacing of 50 ns. The collision optics in 2012 resulted in $\beta^* = 60$ cm with a crossing angle of about 290 µrad.

In the 2012 LHC proton run the bunch spacing was limited to 50 ns due to electron

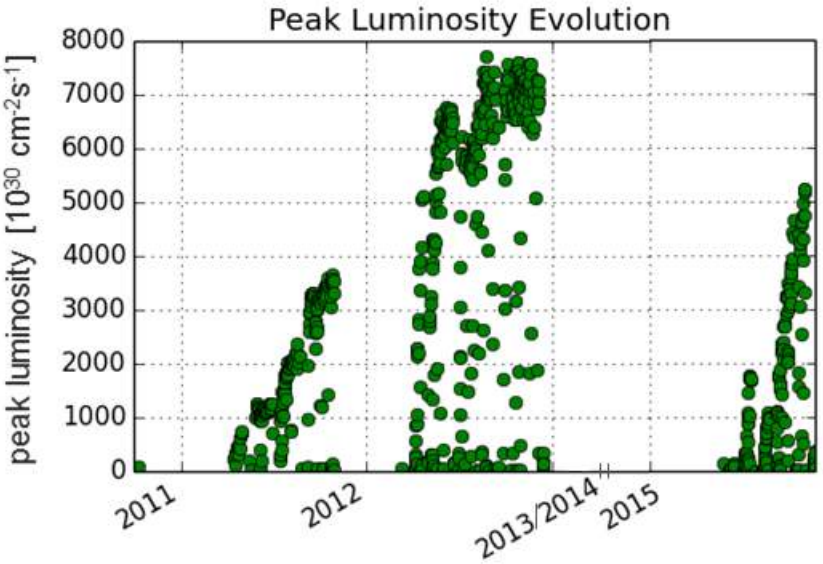

Figure 2.8.: LHC peak performance. Fill-by-fill peak luminosities delivered to the ATLAS experiment from 2011 to 2015. During 2011 and 2012 the peak performance could be gradually increased. After Long Shutdown 1 in 2013/14 the peak luminosity was slowly ramped up again.

cloud effects [17]. The hereby achieved peak luminosity with fewer collisions created a high number of proton collisions per bunch crossing, so-called pile-up in the detectors[8]. The same 2012 beam parameters at an increased collision energy of 6.5 TeV per beam would have exceeded the pile-up limit in ATLAS and CMS[9]. Therefore the nominal bunch spacing of 25 ns was attempted in 2015. Thus more bunches with lower brightness could be injected. For the same collision rate, this results in a lower total number of proton collisions per bunch crossing in the detectors[10].

In 2015 it was possible for the first time to run the LHC with beams of 25 ns bunch spacing. Due to short bunch spacing, high bunch intensity and low emittance electron cloud effects can critically influence LHC operation. Photoelectrons from synchrotron radiation accelerated by the proton beam hit the vacuum chamber walls and secondary electrons are emitted. If in resonance with the bunch spacing, electron clouds build up around the proton bunches [17]. Possible consequences are instabilities, emittance growth, gas desorption from chamber walls, heat load, particle losses, and interference with diagnostics.

In preparation for 25 ns beams a long and intense scrubbing period of the LHC and the SPS was maintained in 2015 [20]. With scrubbing the electron cloud effects are reduced. For this purpose a high intensity beam with short bunch spacing is stored at 450 GeV in the LHC to intentionally create electron clouds around the beam. Hence, the vacuum chamber walls are conditioned by beam-induced electron

[8]In 2012 the mean pile-up was about 30 collisions/crossing at the beginning of a fill with a peak pile-up during some fills of up to approximately 40 collisions/crossing [3].

[9]The pile-up limit of ATLAS and CMS is about 50 collisions/crossing. The 2012 beam parameters at 6.5 TeV flattop energy would yield a pile-up of over 70 collisions/crossing [3].

[10]The nominal 25 ns proton beams give a pile-up of approximately 25 collisions/crossing [3].

bombardment. This decreases the emission of secondary electrons produced by the electron cloud after scrubbing.

The LHC peak luminosity achieved in 2015 was 5.1×10^{33} $\mathrm{cm}^{-2}\mathrm{s}^{-1}$ in ATLAS and 5.2×10^{33} $\mathrm{cm}^{-2}\mathrm{s}^{-1}$ in CMS with 2232 bunches colliding with a normalized transverse emittance of about 3 µm and a bunch intensity of 1.2×10^{11} ppb. The machine was configured with a β^* of 80 cm and a crossing angle of about 290 µm in 2015.

For the LHC proton run in 2016, 2017 and 2018 peak luminosities of up to 1.5×10^{34} $\mathrm{cm}^{-2}\mathrm{s}^{-1}$ are foreseen. This will be achieved with a β^* reduction to 40 cm in IP1 and IP5 and beam parameters pushed to slightly higher brightness.

3. Collider Performance and Concept of Emittance

The performance of a collider is tightly linked to the size of the transverse beam emittance. The emittance is a measure of beam quality and should be conserved in proton accelerators. In the following the key parameters for high luminosity and the concept of emittance will be derived.

3.1. Luminosity

The main parameter to measure the performance of a collider is the luminosity L. Consider the cross section σ_i for a certain scattering process of interest. The event rate R_i is the given by

$$R_i = \sigma_i L. \tag{3.1.1}$$

The luminosity is defined by the machine parameters. It is described as the overlap of the two colliding beams with time dependent beam density distribution functions ρ_1 of beam 1 and ρ_2 of beam 2 [21]:

$$L \propto N_1 N_2 K \cdot \iiiint_{-\infty}^{\infty} \rho_1(x, y, s, -s_0)\rho_2(x, y, s, s_0)\mathrm{d}x\mathrm{d}y\mathrm{d}s\mathrm{d}s_0, \tag{3.1.2}$$

where N_1 and N_2 are the number of particles per bunch for beam 1 and beam 2, respectively. Since the two beams are moving, the overlap integral depends on the longitudinal position s of the bunches. The collision point of the two beams is at s_0. x and y are the horizontal and vertical coordinate, respectively. K is the kinematic factor depending on the velocity difference of the two beams:

$$K = \sqrt{(\vec{v_1} - \vec{v_2})^2 - (\vec{v_1} \times \vec{v_2})^2/c^2}. \tag{3.1.3}$$

$\vec{v_1}$ is the velocity vector of beam 1 and $\vec{v_2}$ is the velocity vector of beam 2. For head-on collision at $s_0 = 0$ and same particle velocities $\vec{v_1} = -\vec{v_2} = \vec{v}$, Eq. 3.1.2 yields

$$L = 2N_1 N_2 f_{\mathrm{rev}} n_{\mathrm{b}} \cdot \iiiint_{-\infty}^{\infty} \rho_{1\mathrm{x}}(x)\rho_{1\mathrm{y}}(y)\rho_{1\mathrm{s}}(s-s_0)\rho_{2\mathrm{x}}(x)\rho_{2\mathrm{y}}(y)\rho_{2\mathrm{s}}(s+s_0)\mathrm{d}x\mathrm{d}y\mathrm{d}s\mathrm{d}s_0. \tag{3.1.4}$$

f_{rev} is the revolution frequency and n_{b} is the number of bunches per beam. The integrals in Eq. 3.1.4 are solved for Gaussian beam distribution functions:

$$\rho_{iu}(u) = \frac{1}{\sqrt{2\pi}\sigma_u} e^{-\frac{u^2}{2\sigma_u^2}}, \tag{3.1.5}$$

$$\rho_{\mathrm{s}}(s \pm s_0) = \frac{1}{\sqrt{2\pi}\sigma_{\mathrm{s}}} e^{-\frac{(s\pm s_0)^2}{2\sigma_{\mathrm{s}}^2}}, \tag{3.1.6}$$

with $i = 1{,}2$ and $u = x, y$. Then Eq. 3.1.4 can be written as

$$L = \frac{2N_1N_2f_{\mathrm{rev}}n_{\mathrm{b}}}{(2\pi)^3\sigma_{1\mathrm{x}}\sigma_{2\mathrm{x}}\sigma_{1\mathrm{y}}\sigma_{2\mathrm{y}}\sigma_{\mathrm{s}}^2}\cdot \iiiint_{-\infty}^{\infty} e^{-\frac{x^2}{2\sigma_{1\mathrm{x}}^2}} e^{-\frac{x^2}{2\sigma_{2\mathrm{x}}^2}} e^{-\frac{y^2}{2\sigma_{1\mathrm{y}}^2}} e^{-\frac{y^2}{2\sigma_{2\mathrm{y}}^2}} e^{-\frac{(s-s_0)^2}{2\sigma_{\mathrm{s}}^2}} e^{-\frac{(s+s_0)^2}{2\sigma_{\mathrm{s}}^2}} \mathrm{d}x\mathrm{d}y\mathrm{d}s\mathrm{d}s_0, \quad (3.1.7)$$

where σ_1 and σ_2 are the transverse beam sizes, horizontal (x) and vertical (y), of beam 1 and beam 2 at the interaction point, respectively. The general solution for this integration type is $\int_{-\infty}^{\infty} e^{-at^2}\mathrm{d}t = \sqrt{\frac{\pi}{a}}$. By summarizing functions with same coordinates the integral transforms to

$$\iiiint_{-\infty}^{+\infty} e^{-\frac{x^2(\sigma_{1\mathrm{x}}^2+\sigma_{2\mathrm{x}}^2)}{2\sigma_{1\mathrm{x}}^2\sigma_{2\mathrm{x}}^2}} e^{-\frac{y^2(\sigma_{1\mathrm{y}}^2+\sigma_{2\mathrm{y}}^2)}{2\sigma_{1\mathrm{y}}^2\sigma_{2\mathrm{y}}^2}} e^{-\frac{(s^2+s_0^2)}{\sigma_{\mathrm{s}}^2}} \mathrm{d}x\mathrm{d}y\mathrm{d}s\mathrm{d}s_0 = \sqrt{\frac{2\pi\sigma_{1\mathrm{x}}^2\sigma_{2\mathrm{x}}^2}{\sigma_{1\mathrm{x}}^2+\sigma_{2\mathrm{x}}^2}}\sqrt{\frac{2\pi\sigma_{1\mathrm{y}}^2\sigma_{2\mathrm{y}}^2}{\sigma_{1\mathrm{y}}^2+\sigma_{2\mathrm{y}}^2}}\pi\sigma_{\mathrm{s}}^2. \quad (3.1.8)$$

Inserting this solution into Eq. 3.1.7 finally gives

$$L = \frac{f_{\mathrm{rev}}n_{\mathrm{b}}}{2\pi}\cdot\frac{N_1N_2}{\sqrt{\sigma_{1\mathrm{x}}^2+\sigma_{2\mathrm{x}}^2}\sqrt{\sigma_{1\mathrm{y}}^2+\sigma_{2\mathrm{y}}^2}}. \quad (3.1.9)$$

In the simple case where $\sigma_{1\mathrm{x}} = \sigma_{2\mathrm{x}} \equiv \sigma_{\mathrm{x}}$, $\sigma_{1\mathrm{y}} = \sigma_{2\mathrm{y}} \equiv \sigma_{\mathrm{y}}$ and $\sigma_{\mathrm{x}} = \sigma_{\mathrm{y}} \equiv \sigma$, the luminosity can be written as

$$L = \frac{f_{\mathrm{rev}}n_{\mathrm{b}}}{4\pi}\cdot\frac{N_1N_2}{\sigma^2} = \frac{f_{\mathrm{rev}}n_{\mathrm{b}}}{4\pi}\cdot\frac{N_1N_2}{\beta^*\varepsilon}. \quad (3.1.10)$$

The luminosity is inversely proportional to the square of the transverse beam size at the interaction point and, hence, inversely proportional to a parameter called emittance ε. The concept of emittance is introduced in detail in [6]. A short summary can be found in the next section. β^* is the beta function at the collision point. It will also be explained in the next section.

The luminosity measurement can be used to determine the emittance of the colliding beams. The emittance obtained from luminosity is the convolution of the real beam emittances. From Eq. 3.1.9 and Eq. 3.1.10, and assuming β^* is the same for the horizontal and the vertical plane, which is the case in the LHC[1], the convoluted emittance equates as:

$$2\beta^*\varepsilon = \sqrt{\sigma_{1x}^2+\sigma_{2x}^2}\sqrt{\sigma_{1y}^2+\sigma_{2y}^2}, \quad (3.1.11)$$

$$\varepsilon = \frac{1}{2}\sqrt{\varepsilon_{1x}+\varepsilon_{2x}}\sqrt{\varepsilon_{1y}+\varepsilon_{2y}}. \quad (3.1.12)$$

Usually the emittances of the two beams and two planes per beam are not the same. The convoluted emittance is dominated by the larger of the two beams. The luminosity measurement is explained in chapter 8.

The LHC design peak luminosity at the interaction points of ATLAS and CMS

[1]The measured β^* values are presented in chapter 6.

is 10^{34} cm^{-2}s^{-1} with a nominal collision rate of 19.02 proton collisions per bunch crossing for a total cross section of 100 mb [1]. To maximize luminosity, beams with a large number of bunches and high bunch intensities are required, as well as small transverse emittances. In an ideal synchrotron the normalized transverse emittance is preserved. Disturbing effects such as machine resonances, noise and particle scattering lead, in general, to emittance growth [22]. Some of these effects will be discussed in chapter 4. To achieve maximum performance, the LHC injectors have to produce beams with as small emittances as possible. The challenge of the LHC is to conserve the small emittances through the cycle until the beams are brought into collision.

3.1.1. Luminosity Reduction Factor

There are many reasons why the two beam distributions might not fully overlap at the collision point. Examples are the introduction of a crossing angle, or accidental or deliberate collision offset. This leads to a reduction of the luminosity. Another effect reducing the luminosity is the hourglass effect, where the transverse beam size is not constant over the entire interaction region due to beta function increase with the distance to the interaction point. The hourglass effect becomes important only at very low β^*. With LHC design parameters, where the bunch length is much smaller than β^* ($\sigma_\mathrm{s} \ll \beta^*$), the luminosity reduction is less than 1 %. The strongest luminosity reduction in the LHC, about 20 % for LHC design parameters, comes from the crossing angle [6]. In this thesis, only luminosity reduction from crossing angle is considered.

In the LHC there are many circulating bunches with short bunch spacing. To prevent unwanted head-on interactions in the long common beam pipe around the interaction points, the two beams collide at an angle of ϕ =285 µrad by design, see Fig. 3.1. If the beams therefore do not fully overlap the luminosity has to be multiplied by a reduction factor F [21]:

$$L = \frac{f_\mathrm{rev} n_\mathrm{b}}{4\pi} \cdot \frac{N_1 N_2}{\beta^* \varepsilon} \cdot F. \tag{3.1.13}$$

For small crossing angles ($\tan\frac{\phi}{2} \approx \frac{\phi}{2}$), bunch lengths larger than the transverse beam sizes ($\sigma_\mathrm{s} \gg \sigma_\mathrm{x,y}$), and crossing in the horizontal ($u = x$) or vertical ($u = y$) plane, the luminosity reduction factor becomes

$$F \approx \frac{1}{\sqrt{1 + \left(\frac{\sigma_\mathrm{s}}{\sigma_u}\frac{\phi}{2}\right)^2}}. \tag{3.1.14}$$

The deduction can be found in [21]. In the LHC experiment CMS, located in interaction point 5 (IP5), the crossing is in the horizontal plane, while in ATLAS (IP1) the crossing is in vertical plane. This alternating crossing scheme is used in the LHC to reduce the overall tune shift that occurs when the two beams enter the joint vacuum chambers at the interaction point. The tune shift of separated bunches has opposite signs for the crossing and the separation plane when the separation is large enough [21].

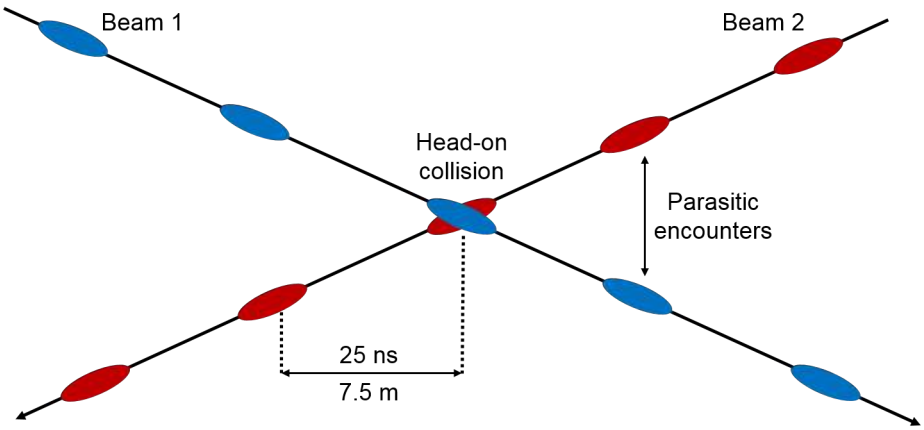

Figure 3.1.: Schematic of LHC collisions with crossing angle. Bunches 25 ns spaced apart collide head on at the interaction point. The crossing angle prevents parasitic head-on interactions but reduces the overlap of the colliding bunches.

3.2. Concept of Emittance

An introduction to basic accelerator physics linked to the concept of emittance can be found in appendix A. The concept of transverse emittance in a circular accelerator is discussed in the following.

Charged particles gain energy by accelerating them in electromagnetic fields. The construction of an accelerator determines the design orbit. To keep the particles on the reference path, which is curved in the case of the LHC, bending and focusing magnets are needed. Their magnetic field generates the necessary electromagnetic forces. The collection of bending and focusing magnets along the ideal path is called the magnet lattice.

The coordinates in six-dimensional phase space describing the particle motion in an accelerator are [23]

$$\vec{X}(s) = \begin{pmatrix} x \\ x' \\ y \\ y' \\ l \\ \frac{\Delta p}{p} \end{pmatrix} . \tag{3.2.1}$$

The ideal orbit for the charged particle beam designed by the beam transport system is called the reference trajectory s. Assuming the ideal particle on the reference path has transverse coordinates $x = 0$ and $y = 0$, the deviation of a particle from the reference path in the deflecting plane is u, where u can be either x or y. The derivatives $x' = \frac{\mathrm{d}x}{\mathrm{d}s}$ and $y' = \frac{\mathrm{d}y}{\mathrm{d}s}$ describe the horizontal and vertical slopes with respect to s. The coordinate l is the longitudinal displacement from the reference particle on the ideal path and $\frac{\Delta p}{p}$ is the relative momentum deviation from a reference particle with the ideal momentum p. The geometrical coordinate system is displayed in Fig. 3.2. The origin of the coordinate system (x, y, s) moves along the orbit of

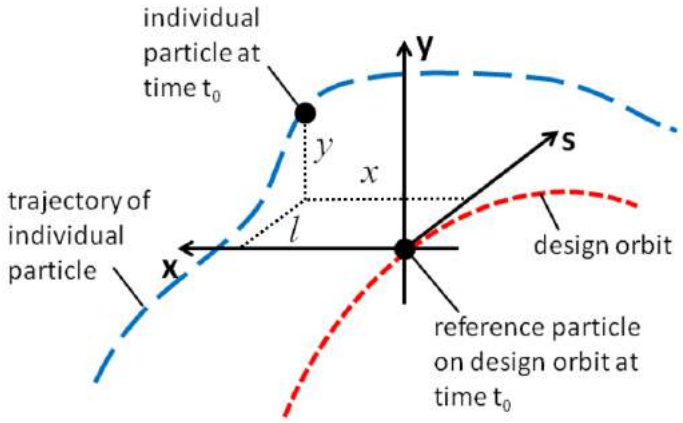

Figure 3.2.: Geometric coordinate system (x, y, s) with the design orbit (red) and a particle's trajectory (blue).

the longitudinal particle motion.

3.2.1. Solution of Hill's Equation

At presence of only linear magnetic fields the particle trajectory in the horizontal plane is solution to the homogeneous differential Hill equation:

$$x''(s) - k(s)x(s) = 0. \tag{3.2.2}$$

The function $x(s)$ defines a transverse motion around the design orbit, called betatron oscillation. $x''(s)$ denotes its second derivative with respect to the longitudinal position s in the accelerator and $k(s)$ is a periodic function that is defined by the accelerator's magnet lattice. The betatron oscillation amplitude and phase depend on the longitudinal position in the accelerator. The Hill equation is solved with the ansatz:

$$x(s) = a \cdot q(s) \cos(\psi(s) + \phi), \tag{3.2.3}$$

where ϕ is the initial phase and $a \cdot q(s)$ is the amplitude of the oscillation with the definition

$$q(s) \equiv \sqrt{\beta(s)}. \tag{3.2.4}$$

The solution to Hill's equation $x(s)$ and its derivative $x'(s)$ with respect to s, as well as the phase $\psi(s)$ are

$$x(s) = a\sqrt{\beta(s)} \cos(\psi(s) + \phi), \tag{3.2.5}$$

$$x'(s) = -\frac{a}{\sqrt{\beta(s)}} \left(\alpha(s) \cos(\psi(s) + \phi) + \sin(\psi(s) + \phi)\right), \tag{3.2.6}$$

$$\psi(s) = \int_0^s \frac{\mathrm{d}\lambda}{\beta(\lambda)}, \tag{3.2.7}$$

where $\beta(s)$ is the well-known beta function. The definition of $\alpha(s)$ is:

$$\alpha(s) \equiv -\frac{\beta'(s)}{2}. \tag{3.2.8}$$

The derivative $\beta'(s)$ is taken with respect to s. The functions $\alpha(s)$, $\beta(s)$ and $\psi(s)$ are called lattice or optics functions. They are defined by the focussing magnets of the accelerator in case of a periodic, circular lattice.

A particle on the design orbit has the ideal momentum p. Particles with momentum offset move on different trajectories, so called dispersive trajectories, which are determined by the particle's momentum deviation $\frac{\Delta p}{p}$ and the accelerator's dispersion function $D_u(s)$.

3.2.2. Emittance and Emittance Preservation

The solution Eq. 3.2.5 of the linear equation Eq. 3.2.2, has the invariant of motion of a single particle in phase space [22]

$$\gamma(s)x^2(s) + 2\alpha(s)x(s)x'(s) + \beta(s)x'^2(s) = a^2 = \text{const.} \tag{3.2.9}$$

Equation 3.2.9 describes an ellipse in phase space at a certain point s in the accelerator. The shape and orientation of the ellipse change when the particle moves through the accelerator. The area of the ellipse πa^2, however, remains constant. α , β and γ are the optical functions, also referred to as twiss parameters, at each point in the ring. The relation between those three functions is:

$$\gamma \equiv \frac{1+\alpha^2}{\beta}. \tag{3.2.10}$$

The invariant is called Courant-Snyder invariant. Equation 3.2.9 describes a skew ellipse in phase space (x, x') as shown in Fig. 3.3. For a periodic lattice, such as a circular machine, where $\beta(s+L) = \beta(s)$, $\alpha(s+L) = \alpha(s)$ and $\gamma(s+L) = \gamma(s)$, a particle's position and angle after one period must again lie on the same ellipse as on the previous pass.

For a beam of particles, there is a whole family of similar ellipses, centred around the origin. All ellipses have the same orientation. A particle which is contained inside an ellipse returns to a point inside the ellipse on a consecutive of the periodic motion through the accelerator. The emittance ε is defined by the ellipse

$$\gamma x^2 + 2\alpha x x' + \beta x'^2 = \varepsilon, \tag{3.2.11}$$

containing a fraction of particles of the beam. This ellipse will always contain the same fraction of beam on consecutive turns. In case of a Gaussian particle distribution

$$\rho(x,y) = \frac{Ne}{2\pi\sigma_\mathrm{x}\sigma_\mathrm{y}} \exp\left(-\frac{x^2}{2\sigma_\mathrm{x}^2} - \frac{y^2}{2\sigma_\mathrm{y}^2}\right), \tag{3.2.12}$$

with the horizontal and vertical beam sizes σ_x and σ_y, the emittance for a particular plane is defined as the ellipse with the fraction of beam contained within one σ_u $(u = x, y)$. The beam envelope $E(s)$ of this ellipse equals therefore

$$E(s) = \sigma_u = \sqrt{\varepsilon_u \beta_u(s)}. \tag{3.2.13}$$

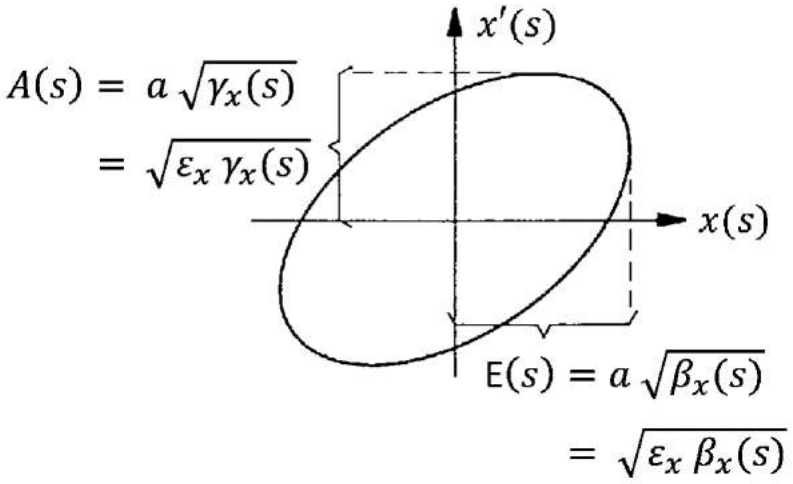

Figure 3.3.: A phase space ellipse in the horizontal plane. $E(s)$ is called beam envelope, $A(s)$ divergence.

Another important parameter of the phase space ellipse is the beam divergence $A(s)$:

$$A(s) = \sqrt{\varepsilon \left(\frac{1 + \alpha_u^2(s)}{\beta_u(s)} \right)} = \sqrt{\varepsilon_u \gamma_u(s)}. \tag{3.2.14}$$

The emittance of the particle beam $\varepsilon_{\text{stat}}$ is then defined in a statistical way: it is the ellipse which contains the particles within one standard deviation around the mean of the Gaussian distribution such that its beam envelope yields [22]

$$\varepsilon_{\text{stat}} = \varepsilon = \frac{\sigma^2(s)}{\beta(s)}. \tag{3.2.15}$$

The emittance is energy dependent. The conserved quantity, the emittance normalized to the beam energy, is defined as:

$$\varepsilon_{\text{N}} = \left(\frac{p}{m_0 c} \right) \varepsilon, \tag{3.2.16}$$

where p is the momentum and m_0 is the particle's rest mass. As proven by Liouville's Theorem, the normalized transverse emittance stays constant during acceleration for particles in an accelerator in absence of any perturbing fields [24], see also appendix A.

The normalized transverse emittance is treated in this document. The unit of the emittance used in this thesis is [µm].

4. Causes for Emittance Growth and Damping in the LHC

Contrary to Liouville's Theorem, numerous effects can lead to emittance increase or even decrease in an accelerator. It is part of the commissioning and optimization of the operational settings of the accelerator to study these effects and keep them to a minimum in the case of blow-up effects. In this chapter some of the typical effects leading to measurable emittance growth in the LHC are discussed. Other diffusion and scattering processes are explained in [25]. Also emittance damping effects are mentioned.

4.1. Injection Mismatch

One of the most import effects of emittance growth is injection mismatch. During the transfer and injection to the LHC, errors can occur that lead to emittance growth. Steering errors, injection oscillations and the complementary transverse damper system will be discussed. A full list of possible LHC injection errors can be found in [26]. To preserve the beam quality from the injectors to the LHC, it is necessary to match the beam trajectory, amplitude functions and dispersion functions at the transfer from one accelerator to the next. The optics matching between transfer line and LHC ring optics has been verified at several occasions and was found to be adequate to preserve the emittance [27]. Focusing errors that cause amplitude function mismatch and dispersion errors are not an issue for transfer line emittance preservation in the LHC. However, steering errors that cause injection oscillations due to a displacement from the design orbit prevail [28].

4.1.1. Emittance Growth from Steering Errors

If the particle phase space distribution is transferred mismatched with a displacement from the ideal orbit the injected beam will start oscillating around the orbit. These oscillations are called injection oscillations. Due to non-linear magnetic field components the betatron oscillation frequency depends on the oscillation amplitude. As a result of the incoherent particle motion, the beam distribution filaments and over time fills a larger phase space area. Hence, the emittance increases. Injection oscillations blow up the transverse emittance by [29]

$$\frac{\varepsilon}{\varepsilon_0} = 1 + \frac{1}{2}\frac{\Delta x^2 + (\beta\Delta x' + \alpha\Delta x)^2}{\beta\varepsilon_0} \equiv 1 + \frac{1}{2}\Delta e^2, \tag{4.1.1}$$

where Δx and $\Delta x'$ are the displacements in phase space from the ideal orbit at the injection point, α and β are the twiss parameters of the emittance ε after filamentation, and ε_0 is the emittance of the incoming beam. The particle distribution can be

disturbed severely such that, for example, initially Gaussian distributions develop large non-Gaussian tails [25].

The LHC has to allow a certain margin for injection oscillations due to shot-by-shot variations and drifts of the transfer lines, and SPS extraction and LHC injection kicker ripples [1] [30]. Injection oscillation amplitudes of up to ± 1.5 mm can occur before correction. To guarantee emittance preservation at injection, the steering errors are compensated by damping the injection oscillation through an external system that provides a damping time τ_d much smaller than the natural filamentation time τ_f, $\tau_d \ll \tau_f$. At the presence of a damping system, the emittance blow-up due to steering errors is [29]

$$\frac{\varepsilon}{\varepsilon_0} = 1 + \frac{1}{2}\Delta e^2 \left(\frac{1}{1 + \tau_f/\tau_d} \right). \tag{4.1.2}$$

4.1.2. The LHC Transverse Damper

In the LHC there are four independent transverse damper systems (ADT) for each beam and plane. The four ADT pick-ups measure the bunch position and kick the bunches back onto the ideal orbit on the next turn [31], see Fig. 4.1. The key elements of the ADT are Beam Position Monitors (BPMs) and electrostatic kickers, which are triggered by the processed BPM signal after time T_{signal} to damp the bunch oscillations at the next revolution n of the beam [32]:

$$T_{\text{signal}} = T_{\text{beam}} + n \cdot T_{\text{rev}}. \tag{4.1.3}$$

T_{beam} is the time the beam takes to arrive from the BPM position to the kicker position. The time for one LHC revolution is T_{rev}.

An example measurement of bunch-by-bunch beam 1 horizontal transverse oscillations damped by the ADT is shown in Fig. 4.2. During Fill 4583 the transverse positions of three single bunches were measured with ADT pick-ups. The envelope of the oscillating bunch position measurement defines the oscillation amplitude, also plotted in Fig. 4.2. The oscillation amplitude, a measure for the transverse activity, is decreasing quickly due to the damping. Assuming an exponential decay time of the oscillation amplitude, the damping time is defined as the time required for the oscillation amplitude to decrease to 1/e of its initial value.

The LHC transverse damper system can damp oscillations of up to 4 mm in less than 50 turns. The transverse damper gain can be adjusted to vary the damping time if needed [30]. A measurement of filamentation and damping times at 450 GeV injection energy of the LHC for single bunches can be found in Table 4.1.

The damper has to be able to deal with bunch-by-bunch differences of trajectory oscillations. Due to various kicker ripples the injection oscillations can vary significantly between different bunches, see Fig. 4.3. Also collective effects can lead to bunch-by-bunch differences of oscillation amplitudes. The LHC transverse damper has a bandwidth of 20 MHz with the kick strength varying according to a first order low pass filter (-3 dB at 1 MHz) [33], see Fig. 4.4. The ADT can stabilize bunch instabilities in a frequency range from 3 kHz to 20 MHz.

The LHC transverse feedback system provides emittance preservation and beam stability not only at injection but during the entire LHC cycle including stored,

[1] For SPS extraction and LHC injection fast pulsed kicker magnets are used.

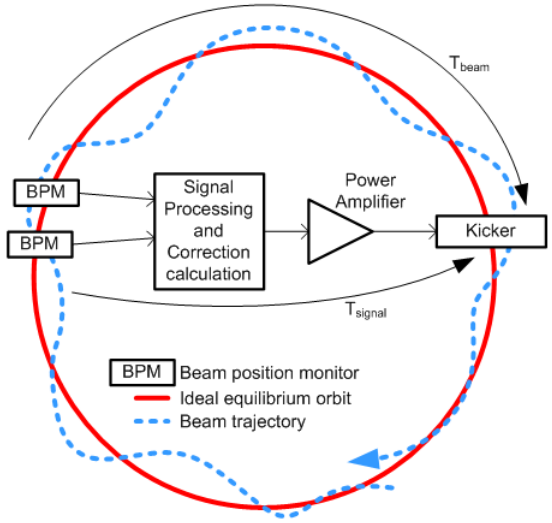

Figure 4.1.: LHC transverse damper (ADT) schematic [32]. Beam Position Monitors (BPMs) provide the transverse beam position feedback. Through a signal processing chain and a power amplifier the signal from the BPM triggers quasi-electrostatic kickers that kick the bunches back onto the ideal orbit on the next turn. T_{signal} is the time needed for the signal to travel from BPM to kicker. The time for the beam to arrive from the BPM to the kicker is T_{beam}.

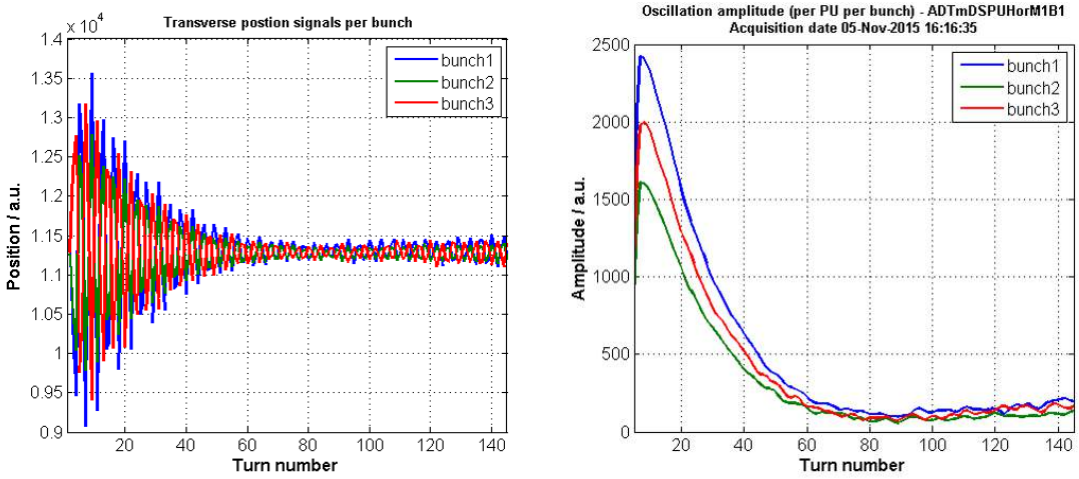

Figure 4.2.: LHC injection oscillations of beam 1 horizontal, damped by the ADT, Fill 4583. The left plots show the bunch-by-bunch transverse beam position measurement of the ADT pick-up ADTmDSPUHorM1B1, which is located in LHC IR4. The different colors, blue, green, and red, represent the pick-up signals for the different bunches. The envelopes of the bunch oscillations, the oscillation amplitudes, are also plotted (right). *Courtesy G. Kotzian, CERN, Geneva, Switzerland.*

colliding beams [34]. The damping time applied for physics fills at injection in 2015 was 5 to 10 turns [35]. For the ramp the gain was reduced to have a sufficiently

	B1H	B1V	B2H	B2V
Filamentation time [number of turns]	59	65	105	98
Damping time [number of turns]	25	21	35	27

Table 4.1.: LHC measured filamentation and damping times at 450 GeV for single bunches (5 November 2015). Measurements were taken in beam 1 (B1) and beam 2 (B2), horizontal (H) and vertical (V). The damping times for 25 ns bunch trains are about a factor 10 faster (5 - 10 turns). *Courtesy G. Kotzian, CERN, Geneva, Switzerland.*

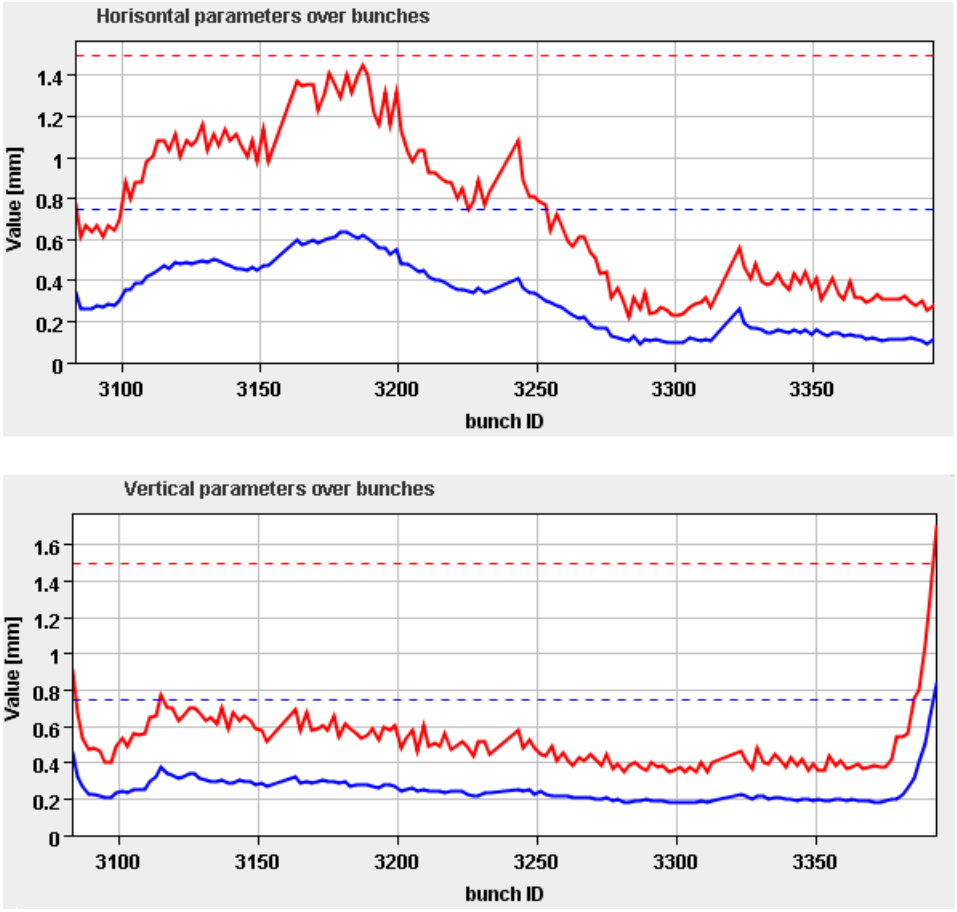

Figure 4.3.: Bunch-by-bunch injection oscillation amplitudes for beam 2 horizontal (top) and vertical (bottom). The maximum (red) and rms (blue) injection oscillation amplitudes over bunches are displayed with reference values (dashed). *Courtesy L. Drosdal, CERN, Geneva, Switzerland.*

good tune signal for the tune feedback system. The damping time at the start of the ramp was lower than 50 turns for physics fills in 2015. The power amplifiers of the transverse damper also allow the simultaneous use of the kickers for cleaning the injection gap and abort gap. An overview of the transverse damper system activities during injection and ramp of a nominal LHC cycle is given in Fig. 4.5.

For injection and beam dump the LHC is equipped with fast pulsed kicker magnets. During LHC filling a gap for the injection kicker and the beam abort kicker

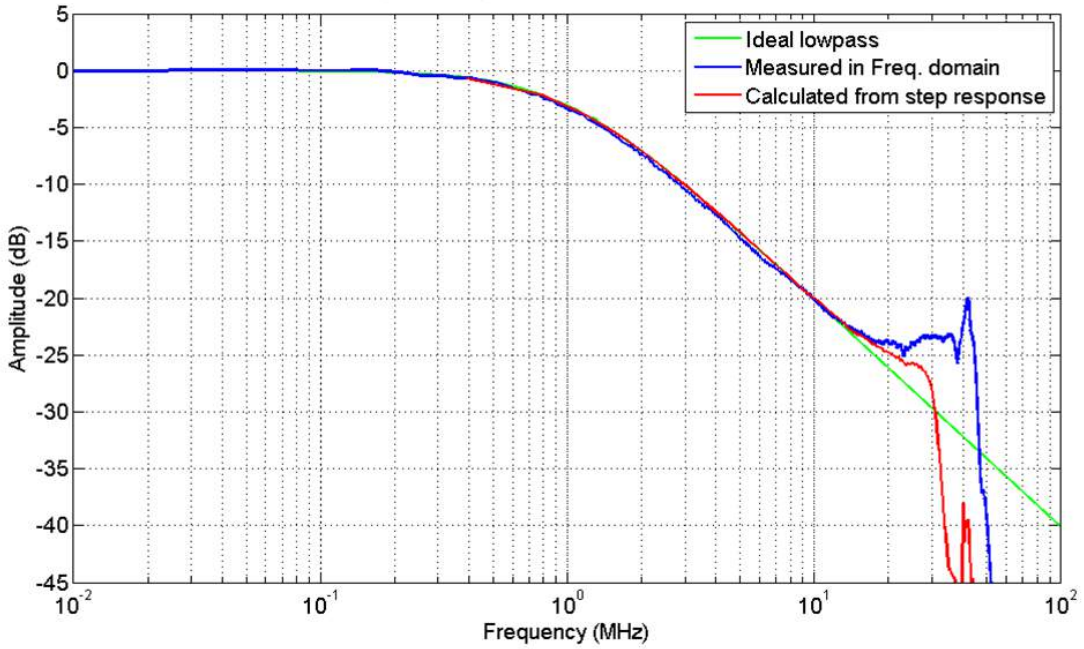

Figure 4.4.: ADT bandwidth [33]. ADT signal chain frequency response calculated from the step response via the HOM (higher order mode) port (red) and measured in frequency domain (blue). For comparison the ideal lowpass is displayed in green.

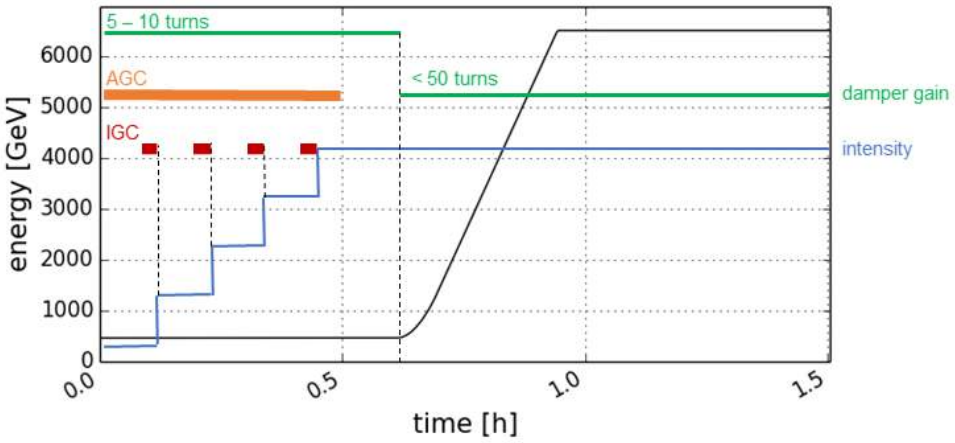

Figure 4.5.: Transverse damper activities through a nominal LHC cycle. The beam intensity is displayed in blue, the energy in black. The injection plateau, ramp and flattop of a nominal LHC cycle are shown. The transverse damper gain (green) is about 5 - 10 turns at the injection plateau and reduced at the start of the ramp to less than 50 turns. Abort gab cleaning (AGC, orange) excites particles in the abort gab during the entire length of the injection process. Injection gab cleaning (IGC, red) is active 10 - 15 seconds at each new injection into the LHC.

rise time of 1 µs and 3 µs, respectively, has to be kept beam free. Uncaptured beam should not populate the injection gap or the abort gap to avoid losses during either injection or extraction. The ADT is used to excite unbunched particles in the gaps in order to keep the gaps clean [36]. The excited particles are absorbed by the LHC collimators. For the cleaning a coherent signal in a defined time window was implemented [34]. While the abort gap cleaning (AGC) is active during the entire injection process, the excitation for the injection gap cleaning (IGC) is executed only 10 - 15 seconds before every injection at the moment when the LHC beam starts to be prepared in the SPS. The cleaning for the injection gab is applied only at the longitudinal space to be occupied by the next LHC injection. The injection gap cleaning signal is applied to the beam in the horizontal plane, while the abort gap cleaning has an effect in the vertical plane. Both cleaning modes are deactivated when the injection process is finished, before the ramp is prepared.

4.2. Intra-Beam Scattering and Synchrotron Radiation Damping

Various diffusion and scattering processes are present in an accelerator and can affect the beam. The particles in the beam can interact with the residual gas in the vacuum chamber, which can lead to increasing emittance and beam losses. Also small-angle scattering among the particles in a bunch can cause the beam sizes to grow. This is called intra-beam scattering (IBS) and will be explained in more detail.

The mechanism counteracting IBS is synchrotron radiation (SR) damping. The transverse emittance of a particle beam radiating energy can decrease. Synchrotron radiation damping for proton beams in the LHC will also be explained. In addition, simulation algorithms of IBS effects and radiation damping effects in the LHC are presented.

4.2.1. Intra-Beam Scattering (IBS)

Intra-beam scattering is multiple Coulomb scattering of the particles within a bunch [37]. The small angle elastic scattering is enhanced by a high particle density in the bunch, such as in the LHC bunches. The collisions change the momenta of the particles. Due to dispersion, a change in energy will cause a change in the betatron amplitude and thus, a coupling between betatron and synchrotron oscillations. Above transition, as it is the case for the LHC[2], transverse and longitudinal emittances will grow. The IBS growth times for the transverse and longitudinal planes scale like [38]:

$$\frac{1}{\tau_{x,y,\Delta p}} \propto \frac{r_0^2 c N}{\gamma^4 \varepsilon_x \varepsilon_y \varepsilon_L} \left\langle f_{x,y,\Delta p}\left(\beta_x, \beta_y, \varepsilon_x, \varepsilon_y, \frac{\Delta p}{p}, D_x, D_y\right)\right\rangle . \tag{4.2.1}$$

This scaling law gives an approximation of the emittance growth times due to IBS effects for the transverse planes (x, y) and the momentum spread Δp. r_0 is the classical particle radius, c is the speed of light, N is the number of particles in the bunch, and ε_L is the longitudinal emittance. The functions $f_{x,y,\Delta p}$ are averaged over the magnetic lattice and depend on the optics parameter, beta function and

[2]The LHC transition energy γ_{tr} is 55.68 [1].

periodic dispersion function[3] $D_{x,y}$, and on the emittance and the relative momentum deviation.

As an introduction to the IBS theory, the original IBS integrals for particle scattering in a classical relativistic way can be found in [37] (Piwinski Model). In the Piwinski Model the momentum changes due to intra bunch particle collisions are calculated. The resulting emittance and synchrotron oscillation amplitudes are computed. The average over all scattering angles and over all momenta and positions of colliding particles is taken into account assuming Gaussian particle distributions in a bunch. Solving such integrals analytically for all particles at each point in the accelerator is often not possible or very time consuming. Therefore a numerical approximation to calculate IBS growth rates is valid for an acceptable short time window.

IBS is more important for proton accelerators than for electron machines, which have sufficient radiation damping already at low energies that counteracts IBS. In a hadron collider such as the LHC, IBS can limit the luminosity lifetime.

With dipoles bending the beam in the horizontal plane in the LHC, dispersion is large in the horizontal plane (LHC design maximum horizontal dispersion in the arc is 2.018 m [1]) and almost negligible in the vertical plane. Thus measurable IBS emittance growth is mainly expected in the horizontal plane. In case of coupling or vertical dispersion the vertical emittance can also be increased by IBS.

IBS becomes less important at higher energies due to the γ^{-4} dependence of the growth rates. Higher beam intensities and smaller transverse and longitudinal emittances increase IBS growth rates [39]. For transverse emittance preservation of protons at the LHC, IBS plays a role mainly in the horizontal plane during the injection plateau and at the start of the ramp. The longitudinal plane is also affected. With LHC design parameters the IBS emittance growth rates presented in Table 4.2 can be expected [1].

	Injection	Collision
RMS beam size in arc [mm]	1.19	0.3
RMS energy spread $\Delta E/E$ [10^{-4}]	3.06	1.129
RMS bunch length [cm]	11.24	7.55
Horizontal emittance growth time [hours]	38	80
Longitudinal emittance growth time [hours]	30	61

Table 4.2.: IBS growth times at injection energy of 450 GeV and collision energy of 7 TeV with LHC design values.

4.2.2. Synchrotron Radiation (SR) Damping

Accelerated charged particles in a circular accelerator emit synchrotron radiation. The radiation is emitted tangentially to the direction of motion of the particle beam in a narrow cone for relativistic speeds [23]. Each particle's momentum is slightly decreased upon emission of a photon. Momentum loss affects the transverse and longitudinal planes. Although the energy loss per turn is restored when the beam

[3] If the magnetic lattice is periodic, the dispersion function has a periodic solution.

is passing the accelerating cavities, the emittances in all planes are decaying due to SR emission.

The emittance decay is called synchrotron radiation damping with damping time τ_i [40]:

$$\tau_i = \frac{2}{j_i}\frac{E_0}{U_0}T_{\mathrm{rev}} \tag{4.2.2}$$

with $i = x, y, L$, revolution period T_{rev}, energy E_0 and energy loss per turn U_0. j_i denotes the damping partition number. The emittance decay is exponential [40]:

$$\varepsilon_i(t) = \varepsilon_i(0)\mathrm{e}^{\frac{-2t}{\tau_i}}. \tag{4.2.3}$$

In a circular accelerator with curvature in the horizontal plane, assuming no coupling and zero vertical dispersion, synchrotron radiation damping is smaller in the horizontal plane than in the vertical plane [40]:

$$j_{\mathrm{x}} = 1 - \frac{I_4}{I_2}, \qquad j_{\mathrm{y}} = 1, \tag{4.2.4}$$

where I_2 and I_4 are the second and fourth synchrotron radiation integral[4] respectively, defined by the magnetic structure of the accelerator [41].

Radiation damping in the transverse and longitudinal planes plays an important role at LHC top energy. The LHC horizontal emittance damping time at 6.5 TeV is about 32 hours. With LHC design beam parameters the horizontal synchrotron emittance damping time is 26 hours at 7 TeV, see Table 4.3.

	Injection	Collision
Instantaneous power loss per proton [W]	3.15×10^{-16}	1.84×10^{-11}
Synchrotron radiation power per ring [W]	6.15×10^{-2}	3.6×10^{3}
Energy loss per turn [eV]	1.15×10^{-1}	6.71×10^{3}
Longitudinal emittance damping time [hours]	48489.1	13
Horizontal emittance damping time [hours]	48489.1	26

Table 4.3.: Synchrotron radiation damping times at injection energy of 450 GeV and collision energy of 7 TeV with LHC design values.

4.2.3. IBS and SR Damping Simulations with MADX

IBS simulations in this thesis were carried out with the MADX IBS module [42]. The IBS growth rates in this module are based on the Bjorken-Mtingwa theory [43].

[4]The integrals I_2 and I_4 [m^{-1}] are taken along the reference trajectory over one complete turn of the ring with radius R:

$$I_2 = \oint \frac{1}{R^2}\mathrm{d}s, \qquad I_4 = \oint \frac{D_{\mathrm{x}}}{R}\left(\frac{1}{R^2} + 2k_1\right)\mathrm{d}s. \tag{4.2.5}$$

$k_1 = \frac{q}{p_0}\frac{\partial B_{\mathrm{y}}}{\partial x}$ is the quadrupole gradient in the dipole field, scaled by the reference momentum p_0.

This formalism gives a solution in the ultra-relativistic limit, but neglecting vertical dispersion. Therefore the module also uses the expansion of the Conte-Martini algorithm [44] generalized to the case of non-zero vertical dispersion and valid even if the beam energy is not ultra-relativistic.

The Bjorken-Mtingwa formalism takes into account the variation of the lattice parameters (beta and dispersion functions) around the accelerator. But the IBS module does not include any treatment of betatron coupling. In addition, perfect Gaussian beams are assumed.

The LHC IBS growth rates are typically in the order of several hours. The time interval used for simulations is $\Delta t = 10$ s. The expected emittance blow-up from IBS in this short time period is also very small. Therefore the following linear approximation is valid to calculate the resulting emittance ε growth from IBS growth rates τ if $\tau \gg \Delta t$:

$$\varepsilon \approx \frac{\varepsilon_0}{\left(1 - \frac{\Delta t}{\tau}\right)}, \tag{4.2.6}$$

where ε_0 is the initial emittance.

IBS Simulation Input Parameters

For this work IBS simulations during the entire LHC cycle have been launched. For the simulations the measured initial beam parameters, such as transverse emittances, bunch length and intensity, are used. The MADX algorithm assumes a bunched proton beam with N number of particles per bunch. The longitudinal emittance ε_L is calculated from the relative energy spread $\frac{\Delta E}{E}$ and the bunch length σ_s:

$$\varepsilon_\mathrm{L} = \sigma_\mathrm{s} \frac{\Delta E}{E}. \tag{4.2.7}$$

The energy spread in the LHC is computed from the RF voltage, the energy and the bunch length assuming a matched distribution. During the 2015 LHC energy ramp the RF voltage is increased from 6 MV at 450 GeV to 10 MV at 6.5 TeV.

The knowledge of the optical functions along the machine is required for MADX simulations. The LHC design optics are used as input. Random quadrupole misalignments are introduced in the code before matching the orbit to account for vertical dispersion. The average vertical dispersion around the ring is assumed to be 20 % of D_x in amplitude. Also crossing angles in all four LHC interaction points are included.

In addition, synchrotron radiation damping is part of the simulations. First, the equilibrium emittance from radiation damping is calculated. Then emittance growth from IBS effects is simulated. MADX computes IBS growth times $\frac{1}{\tau_i}$ in [s]:

$$\frac{1}{\tau_i} = C_i \frac{N}{\gamma_i \varepsilon_\mathrm{x} \varepsilon_\mathrm{y} \varepsilon_\mathrm{L}}, \tag{4.2.8}$$

where C_i stands for IBS constants and the intra beam scattering functions as indicated in Eq. 4.2.1.

All beam parameters are left to evolve according to the IBS algorithms. However, since manipulations on the bunch length are performed during the ramp [45], the measured bunch lengths during the ramp instead of the simulation result are used.

Also, the MADX algorithms assume perfect transmission through the cycle. In the case of the LHC this is a valid guess. As can be seen in Fig. 4.6 intensity losses during the cycle are typically smaller than 2 % on average through the LHC cycle in 2015, which does not change the simulation results quoted in this thesis.

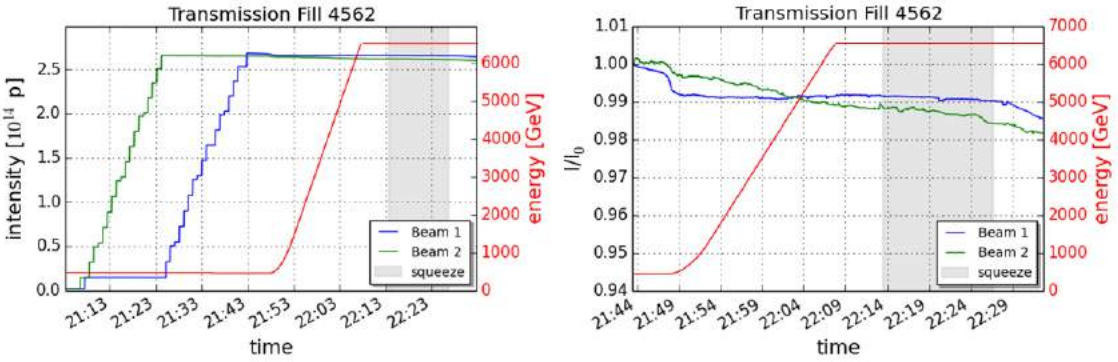

Figure 4.6.: Transmission through the LHC cycle in 2015. The beam intensity evolution for beam 1 (blue) and beam 2 (green) from injection to start of collisions is shown for physics Fill 4562 (1 November 2015). The left plot shows the absolute beam intensity. The energy is plotted in red. The squeeze is indicated in grey. In the right plot the relative intensity losses from end of injection to start of collisions are displayed, normalized to the intensity I_0 after the injection process is finished. Collisions start after the end of the squeeze.

4.3. Emittance Growth from External Noise

Accelerators like the LHC with revolution frequencies in the kHz range are potentially affected by external noise such as random dipole field noise, power supply noise and ground motion. Noise can introduce random kicks on the beam and therefore also increase the emittance [38].

Two mechanisms based on the noise frequency leading to emittance growth have to be distinguished [46]:

- noise at low frequencies, much less than the revolution frequency f_{rev}, and
- noise at frequencies near the resonant betatron frequencies.

The latter resonantly excites betatron oscillations that cause emittance growth with growth rates proportional to the noise frequency. For instance, dipole magnets can produce field noise that gives small random kicks to the beam causing momentum changes. These kicks, averaged over many turns, cause the betatron oscillation amplitude and, hence, the emittance to grow, proportional to the square of the kick angle θ [6]

$$\frac{\mathrm{d}\left\langle r^2\right\rangle}{\mathrm{d}n} = \beta\left\langle\theta^2\right\rangle, \tag{4.3.1}$$

where n is the number of turns and r is the amplitude in phase space. In this formula the average kick angle originates from a location in the ring with beta function β.

The resulting emittance growth over time t is

$$\frac{\mathrm{d}\varepsilon}{\mathrm{d}t} = \frac{1}{2}\beta f_{rev} \left\langle \theta^2 \right\rangle , \tag{4.3.2}$$

For noise created by random fluctuations of the dipole magnetic field $\langle(\Delta B)^2\rangle$, the averaged squared kick angle over many turns yields:

$$\left\langle \theta^2 \right\rangle = \frac{\langle(\Delta B)^2 l^2\rangle}{(B_0 R)^2} \tag{4.3.3}$$

over the length of the dipole l with bending radius R and magnetic field B_0. In the presence of dipole field noise the emittance grows linearly with time [46]. Noise with a frequency equal to the frequency of the betatron sidebands is responsible for emittance growth. In the LHC the lowest resonant noise frequency is $f_{\mathrm{rev}} \cdot Q_H = 3.15$ kHz with a horizontal fractional tune Q_H of 0.28.

Higher order magnetic field perturbations with noise frequencies near the betatron frequencies can also lead to emittance growth. For example quadrupole magnetic field fluctuations $\langle(\Delta B')^2\rangle$ from vibration of sextupoles or quadrupole current ripples kick the beam proportional to the its magnetic field gradient B_0' [46]:

$$\left\langle \theta^2 \right\rangle = \frac{2\pi\varepsilon_0\beta}{f^2} \frac{\langle(\Delta B')^2\rangle}{(B_0')^2}, \tag{4.3.4}$$

with f being the quadrupole focal length. In this case noise frequencies of twice the betatron frequency contribute to emittance growth. The growth rate depends on the initial emittance ε_0.

Perturbations that produce transverse kicks on the beam may also originate from quadrupole vibrations. Ground motion and other external noise sources can kick the beam angularly when the quadrupoles are misaligned. In first approximation, the angular kicks from the quadrupoles with a ground motion amplitude of $\langle(\Delta x)^2\rangle$ are given by [46]

$$\left\langle \theta^2 \right\rangle = \frac{\langle(\Delta x)^2\rangle}{f^2}, \tag{4.3.5}$$

for ground motion wavelengths larger than the betatron wavelength. In the LHC emittance growth from quadrupole vibrations becomes important only if the amplitude of the perturbation is in the range of several hundred nm. Giving for instance an LHC triplet quadrupole with a focal length of 20 m at a β of 1000 m, which suffers from random noise vibrations with an rms amplitude of 100 nm, such a vibration would produce an emittance growth rate of about 0.5 µm/h according to Eq. 4.3.5. Beta functions in the LHC in the km range are only present after the β^* squeeze. At injection energy and during the ramp, the beta function at the above mentioned quadrupole is only about 100 m, as is the case in most quadrupoles in the LHC. Hence, the resulting emittance growth from noise vibrations at these quadrupoles is a factor 10 smaller (0.05 µm/h).

Emittance growth due to noise of several sources was considered for a single magnet in the absence of a transverse feedback system. In case of noise from several magnets the kick angles from each magnet have to be accumulated. In the LHC excitation of betatron oscillations should be suppressed by the LHC transverse damper system, see section 4.1.2. However this is only efficient for a single noise kick. Con-

tinuous noise producing many kicks at each LHC revolution cannot be damped completely. Residual oscillations cause emittance growth through decoherence with slightly lower growth rates than derived above.

4.3.1. The LHC Noise Spectrum

At certain frequencies the LHC beam spectrum reveals pronounced peaks with high amplitudes due to noise. In Fig. 4.7 the LHC beam spectrum for each beam and plane is displayed. It was measured in 2015 at 450 GeV LHC injection energy with the ADT pick-ups in point 4 [47]. The blue and red lines show an FFT (Fast Fourier Transformation) of the measured turn-by-turn transverse beam positions. The FFT is compared to results from a Numerical Analysis of Fundamental Fre-

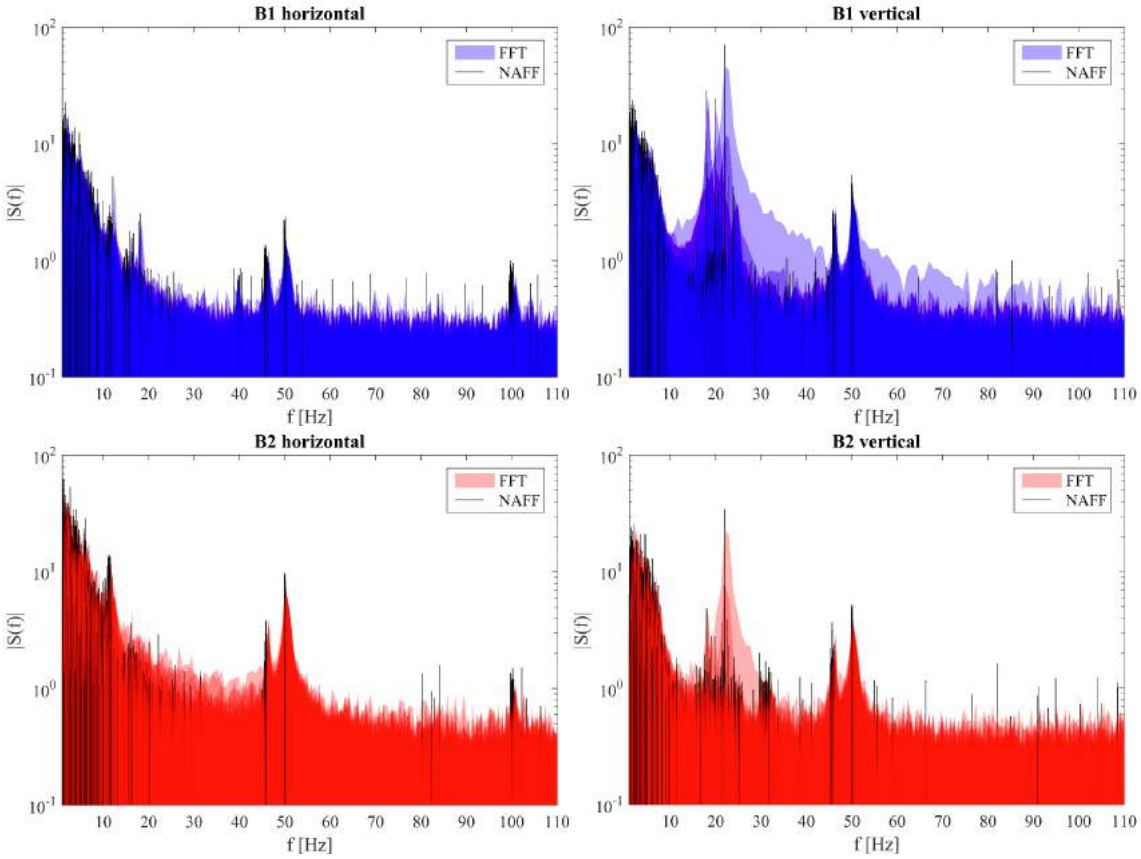

Figure 4.7.: LHC noise spectrum for beam 1 and beam 2, horizontal and vertical [47]. The beam spectrum was measured at 450 GeV with the ADT pick-ups (Q7). The plots show an FFT of the turn-by-turn transverse beam position measurements (blue and red) during Fill 4624 (17 November 2015). The FFT is compared to results from NAFF (black), a Numerical Analysis of Fundamental Frequencies. The dark blue and dark red areas indicate the natural beam spectrum. During certain periods the effect of surface vibrations on the beam at interaction point 1 was enhanced in the vertical planes with external ground vibrations at the dominant frequencies (light blue and red).

quencies (NAFF) [48], which can be used to improve frequency, amplitude and phase resolution. Over a period of about 30 minutes turn-by-turn beam position data was acquired and overlaid in Fig. 4.7. The dark blue and dark red areas indicate the natural beam spectrum. During certain periods surface vibrations on the beam at interaction point 1 were enhanced on purpose in the vertical planes with external ground vibrations at the dominant frequencies. These periods are displayed in light blue and red.

Amplitude and frequency of the peaks in the natural LHC beam spectrum can indicate the source of the noise and the resulting emittance growth. In the horizontal planes, next to the 50 Hz main harmonics, noise lines at 8 Hz and 12 Hz are dominant in the spectrum. In the vertical plane a similar oscillation occurs around 20 Hz. In both planes random noise vibrations of the LHC triplets magnets are suspected [49]. Due to the layout of the magnets in the LHC interaction regions 1 and 5 above mentioned frequencies are resonant. An external vibration with frequencies equal to the triplet resonant frequencies emphasizes the peaks in the beam spectrum significantly. The source of the noise at these frequencies could be ground motion. The LHC ground motion spectrum was measured in the past. Figure 4.8 shows the power spectral densities of the horizontal and vertical displacement in the LHC and its integrals. In the horizontal plane noise from ground motion has an amplitude of about 18 nm in the 10 Hz region. In the vertical plane, however, the amplitude at similar frequency is almost double, around 30 nm. In general, the spectral density decreases with higher frequencies.

To determine the absolute amplitude of the dominant noise peaks, the FFT of the ADT data was converted into µm/Hz with a previously defined calibration factor [47]. Figure 4.9 shows the results for the vertical planes. Looking at the darker shaded area, where no external excitation took place, some peaks around 20 Hz appear in the LHC spectrum with amplitudes of up to 12 µm in beam 1 and up to 4 µm in beam 2. This would result in a large vertical emittance growth at 450 GeV of about 0.2 µm/s in beam 1 and 0.02 µm/s in beam 2 according to Eq. 4.3.5[5]. However, these few measurements in 30 minutes of the ground motion spectrum at the LHC are not fully representative. The ground motion spectrum can differ by several orders of magnitude depending on external conditions such as time of the day.

[5]Assuming a triplet magnet with 20 m focal length and 100 m beta function vibrates constantly with the same ground motion amplitude during the LHC injection plateau.

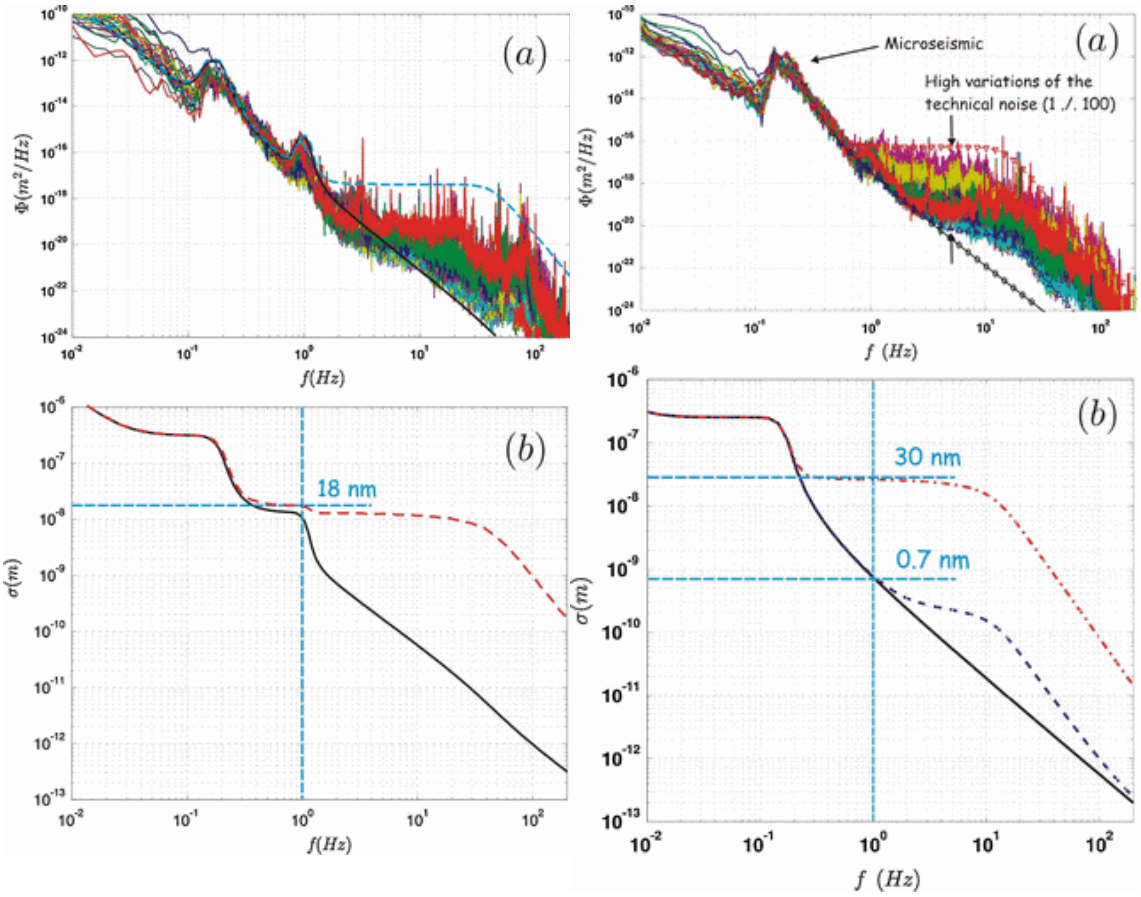

Figure 4.8.: LHC ground motion [50]. (a) Power spectral densities (PSDs) of the measured horizontal (left) vertical (right) displacement in the LHC tunnel due to ground motion. The model is extracted from the measurements (solid circled line). Lower and upper envelopes of the measured PSDs are shown. (b) Integrated rms displacements of the model (solid line) and the lower (dashed line) and upper (dash-dotted line) envelopes shown in (a).

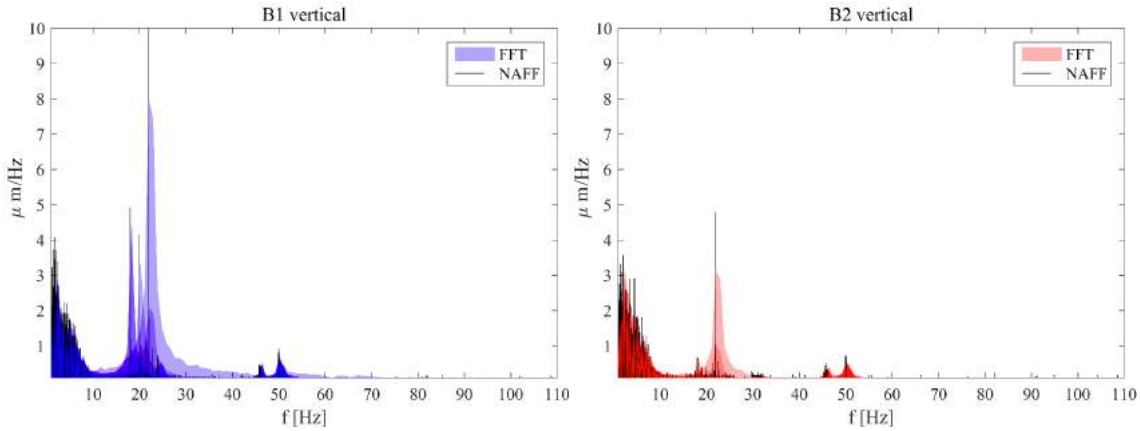

Figure 4.9.: LHC noise spectrum for beam 1 and beam 2 vertical [47]. The beam spectrum was measured at 450 GeV with the ADT pick-ups (Q7) as seen in Fig. 4.7. The amplitude of the FFT data was converted into µm/Hz with a previously defined calibration factor.

Part II.

Motivation: LHC Run 1 Emittance Preservation Studies

5. Emittance Preservation at the LHC in 2012

The luminosity production is tightly linked to emittance preservation in the collider. During the 2012 LHC proton run about 30 % of the potential luminosity performance was lost, mainly due to blow-up of the transverse emittances, compared to the 7 % allowed emittance blow-up in the design report [1]. Investigations during LHC Run 1 showed that a number of sources can cause emittance growth in the LHC, among them intra-beam scattering and 50 Hz noise. This chapter summarizes the outcome of the 2012 LHC emittance growth studies, also in view of the found limitations of Run 1 beam size measurement systems. The presented investigations on emittance measurement and preservation have been published in [6, 51–55]. The findings led to improved diagnostics and additional tools for the Run 2 emittance preservation studies.

5.1. LHC Transverse Profile Monitors in 2012

The different transverse profile measurement systems in the LHC, as well as the advantages and disadvantages of the various instruments are discussed in detail in [6]. In the following a short summary of profile monitors used during the 2012 LHC proton run to measure transverse beam sizes, and hence emittance, is given.

The only available LHC transverse profile monitors in 2012 were:

- wire scanners and
- Beam Synchrotron Radiation Telescopes (BSRT).

Both instruments are capable of measuring bunch-by-bunch transverse profiles.

Wire scanners can only be used with low intensity beams. They serve as a calibration instrument for other profile monitors. In 2012 they were also regularly used to measure the transverse emittance of the first injected batch of physics beams. Each LHC ring is equipped with two operational linear wire scanners, one for the horizontal and one for the vertical plane [1]. The transverse beam profile is scanned by moving the wire through the beam. Wire heating and the quench risk of the LHC superconducting magnets limit the beam intensity with which the wire scanners can be used in the LHC. In 2012 the limit at 450 GeV injection energy was 144 bunches, which corresponds to the first injected batch coming from the SPS. At 4 TeV flattop energy in 2012 the total measurable number of bunches with wire scanners was reduced to about 30 with an intensity of about 1.5×10^{11} protons per bunch (ppb). After a wire had been broken in September 2012, the usage of LHC wire scanners was further limited.

The synchrotron light monitors on the other hand provide continuous, automatic, and passive profile measurements, compatible with high intensity operation. Useful beam size measurements can be obtained at 450 GeV and flattop energy. However,

during the LHC energy ramp BSRT measurements cannot be used because the light source switches from undulator to dipole. Since the image system cannot be focused on both light sources at the same time, image blurring is a concern. Another limitation is the measurement speed. In bunch-by-bunch mode the BSRT scanned 3 to 4 bunches per second in 2012, compared to 1380 bunches in the ring for physics fills. From September 2012 until the end of LHC Run 1 only the BSRT for beam 1 was operational due to heating and deformation of the beam 2 BSRT extraction mirror [56]. No beam profiles for beam 2 were available until the end of the 2012 proton run.

5.2. Emittance Growth during the 2012 LHC Cycle

Emittance preservation studies during early Run 1 revealed a substantial growth of the normalized transverse emittance from LHC injection to collisions. One of the goals during the 2012 LHC run was therefore to quantify, understand and counteract the blow-up. A number of plausible causes of the emittance growth could be found. They are presented in this chapter.

Figure 5.1 shows the evolution of the emittances in collision obtained from luminosity (green dots) and after injection from wire scans (yellow stars) for the different physics fills in the 2012 proton run. Only fills with 1374 bunches per ring and 50 ns bunch spacing were taken into account. The averaged emittance of the first 144 bunches in the LHC is displayed. The injectors managed to produce beams of record brightness, especially with the introduction of the Q20 optics[1] in the SPS after Technical Stop 3 (TS3) [57]. Emittances of 1.5 µm with bunch intensities of up to 1.7×10^{11} protons per bunch (ppb) were injected into the LHC. However, this brightness could not be preserved during the LHC cycle. At the start of collisions the emittances had blown up to 2.3 µm on average almost independent of the initial emittance.

To find out where the emittances are growing in the LHC cycle and to track down the sources of the blow-up, measurements at the different parts of the 2012 cycle were performed:

- shortly after injection into the LHC,
- during the 450 GeV LHC injection plateau,
- during the LHC ramp to 4 TeV flattop energy,
- during the LHC β^* squeeze and
- at the start of collisions.

Low intensity test cycles were used to allow wire scanner measurements through the entire cycle. The LHC BSRTs gave insights into the emittance evolution during the injection plateau and at 4 TeV. Also ATLAS and CMS luminosities were used to shed light on the emittance blow-up in the LHC. A typical example of a low intensity test fill emittance measurement through the cycle with wire scanners (Fill 3217) is

[1]The SPS changed from the so called Q26 optics to Q20 optics to lower the integer part of the tune and therefore the transition energy in the machine and, hence, increase the Transverse Mode Coupling Instability (TMCI) threshold intensity. After this change the emittances from the injectors could be even further reduced, from 1.8 µm to 1.5 µm.

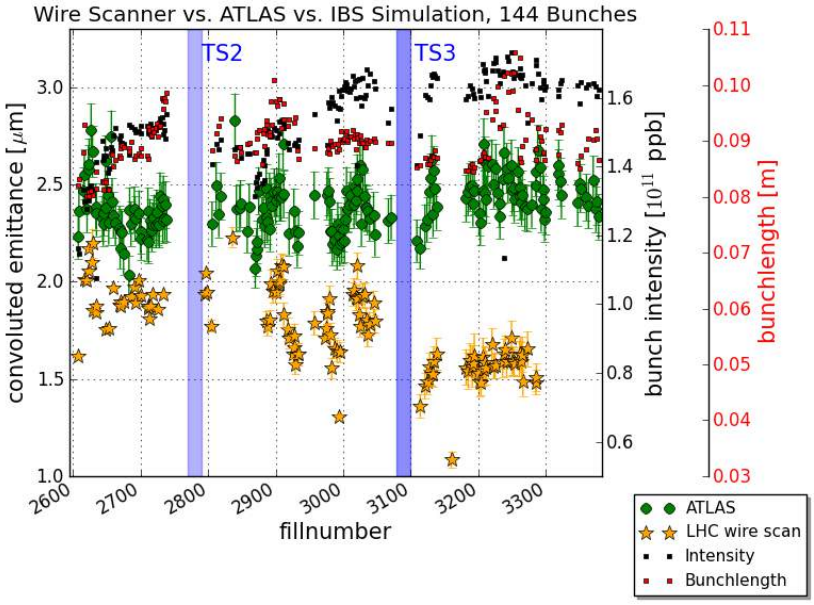

Figure 5.1.: Emittance at LHC injection and start of collisions. Convoluted average emittance of the first 144 bunch batch at injection (orange stars), measured with wire scanners, and at the start of collisions (green dots), calculated from ATLAS bunch luminosity using measured bunch length (red) and intensity (black).

shown in Fig. 5.2. Two six bunch batches per ring with bunch intensities of about 1.6×10^{11} ppb and 50 ns bunch spacing had been injected, ramped, squeezed and brought into collision. The emittances in the horizontal plane blow up more than the vertical ones. Most of the blow-up seems to come from the injection plateau and the ramp. For this particular fill significant growth also occurs towards the end of the squeeze in beam 1 horizontal. The measurements in Fig. 5.2 include the start of collisions.

5.2.1. Emittance Preservation at Injection into the LHC

Wire scan measurements of 144 bunch batches before extraction in the SPS were compared to wire scan measurements of the first 144 bunch batch in the LHC. The emittances in the vertical and horizontal plane are conserved within measurement precision at injection from the SPS into the LHC. This is the result of the good matching of the transfer lines to LHC injection point optics and the excellent performance of the transverse damper system. The effect of the partly large injection oscillations coming from transfer line trajectory instabilities [58] is kept well under control with the LHC transverse damper [31].

5.2.2. Emittance Growth during the LHC Injection Plateau

Emittance Blow-up due to Intra-Beam Scattering (IBS)

The LHC transverse emittances grow slowly when the beams are circulating at 450 GeV. The growth is stronger in the horizontal plane and does not necessarily

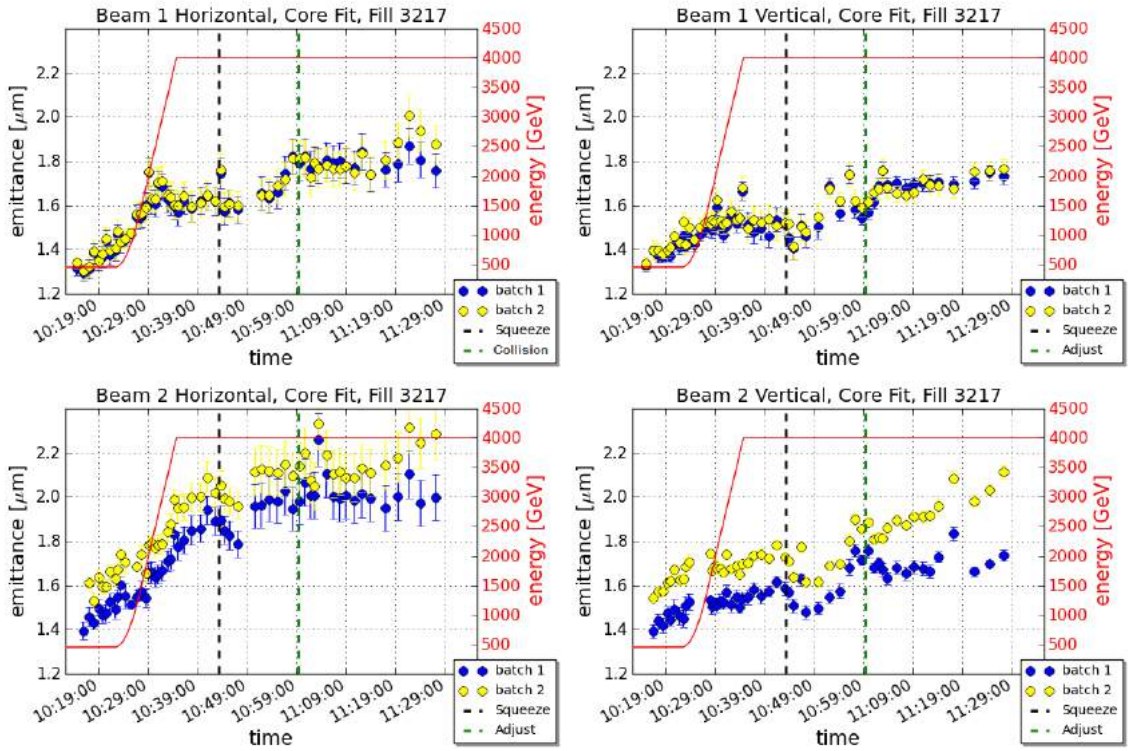

Figure 5.2.: Emittance growth through the LHC cycle for beam 1 and beam 2, horizontal and vertical. The average emittance of six bunches per batch is measured with wire scanners, Fill 3217. Vertical dashed lines indicate the start of the squeeze (black) and the start of collisions (green). Batch 1 is colliding in LHCb, batch 2 in ATLAS and CMS.

manifest itself in the vertical plane in all fills. The measured horizontal growth rate corresponds to about 10 % growth within 20 minutes for typical 2012 injection beam parameters. Simulations[2] suggested that the largest fraction of this growth can be attributed to intra-beam scattering (IBS) [59]. Using the measured beam parameters as initial values, the emittances increase by 8 % in 20 minutes in IBS simulations.

Bunch Lengthening as a Cure for IBS

As a solution for the effects from IBS the longitudinal RF batch-by-batch blow-up was tested at 450 GeV [60]. For MD Fill 2556 wire scans of 12 bunch batches were frequently taken. In Fig. 5.3 the relative emittance evolution of beam 2 horizontal for batches blown up longitudinally in the first minute following injection, and batches left to natural blow-up is plotted. The batches that are not artificially blown up suffer more from emittance growth. Their emittance blow-up is about 20 % in 20 minutes. For the longitudinally blown up batches, the growth is only about 10 % in 20 minutes. The emittance growth is clearly reduced.

At the end of the 2012 LHC proton run, RF batch-by-batch blow-up with target bunch lengths of 1.4 and 1.5 ns at LHC injection of physics beams was tested during several fills. However, no significant improvement of the emittance blow-up for

[2]Simulations were done with the MADX IBS module, see chapter 4.2.3.

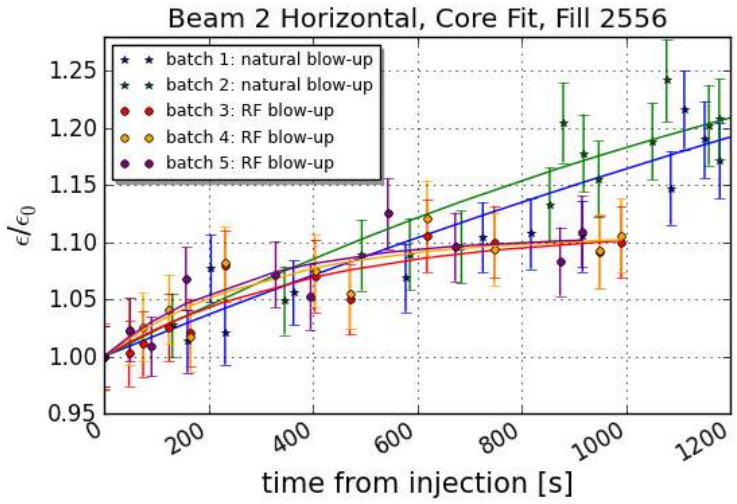

Figure 5.3.: RF batch-by-batch blow-up test with 5 batches of 12 bunches. Batches 1 and 2 are left to natural blow-up. Batches 3, 4 and 5 are longitudinally blown up from a bunch length of 1.1 ns after capture to a target of 1.6 ns. An exponential fit (line) is applied to the relative emittance growth measured with wire scanner (dots). ε_0 is the emittance at injection into the LHC.

physics beams was observed. It is possible that this measure reduced the emittance blow-up after all, but bunches at the end of the cycle became partly unstable and ended up with higher emittances at the start of collisions.

Effect of Noise on Emittance Growth

The emittance growth at 450 GeV is well predicted with IBS, but slightly faster than the simulation in the horizontal plane[3]. The remaining growth could be due to noise. The LHC tune spectrum reveals many noise lines, see Fig. 5.4. Some of the noise lines correspond to multiples of the 50 Hz main harmonics. In addition, the LHC horizontal tune used at injection sits on top of a multiple of 50 Hz, which could slightly excite the beam. A plausible noise source could not be tracked down. The reason for the vertical growth at the same time despite a different tune is not clear. Coupling could explain part of it.

5.2.3. Emittance Preservation during the LHC Ramp

Measurements indicate significant growth of the normalized emittances during the ramp, which is larger in the horizontal plane than in the vertical plane and more pronounced for beam 2 than for beam 1. For Fill 3217 the total average emittance growth during the ramp is about 20 % for beam 2 horizontal, about 15 % for beam 1 horizontal, and approximately 5 % in the vertical plane for both beams. The measured beta functions are used at injection and flattop and a linear interpolation between these values for energies during the ramp is applied. Dispersion

[3]There is about 2 % discrepancy between measured and simulated emittance growth at 450 GeV for 2012 beam parameters.

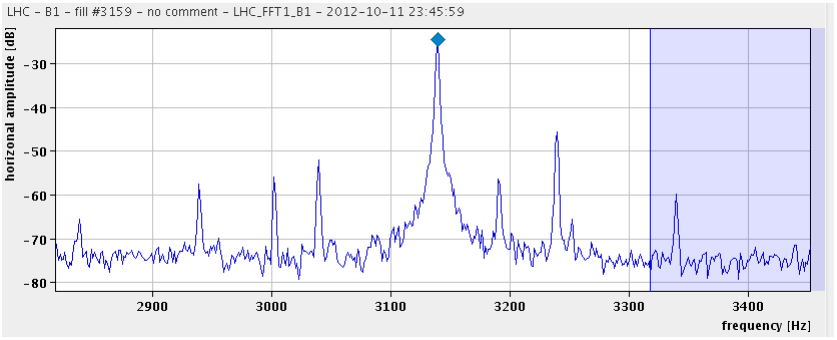

Figure 5.4.: LHC beam spectrum for the nominal tune (0.28 in the horizontal plane) measured with the LHC Base-Band-Tune System (BBQ) for beam 1 horizontal. The frequency of the nominal tune is displayed (blue diamond). The horizontal tune sits at 3149 Hz and the signal has a large amplitude due to 50 Hz noise (approximately -20 dB).

is not taken into account as it has been measured to be small [6]. Note that the absolute emittance blow-up through the ramp is roughly the same, independent of the emittance value at the start of the ramp.

Shrinking Emittance during the LHC Ramp

Measurements through the ramp with wire scanners in the beginning of 2012 revealed emittances partly shrinking with energy. Examples are shown in Fig. 5.5. The normalized emittance is plotted for different planes and different fills. This unphysical behaviour was observed during several ramps measured with wire scanners. The measured emittances decreased by different amounts for the different beams and planes. No correlation between energy, plane and emittance decrease was found.

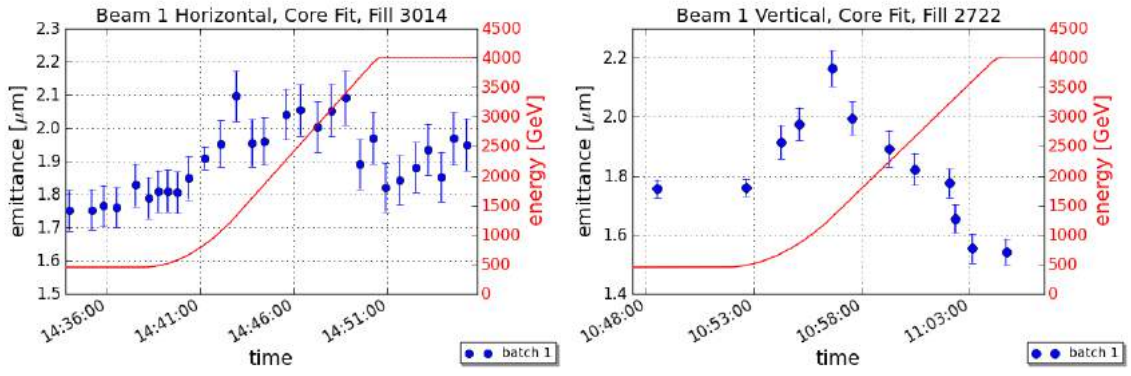

Figure 5.5.: Shrinking emittance during the ramp for different planes and fills. The emittance decreases by different amounts and at different energies. Plot of Fill 3014 depicts the average emittance of six 50 ns bunches. For Fill 2722 the average emittance of 12 50 ns bunches is shown.

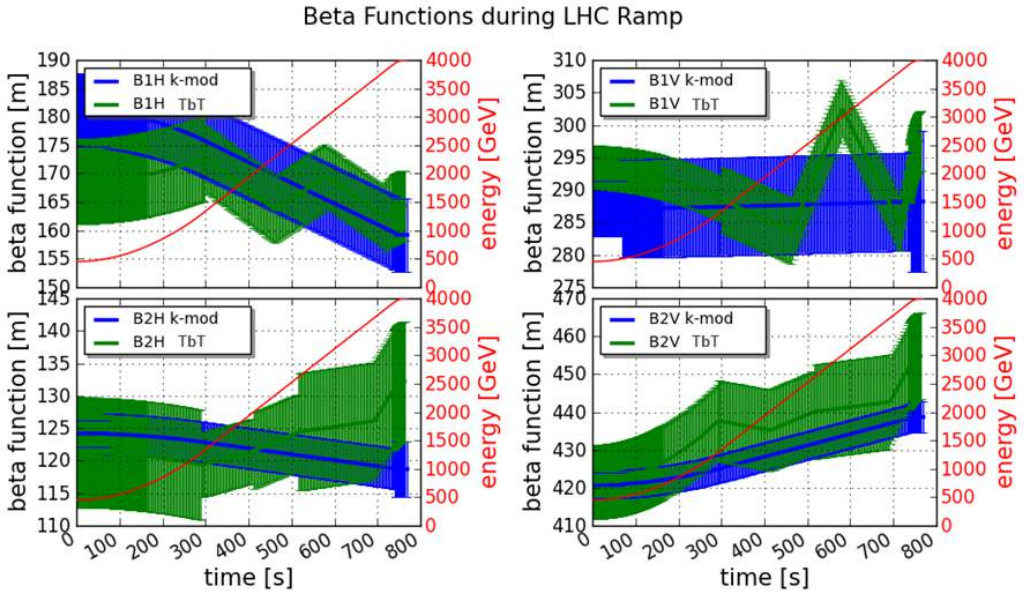

Figure 5.6.: Comparison of measured beta functions during the ramp (TbT, green) and linear interpolation from k-modulation β at injection and flattop energy (k-mod, blue). Measurements during the ramp were performed with the turn-by-turn phase advance method. A linear interpolation is used between the different beta measurement points. Measurement results are given for beam 1 (B1) and beam 2 (B2), horizontal (H) and vertical (V). The energy is plotted in red.

Beta Function Evolution during the LHC Ramp

An important ingredient for analysing the wire scanner data are reliable beta function measurements at locations of the profile monitors. In 2012, the optics had been measured with the turn-by-turn phase advance method at 450 GeV injection energy, at four discrete points during the energy ramp (at 1.33, 2.3, 3.0 and 3.8 TeV for beam 1, and at 1.29, 2.01, 2.62 and 3.66 TeV for beam 2) and at 4 TeV flattop energy before and after the β^* squeeze [61]. But beta function measurement results during the ramp were not available until the end of LHC Run 1. Only in 2014, after refined beta calculation algorithms to compute the beta functions at the profile monitors became available, progress in the understanding came. In Fig. 5.6 the measured beta functions during the 2012 LHC energy ramp are compared to the previously assumed linear interpolation of measured β at injection and flattop energy from k-modulation. In spite of not changing the design optics between injection plateau and the end of the ramp, the beta functions do not stay constant during the ramp.

The measurements of non-physical emittance evolution, e.g. shrinking emittances, can be explained by non-monotonically changing beta functions and not enough beta measurement points during the ramp, see Fig. 5.7. Emittance measurements with wire scanners are shown during the ramp of Fill 3217. The evolution of the energy and measured beta functions is also indicated. Linear interpolation is used between the different beta measurement points. The non-physical emittance evolution during the ramp in both planes of beam 1 and beam 2 vertical can originate from insufficient knowledge of the beta function evolution during the ramp. The beta functions for

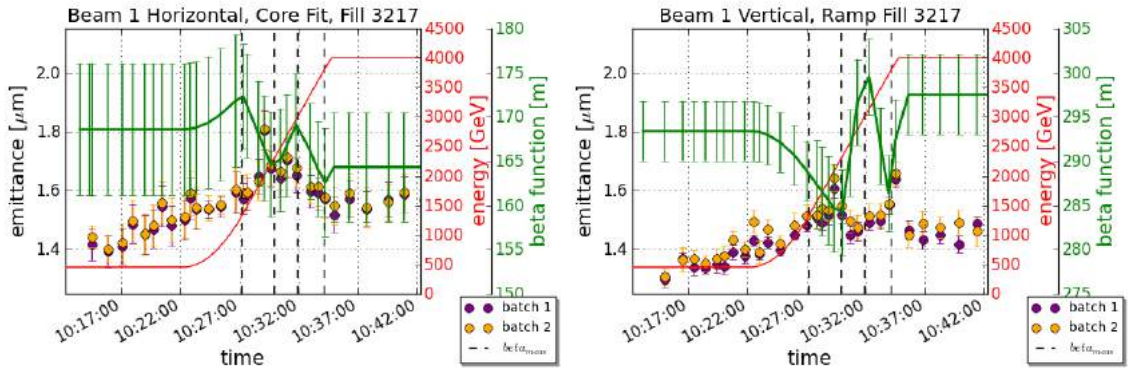

Figure 5.7.: Emittance and beta function evolution during the LHC ramp. Average beam 1 horizontal and vertical emittances of 6 bunches per batch through the LHC ramp for Fill 3217 measured with wire scanner and compared to the beta function evolution (green). The core emittance is displayed. The energy is plotted in red. Vertical black dashed lines indicate a beta function measurement. Beam 2 beta function evolution during the ramp can be found in appendix B.

beam 2 horizontal grow monotonously during the ramp and linear interpolation between two measurement points is justified. Many more beta measurement points will be needed in the future.

Effect of IBS on Emittance Growth during the LHC Ramp

IBS has been found to be the main source of growth in the horizontal plane during the injection plateau. The effect of IBS reduces with increasing energy but is not negligible for the LHC beam parameters during the ramp and flattop energy. Figure 5.8 compares emittance measurements corrected with the measured and interpolated betas during the ramp and predictions from IBS simulations. The simulations were performed with the IBS module of MADX, see chapter 4.2.3. The IBS module assumes no coupling, therefore no growth in the vertical plane is predicted.

For beam 2 the simulated emittance evolution fits remarkably well with the measured one for the horizontal and vertical plane, see Fig. 5.8. Moreover, IBS seems to be the dominant source for emittance growth through the entire cycle for beam 2 horizontal, see Fig. 5.9.

5.2.4. Emittance Preservation during the LHC Squeeze

The β^* squeeze is a delicate operation, where the optic changes, beta beat[4] and chromaticity corrections are fed forward and the orbit feedback has to work well to keep the beams on the reference trajectory. The emittances stayed constant throughout the squeeze within measurement precision for the largest part of the 2012 run, except when singular bunches went unstable. Towards the end of the 2012 proton run a small blow-up at the end of the squeeze for beam 1 horizontal was systematically observed, but not always by the same amount. An example is

[4]Beta beat is the deviation of the real beta function from the nominal β.

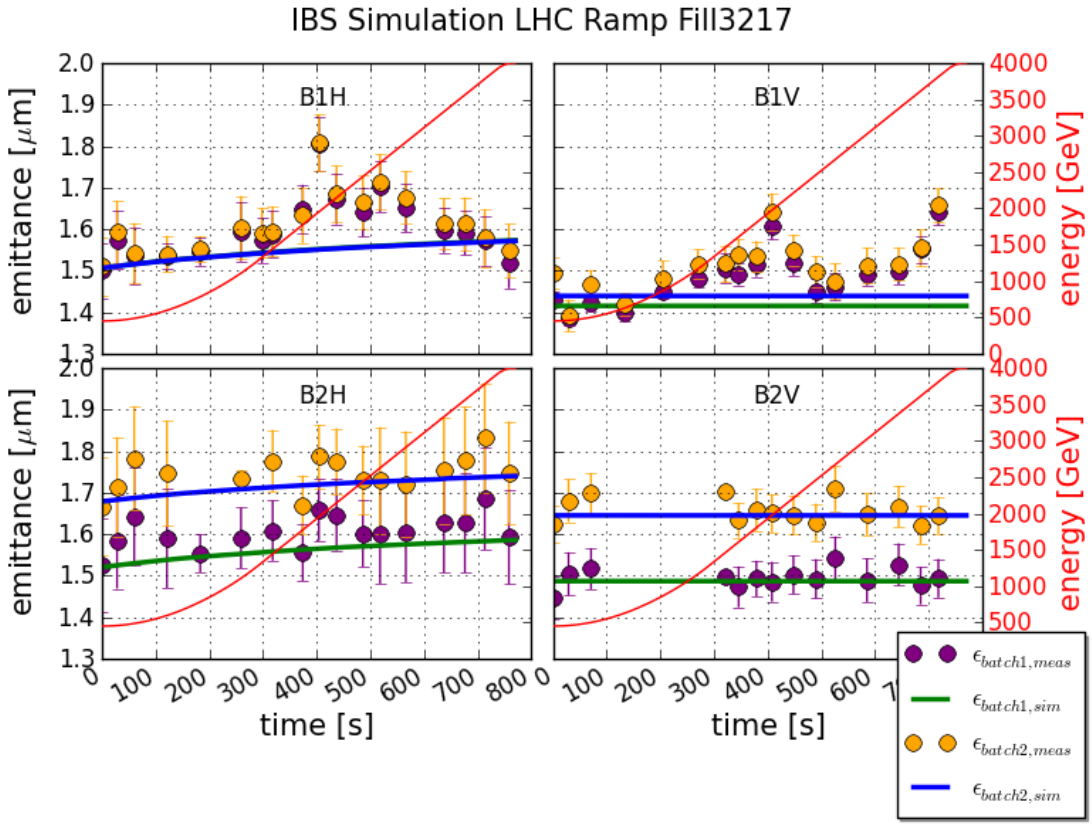

Figure 5.8.: Effect of IBS on emittance growth during the LHC ramp in 2012. The average emittance of six bunches per batch during the LHC ramp for Fill 3217 measured with wire scanners is shown (dots). Measurements are compared to IBS simulations (line). The energy is plotted in red.

given in Fig. 5.2. The sources for the emittance growth could have been introduced with the change of LHC run conditions, such as octupole polarity reversal, higher bunch intensities and chromaticity function adaptations, towards the end of the 2012 proton run. The emittances in the vertical plane, however, remained conserved.

5.2.5. Overall Effect of IBS on Emittance Growth for Physics Beams

IBS simulations for physics fills with typical 2012 beam parameters give an estimated total growth of about 0.4 µm in the horizontal plane for the very bright beams towards the end of 2012. However, convoluted growth in the order of 1 µm was measured.

Figure 5.10 shows the simulated emittance growth for IBS through the cycle in the horizontal plane versus brightness and compares it to the convoluted emittance growth obtained from injection wire scans and luminosity. The measured points are on a different slope than the IBS simulated ones. This is another indication that IBS is not the only source of emittance growth. A large part might have been caused by beam instabilities especially after TS3.

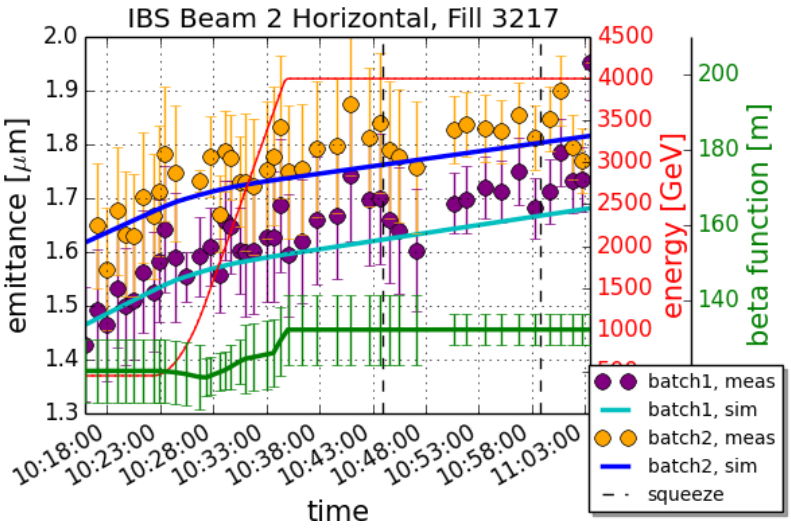

Figure 5.9.: Effect of IBS on emittance growth during the 2012 LHC cycle for beam 2 horizontal. Average emittance of six bunches per batch during the LHC cycle for Fill 3217 measured with wire scanner (dots) and compared to IBS simulations (line). The measured beta functions are plotted in green, the energy in red.

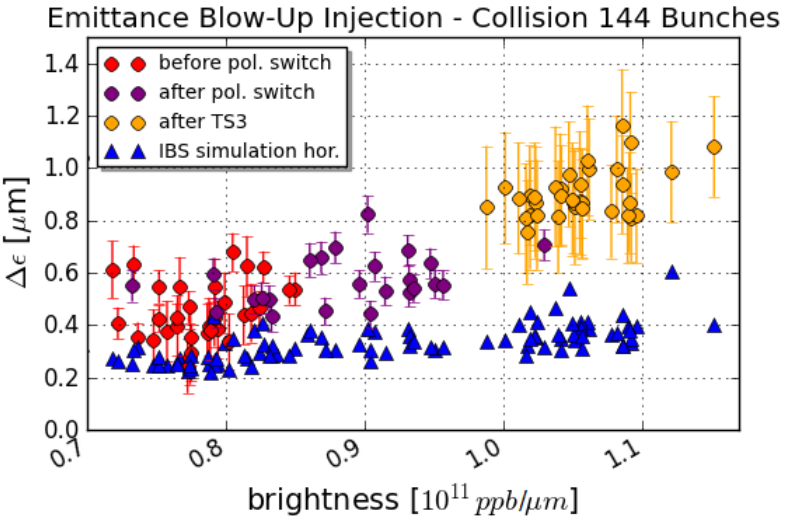

Figure 5.10.: Effect of IBS during physics fills. The average total blow-up of the first 144 bunch batch of the convoluted emittance (dots) from wire scans and ATLAS luminosity is compared to simulated horizontal blow-up due to IBS (triangles). The colors indicate different LHC run configurations in 2012. After Fill 2926 the Landau octupole polarity was reversed (purple) and after TS3 bunches with even higher brightness were produced in the injectors (orange).

5.3. Precision of 2012 Emittance Measurements with Wire Scanners

During many low intensity test fills the different emittance measurement methods could be compared, for example the convoluted emittance from wire scanners with the emittance from luminosity. Table 5.1 gives an example of such measurements done at the start of collisions for the low intensity Fill 3217. Emittance values are obtained from wire scans and ATLAS and CMS luminosity. They are compared to wire scans at injection. The discrepancy between the emittance from luminosity and emittance measured with wire scanners is about 30 %. There is also a significant disagreement between the ATLAS and CMS emittances for this fill. The errors are, however, large. The disagreement between the emittances obtained from wire scans and experiments led to investigations of possible saturation effects of the wire scanner photomultipliers.

	$\varepsilon_{\text{conv}}$ [µm]	growth [µm]
wire scan at injection	1.43 ± 0.03	
wire scan at peak lumi	1.88 ± 0.06	0.45 ± 0.08
ATLAS	2.36 ± 0.35	0.93 ± 0.38
CMS	2.63 ± 0.39	1.20 ± 0.42

Table 5.1.: Emittance at peak luminosity calculated from ATLAS and CMS luminosity compared to the convoluted emittance from wire scanners for Fill 3217 with six colliding bunches in ATLAS and CMS. The absolute average growth during the LHC cycle is given.

Wire Position Measurement Uncertainty

The comparison of various emittance measurement methods indicates that the wire scanners measure too small emittances. First, a bump calibration of the wire scanners in the LHC revealed that the wire scanners overestimate or underestimate the profile position, depending on the scanner. An example wire position measurement calibration is shown in Fig. 5.11. While the centre of the beam was shifted locally at the scanners, wire scans were triggered. The beam position is measured with the surrounding Beam Position Monitors (BPMs) and extrapolated to the wire scanner location. The fitted orbit at the wire scanner is compared to the mean position obtained from a Gaussian fit to the measured wire scanner beam profile. Measurements were carried out at 450 GeV and 4 TeV for each operational scanner in 2012. The slope of the linear fit in Fig 5.11 shows a 1.6 % calibration error for wire scanner B2H2 and 2.6 % error for wire scanner B2V2. The results for all scanners are listed in Table 5.2.

Hence, the true beam size could slightly differ from the measured beam size, but the large discrepancy between the emittance measurement methods cannot be fully explained with this result. Therefore the influence of the wire scanner settings on the resulting beam size was examined.

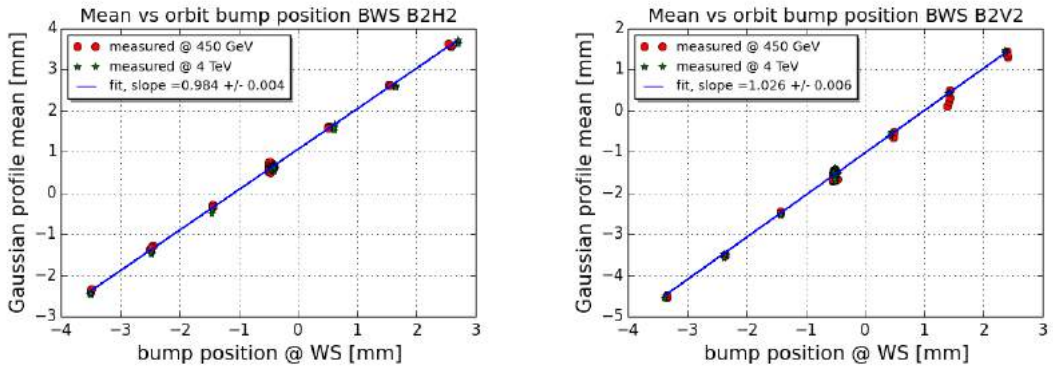

Figure 5.11.: Wire scanner orbit bump calibration 2012. The wire position measurement was verified with beam at different transverse beam positions. The plots show the Gaussian profile mean of beam 2 horizontal (left) vertical (right) measured with wire scanner at different orbit bumps at 450 GeV (red) and 4 TeV (green), Fill 2778 (24 June 2012). A linear fit (blue) is applied. The slope value of the fit is given in the legend. Measurements of beam 1 can be found in appendix B.

Scanner	Position measurement error [%]	$\Delta\varepsilon_{\text{cal}}$ [%]
LHC.BWS.5R4.B1H2 (B1H2)	+0.4	+0.8
LHC.BWS.5R4.B1V2 (B1V2)	+3.4	+6.8
LHC.BWS.5L4.B2H2 (B2H2)	-1.6	-3.2
LHC.BWS.5L4.B2V2 (B2V2)	+2.6	+5.2

Table 5.2.: 2012 wire scanner position measurement uncertainty and emittance calibration error ($\Delta\varepsilon_{\text{cal}}$).

Photomultiplier Working Point Investigations

Filter settings and voltage of the photomultiplier are not automatically chosen by the front end software as a function of intensity and energy, but have to be set by the user. Wrong settings can lead to saturated profiles due to saturation of the read-out electronics or saturation of the photomultiplier. Both induce wrong beam size measurements. Saturation of the ADC (Analogue to Digital Converter) is easily detectable, see Fig. 5.12, and avoidable. The accepted range of profile amplitudes is between 2500 and 7500 a.u. Profiles with higher or lower amplitudes are not taken into account in the offline fitting routine.

Photomultiplier (PM) saturation is less obvious to detect from the obtained profiles and the front end electronics do not return any PM status signal. For optimum PM settings, and thus correct beam size, the maximum gain of the PM in the linear region of each amplification stage should be used. Therefore the optimum settings for the LHC wire scanners at all energies had to be defined in a scan of beam size versus PM voltage and transmission filter.

Figure 5.13 shows an example of the measurements at injection and flattop energy for the wire scanner in beam 1 horizontal. They were repeated for all beams with

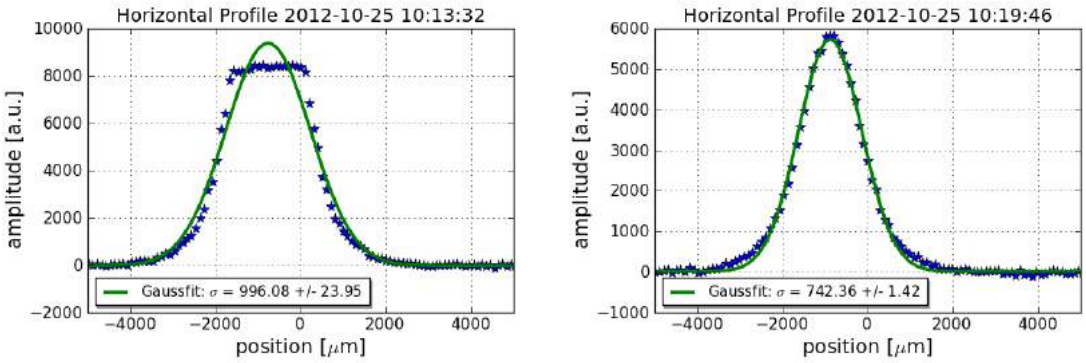

Figure 5.12.: ADC saturated profile (left) and non-saturated profile (right) of the same beam measured with wire scanner during one measurement period. Both profiles are fitted with a Gaussian. The obtained beam sizes, given in the legend, are different.

similar results. In the left plot a measurement at injection energy is shown. The constant linear emittance growth at 450 GeV is due to IBS, but clearly gain and filter changes have a significant influence on the measured emittance. The right plot shows a measurement at 4 TeV. Although the result is noisy, the measured emittance evidently depends on wire scanner settings. All profiles are Gaussian and not ADC saturated. PM saturation was suspected for certain settings.

The long shutdown of the LHC in 2013/2014 enabled investigations of the photomultiplier hardware and possible remedies. The optimum settings for the LHC wire scanners could unfortunately not be established in 2012, resulting in large uncertainties on the measured beam sizes.

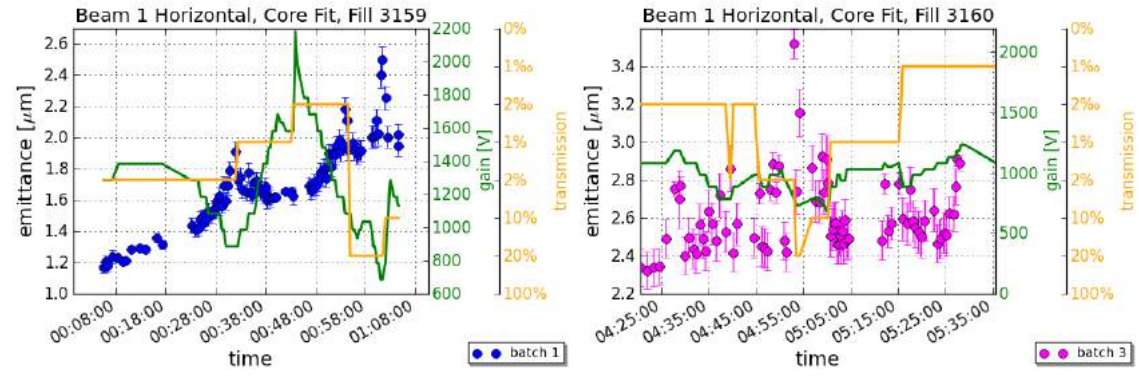

Figure 5.13.: Influence of wire scanner settings for beam 1 horizontal at injection energy of 450 GeV, Fill 3159 (left), and flattop energy of 4 TeV, Fill 3160 (right). Average emittance of six bunches per batch measured with wire scanner with variations of wire scanner filter (orange) and voltage (green).

Part III.

Emittance Measurement at the LHC

6. Beta Function Measurement with K-Modulation

The transverse beam size of a particle beam is defined by the accelerator's magnetic structure. The knowledge of the magnet lattice optics functions, such as the beta (β) function and the dispersion function (D), are important to determine the transverse emittance of the particle beam. In case of non-zero dispersion the beam energy spread needs to be measured as well.

Field errors and magnet misalignments can lead to linear, as well as non-linear, optics different from the design. The optics functions $\beta(s)$ and $D(s)$ therefore have to be measured at the profile measurement systems for accurate emittance reconstruction from beam size measurements. The well-known technique k-modulation was used to obtain the β functions at quadrupole magnets close by the profile measurement systems. A tool was developed for that purpose to fully exploit the possibilities of the LHC power supplies. K-modulation is the most precise method to measure β^*, the beta function at the interaction points in a collider. The aforementioned tool also offers k-modulation for the low-beta insertion quadrupole power supplies, the so-called triplet magnets.

This chapter will summarize the advantages and draw backs of k-modulation as beta function measurement technique in general and in view of the improvements obtained with this method thanks to the LHC power converter capabilities. The online k-modulation tool and its features will be presented. Finally, the obtained beta function results at the beam profile measurement systems in LHC point 4 as well as β^* measurement results will be presented. The measurements have been published in [62,63]. The results will be compared to the LHC conventional technique for beta function measurements with phase advance measurements from turn-by-turn Beam Position Monitor (BPM) data.

6.1. Tolerance on the Linear Optics Functions in the LHC

The measured beta function can deviate from the accelerator's design optics induced by machine imperfections leading to so-called beta beating, which is the ratio of the measured beta function to the nominal beta function. The total allowed maximum peak beta beating in the LHC is 15 %, with rms beta beating of 5 % [64]. Figure 6.1 shows the beta beating around the entire LHC ring before and after correction for the 2015 optics configuration at 450 GeV injection energy. The beta functions were calculated from phase advance measurements from the turn-by-turn beam position data around the ring with a large amplitude oscillation driven by the LHC AC dipole [66]. As can be seen from Fig. 6.1 the optics correction kept the beta beating well within the allocated budget of 15 %, albeit the beta functions around the LHC are not the nominal ones.

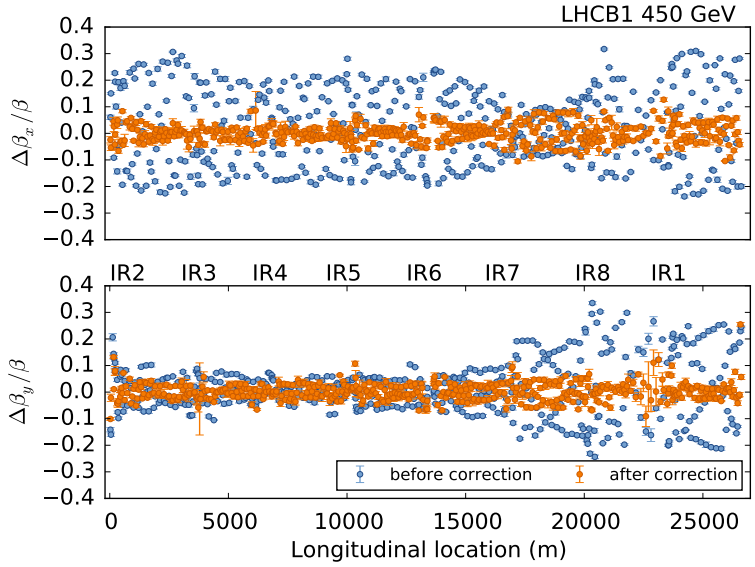

Figure 6.1.: LHC beta beating measurements in 2015 for beam 1 horizontal (top) and vertical (bottom) at 450 GeV injection optics [65]. The beta beating around the ring is shown before correction (blue) and after global corrections have been implemented (orange). Beam 2 beta beating measurements can be found in appendix C.

The dispersion functions can also be measured with the phase advance method. In 2015 no reasonable results could be obtained for beam 1 due to a problem with the AC dipole during the measurements and beam 2 dispersion measurements show large uncertainties [65]. Hence the 2012 dispersion measurements are used, see chapter 7.

The phase advance method has the advantage of delivering beta function results for all functioning BPMs (1166 around the LHC) for one plane in one measurement. The beta functions are calculated by combining the measured phase advance and the transport in between several neighbouring, three minimum, BPMs. For it to give reliable results, the phase advance between the neighbouring BPMs must not be at or close to 180°. There are regions in the LHC where such phase advances cannot be avoided, for instance the phase advance between the triplet BPMs on both sides of the interaction point is 176° [67]. K-modulation does not have this restriction. In addition, the measurement error is much reduced in comparison to the phase advance method. This will be shown later. On the other hand, k-modulation can only be applied at locations with individually powered quadrupoles. In principle, only one beta function location at a time can be measured, where each measurement takes about 2-5 minutes, depending on the LHC circuit, due to the nature of the superconducting circuits and their powering system.

6.2. K-Modulation Method to Measure Beta Functions

K-modulation is a method for measuring beta functions at locations of individually powered quadrupoles. A typical application is the measurement of β^* or the offset

determination of BPMs [68]. Moreover, k-modulation is suitable for crossing angle and orbit measurements.

In a circular accelerator the change of the quadrupole focusing strength Δk at one location in the ring shifts the horizontal tune Q_{x} and the vertical tune Q_{y} of the machine by [22]:

$$\Delta Q_u = \frac{1}{4\pi} \int_{s_0}^{s_0+l} \Delta k \beta_u(s) \mathrm{d}s, \tag{6.2.1}$$

where $u = x, y$. ΔQ_u is the tune change, l is the effective magnetic length of the quadrupole and β_u is the beta function at the quadrupole. Δk is the normalized quadrupole strength change in $[\mathrm{m}^{-2}]$. The quadrupole strength is altered by changing the current of the quadrupole. The tune change is proportional to the change of strength and the beta function at the location of the quadrupole. If the tune change can be measured precisely, the beta function can be calculated from the change in quadrupole strength following the well-known formula [22]

$$\beta_u = \frac{2}{l\Delta k} \left[\cot(2\pi Q_u) - \frac{\cos(2\pi(Q_u + \Delta Q_u))}{\sin(2\pi Q_u)} \right] \tag{6.2.2}$$

In approximation, for small tune changes far away from a resonance, the tune shift is proportional to the mean β value along the length of the quadrupole:

$$\langle \beta_u \rangle \approx \frac{4\pi}{l} \frac{\Delta Q_u}{\Delta k}. \tag{6.2.3}$$

The strength of the quadrupole magnet is altered by changing its current. The transfer function that links the current to the magnetic field gradient, has to be known. Whereas the current can be controlled precisely and the transfer functions are well known in the case of the LHC magnets [69], the biggest error contribution comes from the attainable precision of the tune measurement.

6.3. Tune Measurement in the LHC

The number of betatron oscillations per revolution in a circular accelerator is called the tune Q [22]. For k-modulation the required tune changes are small and only alter the fractional part of the tune. The fractional part of the tune Q_{frac} can be determined by measuring the frequency of the transverse beam oscillations. It is derived from the peak frequency Ω of the Fast Fourier Transformation (FFT) of the turn-by-turn data at a BPM divided by the revolution frequency f_{rev} [22]:

$$Q_{\mathrm{frac}} = \frac{\Omega}{2\pi f_{\mathrm{rev}}}. \tag{6.3.1}$$

Normally a kicker is required to guarantee high enough oscillation amplitudes to measure betatron oscillations above the BPM noise. This however often leads to emittance blow-up. The LHC is therefore equipped with the very sensitive Base-Band-Tune (BBQ) system that can continuously measure the tune without requiring any additional excitation [70]. The BBQ uses a high-sensitivity direct-diode detection technique followed by a real-time FFT spectrum analysis. It can resolve oscillations in the nm range, for instance turn-by-turn resolution of better than 30 nm, which is sufficient for the residual tune oscillations in the LHC with amplitudes of

100 nm to a few µm.

The nominal LHC tunes are listed in Table 6.1. Injection tunes are used from injection to the beginning of the squeeze.

	Injection	Collision
Horizontal tune	64.28	64.31
Vertical tune	59.31	59.32

Table 6.1.: LHC horizontal and vertical tune at injection (to flattop) and collision (from start of squeeze).

6.4. K-Modulation Tool for the LHC

In the course of this thesis, a JAVA application for the LHC control room was developed with the aim to provide automated k-modulation and taking constraints of various systems such as tune measurement, powering limits of the LHC superconducting circuits and limits of their quench protection systems into account. It also exploits the LHC power supply feature to sinusoidally modulate the currents of a given quadrupole with an adequate frequency and amplitude. This mode of measurement with sinusoidal modulation leads to excellent measurement precision, as will be discussed later. Figure 6.2 shows a screenshot of the application.

The application is fully integrated into the LHC control system [71] where it retrieves the circuit characteristics of the quadrupoles chosen by the user, such as inductance and resistance. The modulation frequencies, amplitudes, and time over which current changes will be applied, are pre-calculated by the application according to the power converter limitations.

The architecture of the k-modulation tool is accelerator independent. The LHC control system framework is used in all CERN accelerators. Hence, the application was tested in the SPS. Next to beta function measurements, it was also used for crossing angle and BPM offset measurements in the LHC .

The quadrupole current conversion to strength k [m^{-2}] is obtained from the LHC database, where a transfer function T_f [$\frac{\mathrm{Tm}}{\mathrm{A}}$] that links the integrated magnetic field B_l [Tm] along the magnet length to the current I [A] is stored for every magnet:

$$T_\mathrm{f} = \frac{B_\mathrm{l}}{I}. \tag{6.4.1}$$

The transfer function is based on a parametric model with coefficients obtained from magnetic field measurements for each circuit in the LHC.

The largest fraction of quadrupole magnets in the LHC are powered in series and make up the regular FODO lattice in the LHC arcs. Only the LHC insertion regions, the straight sections connecting the arcs, contain individually powered quadrupoles, all of which are superconducting circuits with unipolar power supplies allowing only positive power supply voltage. If the current is decreased (requiring negative voltage), the programmed current function has to follow the natural current decay given by the circuits characteristics with the time constant $\tau = L/R$, where L is the circuit inductance and R the circuit resistance. As the magnets are superconducting

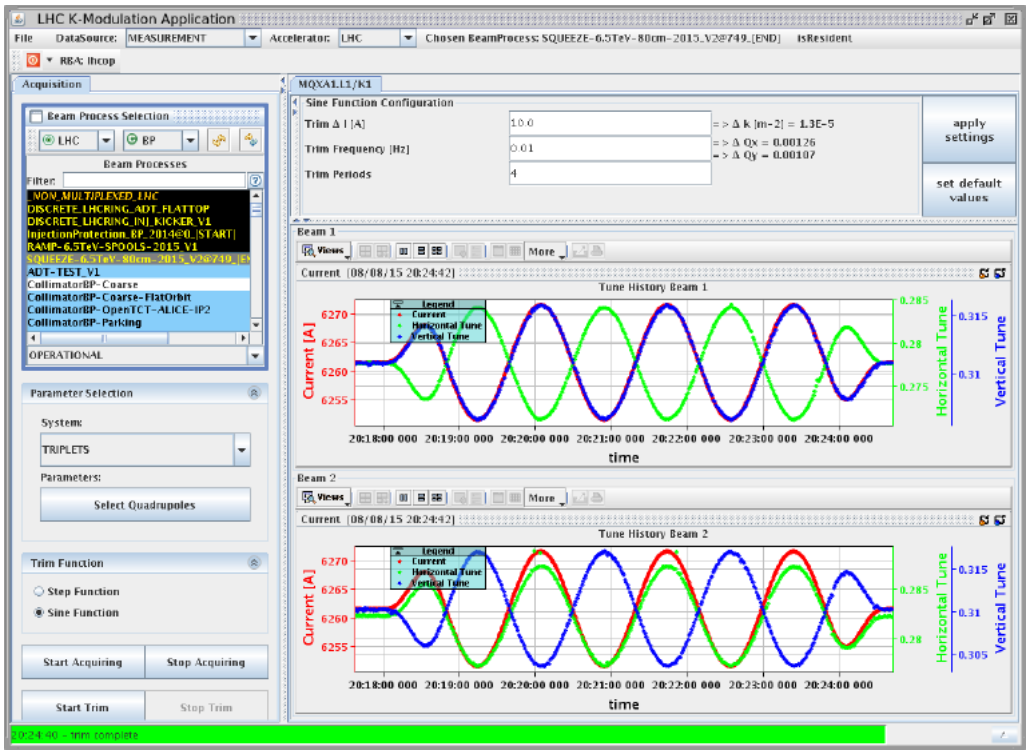

Figure 6.2.: K-modulation application screenshot. Sinusoidal modulation of the triplet magnet MQXA1.L1. For the user the application offers beam process selection, modulation parameter input, step or sine function choice, and tune and current display. A beam process contains the collection of settings for a specific phase in the cycle of the LHC. The sinusoidal modulation parameters that can be chosen by the user are trim amplitude, trim frequency and number of modulation periods. The input amplitude is directly converted from current in [A] to quadrupole strength in [m^{-2}] and subsequent expected tune change $\Delta Q_{x,y}$.

τ tends to be long, for example around 200 s in the quadrupoles surrounding the profile monitors in LHC point 4.

In case of sinusoidal modulation the upper power converter limit of the modulation amplitude ΔI and frequency f is given by

$$\Delta I = \frac{\Delta U}{Z} = \frac{IR}{2\pi f L}, \tag{6.4.2}$$

with voltage ΔU and impedance Z. For example quadrupole MQY.5R4.B1 in LHC point 4 can be modulated with a maximum amplitude ΔI of 26 A at nominal current and 3 A at injection current at a modulation frequency of 0.1 Hz. Modulation of the triplet magnets at high current is slower. Amplitudes of 10 A with frequencies of 0.01 Hz can be achieved. This is well sufficient for sinusoidal k-modulation in the LHC.

The new k-modulation tool also offers simultaneous tune and quadrupole current/strength acquisition and display. The user can choose between two measurement modes:

(A) step function, where the current is trimmed to different plateaus and tune data is accumulated, and

(B) sinusoidal current modulation.

The typical current evolution assuming mode (A) and (B) are illustrated in Fig. 6.3.

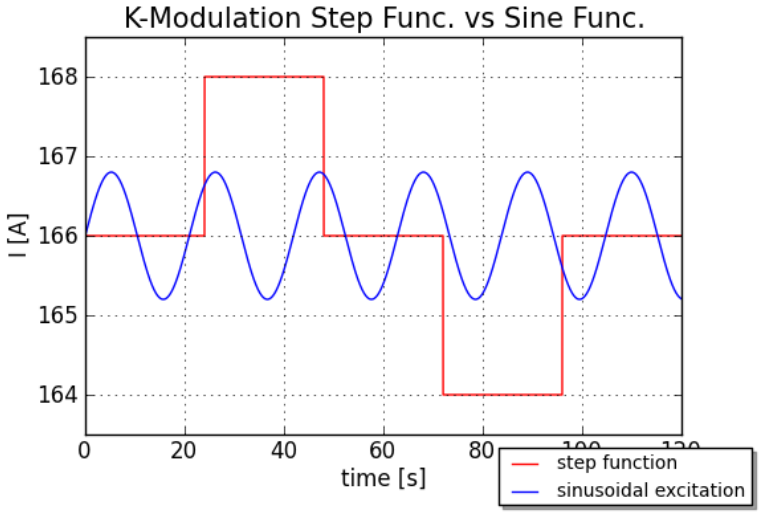

Figure 6.3.: Step function k-modulation versus sine modulation.

In case of current plateaus as for measurement mode (A), the power converter goes through a number of discrete trims built by the application according to its linear rate and acceleration limits to go from one current level to the next. The k-modulation application monitors the quadrupole trims and acquires the current and quadrupole strength only when the power converter has arrived at a plateau. The length of the waiting time on the plateau is defined by the user.

The sinusoidal modulation (measurement mode (B)) is a built-in functionality of the quadrupole power converter. The application continuously acquires current and tune during the modulation.

With k-modulation in discrete steps the waiting time at each current plateau is about 30 - 60 s to obtain a meaningful tune average value. A minimum of three current plateaus is required. Sinusoidal excitation can be faster. It also offers the advantage of modulating several quadrupoles at the same time with different frequencies. The feasibility depends on the quality of the tune signal. Both modulation methods have been tested and the results are presented in this chapter.

6.5. Limitations with K-Modulation in the LHC

With the current implementation of the k-modulation application, a modulation cannot be carried out when the power converters are already executing a current function, for example during the energy ramp or the β^* squeeze. The execution of only one function is possible with the LHC power converters. The LHC power converter controls are equipped with a real time input channel that is used by various feedback systems during the ramp and the squeeze. The possibility of using this channel was not implemented in the k-modulation application. Given the times

required for one k-modulation measurement (minimum 2 minutes compared to the ramp time of 22 minutes and the squeeze time of 13 minutes) it would also not be very meaningful.

Quench Protection

The superconducting quadrupole circuits are equipped with a quench protection system (QPS) [72]. This protection system measures the voltage across the circuit and switches the circuit off in case of voltage above threshold. For QPS the sinusoidal excitation is transparent. Figure 6.4 displays a quench detector output while the power converter of the corresponding circuit performs a sinusoidal current modulation. The common mode caused by sinusoidal excitation is well suppressed [62].

Sinusoidal current modulation of LHC quadrupoles has been tried successfully in the past in the context of BPM offset measurements [73]. Both individually powered quadrupoles and the triplets at the LHC interaction regions were modulated.

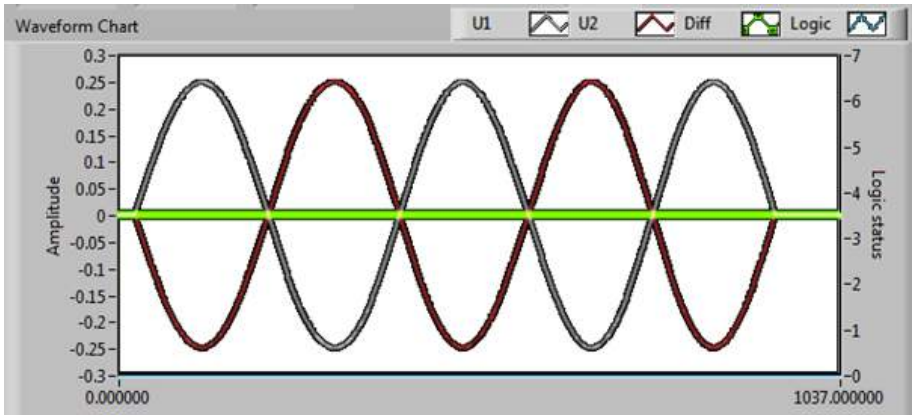

Figure 6.4.: Quadrupole driven with a sinusoidal current of 15 A amplitude and a frequency of 0.25 Hz resulting in a maximum $\mathrm{d}I/\mathrm{d}t$ of about 24 A/s. With a maximum inductance of 21 mH per coil the sinusoidal voltage is 250 mV. The green line is the voltage difference between the compared coils in the magnet which are used to detect a quench. *Courtesy J. Steckert, CERN, Geneva, Switzerland.*

Orbit Change

A misaligned quadrupole, or similarly a non-zero orbit amplitude in a quadrupole, results in a dipole kick proportional to strength and beam offset from the quadrupole center. If quadrupoles are modulated with non-zero orbit, k-modulation leads to an orbit change. The induced orbit change along the ring $\Delta u(s)$ is proportional to the average beam offset in the quadrupole u_q modulated with a strength amplitude of Δk [74]:

$$\Delta u(s) = \frac{\sqrt{\beta(s)\beta_\mathrm{q}}\cos\left(\mu(s) - \mu_\mathrm{q} - \pi Q\right)\Delta k l u_\mathrm{q}}{2\sin\left(\pi Q\right)}. \tag{6.5.1}$$

The peak orbit change amounts to

$$\Delta u(s) = \frac{\sqrt{\beta(s)\beta_{\mathrm{q}}}\Delta k l u_{\mathrm{q}}}{2\sin(\pi Q)}. \tag{6.5.2}$$

For typical modulation parameters used in 2015 the simulated maximum orbit change is less than 1 % ($<$ 10 µm) at the location of the modulated quadrupole in LHC point 4 and can be neglected. However, the resulting orbit change from k-modulation of the triplet quadrupoles in the LHC regions with small aperture limits the maximum possible modulation amplitude when crossing and separation bumps are switched on. A region with such a small aperture are the primary collimators in LHC point 7 (TCPs). They are very close to the beam to protect the machine from possible beam losses. In 2015 the smallest half gab opening of the TCPs was 1.1 mm at a β^* of 80 cm and crossing angle of about 290 µrad [75]. For a k-modulation amplitude of 15 A, the orbit amplitude in the modulated triplet magnet is about 200 µm[1] with a beam offset at this position of 3 mm. This results in a maximum orbit change in the TCPs of about 60 µm during k-modulation. With a beam size at the TCPs of about 20 µm and taking into account margins for small orbits drifts and beta beat, modulation amplitudes below 15 A for the given scenario are within the orbit excursion limits given by the collimator opening gaps. Higher amplitudes are, however, not possible.

Injection Tunes

For k-modulation injection tunes are preferred as opposed to collision tunes due to the larger tune separation and larger distance from the third order resonance of the vertical tune. In addition, with injection tunes the beam is less sensitive to coupling. With collision tunes and high coupling, β^* measurements are not possible.

Low Beam Intensity

K-modulation measurements, as well as measurements with the phase advance method, in the LHC can only be carried out with low intensity beams. The quality of the tune signal deteriorates significantly with increasing intensity partly due to instrumental effects and partly due to collective effects. Also, the transverse damper needs to be switched off during the measurement in order to get a good tune signal, which is only possible with low intensity. In addition, for machine protection reasons with non-operational settings it is preferable to use low beam intensity for k-modulation. Usually only one very low intensity bunch (pilot bunch with $\sim$ 10^{10} protons) is used for k-modulation measurements.

It has to be verified that the obtained beta function results are representative for a full machine. Effects from high beam intensity might cause additional focusing or defocusing. However, the nominal LHC orbit is defined for the single particle case since the orbit corrections and beta beating measurements and corrections are also done exclusively with pilot bunches in the LHC.

Both indirect space charge (direct current penetrating magnetic fields) and long range wake fields can cause additional, usually defocusing, forces when the number of bunches in the machine is increased [76]. This can be significant if the intensity of the bunches is large enough. Usually it also depends on the longitudinal coordinate

[1]The beta function at the triplet magnet closest to the IP is about 1000 m for a β^* of 80 cm.

along the bunch and the position of the bunch in the train. These effects are assumed to be a perturbation to the single particle model and are not accessible with this method.

6.6. LHC K-Modulation Data Analysis

The measurement results presented in this document were obtained offline with fitting algorithms in Python. Online analysis of the k-modulation data in the introduced application is foreseen for the near future. The framework of the tool already provides this feature. The conversion from current I to quadrupole strength k, however, was already obtained from the application through the LHC control system. K-modulation with current plateaus and sinusoidal modulation follow a different fitting routine, which are explained in the following.

K-Modulation with Current Plateaus

During a k-modulation measurement with current plateaus, the quadrupole current and the horizontal and vertical tunes are recorded over time t. An example is shown in the left plot of Fig. 6.5. Quadrupole MQM.7R4.B2 was modulated with current steps of $\Delta I = 8$ A. The waiting time at each current plateau was 60 s. Δk from ΔI is obtained in the application through the LHC control system. For the analysis only tune values recorded during the current plateau are taken into account. The resulting tune change ΔQ is plotted versus the quadrupole strength change Δk and fitted linearly, see right plot in Fig. 6.5. According to Eq. 6.2.3 the slope of the linear fit $\frac{\Delta Q}{\Delta k}$ gives the beta function at the modulated quadrupole.

Sinusoidal K-Modulation

For a sinusoidal k-modulation the quadrupole current, its strength and the horizontal and vertical tunes are recorded over time t. An example is shown in the left plot of Fig. 6.6. Quadrupole MQXA1.R1.B2 was modulated with an amplitude ΔI of 3 A and a frequency f of 0.01 Hz. Each modulation starts and ends with a half cosine function that has to be discarded for the analysis. Only the values during which the quadrupole is sinusoidally excited are taken into account. The recorded tunes are plotted as a function of the phase $(2\pi ft)$ and fitted with a sine function, see right plot in Fig. 6.6. The amplitude of the fit gives the applied tune change ΔQ. According to Eq. 6.2.3 the beta function at the modulated quadrupole can be computed with the known excitation amplitude Δk from ΔI.

6.7. LHC K-Modulation Measurement Errors

6.7.1. Systematic Errors

Transfer Function and Hysteresis

During the k-modulation experiment the quadrupole current is modulated and converted to the quadrupole strength via the transfer function. The absolute error on the measured transfer function is estimated to be 0.1 % at injection and 0.05 % at

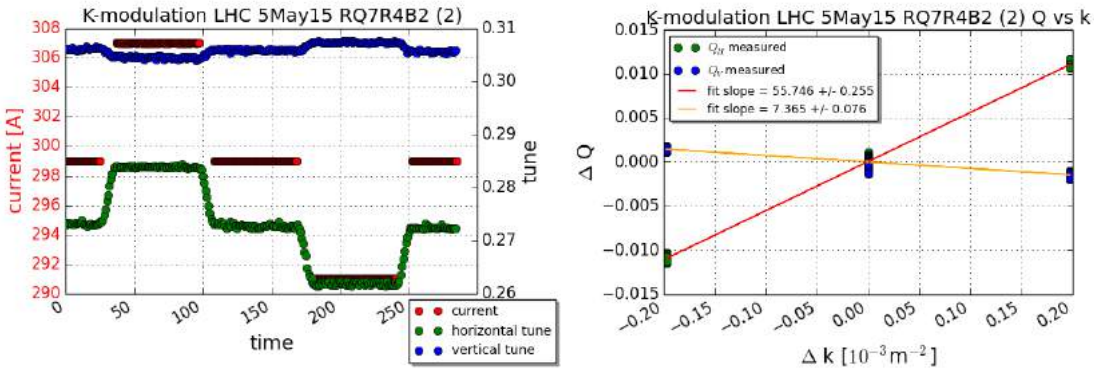

Figure 6.5.: K-modulation with current plateaus and data analysis. Quadrupole MQM.7R4.B2 was modulated with discrete trims to current plateaus of $\Delta I = 8$ A. The waiting time at each current plateau was 60 s. The recorded current (red), horizontal (green) and vertical (blue) tune versus time are shown in the left plot. Δk from ΔI is obtained in the application through the LHC control system. For the analysis only tune values during the current plateau time are taken into account. In the left plot the tune change ΔQ versus the quadrupole strength change Δk are plotted (green, blue) and fitted linearly (red, orange). The slope $\frac{\Delta Q}{\Delta k}$ of the fit is given in the legend.

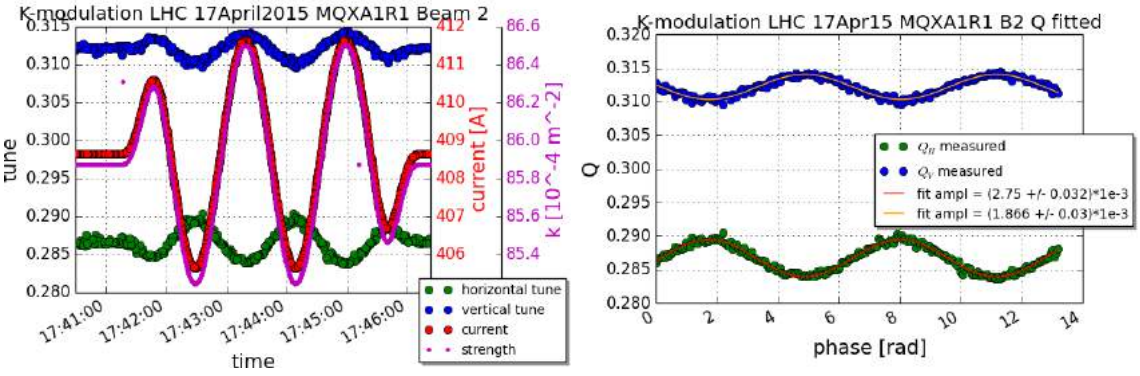

Figure 6.6.: Sinusoidal k-modulation and data analysis. Quadrupole MQXA1.R1.B2 was modulated with an amplitude of 3 A and a frequency f of 0.01 Hz. The left plot shows the recorded data during the modulation with current (red) and quadrupole strength (purple) versus time t. The horizontal tune is plotted in green, the vertical tune in blue. The half cosine at the beginning and end of the modulation is discarded for the sinusoidal fit. The result of the analysis (right) shows the horizontal and vertical tune with fits (red, orange) versus phase ($2\pi ft$). The amplitude from the fit can be found in the legend.

top energy for the LHC magnets [69]. In addition, hysteresis effects are present at low current. The magnets in the LHC usually work on the lower branch of the hys-

teresis curve. A typical hysteresis curve is shown in Fig. 6.7. The measured transfer function (TF) deviation from the nominal transfer function is plotted versus the current in quadrupole MQM.7R4.B1. This magnet is located in LHC point 4 next to the profile monitors. Other individually powered quadrupoles in point 4 have similar hysteresis curves. The error on the nominal transfer function due to hysteresis effects is maximum 0.2 % or smaller, see Fig. 6.7, corresponding to the maximum opening of the hysteresis curve.

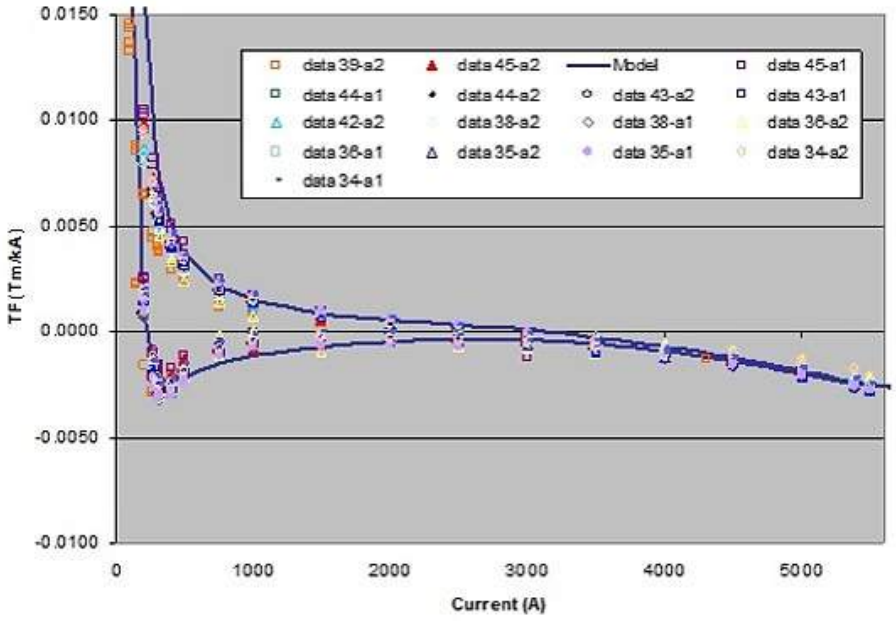

Figure 6.7.: Measured transfer function deviation from the nominal transfer function for quadrupole MQM.7R4.B1. The maximum opening of the hysteresis curve is about 23 units (= 0.23 % uncertainty on the nominal transfer function). Similar for other quadrupoles in LHC point 4.

Figure 6.8 shows the results of a simulated sinusoidal modulation of a quadrupole in LHC point 4 assuming a tune noise of 10^{-3} and the effect from a maximum opening of the hysteresis curve of 23 units. The tune sampling frequency is 1 Hz and the sinusoidal oscillation frequency is 0.02 Hz.

For quadrupols in LHC point 4 with typical beta functions of 100 - 400 m, hysteresis alone would result in an error on the beta function in the order of 10^{-4} dominated by tune noise. The error is independent of the size of β. Hence, the hysteresis effects are much smaller than the typical k-modulation measurement precision, which is in the order of 10^{-2} for quadrupoles in LHC point 4. For the LHC triplet magnets hysteresis can be neglected, as they are at top field during β^* measurements.

Eddy Currents

Eddy currents can be induced in conductors when changing its magnetic field. They are proportional to the field change rate. In case of sinusoidal k-modulation, induced eddy currents are proportional to the ratio of the amplitude and frequency of the modulation. The amplitude of the quadrupole field change and the amplitude of the current modulation were compared during sinusoidal k-modulation measurements

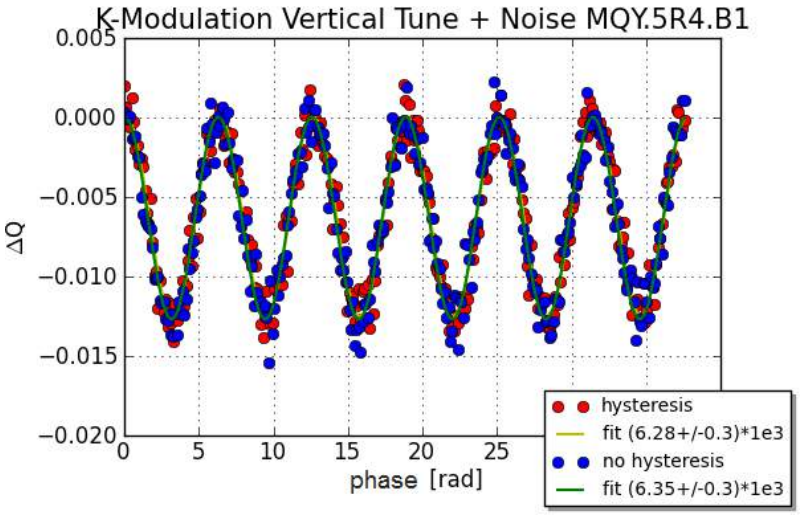

Figure 6.8.: Simulated sinusoidal excitation of quadrupole MQY.5R4.B1 with 10^{-3} noise on the tune measurement, including (red) and excluding (blue) hysteresis effects. The noisy tune response is fitted with a sine function: $\Delta Q = C + \Delta Q_0 \cdot \sin(2\pi f t)$,with offset C, amplitude ΔQ_0 and modulation frequency f. The fitted amplitude results are given.

in the laboratory. It was found that the transfer function increases by approximately 6 % with higher modulation frequencies in the frequency range of 0.1 to 1 Hz [77]. However, the transfer function does not depend on the modulation amplitude. Hence, eddy currents cannot be the source of the transfer function change with sinusoidal k-modulation. The origin of the frequency dependency is unclear. Sinusoidal k-modulation with a maximum transfer function deviation of 1 % is possible up to frequencies of 0.3 Hz [77]. This threshold is well above the tested frequency range of k-modulation in the LHC in 2015, where a maximum frequency of 0.1 Hz was used. A systematic transfer function error of 1 % from eddy currents is included in the presented results.

Fringe Fields

The obtained beta function results from k-modulation assume quadrupole magnetic fields according to the hard-edge model, where the field strength is uniform inside the quadrupole and zero outside. This assumption is, however, unrealistic. At the edge of the quadrupole the field decays not linearly and generates higher order magnetic fields, so called fringe fields, see Fig. 6.9. They can induce an additional kick to the beam.

The effect of fringe fields on the calculation of the beta function can be simulated in MAD-X. For example fringe fields in the triplet magnets at the interaction points can induce a waist shift. For a β^* of 0.8 m the beta beat from fringe fields was simulated to be 0.1 % [78]. Thus fringe fields of the triplet magnets have small effect on the β^* measurement. At lower β^*, for instance for the high luminosity upgrade of the LHC ($\beta^* < 0.2$ m), the effect of fringe fields becomes more important. A beta beat of up to 5 % could be induced [78]. The k-modulation β results presented in this thesis are unchanged when taking into account fringe fields.

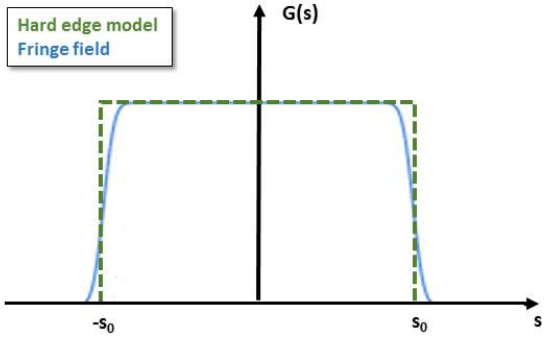

Figure 6.9.: Schematic of quadrupole with fringe field. The magnetic field according to the hard edge model (green) and the non-linear fringe fields (blue) at the edge of the quadrupole are shown.

6.7.2. Tune Precision

Tune Signal Quality

The precision of the beta function measurement with k-modulation in the LHC is limited by tune noise. The statistical LHC tune noise level is about 10^{-3} for measurements carried out with a pilot bunch ($\sim 10^{10}$ p). According to the 2012 experience, with k-modulation in current plateaus, the typical measurement error on the beta function was about 10 %, mainly due to tune noise. An example k-modulation from 2012 can be seen in Fig. 6.10. The current plateau duration was not long enough to reduce the statistical tune error.

The tune noise originates from multiples of the 50 Hz main harmonics in the tune spectrum that are very close to the actual tune and sometimes mistaken for the tune peak by the peak finder algorithm, see Fig. 6.11. In addition, the LHC horizontal tune used at injection sits close to a multiple of the 50 Hz line (3149 Hz).

However, after extensive progress on the LHC tune acquisition and filtering tool [79], this uncertainty could be greatly reduced in 2015. It was found that multiples of the 50 Hz line are probably not real but an instrumental effect of the BBQ. The 50 Hz lines were removed from the spectrum through an offline filtering algorithm.

The required k-modulation steps have to be significantly larger than the tune noise, in the range of 10^{-2} in tune change. Yet the maximum possible tune change is limited by the third order resonance in the LHC ($\Delta Q \leq \pm 0.015$ at nominal injection tunes of $Q_{\mathrm{x}} = 64.28$ and $Q_{\mathrm{y}} = 59.31$).

To improve the tune signal, tune chirp can be used to excite the beam. The chirp is done with fast frequency sweeps by the LHC transverse damper [80]. Oscillations with only a few µm amplitude can improve the tune measurement significantly.

K-Modulation Measurement Resolution

The dependence of the k-modulation type and modulation parameters on the measurement resolution has been tested. For the analysis, 2015 k-modulation measurements at 450 GeV in LHC point 4 and at 26 GeV in the SPS were used.

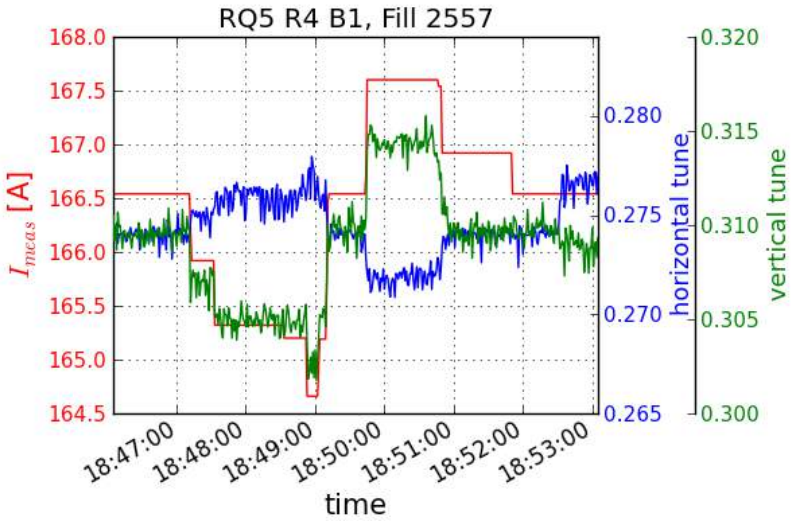

Figure 6.10.: K-modulation measurement with current plateaus of quadrupole MQY.5R4.B1 during Fill 2557 in 2012. The measured quadrupole current (red) and the horizontal (blue) and vertical tune (green) are displayed.

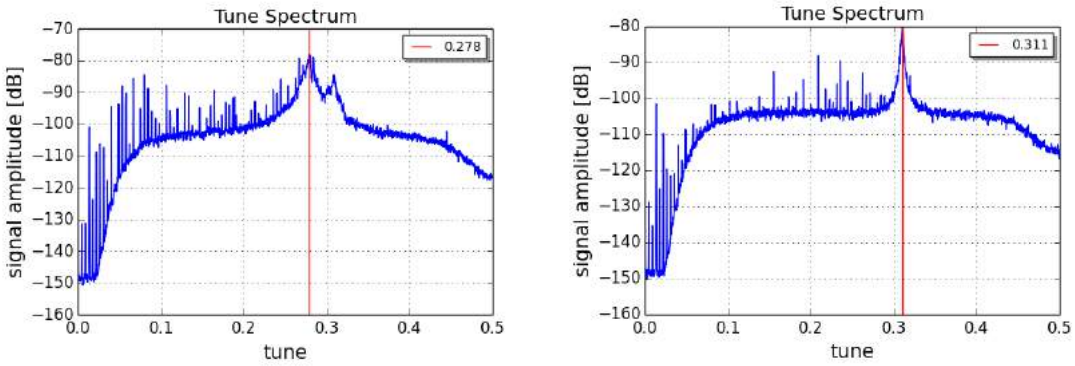

Figure 6.11.: LHC tune spectrum for beam 1 horizontal with dominant multiples of 50 Hz lines close to 0.28 (left) at injection tunes of nominal 0.28, and with clearer tune peak (right) at collision tunes of nominal 0.31. The LHC tune is measured with the LHC Base-Band-Tune System (BBQ).

K-modulations with current plateaus and sine modulations were performed on the same quadrupoles (MQM.7R4.B1 and MQM.7R4.B2) in the LHC with identical amplitudes and periods to compare the measurement resolution. An example is shown in Fig. 6.12. In general, the measurement uncertainty is very small and the results are consistent, see Table 6.2. The measurement error for k-modulation in current plateaus ranges from 1.4 to 2.8 %. The measurement error for sinusoidal modulation is similar, in the range of 1.5 to 2.7 %.

The measurement resolution also depends on the modulation amplitude, frequency and number of periods. If the tune signal is noisy a longer modulation improves the measurement uncertainty. As the frequency is limited by the given amplitude, the measurement error cannot be reduced by modulating faster. The tune acquisition frequency (1 Hz) has to be higher than the chosen modulation frequency to obtain a reasonable fit. When doubling the amplitude the measurement resolution typically

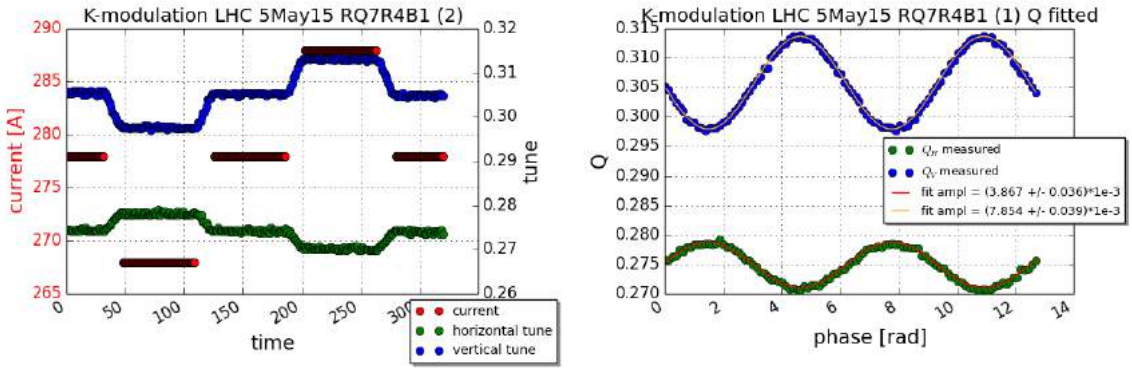

Figure 6.12.: Comparison of K-modulation with current plateaus (left) and sinusoidal excitation (right) at quadrupole MQM.7R4.B1 at 450 GeV injection optics (5 May 2015). The current (red) and horizontal (green) and vertical (blue) tune are displayed with fits. During both measurements the tune chirp was on. The amplitude during both modulations was 10 A. Sinusoidal excitation was carried out with a frequency of 0.02 Hz. The beta function measurement results are listed in Table 6.2.

Quadrupole	β_{nom} [m]	β_{sine} [m]	$\frac{\beta_{\text{sine}}}{\beta_{\text{nom}}}$ [%]	β_{step} [m]	$\frac{\beta_{\text{step}}}{\beta_{\text{nom}}}$ [%]
MQM.7R4.B1 (x)	62.51	58.08 ± 1.20	7.1	59.62 ± 1.31	4.6
MQM.7R4.B1 (y)	114.86	117.97 ± 1.90	2.7	115.91 ± 2.48	0.9
MQM.7R4.B2 (x)	201.00	203.47 ± 3.10	1.2	206.04 ± 2.94	3.0
MQM.7R4.B2 (y)	29.04	28.90 ± 0.78	0.5	27.22 ± 0.77	6.3

Table 6.2.: K-modulation measurement resolution depending on modulation type. LHC measurement of quadrupoles MQM.7R4.B1 and MQM.7R4.B2 with sinusoidal excitation (sine) and modulation in current plateaus (step). The nominal beta functions (nom) at each quadrupole are listed as well and compared to the measurements for the horizontal (x) and vertical (y) plane. The measurement errors β_{err} include the statistical tune measurement error, 0.2 % error on the transfer function from hysteresis effects, 0.1 % error on the measured transfer function and 1 % error on the transfer function from eddy currents.

improves by 1 %. The same is true for noisy tune signal and doubling the number of periods, see Table 6.3. The typical k-modulation measurement error is 1 - 3 % depending on the quadrupole. Hence, using the optimum modulation parameters can greatly reduce the measurement uncertainty. In general, the relative β error is smaller for locations with higher beta functions, as would be expected.

n_p	$\Delta Q_\mathrm{y}[10^3]$	$\Delta Q_\mathrm{y,err}[10^3]$	β_y [m]	$\beta_\mathrm{y,err}$ [m]	$\beta_\mathrm{y,err}$ [%]	$\frac{\beta_\mathrm{meas}}{\beta_\mathrm{nom}}$ [%]
1	8.949	0.326	36.11	1.35	3.7	4.0
2	8.958	0.227	36.11	0.95	2.6	4.0
3	8.979	0.179	36.11	0.76	2.1	4.0
4	8.962	0.159	36.11	0.68	1.9	4.0
5	9.078	0.149	36.11	0.63	1.7	4.0

Table 6.3.: K-modulation measurement resolution depending on number of modulation periods (n_p). SPS measurement of quadrupole QE60502 with $\beta_\mathrm{nom} = 34.73$. Errors include the statistical tune measurement error and 0.1 % transfer function error. The vertical tune change ΔQ_y with error $\Delta Q_\mathrm{y,err}$ and the measured vertical beta function β_y with error $\beta_\mathrm{y,err}$ are listed. The beta beat $\frac{\beta_\mathrm{meas}}{\beta_\mathrm{nom}}$ is given as well.

6.7.3. Tune Decay at 450 GeV

At the 450 GeV LHC injection plateau the superconducting magnets are at constant current, but the magnetic field multipoles drift. This changes the tune and the chromaticity. The tune decay with time is best described by a double exponential function with a fast time constant τ in the order of 1000 s [69]:

$$Q(t) = Q_0 + c\left[d\left(1 - e^{-(t/\tau)}\right) + (1-d)\left(1 - e^{-(t/9\tau)}\right) + ...\right]. \tag{6.7.1}$$

Q_0 is the initial tune, c is the asymptotic decay amplitude as $t \longrightarrow \infty$, and d is the weight between the fast and the slow components. An example measurement of the bare tune decay at LHC injection energy is shown in Fig. 6.13 with corresponding exponential fits.

The tune decay model is implemented in the LHC control system as a feed forward correction to keep the tune at the reference value [69]. Still, tune decay can be observed on a small time scale, especially for measurements at the beginning of the injection plateau. The typical k-modulation measurement length ranges from 2 to 5 minutes at injection energy. Thus a linear fit is used to remove the effects of tune decay.

6.8. LHC Point 4 Measurement Results

K-modulation measurements at the 450 GeV LHC injection plateau in LHC point 4 were carried out during the LHC commissioning phase in 2015. The beta functions at quadrupoles in the vicinity of the transverse profile monitors were measured. Quadrupoles Q5, Q6 and Q7, left and right of interaction point 4 (IP4), were modulated. The corresponding circuit names and nominal beta functions can be found in Table 6.4. To ensure a good tune signal the tunes and the chromaticity had to be corrected before each measurement. Coupling was also measured and corrected. Modulations were done with one pilot bunch (about 9×10^9 protons) per beam. The tune decay at the injection plateau was removed with offline analysis. Where possible, measurements were repeated to check reproducibility and the average beta

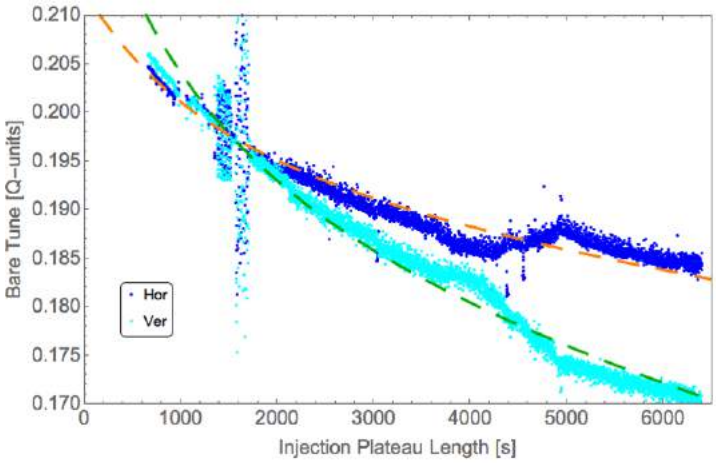

Figure 6.13.: LHC tune decay at 450 GeV [79]. The measurement was recorded during Fill 4526. The kink at around 4000 s is related to beam intensity increase.

Quadrupole	$\beta_{x,nom}$ [m]	$\beta_{y,nom}$ [m]	Quadrupole	$\beta_{x,nom}$ [m]	$\beta_{y,nom}$ [m]
MQY.5L4.B1	441.92	249.72	MQY.5L4.B2	198.34	532.00
MQY.5R4.B1	206.26	442.05	MQY.5R4.B2	456.29	174.14
MQY.6L4.B1	146.09	603.40	MQY.6L4.B2	480.89	187.06
MQY.6R4.B1	514.24	133.84	MQY.6R4.B2	153.65	418.29
MQM.7L4.B1	146.15	66.49	MQM.7L4.B2	77.99	176.87
MQM.7R4.B1	62.51	114.86	MQM.7R4.B2	201.00	29.04

Table 6.4.: Circuit names of the k-modulated quadrupoles in LHC point 4 and their nominal beta functions in the horizontal (x) and vertical (y) plane.

function was computed. K-modulation in discrete current steps and sinusoidal excitation was tested with different modulation parameters. For some measurements the tune was chirped, which enhanced the tune signal but caused large beam intensity losses. The beta function measurement results are listed in Table 6.5.

To obtain the β values at the transverse profile monitors, the measured optics functions at the quadrupoles are transported to the instruments using linear transfer matrices. The results are summarized in Table 6.6. Measurement errors from k-modulation are smaller than 3 % at the location of the modulated quadrupole. Hence, using the optimum combination of quadrupoles to transport the beta function to the transverse profile monitors results in β uncertainties smaller than 2 % with a beta beat of maximum 4 %. In 2012 k-modulation measurement results were also matched with MADX [42] from the quadrupoles in point 4 to the transverse profile monitors [81]. However, compared to the analytical method, the beta beat and the beta function error at the profile monitors could not be reduced. In addition, matching in MADX is complex and time consuming.

Unfortunately time constraints did not allow beta functions measurements with

Quadrupole	β_x [m]	$\beta_{x,err}$ [%]	$\frac{\beta_x}{\beta_{nom}}$ [%]	β_y [m]	$\beta_{y,err}$ [%]	$\frac{\beta_y}{\beta_{nom}}$ [%]
MQY.5L4.B1	456.71 ± 5.97	1.3	3.3	248.52 ± 3.39	1.4	0.5
MQY.5R4.B1	207.00 ± 3.34	1.6	0.4	435.97 ± 6.17	1.4	1.4
MQY.6L4.B1	153.89 ± 3.44	2.2	5.3	607.71 ± 9.30	1.5	0.7
MQY.6R4.B1	509.92 ± 7.18	1.4	0.8	135.51 ± 2.95	2.2	1.2
MQM.7L4.B1	136.93 ± 2.29	1.7	6.3	67.61 ± 1.38	2.0	1.7
MQM.7R4.B1	58.85 ± 1.26	2.1	5.9	116.94 ± 2.21	1.9	1.8
MQY.5L4.B2	203.22 ± 3.42	1.7	2.5	549.20 ± 7.60	1.4	3.2
MQY.5R4.B2	471.43 ± 6.76	1.4	3.3	173.31 ± 3.73	2.2	0.5
MQY.6L4.B2	480.37 ± 6.55	1.4	0.1	199.66 ± 3.83	1.9	6.7
MQY.6R4.B2	158.63 ± 3.35	2.1	3.2	409.24 ± 6.26	1.5	2.2
MQM.7L4.B2	78.00 ± 1.46	1.9	0.0	174.96 ± 2.88	1.6	1.1
MQM.7R4.B2	205.20 ± 3.02	1.5	2.1	28.06 ± 0.78	2.8	3.4

Table 6.5.: Beta function measurement results from k-modulation at quadrupoles in LHC point 4 in the horizontal (x) and vertical (y) plane. The measurement errors β_{err} include the statistical tune measurement error, 0.2 % error on the transfer function from hysteresis effects, 0.1 % error on the measured transfer function and 1 % error on the transfer function from eddy currents. The measured beta function is also compared to the nominal beta function (nom).

Instrument	β_{nom} [m]	β_{meas} [m]	β_{err} [m]	β_{err} [%]	$\frac{\beta_{meas}}{\beta_{nom}}$ [%]
Undulator B1H	203.55	205.76	2.00	0.97	1.09
Undulator B1V	317.26	313.52	3.51	1.12	1.18
Undulator B2H	200.66	208.04	2.86	1.38	3.68
Undulator B2V	327.75	335.01	3.75	1.12	2.22
Wire scanner B1H	194.02	194.85	2.06	1.06	0.43
Wire scanner B1V	368.07	369.82	4.40	1.19	0.48
Wire scanner B2H	188.67	193.96	2.28	1.18	2.81
Wire scanner B2V	411.68	417.94	4.48	1.07	1.52

Table 6.6.: Measured β_{meas} values in LHC point 4 at the transverse profile monitors at injection energy. The undulator is the BSRT light source at 450 GeV. Results are given for beam 1 (B1) and beam 2 (B2), horizontal (H) and vertical (V). The measured beta function error β_{err} and the beta beat $\frac{\beta_{meas}}{\beta_{nom}}$, as well as the nominal beta function β_{nom}, are listed.

k-modulation in LHC point 4 at 6.5 TeV flattop energy in 2015. Therefore β measurement results from the phase advance method are used in this thesis to compute the emittance at 6.5 TeV, before and after the β^* squeeze. In 2012 the beta func-

tions in IR4 during the ramp were measured with the phase advance method. The results are presented in chapter 5. The measured beta functions at the BPMs are also transported to the transverse profile monitor locations using transfer matrices. The results can be found in appendix C.

6.9. Comparison with the Phase Advance Method

Beta function measurement results from k-modulation and the conventional method to measure beta functions in the LHC, the phase advance method, have been compared. An example analysis of the measured beta beat of quadrupoles in LHC point 4 for each method can be found in Fig. 6.14. For most quadrupoles the results are consistent, but k-modulation has significantly smaller measurement errors.

K-modulation measures an average beta function along the magnet length. Whereas with the phase advance method an interpolation of the beta function at the end of the magnet is derived. For the comparison in Fig 6.14 the average beta function of the quadrupole is calculated from the phase advance data.

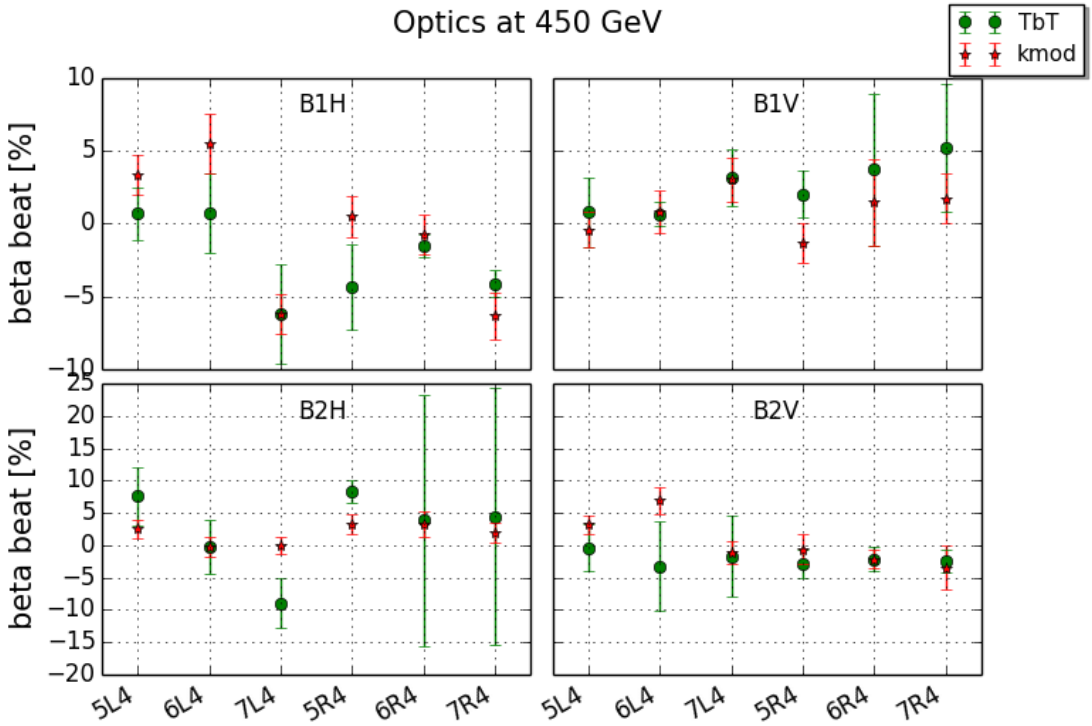

Figure 6.14.: Comparison of beta function measurement results from k-modulation and phase advance method. The beta beat for beta function measurements at 450 GeV in LHC point 4 with the phase advance method (green) and k-modulation (red) after the optics measurement correction campaign in April 2015 is given.

6.10. Beta* Measurements in the LHC

The LHC inner triplet quadrupole magnets on either side of the interaction point (IP) provide the final focusing of the proton beams at the collision points in the LHC. A schematic view of the left triplet in a high luminosity interaction region located at IP1 and IP5 is shown in Fig. 6.15. Each inner triplet consists of three quadrupoles, Q1, Q2 and Q3. The quadrupoles operate at a gradient of 205 T/m at nominal LHC collision energy of 7 TeV per beam [82]. Beam sizes at the interaction points of about 17 µm at IP1 and IP5 with β^* as small as 55 cm are achievable. The performance of the LHC depends critically on β^*. It needs to be measured and corrected as part of the overall correction scheme to optimize performance. Potential luminosity can be lost if the beta functions at the interaction points are larger than nominal. In addition the experiments ATLAS and CMS demand equal β^* for equal luminosity production.

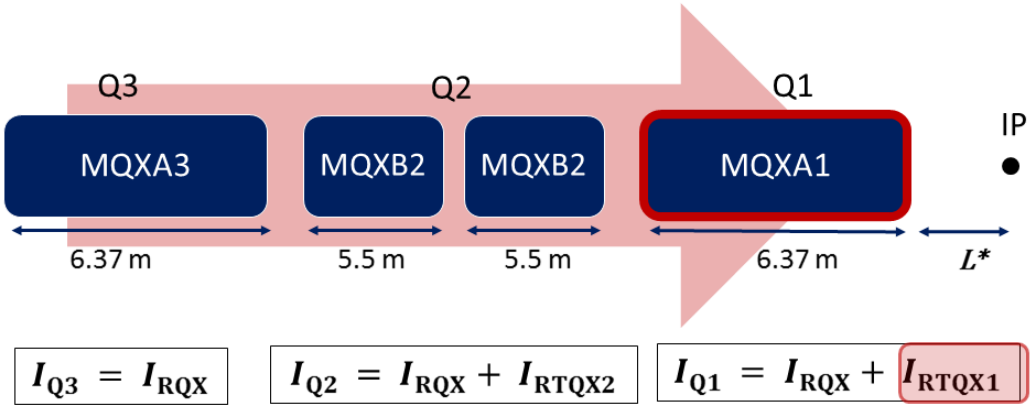

Figure 6.15.: Schematic of the LHC inner triplet with quadrupoles Q1 (MQXA1), Q2 (MQXB2) and Q3 (MQXA3) at the left side of IP1 and IP5. The magnet names and lengths are displayed. The nested powering scheme using three powering currents is indicated below. I_{Q1}, I_{Q2} and I_{Q3} are the currents in the three magnets. RQX, RTQX2 and RTQX1 are the names of the power converters. $L^* = 22.956$ m is the length between the IP and Q1.

To measure β^* the current of the quadrupoles closest to the IP, Q1, have to be modulated. The LHC inner triplet has a nested circuit of magnets Q1, Q2 and Q3, see Fig. 6.16. The current at power converter RTQX1 is trimmed individually to achieve a modulation only on Q1.

After the beta functions were measured at Q1 left and right of the IP, they are transported analytically with transfer matrices to the interaction point to compute β^*. For this purpose an algorithm in Python was developed. According to the optics layout in the interaction region, there is only drift space between Q1 and the IP. Thus β^* only depends on the distance between Q1 and the IP (L^*), the waist (w) and the beta function at the waist (β_w). The known ratio between the average beta functions along quadrupole Q1 left and right of the IP can be expressed in terms of

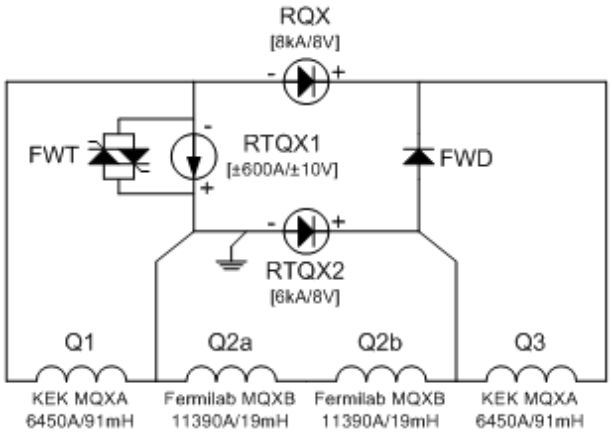

Figure 6.16.: LHC inner triplet circuit. Main quadrupole magnet circuit of the inner triplet system for IP1 and IP5.

L^* and w [78]:

$$\frac{\beta_{\mathrm{Q1,left}}}{\beta_{\mathrm{Q1,right}}} = \frac{(L^*+w)^2 d_0 + (L^*+w)d_1 + d_2}{(L^*-w)^2 f_0 + (L^*-w)f_1 + f_2} = \frac{\beta_{\mathrm{w,right}}}{\beta_{\mathrm{w,left}}}. \tag{6.10.1}$$

The functions d_0, d_1, d_2, f_0, f_1 and f_2[2] depend on the quadrupole strength k and its length l. Equation 6.10.1 is solved for w with $L^* = 22.965$ m. The result can be used to compute the beta function at the waist, which is averaged to $\beta_{\mathrm{w}} = \frac{1}{2}(\beta_{\mathrm{w,left}} + \beta_{\mathrm{w,right}})$. Finally, the beta function at the interaction yields

$$\beta^* = \beta_{\mathrm{w}} + \frac{w^2}{\beta_{\mathrm{w}}}. \tag{6.10.2}$$

A full deduction can be found in [78]. The previously defined error on the beta function measured at Q1 is transported from both sides to the β^* result. The length between the IP and Q1 has an rms alignment error of ± 6 mm. The error is also included in the analysis.

For the 2015 LHC proton run with 80 cm β^* optics, the beta functions at IP1 and IP5 were measured with k-modulation. The measurements were carried out after the optics measurement and correction campaign in 2015. The Q1 quadrupoles, left and right of the IP, were modulated with a sine function. One pilot bunch per beam with an intensity of about 9×10^9 protons was used for the modulation. The

[2]

$$d_0 = \frac{1}{2}\left(1 + \frac{\sinh 2\sqrt{k}l}{2\sqrt{k}l}\right), \quad f_0 = \frac{1}{2}\left(1 + \frac{\sin 2\sqrt{k}l}{2\sqrt{k}l}\right)$$
$$d_1 = \frac{\sinh \sqrt{k}l^2}{kl}, \qquad f_1 = \frac{\sin \sqrt{k}l^2}{kl}$$
$$d_2 = \frac{1}{2k}\left(\frac{\sinh 2\sqrt{k}l}{2\sqrt{k}l} - 1\right), f_2 = \frac{1}{2}\left(1 - \frac{\sin 2\sqrt{k}l}{2\sqrt{k}l}\right)$$

measurements were carried out after the β^* squeeze with LHC injection tunes and modulation parameters of 10/15 A and 0.01/0.008 Hz. No tune chirp was needed. The two pilot bunches were not colliding, but crossing angle and separation bumps were on.

An example of a 2015 k-modulation on a Q1 magnet can be seen in Fig. 6.17. Overall, the β^* measurement precision with k-modulation is better than 2 %. This remarkable high precision can be attributed mostly to the good tune signal in the LHC. The other ingredient is the optimized modulation technique. Sinusoidal excitation with a maximum possible modulation amplitude was used. Each measurement was repeated once and it was found that the results are reproducible within the measurement uncertainty. The value for the measured β^* is averaged over the two measurements and the error from averaging is included. The final β^* results are listed in Table 6.7.

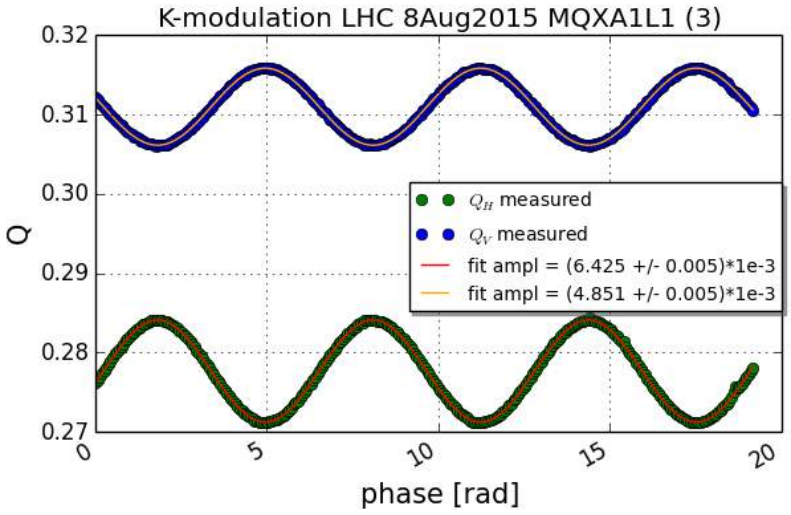

Figure 6.17.: Beta function measurement in LHC IP1 with k-modulation. Quadrupole MQXA1L1 was modulated with a sine function with an amplitude of 10 A and a frequency of 0.01 Hz. The horizontal (green) and vertical (blue) tune are displayed with fits.

In most planes the measured beta function is larger than nominal, which leads to potential luminosity losses in both IPs. The beta beat was as high as 10 %. The k-modulation measurements indicate a positive β waist shift in all planes, see Fig. 6.18

	IP1	IP5		IP1	IP5
β_{1H} [m]	0.88 ± 0.01	0.86 ± 0.01	w_{1H} [m]	0.25 ± 0.02	0.22 ± 0.02
β_{1V} [m]	0.86 ± 0.01	0.86 ± 0.05	w_{1V} [m]	0.23 ± 0.01	0.24 ± 0.09
β_{2H} [m]	0.82 ± 0.01	0.87 ± 0.01	w_{2H} [m]	0.18 ± 0.02	0.24 ± 0.02
β_{2V} [m]	0.79 ± 0.01	0.83 ± 0.02	w_{2V} [m]	0.21 ± 0.01	0.16 ± 0.05
β^* [m]	0.85 ± 0.03	0.84 ± 0.03			

Table 6.7.: Measured β^* and waist shift (w) values in IP1 and IP5 with measurement errors. The nominal β^* value during this measurement is 0.8 m.

for explanation. The minimum beta function is not at the interaction point, but shifted longitudinally about 20 cm in all planes towards the focusing magnet Q1, see Table 6.7. The waist shift was probably caused by residual errors in the triplets and/or local corrections [83]. Other possible sources for a waist shift are listed in Table 6.8. Non-linear errors and dispersion can be excluded as cause for the shifted beta waist.

With lower β^* the above mentioned errors will become larger. For the 2016 LHC proton run it is foreseen to reduce β^* to 40 cm. Therefore k-modulation will be performed in parallel with optics correction measurements to guarantee a low beta beat and waist shift at the IPs. The k-modulation application is now an operational tool and can be used for that purpose.

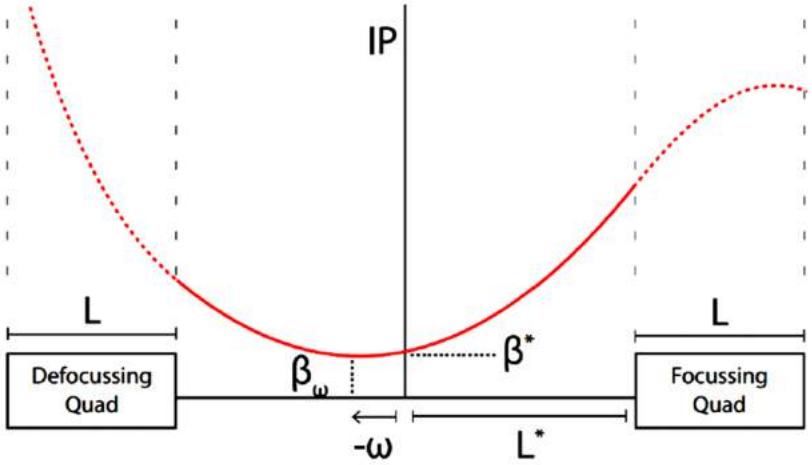

Figure 6.18.: Schematic layout of the beta function at the interaction point (IP) [78]. The quadrupoles left and right closest to the IP are shown (Focusing and Defocusing Quad) with length L. The beta function at the center of the IP is called β^*. The minimum of the beta function (β_w) can, however, be shifted by w. L^* is the length from quadrupole to IP. In this example the waist is shifted towards the defocusing quadrupole resulting in a negative waist shift value.

Possible source of waist shift	Estimated waist shift [cm]
Injection instead of collision tunes	1
Global corrections	3
Local corrections	15
Residual errors in the triplets	n.a.

Table 6.8.: Possible causes for a beta waist shift and estimated shift of β^* in the longitudinal plane. The estimated waist shift can be positive or negative. *Courtesy T. Persson [83], CERN, Geneva, Switzerland.*

6.11. Summary of LHC Beta Function Measurement with K-Modulation

K-modulation is an alternative method for measuring the beta functions at locations of individually powered quadrupoles. The method was used in 2015 to measure beta functions in LHC point 4 and in the interaction points to obtain β^*. I developed a new and safe, dedicated online tool that is operational since the start of LHC Run 2, which simplifies and speeds up the measurements. The beta function measurement accuracy via k-modulation in the LHC is mainly limited by tune noise. Nevertheless, measurement errors smaller than 2 % could be achieved with sinusoidal excitation of quadrupoles. These are very promising results and pave the way for high precision beta function measurements at the interaction points and beam profile monitors to further decrease the emittance measurement uncertainty.

The beta function measurement accuracy is not only competitive with the phase advance method in the LHC but also with measurement uncertainties achieved in other accelerators, see Table 6.9. In the future the LHC will be operated with even lower β^* which makes k-modulation measurements essential.

Accelerator	Year	Method	β_{err} [%]
Tevatron	1995	Phase advance method	$\leq$ 10 % [84]
LEP	2001	K-modulation	$\sim$ 1 % [85]
SPS	2012	Phase advance method	$\sim$ 5 - 10 % [86]
LHC IP1/5	2011	K-modulation	3 - 5 % [87]
	2015	K-modulation	$\leq$ 1.5 %
LHC point 4	2012	K-modulation in steps	1 -11 % [88]
(450 GeV)	2012	Phase advance method	$\sim$ 10 %
	2015	K-modulation with sine function	$\leq$ 2.8 %
	2015	Phase advance method	1 - 19 %

Table 6.9.: Comparison of β measurement accuracy β_{err} in different accelerators. *LHC phase advance measurement results courtesy of A. Langner, CERN, Geneva, Switzerland.*

7. Transverse Beam Size Measurement

The knowledge and preservation of the transverse emittance of a particle beam in a collider is essential for luminosity performance. But emittance cannot be measured directly. It is determined from the transverse beam size through transverse profile measurements. This chapter discusses the different transverse profile measurement systems in the LHC and presents the measurement uncertainties of these instruments.

7.1. Transverse Profile Monitors in the LHC

The two main types of transverse profile monitors used in the LHC for beam size measurements in 2015 are:

- wire scanners and
- Beam Synchrotron Radiation Telescopes (BSRT).

They are used to measure the transverse beam size through the LHC cycle. For a detailed description of these measurement systems refer to [6] and chapter 5 of this thesis. In the following the specifications of the two systems are discussed and advantages and limitations are outlined.

Wire Scanner and BSRT Limitations

The LHC wire scanners can only be used with a small fraction of the total nominal intensity per ring due to wire heating. The carbon wire should be able to take 2 - 3×10^{13} charges/mm[1] before sublimating. The close-by LHC superconducting magnets limit the maximum scan intensity further, to 5×10^{12} charges/mm [89], because the particle showers produced by the wire passing through the beam can quench the magnets. This limit corresponds to about 240 bunches per beam (2.7×10^{13} p), less than one injected nominal batch (288 bunches). At 6.5 TeV flattop energy in 2015 scans were possible with up to two nominal bunches (2.3×10^{11} p). The flattop limit has recently been redefined to 1.6×10^{12} p after the first experience at 6.5 TeV.

The emittance evolution of high intensity physics fills cannot be measured with the LHC wire scanners. The BSRT is used for that purpose. The BSRT absolute beam size measurement is obtained from a cross-calibration with wire scanners. In this work BSRT measurement results will be presented when wire scans were not available. The working principle and the calibration of the synchrotron light monitor is documented in [56]. In 2015 the BSRT beam size measurement accuracy was found

[1] Elementary charge $e = 1.602 \times 10^{-19}$ C.

to be better than 6 % with a precision of about 5 %, which was systematically better for beam 2 than for beam 1 [90].

The wire scanner is currently the only operational device that can accurately measure beam sizes through the LHC energy ramp. Low intensity test fills during the commissioning phase and intensity ramp-up phases are used for the calibration of the emittance measuring instruments and emittance preservation studies.

Availability and measurement accuracy of the LHC transverse profile monitors during LHC Run 1 was poor, see chapter 5. Thus the profile monitors underwent upgrade works during Long Shutdown 1 (LS1). The wire scanner changes during LS1 will be explained in detail in section 7.3.3. An overview of the BSRT improvements can be found in [90]. Problems with the synchrotron radiation extraction system in Run 1 triggered a new design study[2]. During LS1 the BSRT was upgraded with a novel design and new mirrors with reduced longitudinal impedance. Availability and measurement accuracy improved greatly in Run 2. The BSRT can now acquire 5 to 6 bunches per second, which is slightly faster than in 2012 but still not fast enough for physics fill observations during injection and squeeze.

In 2015 an intensive calibration and verification campaign was carried out to improve the measurement accuracy of the transverse profile monitors. The details will be explained to determine the systematic measurement uncertainty on beam size measurements in the LHC.

7.2. LHC Point 4 Layout and Optics Changes during Long Shutdown 1

Transverse profile monitors are typically located at places with large beta functions. The profile monitors in the LHC are positioned in insertion region 4 (IR4). A schematic overview is given in Fig. 7.1. The location of the wire scanners and the synchrotron light extraction points of the BSRT are shown. In total the LHC has four operational wire scanners, one for each beam and plane and four spare wire scanners. The names of the operational scanner and the spare system in 2015 are listed in Table 7.1. The synchrotron radiation for the BSRT is generated by a superconducting undulator at injection energy and the dipole D3 at flattop energy. The light source is switched during the energy ramp.

The LHC is equipped with additional profile measurement systems. The Beam-Gas Ionization Profile Monitor (BGI) could not be used for transverse profile monitoring of proton beams in the LHC in 2015 (and during LHC Run 1). A demonstrator Beam Gas Vertex Detector (BGV) [91] was installed in 2015 in beam 2. After commissioning in 2016, it will serve as an additional transverse profile monitor in the following years.

The measurement uncertainty of the transverse profile monitors depends on the transverse size of the beam. Smaller beam sizes are more difficult to measure for wire scanners and synchrotron light monitors due to the limited resolution of the instruments. At 450 GeV LHC injection energy the beam sizes at wire scanner and BSRT are typically 800 - 1500 µm depending on the location. However, at 4 TeV LHC flattop energy in 2012 the beam sizes were only 200 - 400 µm large.

[2]From September 2012 until the end of LHC Run 1 only the BSRT for beam 1 was operational due to heating and deformation of the beam 2 BSRT extraction mirror [56]. No beam profiles for beam 2 were available until the end of the 2012 proton run.

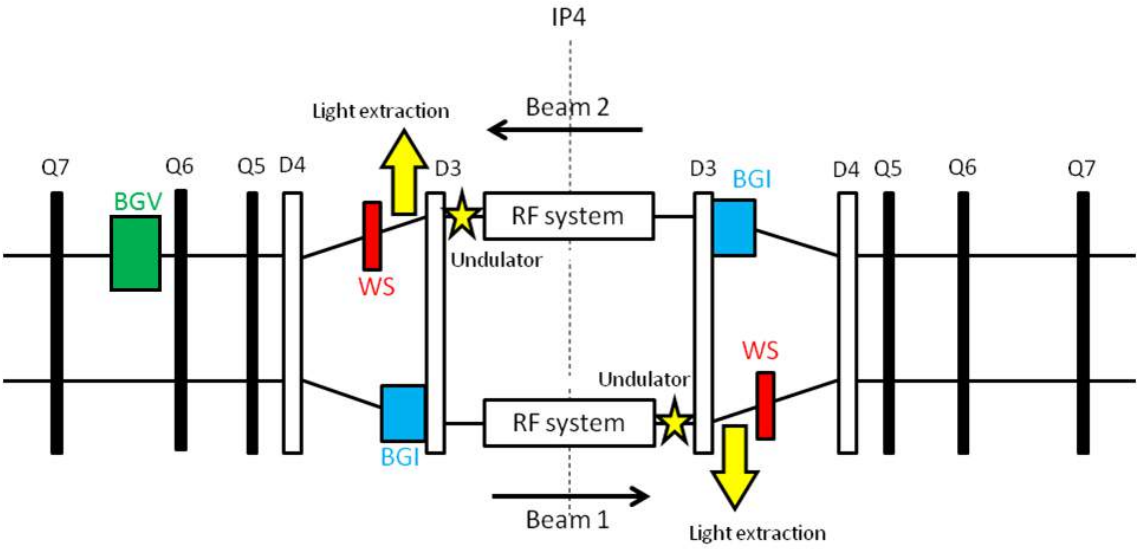

Figure 7.1.: Schematic outline of IR4 (figure not to scale). The beam line in point 4 with RF cavities, quadrupoles Q4, Q5, Q6 and Q7, dipoles D3 and beam instruments is presented. There are four wire scanners (WS) for each beam, two for each plane, including a spare wire system. The Beam-Gas Ionization Profile Monitor (BGI) also has a horizontal and a vertical component for each beam. The Beam Synchrotron Radiation Telescope (BSRT) works with a superconducting undulator at injection energy and the dipole D3 at flattop energy. A Beam Gas Vertex Detector (BGV) was installed in beam 2 in 2015.

With higher flattop energy in LHC Run 2 the beam sizes would have been further reduced below the resolution of the systems. It was therefore decided to increase the beta functions in IR4 at the transverse profile monitors for Run 2 to ensure similar flattop beam sizes as in Run 1 [92]. The beta function measurement results are presented in chapter 6 and in appendix C.

7.3. LHC Wire Scanners

LHC transverse beam size measurements for this thesis were primarily recorded with wire scanners. This section deals with the improvements of the LHC wire scanners during Long Shutdown 1 and the calibration verification of the operational scanners. The LHC wire scanner system is explained in detail in [6]. For accurate beam size measurements it is crucial to achieve a high measurement precision with the wires.

A transverse beam profile with a wire scanner is obtained from two simultaneous measurements:

- wire position measurement while the wire passes through the beam, and
- measurement of the signal from the scattered particles at each wire position.

Beam	Plane	Operational Wire Scanners	Spare Wire Scanners
1	H	LHC.BWS.5R4.B1H2 (B1H2)	LHC.BWS.5R4.B1H1
1	V	LHC.BWS.5R4.B1V2 (B1V2)	LHC.BWS.5R4.B1V1
2	H	LHC.BWS.5L4.B1H2 (B2H1)	LHC.BWS.5L4.B2H2
2	V	LHC.BWS.5L4.B2V1 (B2V1)	LHC.BWS.5L4.B2V2

Table 7.1.: LHC Run 2 operational wire scanners and spare wire scanners for beam 1 and 2 in the horizontal (H) and vertical (V) plane.

The general layout of a wire scanner is shown in Fig. 7.2. The wire interacts with the proton beam and secondary particles are produced. Their signal is measured outside the beam pipe with a scintillator. Through optical filters the signal is transported to a photomultiplier (PM). The transverse profile is reconstructed from the PM current and the position of the wire fork, see profile in Fig. 7.3. The wire scanner position is measured with a high precision potentiometer. The potentiometer is also used for controlling the position of the wire. The transverse beam size is then derived from the obtained profiles. Typically, the particle distribution around the LHC orbit is Gaussian.

In the LHC the four operational wire scanners are controlled via a user interface as shown in Fig. 7.3. The JAVA application was developed in the course of this work. It is used from the LHC control room. Wire scanner intensity limitations are

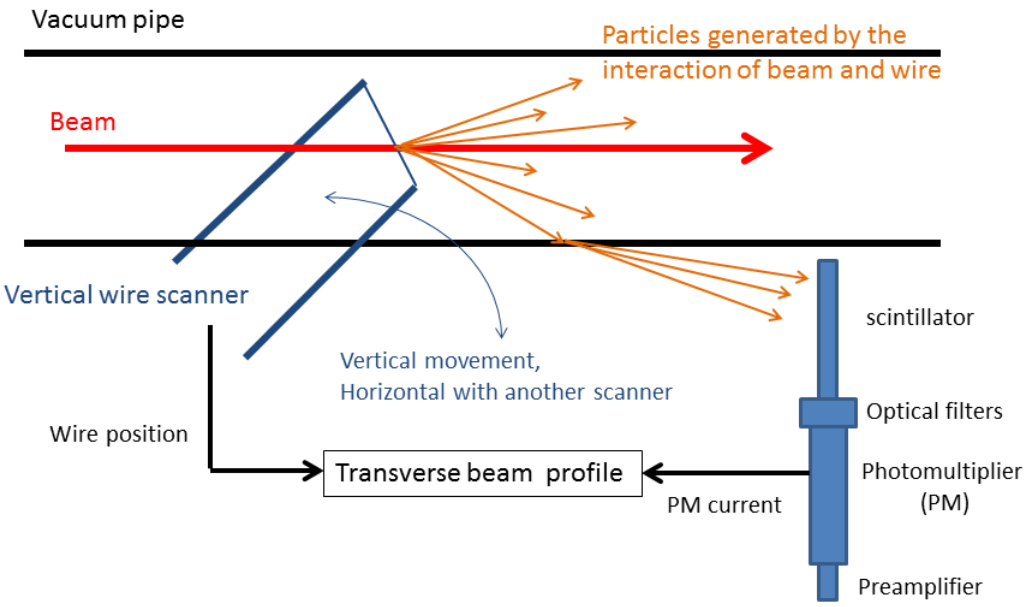

Figure 7.2.: Schematic drawing of the different components of a wire scanner. The basic operational principle of a vertical wire scanner is displayed. The wire scanner consists of a fork with a wire that moves through the beam and produces secondary particles, which are measured with a scintillator.

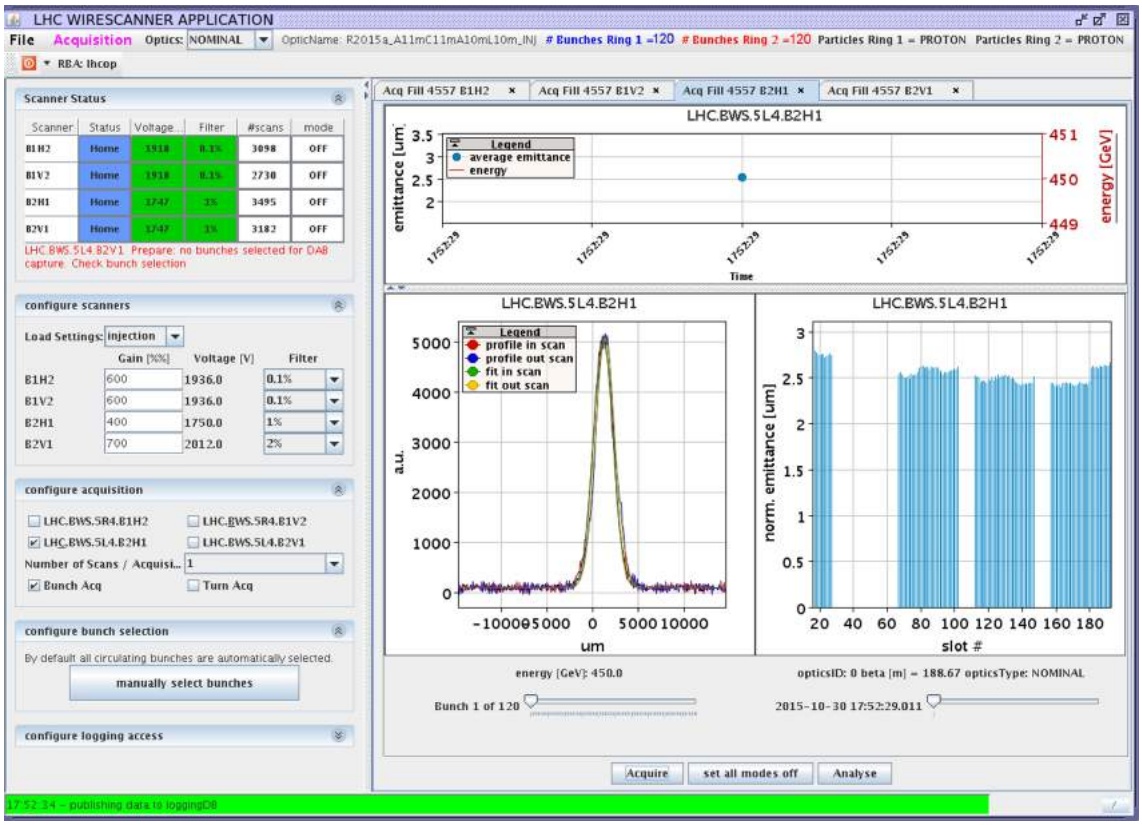

Figure 7.3.: LHC wire scanner application. The screenshot shows the application after a scan of 120 bunch profiles was performed on beam 2 horizontal. The status of the operational wire scanners is displayed in the top left corner. Photomultiplier gain and filter can be set for each scanner. Typically a bunch-by-bunch acquisition is used in the LHC. Only one scanner at a time can be moved into the beam pipe. The transverse profiles for each bunch are displayed after the scan, for in and out scan (which means both directions of motion), and fitted with a Gauss function. An overview of the online calculated bunch emittances averaged over in and out scan is given in a bar chart. On the top graph a time evolution of the different emittance measurements can be given; usually the average emittance of all bunches is displayed for high bunch numbers. After each scan the data is published to the logging data base.

implemented and the analysis after each scan is done online. The raw and fitted data is published to the logging data base for possible offline analysis.

7.3.1. Transverse Profiles and Fitting

The LHC wire scanners are equipped with a 36 µm thick carbon wire attached to a linearly moving fork [89]. The wire crosses the beam at a constant speed of 1 m/s. For each measurement the beam profile is scanned twice as the wire passes through the beam with an in and out scan. In this thesis only the average beam size

obtained from in and out scan is used for the emittance calculations and the error from averaging is included in the results.

After each scan, once the transverse beam profile is obtained, it is fitted with a five parameter Gauss function to obtain the beam size σ:

$$f(x) = d + k \cdot x + a \cdot \exp\left(-\frac{x-b}{2 \cdot \sigma^2}\right), \tag{7.3.1}$$

where d is the PM signal offset, k is the slope of the baseline, a is the signal amplitude, and b is the mean of the Gaussian distribution. A horizontal beam profile measured with the wire scanner and fitted offline with a Gauss function is shown in Fig. 7.4.

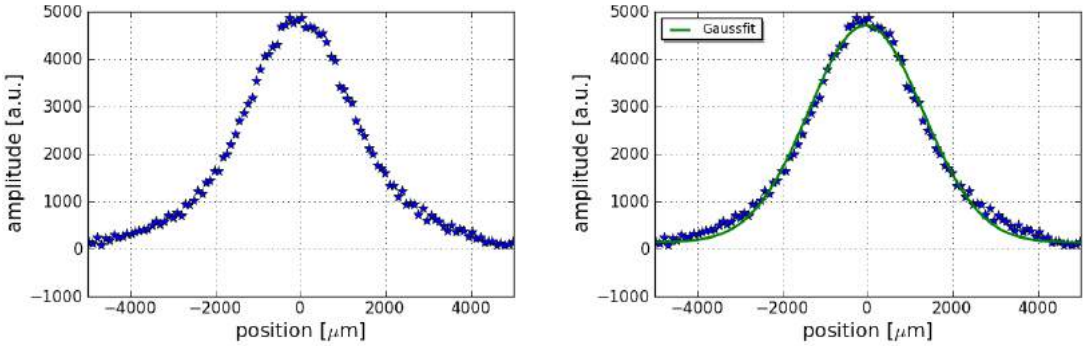

Figure 7.4.: Transverse beam profile (left) with Gauss fit (right), measured with wire scanner. The measurement points (blue) are fitted with a five parameter Gauss (green). Non-Gaussian tails are visible.

The calculated σ is the beam size value of the entire proton bunch. In dispersion free regions the emittance is obtained from the beam size and the beta function (β) at that point:

$$\varepsilon = \frac{\sigma^2}{\beta}. \tag{7.3.2}$$

Dispersion is not taken into account as it has been measured to be small[3]. In 2012 the dispersion was measured at the wire scanner location and values of $D_x \leq 10$ cm and $D_y \leq 15$ cm were found for the horizontal and vertical dispersion, respectively. 2015 dispersion measurements were not available, but the measured optics is similar to the optics in 2012 [65].

Thus the obtainable emittance measurement accuracy for a wire scanner at location with no dispersion depends on the accuracy of the optics knowledge (β) and measurement error ($\Delta\beta$) as well as on the beam size measurement accuracy ($\Delta\sigma$) of the given device:

$$\frac{\Delta\varepsilon}{\varepsilon} = \sqrt{\left(2\frac{\Delta\sigma}{\sigma}\right)^2 + \left(\frac{\Delta\beta}{\beta}\right)^2}. \tag{7.3.3}$$

[3]The beam size contribution from dispersion σ_D to the observed beam size $\sigma_{obs} = \sqrt{\sigma_{beta}^2 + \sigma_D^2}$ is $\sigma_D = D\,\frac{\Delta p}{p}$. With $\frac{\Delta p}{p} \sim 3 \times 10^{-4}$ at injection and $\frac{\Delta p}{p} \sim 1 \times 10^{-4}$ at flattop energy, the horizontal beam size from dispersion is $\sigma_D \approx 10$ -20 µm at injection and $\sigma_D \approx 5$ µm at flattop. The vertical beam size from dispersion is $\sigma_D \approx 40$ µm at injection and $\sigma_D \approx 15$ µm at flattop. With observed beam sizes of $\sigma_{obs} \sim 800$ - 1000 µm at injection and $\sigma_{obs} \sim 200$ - 400 µm at flattop energy in both planes, dispersion is negligible.

After upgrades to the LHC wire scanner system an intense measurement campaign was launched in 2015 to reduce the wire scanner measurement uncertainty on the transverse beam size.

7.3.2. Wire Position Measurement Uncertainty

Wire Position Measurement Calibration

A standard procedure to verify the calibration of the wire position measurement is an orbit bump scan with beam at the wire scanner location. While the centre of the beam is shifted locally at the scanners, wire scans are triggered to determine the accuracy of the position measurement of the wire scanners. For such a scan in the LHC a closed orbit bump at the wire scanner location is generated with four corrector magnets in the vicinity of the scanner. An example for scanner B1V2 is shown in Fig. 7.5. Orbit bump amplitudes of up to ± 4 mm in steps of typically $\pm 1 - 2$ mm were used for the calibration.

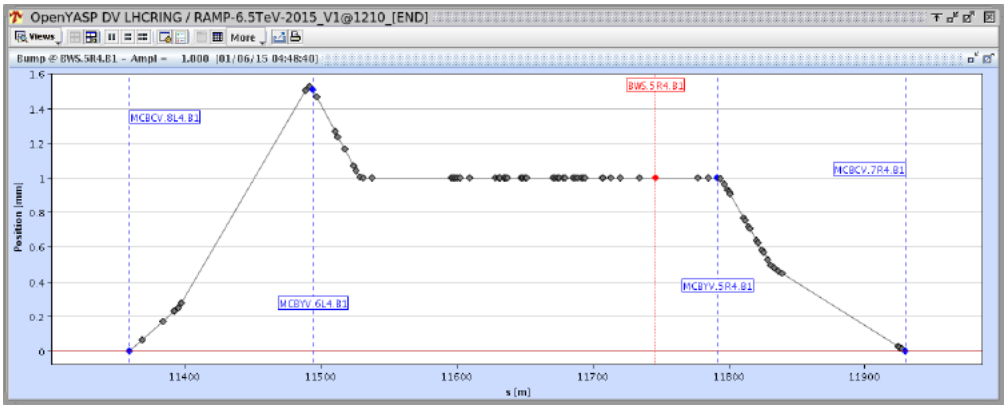

Figure 7.5.: Four corrector closed orbit bump at beam 1 vertical wire scanner. The closed orbit bump is generated with four corrector magnets, MCBCV.8L4.B1, MCBYV.6L4.B1, MCBYV.5R4.B1 and MCBCV.7R4.B1, in the vicinity of the beam 1 vertical wire scanner.

The beam position at the wire scanner was measured with the surrounding Beam Position Monitors (BPMs). The BPMs used were BPMWA.B5L4, BPMWA.A5L4, BPMWA.A5R4 and BPMWA.B5R4. Since these BPMs and the wire scanner are on the bump plateau, the measured beam positions are fitted linearly and extrapolated to the wire scanner.

The above mentioned BPMs are buttons with a diameter of 34 mm installed in a beam pipe where the aperture is about 61 mm [93]. Since LS1 the beam position is corrected with respect to non-linearity errors. The residual error is estimated to be below 100 µm for orbit amplitudes smaller than 6 mm, which is within the margins of the applied bumps. In addition, the electronics intrinsic non-linearity error yields about 160 µm. In total the BPM resolution, the relative positions between the orbit bumps, for the BPMs used is about 260 µm [93]. Since the beam position measurements were found to be reproducible within the resolution limits of the wire scanners, BPM uncertainties are neglected for this study.

To analyse the measurements with orbit bumps, the fitted orbit at the wire scanner is compared to the mean position obtained from a Gaussian fit of the measured wire

scanner beam profile. Measurements were carried out at 450 GeV and 6.5 TeV with each operational scanner and found to be consistent. The 2015 calibration results of the operational LHC wire scanners are shown in Fig. 7.6. The slope of the linear fit shows a 4.5 % calibration error for the beam 2 horizontal scanner and a 3.3 % calibration error in the case of the beam 2 vertical scanner. The results in terms of emittance for all operational wire scanners are listed in Table 7.2. In summary, the calibration error on the emittance can be as large as 9 %. However, a calibration verification was already attempted in 2012 with slightly different results, see chapter 5. Another set of orbit bump scans is foreseen for the future to check reproducibility, but was not possible in 2015. Therefore measurement results in this thesis do not include a calibration error.

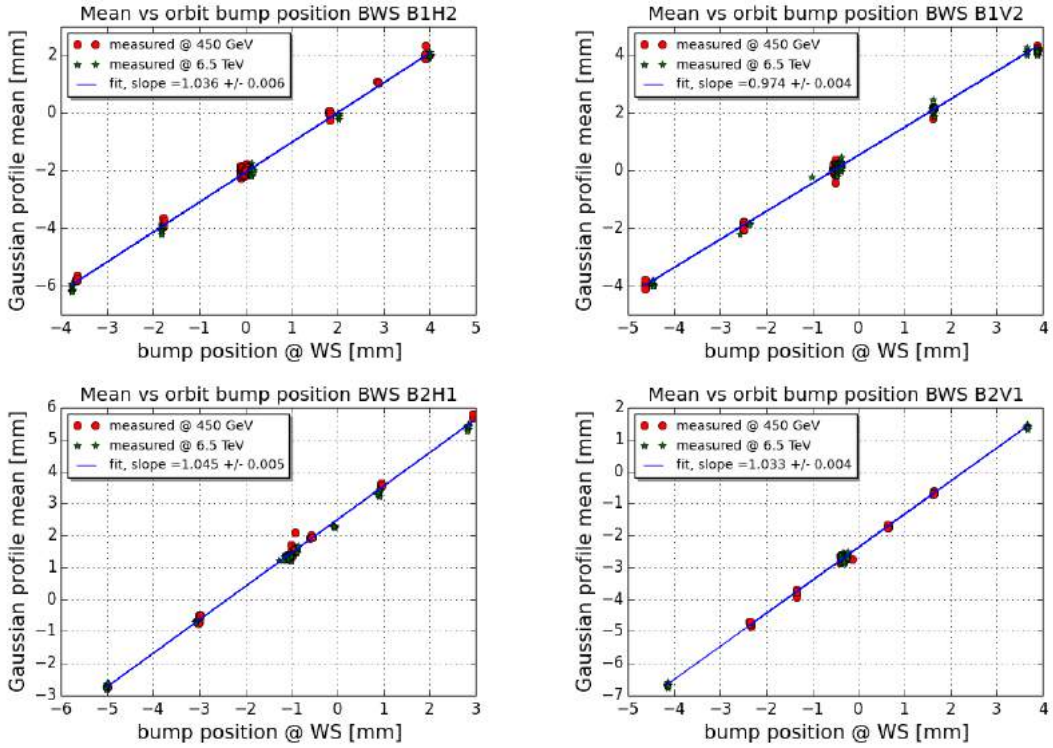

Figure 7.6.: LHC wire scanner orbit bump calibration in 2015 for the operational beam 1 and beam 2 scanners in the horizontal and vertical plane. The wire position measurement was verified with beam at different transverse beam positions. A single bunch was injected. The plots show the Gaussian profile mean measured with the respective wire scanner at different orbit bumps at 450 GeV (red) and 6.5 TeV (green). Measurements of beam 1 were carried out during Fill 3718 (14 May 2015) and Fill 3809 (1 June 2015). Beam 2 measurements took place during Fill 3644 (24 April 2015). A linear fit (blue) is applied. The slope value of the fit can be found in the legend.

Scanner	Position measurement error [%]	$\Delta\varepsilon_{\text{cal}}$ [%]
B1H2	+3.6	+7.2
B1V2	-2.7	-5.2
B2H1	+4.5	+9.0
B2V1	+3.3	+6.6

Table 7.2.: LHC Run 2 wire scanner position measurement uncertainty and resulting emittance calibration error ($\Delta\varepsilon_{\text{cal}}$).

Scan to Scan Beam Size Spread

The LHC wire scanners suffer from a large scan-to-scan beam size measurement variation, which depends on the scanner and the energy. An example for emittance measurements through the LHC cycle with an LHC wire scanner can be seen in Fig. 7.7. The emittance evolution of a single bunch for beam 2 horizontal at different energies is shown. Without intensity losses and even in case of constant wire scanner PM settings the emittance varies from scan to scan. The absolute and relative scan-to-scan spread in terms of beam sizes for four consecutive scans are listed in the first columns of Table 7.3. At 450 GeV and transverse beam sizes of about 1 mm, the spread is 100 µm. At 6.5 TeV and beam sizes of maximum 350 µm, the spread is 20 µm. Despite the smaller scan-to-scan beam size spread in absolute terms at flattop energy, the relative spread is only slightly reduced at higher energy, on average from about 11 % at 450 GeV to about 7 % at 6.5 TeV. Thus at higher energies the scan-to-scan spread of the normalized emittance is larger, see Fig. 7.7.

Part of the beam size measurement spread can be attributed to a limited resolution

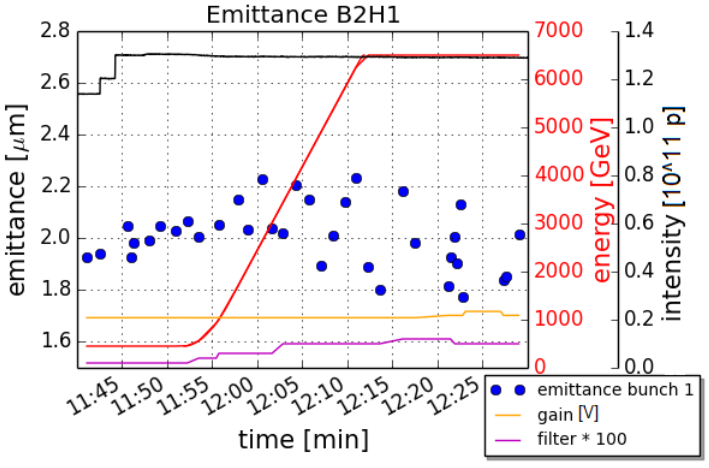

Figure 7.7.: Scan to scan emittance spread through the LHC cycle. Emittance evolution of a single bunch (blue) during the LHC cycle measured with a wire scanner during Fill 3721 (15 May 2015). The energy is shown in red and the bunch intensity in black. Emittances in beam 2 horizontal are displayed. The wire scanner photomultiplier gain and filter settings for each scan are indicated.

of the wire position measurement ($\sigma \approx \pm$ 40 µm). Assuming a linear movement of the wire, the recorded wire position measurement during a scan can be fitted linearly. The wire position measurement is recorded in pixels. The profile measurement is also recorded in pixels and fitted with a Gaussian. To obtain the beam size σ in µm, the slope k of the linear fit to the position data is multiplied by the σ in pixel:

$$\sigma_{\mu m} = k \cdot \sigma_{\text{pixel}}. \tag{7.3.4}$$

The obtained beam size spread after correction is much reduced for beam 1 scanners at all energies and beam 2 scanners at 450 GeV to about 3 %, see Table 7.3. The absolute spread is slightly larger for larger beam sizes.

	Scanner	B1H2	B1V2	B2H1	B2V1
	$\sigma_{450\text{GeV}}$ [µm]	800	1100	800	1200
before corr	$\Delta\sigma_{450\text{GeV}}$ [µm]	100 (13 %)	100 (9 %)	100 (13 %)	100 (8 %)
after corr	$\Delta\sigma_{450\text{GeV}}$ [µm]	25 (3 %)	35 (3 %)	20 (3 %)	40 (3 %)
	$\sigma_{6.5\text{TeV}}$ [µm]	250	310	240	350
before corr	$\Delta\sigma_{6.5\text{TeV}}$ [µm]	20 (8 %)	20 (6 %)	20 (8 %)	20 (6 %)
after corr	$\Delta\sigma_{6.5\text{TeV}}$ [µm]	8 (3 %)	9 (3 %)	17 (7 %)	35 (10 %)

Table 7.3.: Wire scanner beam size measurement spread $\Delta\sigma$ from scan to scan for four consecutive wire scans at 450 GeV and 6.5 TeV for the operational LHC wire scanners in 2015. Typical beam sizes σ at 450 GeV and 6.5 TeV at the wire scanner location are listed. The scan-to-scan spread before correction (before corr) and after correction (after corr), with the position read-out smoothing, are shown. After the position measurement correction the spread could be greatly reduced for beam 1 scanners.

However, beam 2 scanners still show a large spread at 6.5 TeV even after the position read-out smoothing. The measured wire profile can have a spread not only in position, but also in signal amplitude, which also produces a spread in the measured beam sizes from scan to scan. A possible explanation could be noise on the amplitude read-out which might originate from a noisy photomultiplier signal [90]. Noise in the PM signal acquisition chain could originate from high voltage or it could be coupled to the analogue signal in long cables or in the ADC chain. Investigations are ongoing in the extended 2016 LHC winter shutdown.

7.3.3. Photomultiplier Working Point Investigations

The wire scanner shower product is amplified by a photomultiplier. The amplification can be tuned with different gain and filter settings, but should not have an impact on the obtained beam size. Each LHC wire scanner PM has eight transmission filters, see Table 7.4, with PM gains between 0 and 2200 V. During LHC Run 1 a strong dependence of PM settings on the measured beam size was observed [6]. A non-linear response regime of the photomultiplier, which will be referred to as PM saturation in the following, was entered with certain settings.

Filter	0	1	2	3	4	5	6	7
Transmission [%]	100	20	10	2	1	0.02	0.1	0

Table 7.4.: LHC wire scanner photomultiplier filters with corresponding light transmission.

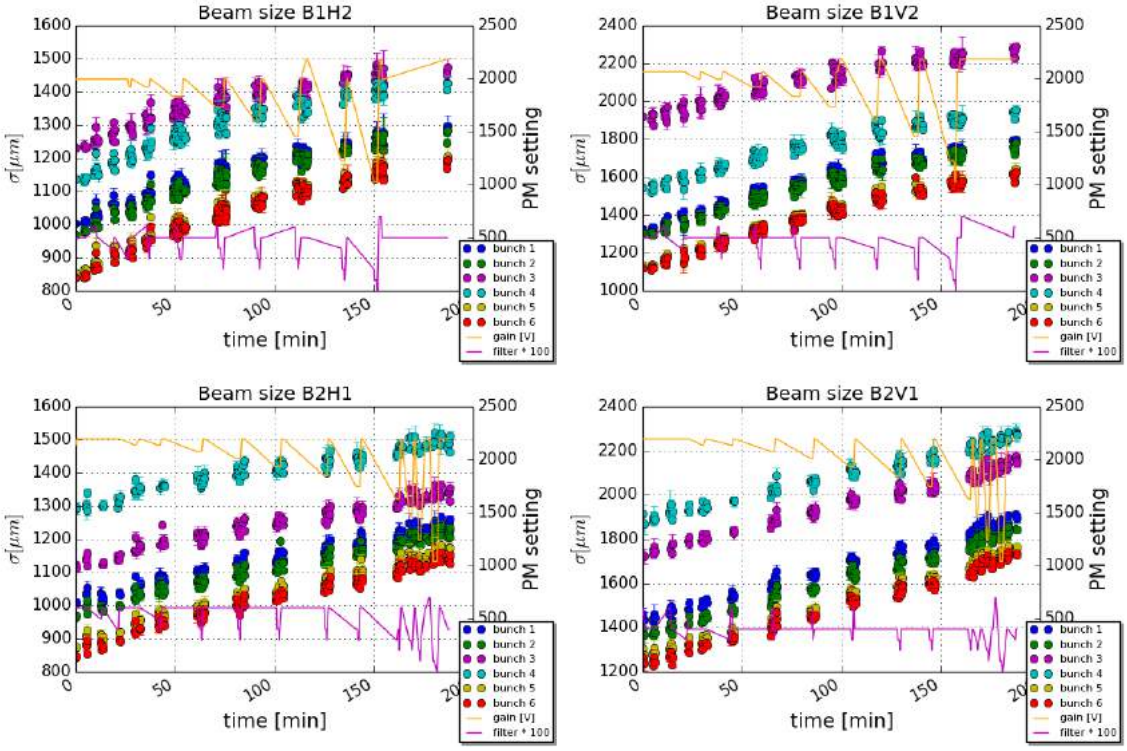

Figure 7.8.: Photomultiplier working point investigations at 450 GeV. Beam 1 and beam 2, horizontal and vertical, beam size of six single bunches from wire scans at 450 GeV, Fill 3808 (31 May 2015). The beam size value σ is indicated on the left scale. The PM voltage (orange) and filter (purple) are displayed, right scale.

To find the optimum working point of the wire scanners, measurements with all available PM gain and filter setting combinations were performed. Figure 7.8 shows the 2015 measurement results for all operational LHC wire scanners at 450 GeV. Six bunches with different beam sizes were injected into the LHC. The beam size evolution is plotted over time with the applied gain and filter settings. To remove the natural emittance growth at the injection plateau, scans with a fixed reference settings were done after each settings change and fitted assuming an exponential function, see example in Fig. 7.9. An exponential fit was chosen regardless of the origin of the growth. Figure 7.10 then shows measured beam sizes minus the fitted growth. In addition, the results of measurements with same gain and filter settings were averaged to one data point in Fig. 7.10. At 450 GeV no sign of PM saturation could be detected within the measurement resolution of the wire scanners. Moreover, all combinations of settings below ADC saturation, for profile amplitudes between 2500 and 7500 a.u., result in adequate profiles.

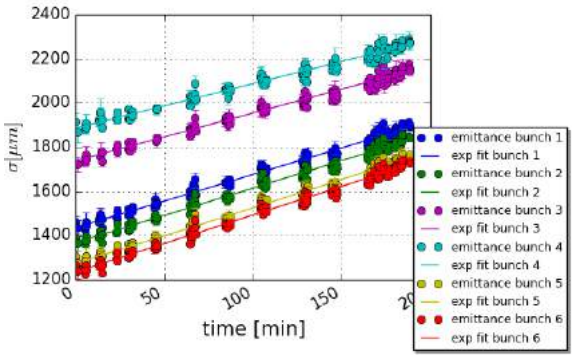

Figure 7.9.: Beam 2 vertical beam size of six single bunches from wire scans at 450 GeV, Fill 3808 (31 May 2015). The beam size evolution over time, of the scans done with the fixed PM reference settings, is fitted exponentially for each bunch.

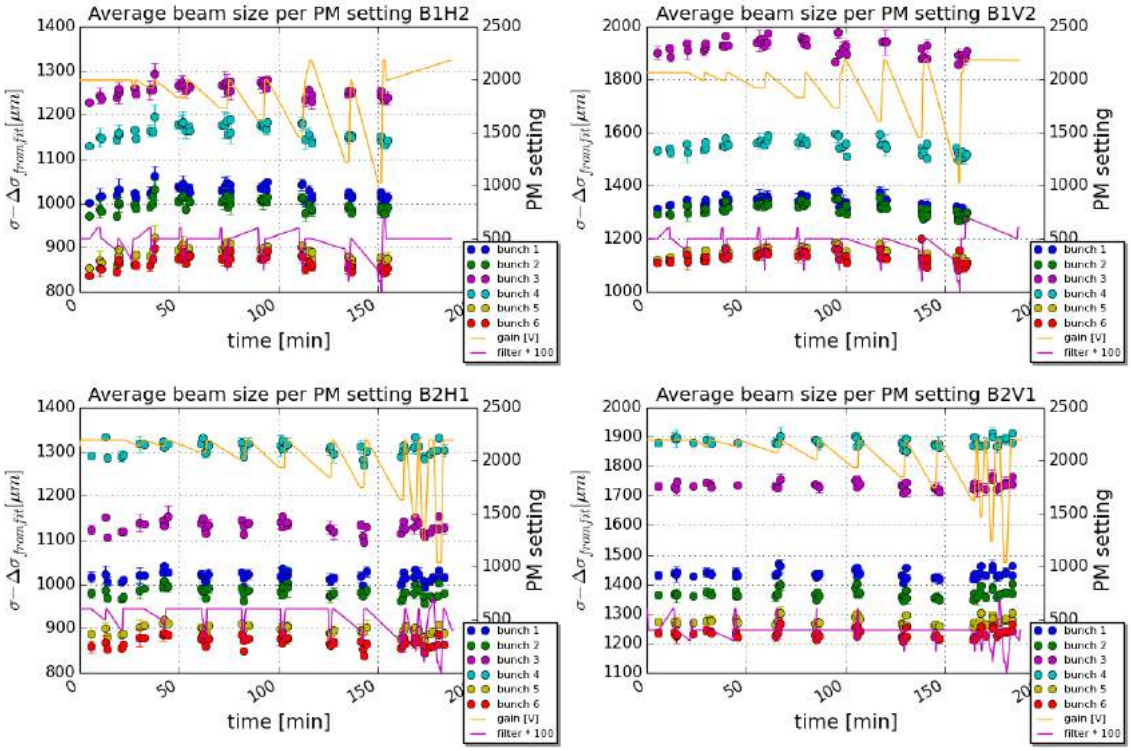

Figure 7.10.: Average beam 1 and beam 2, horizontal and vertical, beam size per PM setting minus growth from exponential fit of the scans done with fixed reference settings. The beam size evolution of six single bunches from wire scans at 450 GeV is plotted, Fill 3808 (31 May 2015), left scale. The PM voltage (orange) and filter (purple) for each scan are also displayed, right scale.

For the studies at 6.5 TeV two bunches with different emittances were injected and ramped to flattop energy. Measurements at 6.5 TeV were more difficult because the possible range of PM settings before ADC saturation is much smaller than at 450 GeV. While at 450 GeV all filters could be tested with a PM voltage range

from around 1000 to 2200 V, only three filter settings were possible at 6.5 TeV with voltages between 1000 and 1200 V. Nevertheless, also at flattop energy no PM saturation can be found, see Fig. 7.11. Despite the large measurement spread, the applied settings result in similar beam sizes.

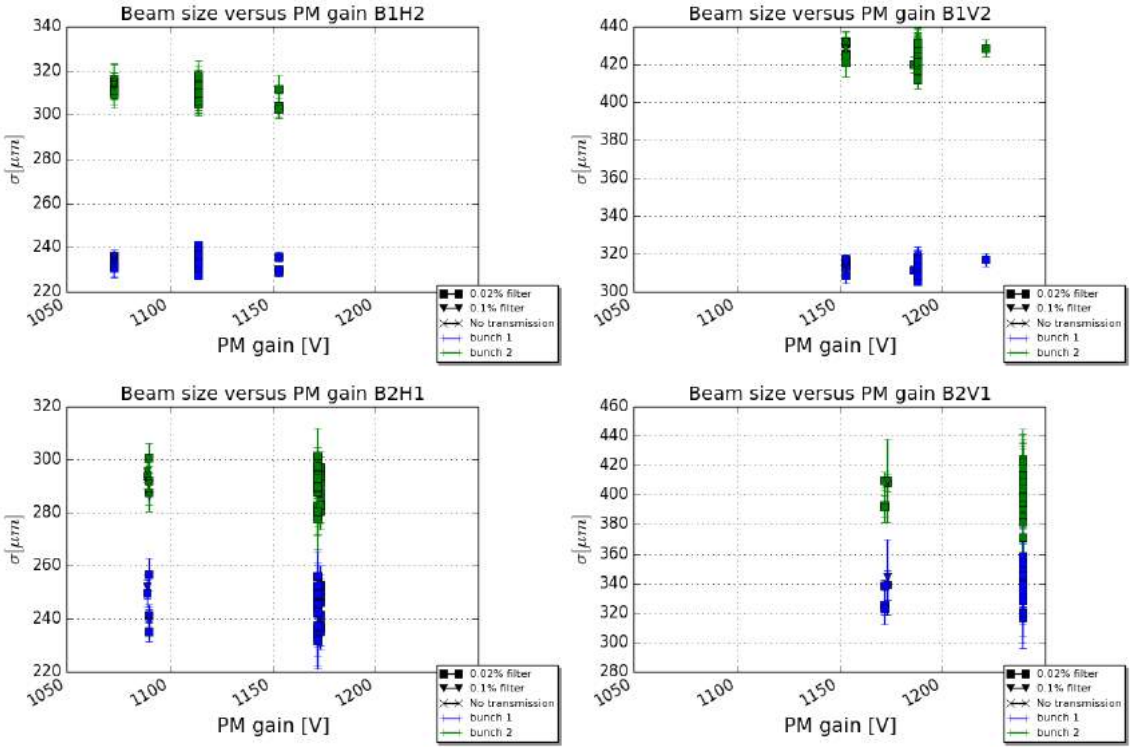

Figure 7.11.: Beam 1 and beam 2, horizontal and vertical, beam size of two single bunches from wire scans at 6.5 TeV, Fill 3809 (1 June 2015), as a function of the applied PM voltage. The different PM filters are marked.

The upgrade of the LHC wire scanners during Long Shutdown 1 could explain the improved situation, see below. In conclusion, all profiles with amplitudes in the range of 2500 and 7500 a.u. are non-saturated, independent of the beam size. Typical PM settings used for the 2015 emittance preservation studies are low filters with 0.02 to 1 % transmission and gains between 1000 and 2000 V.

Changes during Long Shutdown 1 (LS1)

During Long Shutdown 1 (LS1) the LHC wire scanner system was inspected and upgraded. Following the findings in 2012, see chapter 5, the system had to be improved to achieve better measurement accuracy. After vacuum leaks were detected in Run 1 and the predicted lifetime of the wire scanner (10'000 scans) was approached, bellows and compensations springs were changed during LS1. One broken PM was replaced (beam 2) and power supply schematics were upgraded [94]. The high voltage PM voltage divider was modified to improve the linearity response of the photomultiplier. Additional capacitors were added to keep the voltage constant. As a consequence a wire scan in 2015 took approximately 30 seconds due to high voltage setting time. Also the PM gain dependency on light intensity had been reduced. The photomultipliers were shielded with tape and one PM filter was

exchanged for a higher filter (the transmission changed from 0.2 % to 0.02 % for filter 5, see Table 7.4). To prevent wire breakage due to errors in the software, the firmware was also upgraded in 2015. A new motion card firmware was deployed to solve safety critical issues [90].

7.4. Validation of Wire Scanner Beam Size Measurement Precision

During head-on collisions it is possible to derive emittance from luminosity and directly compare it to the convoluted emittance from simultaneous wire scans and BSRT measurements in case of low intensity fills. The method assumes identical Gaussian shaped and perfectly aligned beams. During collisions of Fill 4585 the convoluted emittance from wire scans and BSRT measurements was compared to emittance from ATLAS and CMS luminosity, see Table 7.12. The values were taken after the interaction points had been optimized. Emittances from the different measurement techniques at collision agreed well within measurement uncertainties. This procedure was repeated during many low intensity test fills and the presented results were reproducible. For the calculation of the emittance the measured β and β^* values were used, see chapter 6. The luminosity measurement and its uncertainties are explained in chapter 8. The BSRTs were cross-calibrated with wire scanners.

The large discrepancy between emittance from luminosity and wire scanner as found during Run 1 has not been observed any more during Run 2. A possible explanation is the better understanding of the wire scanners.

	ε [µm]
Wire scanner	2.12 ± 0.27
BSRT	2.32 ± 0.33
ATLAS	2.06 ± 0.28
CMS	2.33 ± 0.32

Figure 7.12.: Comparison of the convoluted emittance from wire scanners and BSRTs, as well as emittance derived from peak luminosity in ATLAS and CMS for Fill 4585 (5 November 2015).

7.5. Summary of LHC Beam Size Measurement with Wire Scanner

Wire scanners are an important tool for high precision beam size measurements in the LHC. Even though they can only be used with low intensity beams, wire scanners are currently the only instrument that can measure useful transverse profiles throughout the entire LHC cycle. They are also used to calibrate other profile monitors such as the BSRT.

A transverse beam profile with a wire scanner is obtained from two simultaneous measurements: wire position measurement and signal amplitude measurement of

the shower particles. Both measurements are error prone.

During calibration studies in 2015 an uncertainty on the wire position measurement was observed. The systematic error can be as large as 9 % in terms of emittance. The position measurement calibration could not be included in this thesis. A verification of the results could not be carried out.

The wire scanner position measurement read-out has a limited resolution of $\sigma \approx \pm 40$ µm. Beam size measurements scan after scan show a large variation. A statistical error on the emittance of up to 25 % for a single scan has to be added. However, the error can be significantly reduced with a linear fit of the wire position measurement. A statistical error of 6 % on the emittance remains, independent of the beam size. It can only be further reduced when averaging over several consecutive scans.

Also the photomultiplier signal can be noisy and causes a spread from scan to scan in the beam size measurement. Especially for the photomultiplier of beam 2 these fluctuations are thought to lead to a large statistical error, about additional 10% in emittance.

Photomultiplier gain below 1000 V should be avoided and only profiles with amplitudes higher than 2500 a.u. and smaller than 7500 a.u. should be taken into account. Then the obtained beam size is independent of PM settings.

In the future, the wire position measurement calibration needs to be repeated and verified calibration factors implemented. The wire scanner electronics should also be calibrated with an external additional position read-out system and an additional external photomultiplier consisting of a scintillator and a scope. At the moment the electronics of all wire scanners have the same calibration factor.

8. Emittance from Luminosity

The luminosity measurement can be used to determine the transverse emittance of the colliding beams. It is, however, the convolution of the real beam emittances. As discussed in chapter 3, the luminosity L is defined by

$$L = \frac{f_{\mathrm{rev}} n_{\mathrm{b}}}{4\pi} \cdot \frac{N_1 N_2}{\beta^* \varepsilon} \cdot \frac{1}{\sqrt{1 + \left(\frac{\sigma_{\mathrm{s}}}{\sigma_u} \frac{\phi}{2}\right)^2}}, \tag{8.0.1}$$

where ε is the normalized transverse emittance, f_{rev} is the revolution frequency, n_{b} is the number of bunches per beam, N_1 and N_2 are the number of protons per bunch for beam 1 and beam 2 and β^* is the beta function at the interaction point. The luminosity also depends on the crossing angle ϕ and the bunch length σ_{s}. σ_u is the transverse beam size in the crossing plane ($u = x, y$). The emittance from luminosity can be obtained by knowledge of all other parameters. In this document measured values are used for crossing angle and β^*. Table 8.1 summarizes the current knowledge of the 2015 parameters.

	nominal	measured
Crossing angle IP1 [µrad]	285	320 ± 20
Crossing angle IP5 [µrad]	285	346 ± 26
β^* in IP1 [m]	0.8	0.847 ± 0.027
β^* in IP5 [m]	0.8	0.843 ± 0.028
Revolution frequency [kHz]	11.245	-
γ at 6.5 TeV	6929.638	-

Table 8.1.: LHC proton beam collision parameters in 2015. Crossing angle and β^* were measured with k-modulation, see chapter 6.

In the LHC, bunch intensity, bunch length and luminosity are measured. The bunch intensities are monitored with a Fast Beam Current Transformer [1]. The longitudinal bunch size is obtained from the LHC Beam Quality Monitor [1] and the luminosity is measured by ATLAS and CMS. The different measurements and their uncertainties are explained in the following.

8.1. Luminosity Measurement

The bunch luminosity L_{b} in a proton collider is derived from the measured collision rate R_{rel} of a reference collision process with the corresponding cross section σ_{rel} [95]:

$$L_{\mathrm{b}} = \frac{R_{\mathrm{rel}}}{\sigma_{\mathrm{rel}}} = f_{\mathrm{rev}} \frac{\mu}{\sigma_{\mathrm{inel}}}. \tag{8.1.1}$$

Typically inelastic proton-proton (pp) collisions are chosen as the reference process, where μ is the average number of inelastic interactions per collision of two bunches and σ_{rel} is the inelastic pp cross section. The cross section expresses the likelihood of an interaction event between two particles.

The simplest way to measure the luminosity is to count the number of inelastic pp collisions recorded in a detector. The inelastic pp collision rate can be measured with different parts of the detector. In the following to most popular devices in ATLAS and CMS for luminosity measurement, the luminometers, are mentioned.

In 2015, CMS based its luminosity measurements of the 25 ns physics beams primarily on the Pixel Luminosity Telescope (PLT) [96]. The PLT consists of silicon pixel sensors; it is described in [97]. In ATLAS the luminosity in 2015 was measured using signals from the Cherenkov detector LUCID (LUminosity measurement using a Cherenkov Integrating Detector) [98]. Tubes filled with gas around the beam pipe act as a Cherenkov detector; the luminometer is explained in [99].

Each luminosity measurement provides online data for machine optimization. The data is also stored for offline analysis. The luminosity published to the logging database is often post processed and corrected. In 2015 the bunch-by-bunch luminosity was measured typically once per minute.

Counting the number of inelastic pp collisions only gives the relative luminosity. A major challenge associated with the luminosity measurements at the LHC is the determination of the absolute luminosity calibration, which requires a time intensive dedicated measurement and analysis.

8.1.1. Absolute Luminosity Calibration

To determine the bunch luminosity from Eq. 8.1.1, not only the collision rate of the inelastic pp collisions has to be measured, but also the inelastic cross section has to be determined accurately for the given process.

At the LHC, the primary technique to determine the absolute luminosity scale in ATLAS and CMS is based on a series of van der Meer (vdM) scans [95]. These are dedicated beam separation scans with beam parameters optimized for the purpose of achieving high accuracy on the absolute luminosity measurement. The technique involves scanning the two LHC beams through each other to determine the cross section. These measurements, when combined with information on the number of circulating protons, allow the determination of an absolute luminosity scale, which in turn is used to calibrate the luminometer.

The ATLAS and CMS luminosity values presented in this thesis were calibrated with van der Meer scans. The final calibration result, which varies over different running periods, was implemented offline. Averaged over the 2015 LHC proton run at 6.5 TeV the published ATLAS luminosity has a systematic uncertainty of 5 % [98]. The CMS luminosity measurement uncertainty is 4.8 % for 50 ns fills and 4.6 % for 25 ns fills.

8.2. Bunch Intensity Measurement

In the LHC the bunch-by-bunch intensity is measured with two Fast Beam Current Transformers (FBCTs) per ring. They are installed in LHC point 4 and measure the bunch current in each filled RF bucket and also provide turn-by-turn beam intensity measurements [100]. The bunch-by-bunch intensity is acquired at 200 MHz, while the turn acquisition rate is $\sim$ 2 MHz. In the LHC a bunch-by-bunch intensity measurement is published to the logging database once per minute. Currently the FBCT uses a toroid transformer as measurement device and analogue integrators for the signal acquisition. The absolute FBCT measurement error is difficult to define due to the mechanical layout. The measurement accuracy depends on the RF phase and is bunch length and bunch position dependent. DC Current Transformers (DCCTs) [101] are used to calibrate the FBCTs. The DCCTs measure the mean circulating bunch current. They are installed in LHC point 4 and use the fluxgate magnetometer principle [102]. The measurement uncertainty of the LHC DCCT beam intensity measurement is in the sub percent level (0.32 % per beam for physics fills) [103]. Several times per year, usually during vdM scans, the reproducibility of the FBCTs is cross checked with DCCT measurements. The sum of several FBCT measurements in turn mode is compared to the DCCT beam intensity. Thus the measurement uncertainty of the LHC bunch intensity measurement with FBCTs results in about 2 % (2×10^9 p) measurement accuracy per bunch with a resolution of about 1 % (1×10^9 p) [100]. When deriving emittance from luminosity, the error on the bunch intensity measurement is included.

8.3. Bunch Length Measurement

The LHC Beam Quality Monitor (BQM) provides the bunch lengths and the longitudinal bunch positions in each ring. A wall current monitor is used to measure the longitudinal bunch-by-bunch profiles of the beam. An acquisition of all bunch profiles is obtained every 5 s. Along the acquisition chain the signal from the wall current monitor is falsified. The distorted longitudinal profiles are analysed with a Full Width Half Maximum (FWHM) algorithm assuming Gaussian particle distributions. A transfer function specific to the signal chain relates the obtained FWHM to the rms width σ of the bunch [104]. The quoted bunch lengths are the 4σ values. The individual bunch lengths of all bunches are published to the LHC logging database twice per minute.

Assuming Gaussian longitudinal profiles is, however, not always true. It was found that the longitudinal bunch shape at 6.5 TeV differs from a Gaussian distribution, see Fig. 8.1. probably due to the controlled longitudinal RF blow-up during acceleration, where phase noise is injected to keep the bunch length constant [45]. From the FWHM algorithm the estimated error on the (4σ) bunch length measurement due to non-Gaussian profiles is typically $\pm$ 1 cm [105]. The error is included in the emittance calculation from luminosity.

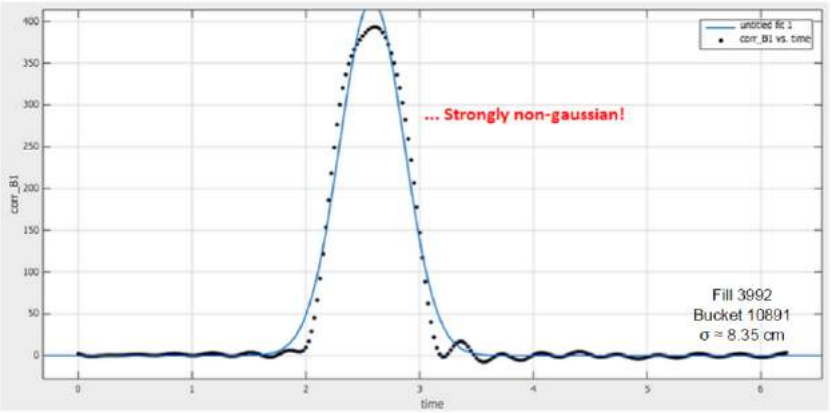

Figure 8.1.: LHC longitudinal bunch profile measured with the LHC BQM (black). A Gaussian fit is applied (blue) but deviates from the original profile. *Courtesy M. Hostettler, CERN, Geneva, Switzerland.*

Part IV.

LHC Run 2 Emittance Preservation Studies

9. Emittance Preservation at the LHC in 2015

During LHC Run 1 significant transverse emittance growth through the LHC cycle was observed. Measurements indicated that most of the blow-up occurred during the injection plateau and the ramp. Intra-beam scattering (IBS) was one of the main drivers of emittance growth. In April 2015 the LHC re-started with a collision energy of 6.5 TeV per beam. This chapter presents the first transverse emittance measurements through the LHC Run 2 cycle with low beam intensity. The emittance was measured with wire scanners and synchrotron light monitors. The emittance growth results will be compared to intra-beam scattering simulations. The findings have also been published in [106, 107]. More evidently in 2015 than in 2012 the vertical emittances blow up during the injection plateau. Possible causes such as transverse damper and noise will be investigated and results summarized.

9.1. Performance of the LHC in 2015

In 2012 the LHC was operated with high brightness beams with beam parameters pushed to their limits for outstanding luminosity production. With a bunch spacing of 50 ns the LHC was filled for physics with 1374 bunches per ring, containing up to 1.7 $\times 10^{11}$ protons per bunch (ppb) with normalized transverse emittances as small as 1.5 µm at injection. However, the high brightness could not be preserved during the LHC cycle. Measurements in 2012 revealed a transverse emittance blow-up of about 0.4 to 0.9 µm from injection into the LHC to the start of collisions, see chapter 5.

At the start of Run 2 in 2015 beams of reduced brightness with bunch intensities of 1.1 $\times 10^{11}$ ppb and a transverse emittances of 2.4 µm were injected into the LHC. With a bunch spacing of 25 ns the LHC was filled with up to 2244 bunches per ring[1].

To understand the emittance evolution for LHC physics fills, the transverse emittance at the end of the cycle is derived from ATLAS and CMS peak luminosity. The measurement technique is explained in chapter 8. The emittance at the start of the cycle can be measured at LHC injection with wire scanners. When LHC injection wire scans were not available, wire scans at SPS extraction were used. To compare to the emittance value from luminosity, the wire scanner emittances of all beams and planes are convoluted[2]. Transverse beam size measurement and uncertainties in the LHC are mentioned in chapter 7. Measured beta functions are used to compute the emittance, see chapter 6.

[1] The beam parameters of the 2015 physics beams are listed in Table 2.3.
[2] The convoluted emittance is explained in chapter 3.

Performance of the 50 ns LHC Beams

LHC Run 2 started in 2015 with a short period of 50 ns physics fills to commission the machine after the long shutdown. An overview of the convoluted measured emittances at LHC injection and start of collisions for all 50 ns physics fills can be seen in Fig. 9.1. Overall, the emittance blow-up is much reduced with respect to the 2012 LHC proton run. For the few fills in 2015 with 50 ns bunch spacing the average convoluted emittance growth is about 25 % ($\sim$ 0.4 µm averaged over all fills), derived from ATLAS luminosity. Note that the values from CMS luminosity could not be used for this study. The detector faced calibration issues at the start of Run 2 due to cryogenic problems and consequent problems with the solenoid magnetic [108]. Therefore only ATLAS luminosity is taken as reference value in collision.

Since there were not many 50 ns fills in 2015, it is not feasible to look at the average emittance growth. Figure 9.1 shows a large spread in injected emittances and also in resulting emittance blow-up. For some fills the growth is negligibly small, for example for Fill 3974 and Fill 3988. The convoluted emittances during other fills blow up between 0.3 and 0.65 µm, independent of the initial emittance and intensity. IBS simulations with MADX [42] revealed that 0.05 up to 0.15 µm (for the smallest injected emittances) of the horizontal emittance growth can be attributed to intra-beam scattering. Even though the overall growth is slightly reduced with respect to the 2012 50 ns physics fills, only a small fraction of the blow-up can be explained with the IBS theory.

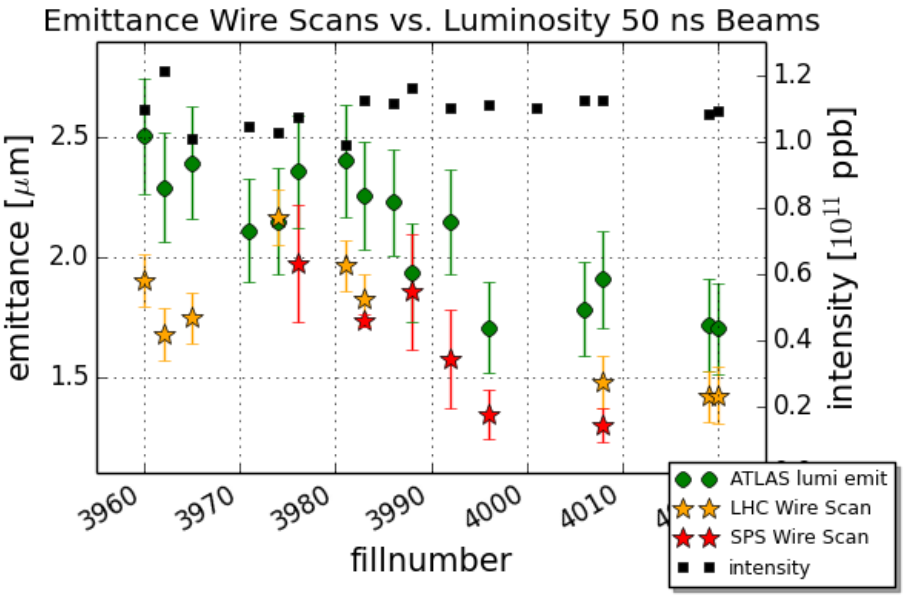

Figure 9.1.: Emittance growth of 50 ns beams in 2015. The emittance of 50 ns physics beams is derived from ATLAS (green) peak luminosity at the start of collisions and compared to the convoluted emittance at LHC injection (orange) or SPS extraction (red) measured with wire scanners. For each fill the injected average bunch intensity is shown (black).

Performance of the 25 ns LHC Beams

In August 2015, starting from Fill 4200, the LHC was operated with 25 ns beams. The intensity ramp-up with the shorter bunch spacing took about two weeks. A total maximum number of 2244 bunches was reached at the end of August 2015. The fill-by-fill emittance evolution of the 25 ns physics beams from LHC injection to start of collisions is shown in Fig. 9.2. Since problems with the CMS luminosity calibration prevailed, only ATLAS luminosity values are presented. The emittance at LHC injection is roughly 2.4 µm in the period after Technical Stop 2 (TS2). The growth through the cycle is similar for 25 ns beams and for 50 ns beams. On average 25 % emittance blow-up was measured after TS2, corresponding to about 0.6 µm.

The LHC wire scanners can only be used with a small fraction of the total nominal intensity per ring due to wire heating. The emittance evolution of high intensity physics fills cannot be measured with the LHC wire scanners. The synchrotron light telescope (BSRT) is used for that purpose. But emittance measurements with the BSRT are unfortunately not useful for a short time frame and many bunches due to a long integration time. The BSRT can acquire 5 to 6 bunch profiles per second. Hence, low intensity test fills during the commissioning phase and intensity ramp-up were used for emittance preservation studies.

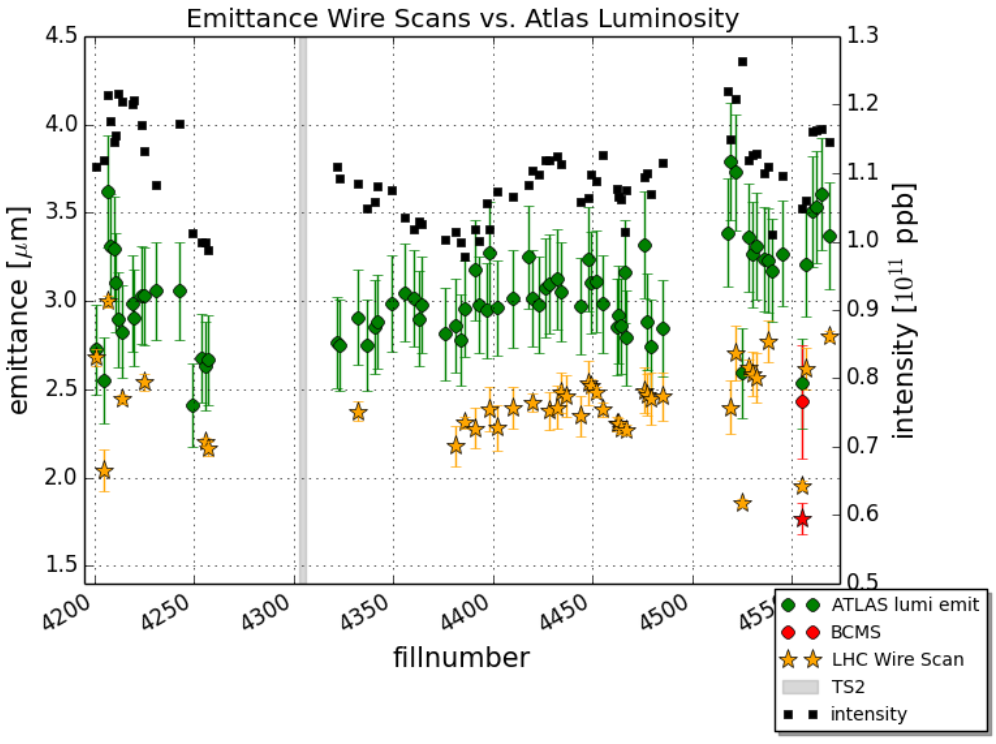

Figure 9.2.: Emittance growth of 25 ns beams in 2015. The emittance of 25 ns physics beams is derived from ATLAS peak luminosity (green) at the start of collisions and compared to the convoluted emittance at LHC injection (orange) measured with wire scanners. A special high brightness fill (BCMS) is marked in red. The period of Technical Stop 2 (TS2) in 2015 is also indicated. For each fill the injected average bunch intensity (black) is shown.

9.2. Emittance Growth during the 2015 LHC Cycle

The emittance evolution through the different parts of the LHC cycle has been studied in 2015 for over 30 low intensity fills. As an example Fill 4287 was analysed in detail through the cycle with the following phases:

- Injection process from SPS to LHC
- 450 GeV injection plateau ($\sim$ 30 minutes)
- Ramp from 450 GeV to 6.5 TeV (20.2 minutes)
- β^* squeeze from 11 m to 80 cm in ATLAS/CMS (12.5 minutes)

During Fill 4284 three bunches were injected into the LHC with different initial emittances, intensities ($0.6 - 1.12 \times 10^{11}$ ppb) and bunch lengths (1.0 - 1.24 ns), see Table 9.1. An overview of the measured emittances through the cycle can be found in Fig. 9.3. The energy and β^* squeeze are indicated. The emittance evolution of all three bunches is compared to results from IBS simulations with MADX [42] since it has been shown in chapter 5 that IBS is the major cause for horizontal emittance blow-up at low energies.

	Bunch intensity [10^{11} ppb]			4σ rms bunch length [ns]		
Beam	Bunch 1	Bunch 2	Bunch 3	Bunch 1	Bunch 2	Bunch 3
1	0.60	1.02	1.12	1.00	1.21	1.24
2	0.60	1.12	0.87	1.03	1.13	1.22

Table 9.1.: Beam parameters for Fill 4284. The bunch intensities and bunch lengths at LHC injection are given.

Although the injected emittance is different for all three bunches, the absolute emittance growth is similar for all bunches. The total measured and simulated emittance growth through the LHC cycle of bunch 3 (purple) in Fig. 9.3 is enumerated in Table 9.2. Note that the large emittance measurement spread in beam 2 vertical complicates the calculation of the true emittance growth. The average emittance of several consecutive wire scans is computed.

Beam 1 and beam 2 horizontal emittances blow up by about 10 % during the cycle, which corresponds to < 0.2 µm. A comparison with the IBS simulation result shows that, despite the large emittance spread, the mean measured horizontal growth matches the simulated values. In the vertical planes, however, a transverse emittance growth of about 20 % ($\sim$ 0.3 - 0.4 µm) is measured. This large blow-up cannot be reproduced with the simulations. Due to radiation damping effects at LHC flattop energy, simulations even predict a slight emittance shrinking. The vertical growth seems to occur during the ramp, but also after the squeeze.

The convoluted emittance growth through the cycle for Fill 4284 is about 0.3 µm, as can be seen in Table 9.2. Similar growth was measured during some of the physics fills in 2015 with 50 ns and also with 25 ns bunch spacing. However, on average, the growth for 25 ns physics fills in 2015 was larger than during this test fill.

To check reproducibility many test cycles were analysed and compared to IBS simulations. Another example of emittance evolution measured with wire scanners

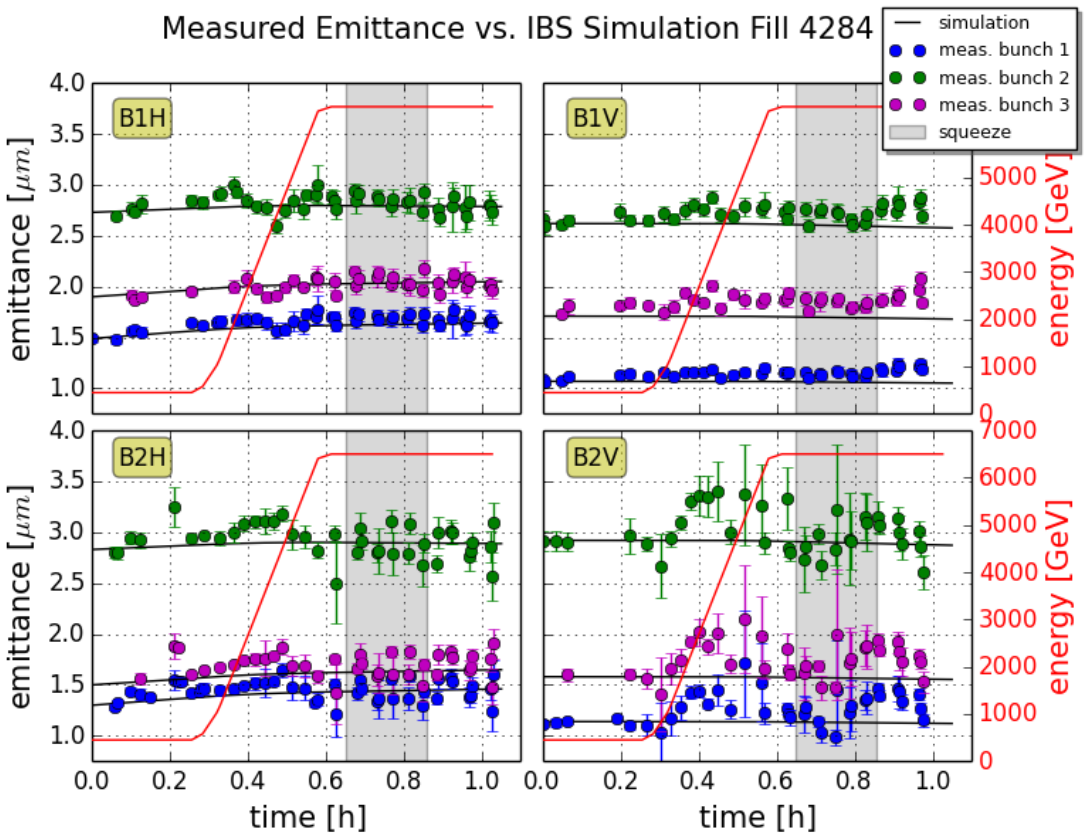

Figure 9.3.: Emittance evolution during the 2015 LHC cycle. Emittances in beam 1 and beam 2, horizontal and vertical, were measured with wire scanners during the LHC cycle. Three single bunches were injection for Fill 4284 (28 August 2015). The measured emittance growth is compared to IBS simulations with MADX (black). The energy (red) and β^* squeeze (grey) are displayed.

during a low intensity fill is shown in Fig. 9.4. For Fill 3954 two bunches with intensities of about 1.1 $\times$ 10^{11} ppb and initial emittances between 2 and 3 µm were injected in the LHC. Emittance measurements are extremely noisy at flattop energy, especially in beam 2 vertical. IBS simulations only match the emittance growth in beam 2 horizontal. The total measured emittance blow-up in this plane is less than 0.1 µm for both bunches. The growth in the other planes, however, is more pronounced. Up to 0.3 µm and 0.4 µm emittance blow-up was measured in beam 1 horizontal and vertical, respectively. Most of the horizontal emittance growth occurs at the injection plateau, as expected from IBS. During this fill also vertical growth can be seen for beam 1 at the injection plateau. In the following sections a breakdown of the growth through the different phases of the LHC cycle is given.

9.2.1. Emittance Preservation from SPS Extraction to LHC Injection

The emittance at SPS extraction of bunch 3 in Fill 4284 measured with wire scanners was 1.9 µm in the horizontal plane of LHC beam 1 and 1.5 µm in the vertical plane of

	ε_0 [µm]	ε_1 [µm]	$\Delta\varepsilon$ [µm]	$\Delta\varepsilon/\varepsilon$	$(\Delta\varepsilon/\varepsilon)_{\text{sim}}$
B1H	1.90 ± 0.05	2.08 ± 0.12	0.18 ± 0.17	0.09 ± 0.07	0.08
B1V	1.71 ± 0.04	2.04 ± 0.13	0.33 ± 0.17	0.19 ± 0.08	-0.02
B2H	1.50 ± 0.10	1.65 ± 0.12	0.15 ± 0.22	0.10 ± 0.10	0.10
B2V	1.58 ± 0.03	1.95 ± 0.17	0.37 ± 0.20	0.23 ± 0.11	-0.02
convoluted	1.67 ± 0.06	1.93 ± 0.11	0.26 ± 0.17	0.16 ± 0.10	0.03

Table 9.2.: Emittance growth through the 2015 LHC cycle. Emittance blow-up for bunch 4 in Fill 4284 from injection (0) to end of squeeze (1) measured with wire scanners and compared to simulated growth (sim) from MADX IBS simulations. The emittances in each plane are listed as well as the convoluted emittance.

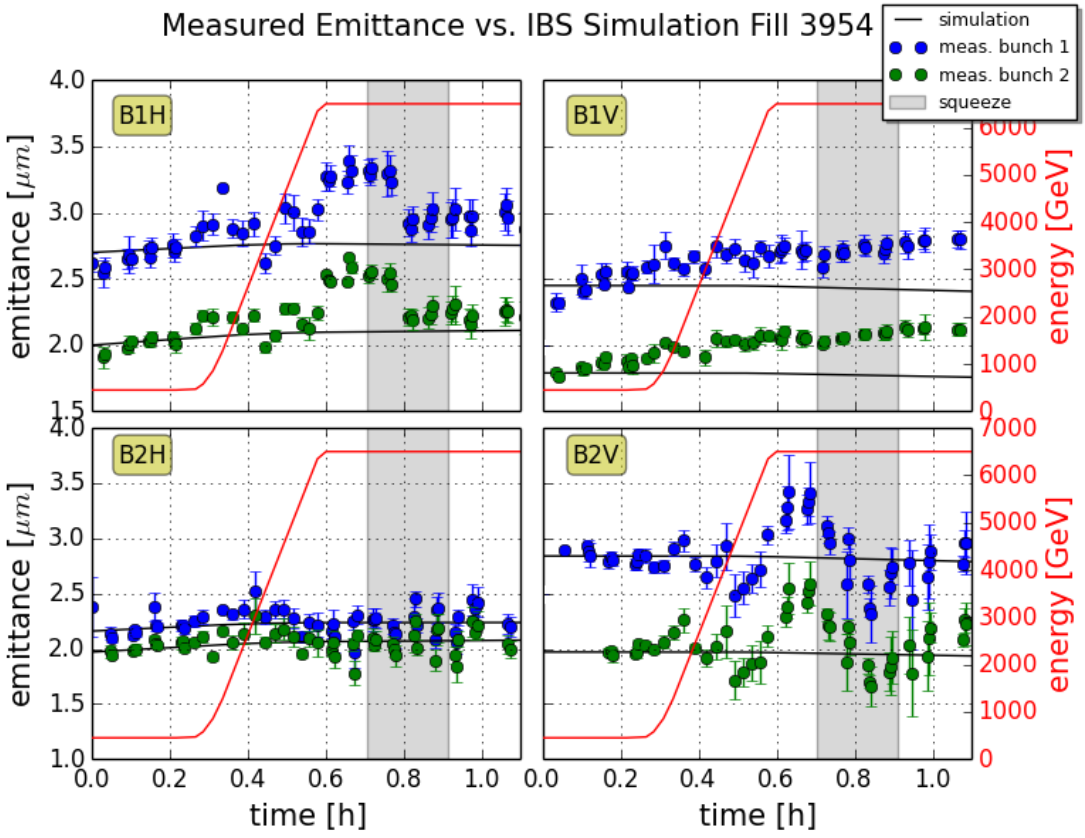

Figure 9.4.: Emittance evolution during the 2015 LHC cycle. Emittances in beam 1 and beam 2, horizontal and vertical, were measured with wire scanners during the LHC cycle. Two single bunches were injection for Fill 3954 (4 July 2015). The measured emittance growth is compared to IBS simulations with MADX (black). The energy (red) and β^* squeeze (grey) are displayed.

LHC beam 2. Within the measurement uncertainties of SPS and LHC wire scanners, this compares well to the measured emittances at LHC injection, see Table 9.2. The

procedure was repeated during many fills. No measurable emittance growth could be observed during the transfer from SPS to LHC.

9.3. Emittance Blow-Up during the LHC Injection Plateau

9.3.1. Intra-Beam Scattering at 450 GeV

For the measured test fills in 2015 with low beam intensity, the LHC transverse emittances grow significantly when the beams are circulating at 450 GeV. Studies in 2012 showed, that most of the horizontal emittance growth can be attributed to IBS. A typical measurement recorded in 2015 with wire scanners is shown in Fig. 9.5. The measured average emittance evolution of a 12 bunch train with 25 ns bunch spacing is compared to IBS simulations. The bunches of Fill 4547 had typical 2015 beam parameters with an initial emittance of about 2.5 µm and a bunch intensity of 1.1×10^{11} ppb. In both planes the emittance growth is stronger than simulations suggest. The horizontal growth rate is about 0.3 µm/h, much larger than the IBS simulation predicts (0.2 µm/h). Significant vertical emittance growth at 450 GeV was recognized for the first time in 2015. In one hour the vertical emittance of Fill 4547 grew by about 0.4 µm. A similar growth rate was measured with the BSRT during the same fill, see appendix D.

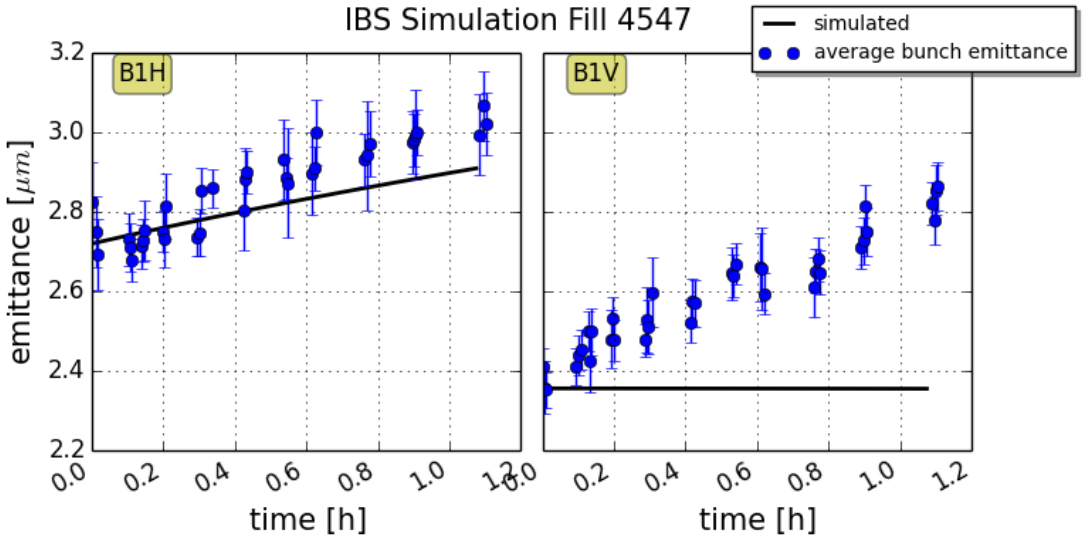

Figure 9.5.: Emittance growth at 450 GeV LHC injection energy. Emittances of beam 1 horizontal and vertical were measured with wire scanners during Fill 4547 (29 October 2015). 12 bunches with 25 ns bunch spacing were injected into the LHC and stayed about 1 hour at the injection plateau. The average emittance of all bunches is plotted (blue), compared to IBS simulations (black). The mean bunch length was 1.05 ns and the mean bunch intensity was 1.1 10^{11} ppb.

9.3.2. Vertical Emittance Growth at 450 GeV

Almost all measured low intensity test fills in 2015 indicated strong vertical growth at the injection plateau. 21 out of 22 test fills with an injection plateau length longer than 10 minutes showed vertical growth at 450 GeV. On average 5 % in 10 minutes in both vertical planes was observed with similar emittance growth times for single bunches and 25 ns bunch trains with up to 12 bunches. Bunches with emittances between 1.5 and 3.5 µm were injected. The vertical growth rate at 450 GeV was about 0.05 - 0.15 µm/10 minutes independent of the initial emittance. For instance, during Fill 4547 the vertical emittance blows up by 0.07 µm in 10 minutes. Even higher vertical growth rates were observed in 2015. Usually, when the vertical emittance is increasing, also horizontal growth is stronger than IBS suggests.

This type of vertical growth was already observed during some test fills measured with wire scanners in 2012. During 11 out of 19 fills the vertical emittances blew up at 450 GeV. In summary, investigations showed that the vertical blow-up

- decreases with energy,
- does not depend on brightness in the tested parameter range (0.6 - 3.0 $\times$ 10^{11} ppb),
- does not depend on bunch length (tested 1.0 - 1.3 ns),
- does not depend on octupole polarity or strength (used range of -6.52 - +19.56 A),
- does not depend on chromaticity (used range of 2 - 15 units),
- does not depend on vertical tune (vertical tune between 0.29 and 0.31 tested),
- cannot solely originate from coupling, and
- cannot originate from vertical dispersion.

An overview of selected fills with corresponding vertical growth and beam and machine parameters is given in Table 9.3 and a detailed description is provided in the following.

The LHC was operated with different octupole current and polarity throughout the running years 2012 and 2015, ranging from -6.52 A to 19.56 A. The machine chromaticity was also changed several times between values of 2 and 15 units. Operational horizontal and vertical tunes remained nominal in 2012 and during most of 2015. Only at the end of 2015 the tunes were lowered from 0.28 to 0.275 in the horizontal plane and from 0.31 to 0.29 in the vertical plane to move further away from the third order resonance. None of the above mentioned machine settings correlates with the measured vertical growth rate. However, a dedicated tune scan was not performed in 2015. To see the influence of injection tunes on emittance growth, a larger range of tunes has to be scanned.

Betatron coupling was relatively high during all measured low intensity test fills in 2012 and 2015, about $|C^-| \approx 0.004$ - 0.013. The coupling acceptable for physics fills is $|C^-| \approx 0.002$, a factor 2 or more smaller than the coupling during test fills. However, coupling alone cannot explain the large measured growth rates in both horizontal and vertical plane. The IBS theory suggest that if coupling is present, the horizontal growth is simply reduced and transferred to the vertical plane. Random vertical dispersion in the LHC is already included in the IBS simulation algorithm. With these values practically zero vertical growth is predicted, see Fig. 9.5.

Fill	ε_{y0} [µm]	$\Delta\varepsilon_y$ [µm]	$\frac{\Delta\varepsilon_y}{\varepsilon_{y0}}$	bl [ns]	I_b [10^{11} p]	Q_x, Q_y	Q'_x, Q'_y	Oct [A]
2548	1.7	**0.0**	0.0	1.3	1.5	nom	2, 2	-6.52
2555	2.0	0.2	0.1	1.1	1.3	nom	2, 2	-6.52
2556	2.5	0.08	0.03	1.1	1.3	nom	2, 2	-6.52
2595	2.5	**0.0**	0.0	1.25	0.9	nom	2, 2	-6.52
2823	2.1	**0.0**	0.0	1.2	3.0	nom	5, 5	-6.52
3014	1.9	0.06	0.03	1.1	1.6	nom	2, 2	6.52
3160	0.9	0.04	0.04	1.0	1.0	nom	2, 2	6.52
3217	1.5	0.05	0.03	1.1	1.6	nom	2, 2	6.52
3644	3.4	0.15	0.04	1.05	1.0	nom	4, 4	0.0
3738	1.5	0.07	0.04	1.1	1.0	nom	4, 4	-6.25
3742	1.6	0.1	0.06	1.1	1.1	nom	4, 4	6.25
3954	1.8	0.13	0.06	1.3	1.1	nom	4, 4	6.25
4284	1.1 - 2.9	**0.0**	0.0	1.0 - 1.25	0.6 - 1.1	nom	15, 10	19.56
4547	2.4	0.07	0.03	1.05	1.0	nom	7, 7	19.56
4572	1.5	0.12	0.08	1.1	1.0	nom	7, 7	19.56
4582	1.6	0.1	0.06	1.1	0.8	0.275, 0.295	15, 15	19.56
4583	1.6	0.13	0.08	1.1	0.8	0.275, 0.295	15, 15	0.0
4585	1.6	0.15	0.09	1.15	0.8	0.275, 0.29	15, 15	19.56

Table 9.3.: Vertical emittance growth at the 450 GeV LHC injection plateau. For a selection of low intensity test fills the vertical growth rate per 10 minutes is shown. The initial emittance ε_{y0}, bunch length (bl) and bunch intensity (I_b) are given. Also the injection tunes $Q_{x,y}$, chromaticity $Q'_{x,y}$ and octupole current (Oct) are displayed. Nominal fractional injection tunes (nom) are 0.28, 0.31. Fill 2548 - 3217 were recorded during the 2012 LHC proton run. Fill 3644 - 4585 are test fills of the 2015 LHC proton run. During many fills in 2012 and 2015 vertical emittance growth at 450 GeV was measured. Only during a few fills no vertical growth was observed (bold). No correlation between vertical growth and the listed beam and machine parameters was found.

A few theories on emittance growth have been tested with beam in the LHC in 2015. The remaining growth could, for instance, originate from the wire scans themselves. Passing a wire through the beam causes emittance growth. The bunch

tail evolution along the injection plateau can indicate if the particle distribution is disturbed or remains Gaussian. The blow-up could also originate from noise created by the LHC transverse damper system or from other external noise sources such as vibrations or power supplies.

9.3.3. Emittance Growth from Wire Scans

The emittance increase due to the interaction of the wire with beam during a wire scan has been studied in [109]. Theoretically the emittance increase $\Delta\varepsilon$ due to a single wire scan is

$$\Delta\varepsilon_u = \frac{\pi d f_{\text{rev}}}{4v}\frac{1}{2}\beta_u\langle\Theta^2_{\text{rms}}\rangle(\beta\gamma), \tag{9.3.1}$$

where $u = x, y$. $d = 36$ µm is the carbon wire diameter, f_{rev} the LHC revolution frequency, $v = 1$ m/s the wire speed, β_u the beta function at the wire scanner location and $\langle\Theta^2_{\text{rms}}\rangle$ the squared rms scattering angle due to Coulomb multiple scattering. The emittance growth is normalized to the beam energy ($\beta\gamma$). The rms scattering angle depends on the wire geometry, material and speed, as well as on the beam energy and particle type. For wire scans of a beam with design parameters in the LHC at 450 GeV the emittance blow-up per scan was calculated to be 2 nm at a location with $\beta = 370\ m$. In 2015, usually about 30 wire scans per beam and per plane were carried out during one hour at 450 GeV in a test fill. This would result in an emittance growth at 450 GeV of about 0.03 µm/h in the horizontal plane and 0.06 µm/h in the vertical plane if emittance blow-up due to wire scans in both planes is uncorrelated.

The above calculated emittance growth is significant, but can only explain a very small fraction of the measured horizontal and vertical emittance growth. The source of the remaining blow-up in the horizontal and vertical plane is still unclear.

In fact some fills in 2012 and 2015 show no vertical emittance growth at all. An example is given in Fig. 9.6. Emittances at injection of a 25 ns physics fill with 296 bunches were measured with the BSRT. Only the evolution of three selected single bunches is plotted. While the emittances in the horizontal plane blow up by about 0.1 µm/h, the vertical emittances are preserved within the measurement uncertainties.

9.3.4. Evolution of Transverse Bunch Tails at 450 GeV

To get an indication of the source of the remaining emittance growth in the horizontal and vertical plane that cannot be explained with IBS, the evolution of the transverse bunch profiles was investigated. If, for instance, the beam is close to a resonance, the bunch tail population in the transverse planes would increase so that the particle distribution is no longer Gaussian. For that purpose the bunch tail evolution during the 450 GeV injection plateau of Fill 4547 was analysed. Each profile obtained from wire scans was fitted with a double Gaussian $\phi_{\text{doubleGauss}}$[3]. A second Gauss fit was applied to the core of the profile $\phi_{\text{coreGauss}}$ (with an 80 % intensity cut), see Fig. 9.7. The area between the two fits in the range from 1.5 to 4σ was computed according

[3] $\phi_{\text{doubleGauss}} = d + k\cdot x + a_1\cdot\exp\left(-\frac{x-b}{2\cdot\sigma_1^2}\right) + a_2\cdot\exp\left(-\frac{x-b}{2\cdot\sigma_2^2}\right)$

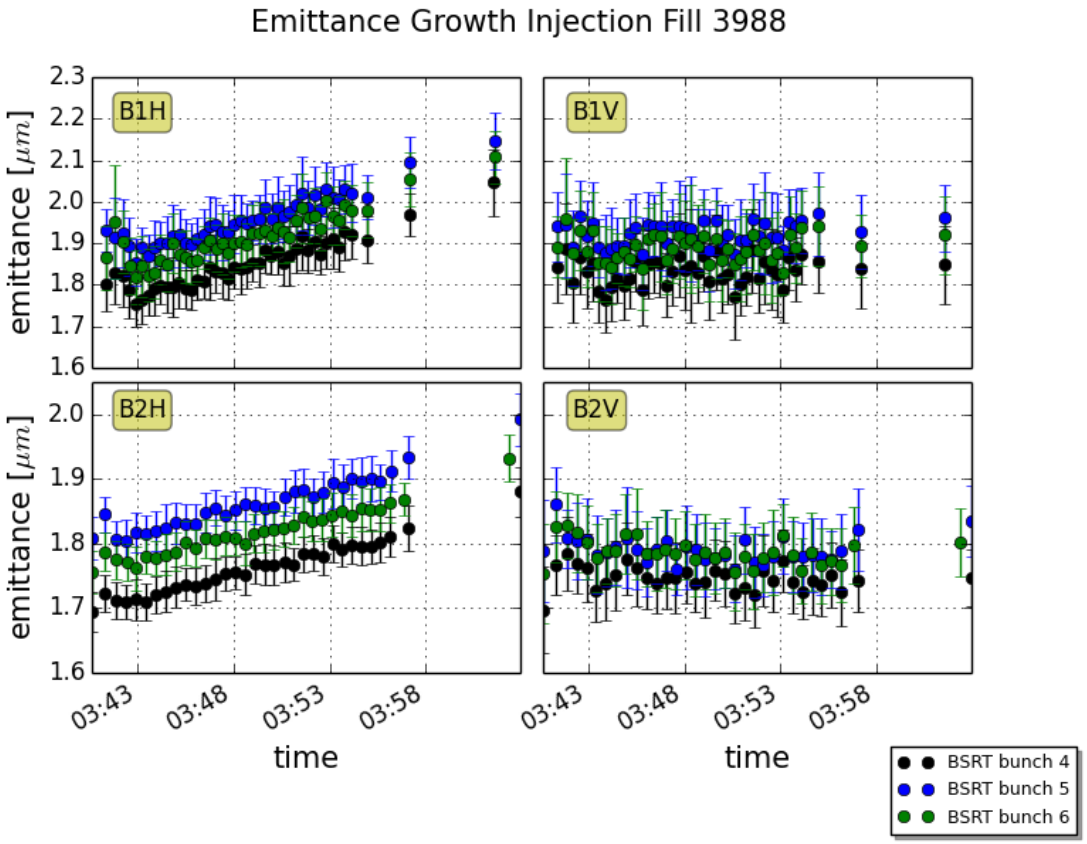

Figure 9.6.: Emittance growth at 450 GeV LHC injection energy. Emittances of beam 1 and beam 2, horizontal and vertical, were measured with BSRTs during Fill 3988 (12 July 2015). 296 bunches with 25 ns bunch spacing were injected into the LHC for a physics fill. The average emittance of several BSRT measurements of three bunches is plotted.

to

$$\frac{I_{\text{tail}}}{I_{\text{total}}} = \frac{\int_{-4\sigma}^{-1.5\sigma}(\phi_{\text{doubleGauss}} - \phi_{\text{coreGauss}}) + \int_{+1.5\sigma}^{+4\sigma}(\phi_{\text{doubleGauss}} - \phi_{\text{coreGauss}})}{\int_{-4\sigma}^{+4\sigma}\phi_{\text{doubleGauss}}}. \quad (9.3.2)$$

The left and right tail populations are added with this formula and normalized to the entire bunch population. The results for a single bunch are shown in Fig. 9.8. Within the spread of the measurements, the bunch tails in the horizontal and vertical plane stay constant during long periods at 450 GeV. In other words, the emittance growth mechanism at hand impacts the core particles in the same way as the tail particles.

9.3.5. Transverse Damper Studies

During a dedicated experiment with low intensity test beams the effect of injection gap cleaning (IGC), abort gap cleaning (AGC), and the transverse damper itself on emittance growth was tested. The cleaning and damping effects on the beam are explained in chapter 4. The studies were carried out with single bunches (nominal bunch intensity and bunch length) at the 450 GeV LHC injection plateau. The

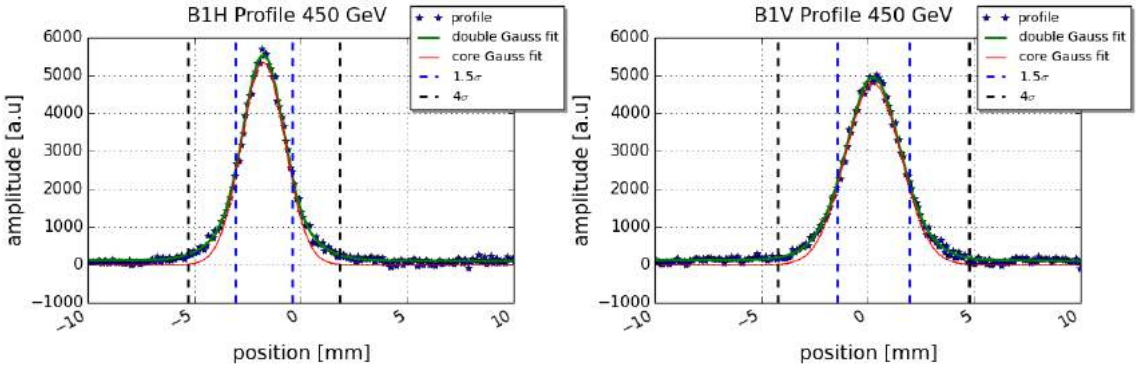

Figure 9.7.: Beam 1 horizontal and vertical bunch profile at 450 GeV measured with wire scanners. The entire profile (green) and the core of the profile (green) are fitted with a double Gaussian. For the core fit an 80 % intensity cut is applied to the profile. The 1.5σ (blue) and 4σ (black) boundaries of the profile are indicated.

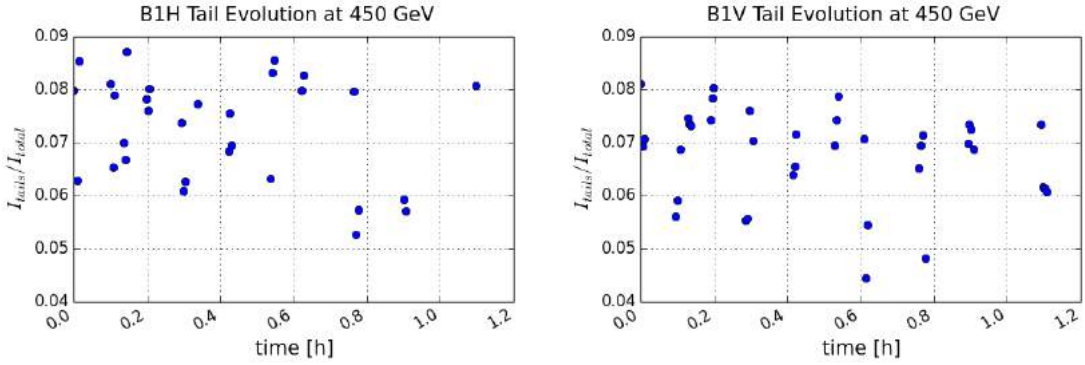

Figure 9.8.: Beam 1 horizontal and vertical bunch tail evolution of a single bunch at 450 GeV of Fill 4547. The area between the two curves in Fig. 9.7 is computed between 1.5 and 4σ on the left (blue) and right (red) side of the profile. The bunch tails on both sides are added and normalized to the total bunch population. For a perfect Gauss the ratio is $\frac{I_{\text{tail}}}{I_{\text{total}}} = 0$.

cleaning and the damper were switched on and off to see a possible influence on emittance blow-up. In the following BSRT measurement results are shown because more measurement points per 10 minute intervals could be obtained. Complementary wire scans during this experiment are given in appendix D.

The effect of injection gap cleaning on emittance growth was tested with two single bunches, a bunch injected next to the injection gap and a witness bunch. In Fig. 9.9 the results from BSRT measurements are presented. The IGC, effective in the horizontal planes, was constantly exciting bunch 2 for a period of 10 minutes and then was switched off. The procedure was repeated with the transverse damper switched off. Indeed, an effect on emittance growth is visible in the horizontal planes for the bunch near the injection gap when betatron oscillations are not damped. During normal operation, however, the transverse damper is always activated and IGC is on for less than a minute during the injection process.

A similar experiment was carried out for the abort gap cleaning. Two single

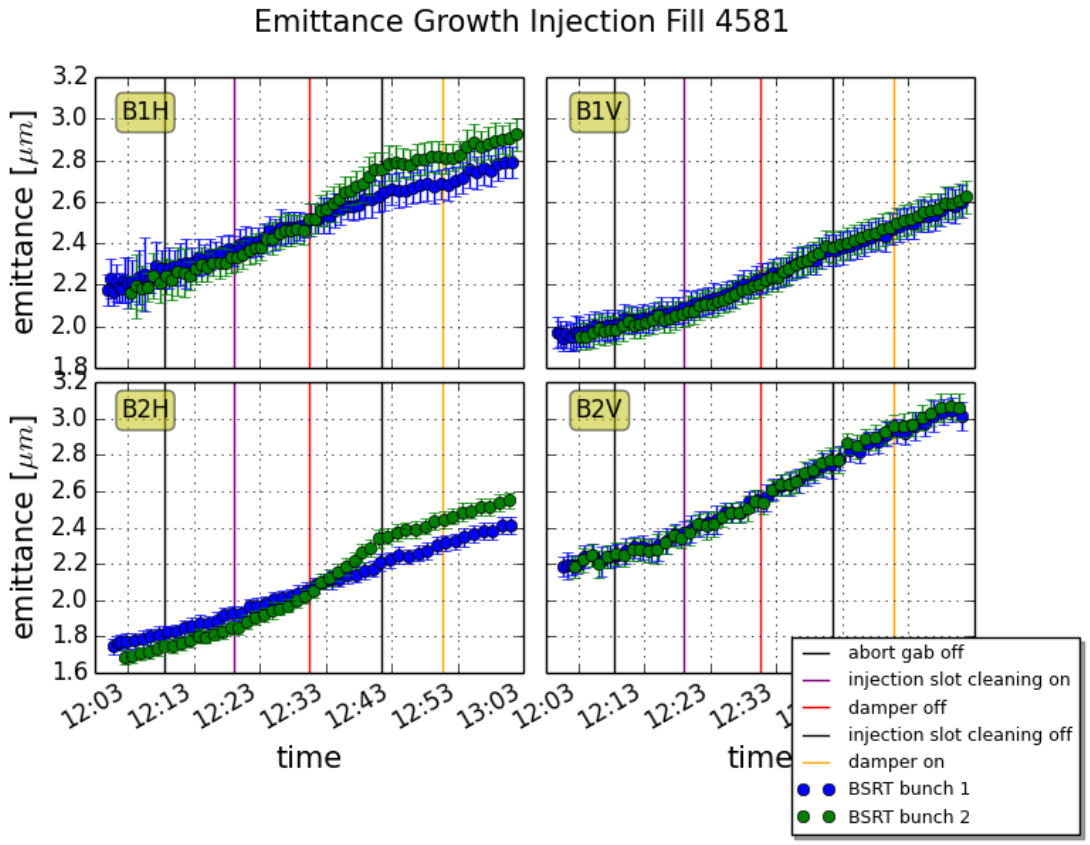

Figure 9.9.: Effect of injection gap cleaning on emittance growth. Emittances in all planes are measured with the BSRT. Two single nominal bunches were injected. Bunch 1 (blue) is positioned next to the injection gap. Bunch 2 (green) is a witness bunch. Vertical lines indicate the activation or disabling of the IGC and the transverse damper. IGC has an effect on close-by bunches in the horizontal plane.

bunches were injected left and right of the abort gap (bunch 1 and bunch 4), respectively. Another two bunches served as witness bunches. Figure 9.10 shows the emittance evolution during the fill measured with the BSRT. The AGC was switched on for 10 minutes and then switched off again. After 10 minutes the transverse damper was disabled and the procedure repeated. The AGC excites bunches near the abort gap in the vertical planes. No effect on emittance growth could be observed.

Finally, the influence of the transverse damper itself on emittance growth was tested. Three single nominal bunches with different initial emittances were injected into the LHC for that purpose. The BSRT measurement results for this experiment are shown in Fig. 9.11. Damping of betatron oscillations was simply switched on for 10 minutes and then switched off for 10 minutes. Overall, there was no effect of transverse damping on emittance growth visible.

Note that again all test fills in this experiment show large horizontal and vertical emittance growth, almost independent of the initial emittance. The growth rates do not change with time spent at the injection plateau.

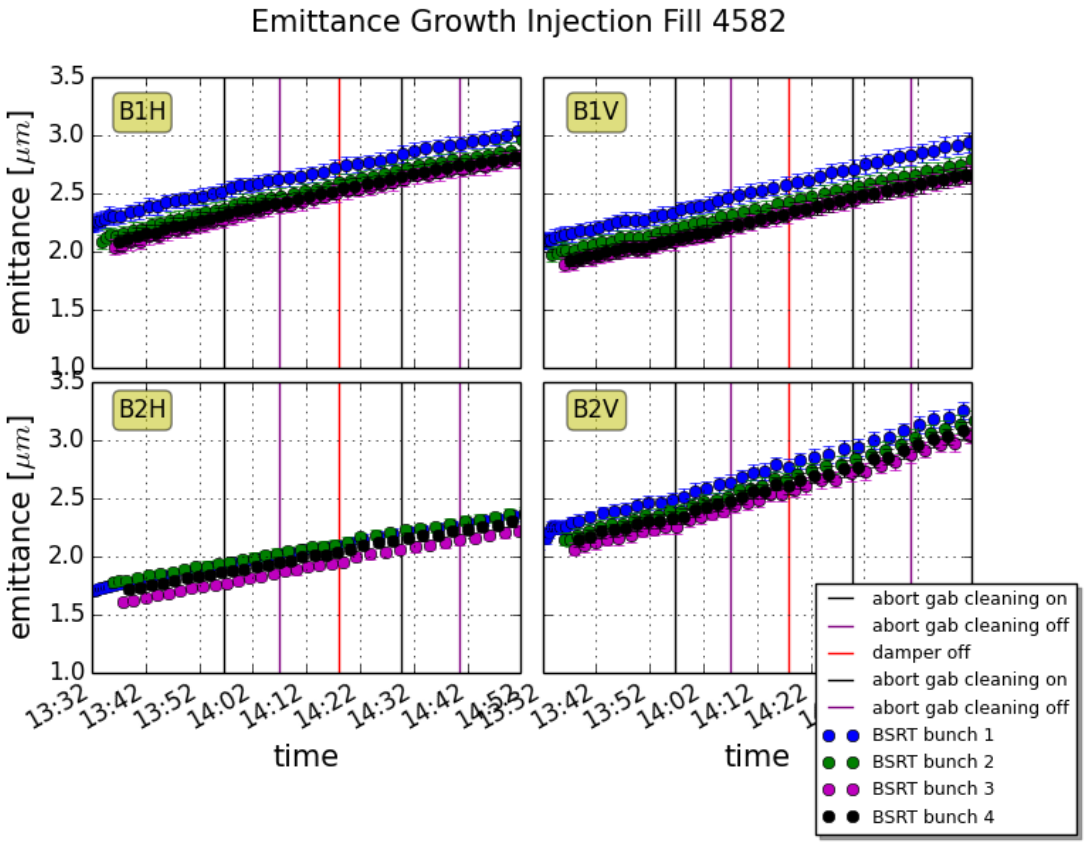

Figure 9.10.: Effect of abort gap cleaning on emittance growth. Emittances in all planes are measured with the BSRT. Four single nominal bunches were injected. Bunch 1 (blue) and bunch 4 (black) are positioned left and right of the abort gap, respectively. Bunch 2 (green) and 3 (purple) are witness bunches. Vertical lines indicate the activation or disabling of the AGC and the transverse damper. No effect of AGC on emittance growth could be observed.

9.3.6. Effect of Noise on Emittance Growth

External noise caused by, for instance, magnetic field perturbations or magnet vibrations due to ground motion can excite the beam. Sufficiently high perturbations or vibration amplitudes can lead to transverse emittance growth as was discussed in chapter 4. The aforementioned typical vertical growth and remaining horizontal emittance growth not caused by IBS is linear in time and independent of the initial emittance. Figure 9.12 shows again emittance measurements at 450 GeV during Fill 4547. The simulated IBS emittance growth given in Fig. 9.5 was subtracted from the measured emittances and fitted linearly. In the vertical plane an emittance growth rate of 0.45 µm/h was measured. The LHC emittance growth rates caused by noise calculated in chapter 4 could fit this type of growth. Ground motion with an amplitude of only 300 nm causing a triplet magnet to vibrate can result in vertical emittance growth of 0.45 µm/h according to Eq. 4.3.5[4].

[4]Assuming a triplet magnet with 20 m focal length and 100 m beta function vibrates constantly with the same ground motion amplitude during the LHC injection plateau.

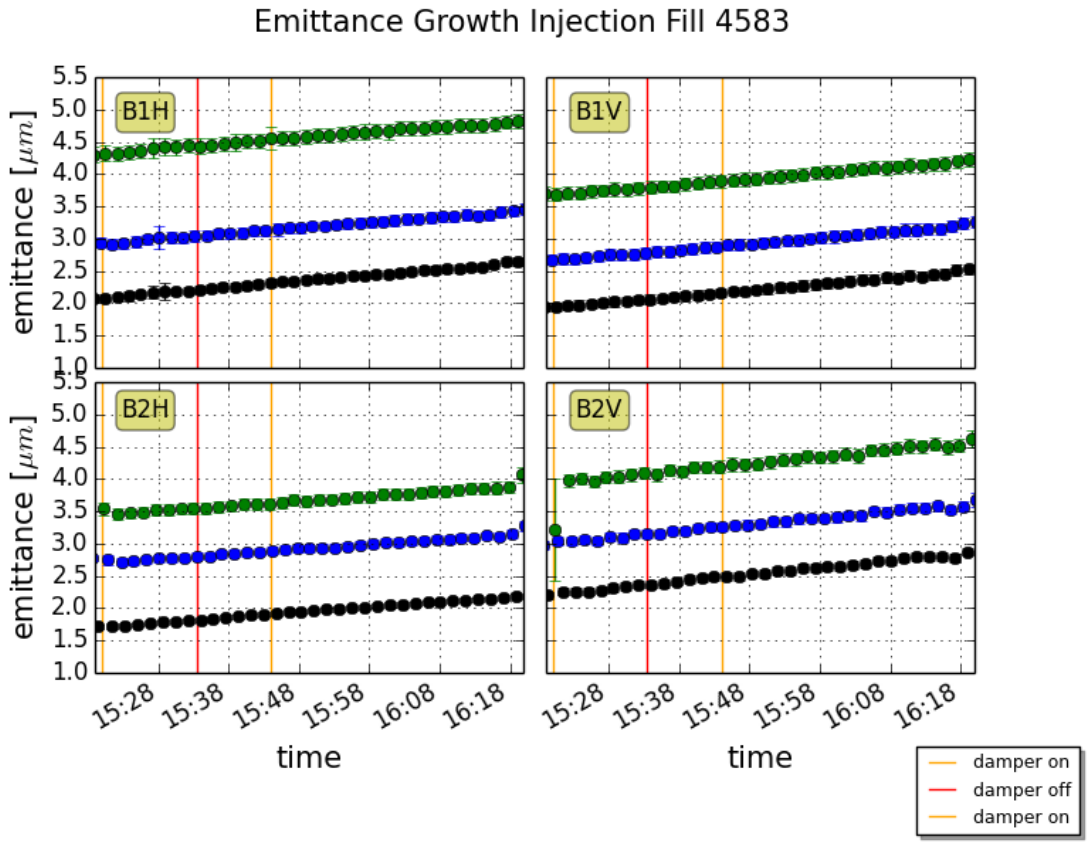

Figure 9.11.: Effect of transverse damper on emittance growth. Emittances in all planes are measured with the BSRT. Three single nominal bunches with different emittances were injected. Vertical lines indicate the activation or disabling of the transverse damper. No effect of transverse damping on emittance growth could be observed.

9.4. Emittance Growth during the LHC Ramp

With a collision energy of 6.5 TeV, the ramp in 2015 took about 20 minutes. Compared to other accelerators, the LHC has a uniquely long energy ramp because the superconducting magnets need to be ramped adiabatically. The main limitation comes from the maximum linear ramp rate of the LHC power converters (10 A/s). Also persistent currents and other dynamic effects induce large multipole components in the magnetic field that limit the ramp rate of the superconducting magnets. Other normal conducting machines ramp within seconds, such as the SPS[5]. Many effects that cause emittance growth decrease with higher energy. In case of the LHC, due to the long energy ramp, the emittance evolution can still be affected during the ramp. Studying transverse emittance growth during the energy ramp is therefore an important puzzle piece in the LHC and not easily comparable with other hadron accelerators.

Measured β functions for the 2015 energy ramp are not available. A linear interpolation of the measured beta functions from injection to flattop energy is used. The result of the insufficient knowledge of the beta function are again non-physically

[5]The SPS ramp from 26 GeV to 450 GeV takes only a few seconds.

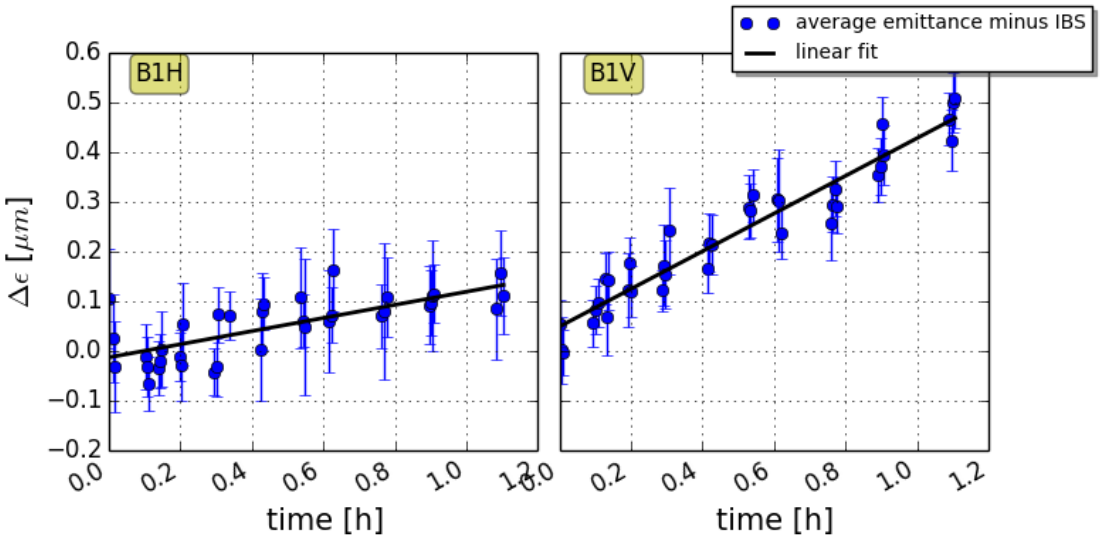

Figure 9.12.: Remaining emittance growth after subtraction of IBS growth. The emittances (blue) were measured with wire scanners at 450 GeV in the LHC during Fill 4547 and averaged over 12 bunches. A linear fit is applied (black).

growing and shrinking emittances in all planes as was already the case during LHC Run 1. Non-monotonically changing β functions during the ramp were found to be the cause, see chapter 5. An example emittance measurement through the ramp with wire scanners is shown in Fig. 9.13. Also the predicted growth from IBS simulations is plotted. With the beam parameters for Fill 4284 IBS simulations suggest less than 0.1 µm (5 %) horizontal emittance blow-up during the ramp for beam 1, which is within the measurement accuracy and consistent with measurements. The horizontal emittance growth in beam 2 is negligibly small and also matches the IBS simulation result. Vertical emittances, however, experience an emittance blow-up during the ramp of about 0.1 µm (5 %) in beam 1 and 0.2 - 0.3 µm (15 - 20 %) in beam 2, which cannot be reproduced with IBS simulations. However, it is difficult to define the true emittance of beam 2 vertical at the end of the ramp due to the large measurement spread.

Wire scanner data from 30 low intensity test ramps was combined to define the average emittance growth during the energy ramp. In summary, beam 1 horizontal emittances blow up by about 0.1 µm (5 %) and beam 2 horizontal emittances are conserved during the LHC ramp. The average vertical growth in beam 1 during the ramp is less than 0.1 µm (5 %) and sometimes no growth was observed. However, beam 2 vertical emittances typically blow up by 0.1 - 0.2 µm (5 - 10 %).

9.5. Emittance Preservation during the LHC Squeeze

Once the flattop energy is reached, the tunes are changed from injection to collision tunes. The fractional tune is increased from 0.28 to 0.31 in the horizontal plane and from 0.31 to 0.32 in the vertical plane[6]. This only takes a few minutes. Then the β^* squeeze is launched. In 2015 the β^* in ATLAS and CMS was squeezed from 11 m

[6]The injection and collision tunes are also displayed in Table 6.1.

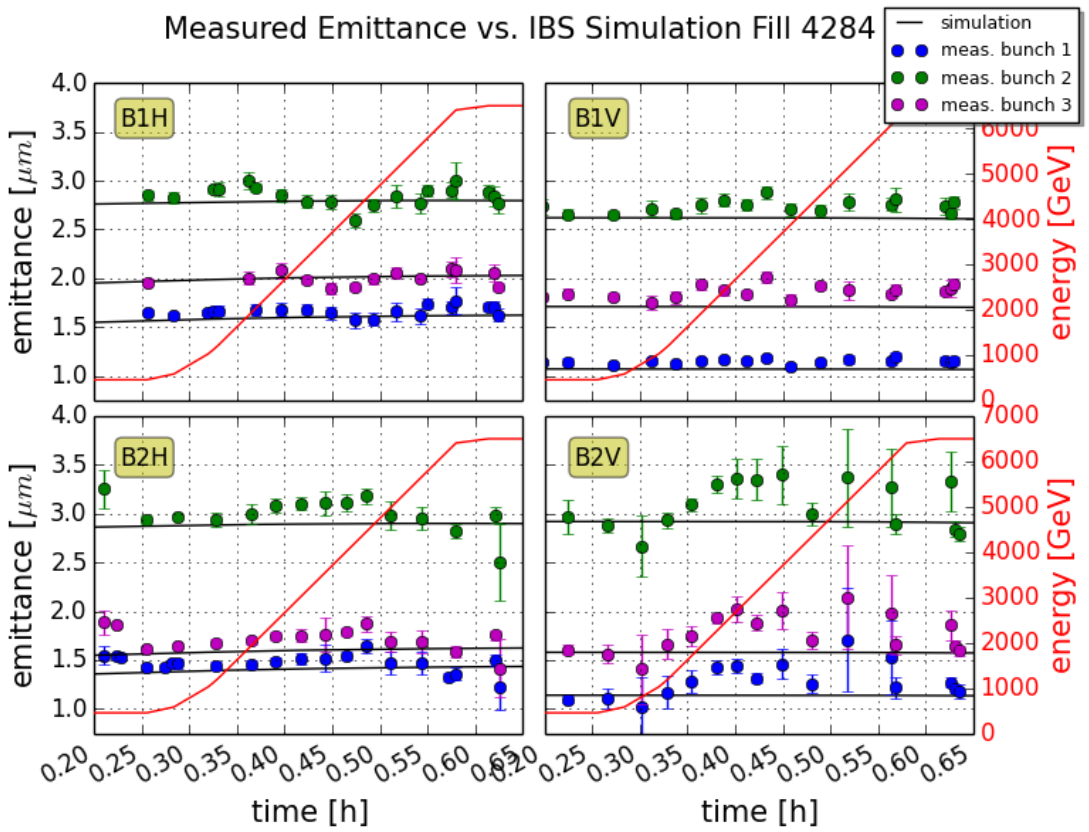

Figure 9.13.: Emittance evolution during the 2015 LHC ramp. Emittances in beam 1 and beam 2, horizontal and vertical, were measured with wire scanners during the ramp to 6.5 TeV. Three single bunches were injection for Fill 4284 (28 August 2015). The measured emittance growth is compared to IBS simulations with MADX (black). The energy (red) is displayed.

to 80 cm in 13 minutes.

Similar to the LHC ramp, measured β functions in LHC point 4 at the transverse profile monitors are not available during the squeeze. A linear interpolation of the measured beta functions before and after the squeeze is used. The non-physical emittance evolution, see Fig. 9.14 and Fig. 9.15, is possibly also due to non-monotonically changing β functions during the squeeze.

Contrary to LHC Run 1, no instabilities were observed during the squeeze in 2015. Unfortunately the BSRT and wire scanner measurements suffer from large measurement noise as can be seen in Fig. 9.14 and Fig. 9.15. Two different low intensity test fills are displayed as an example. The emittances shown in Fig. 9.14 were measured with the BSRT and in Fig. 9.15 with wire scanners. BSRT emittances are averaged over several hundred measurements. Beam 1 horizontal always shows large statistical fluctuations from measurement to measurement. After the final β^* value is reached, the beams are brought into collision.

Within measurement precision the emittances of beam 2 horizontal and vertical are conserved during the β^* squeeze. In both fills the emittances of beam 1 horizontal and vertical show small growth during the squeeze, less than 0.1 µm (5 %). This result is not reproducible. However, there were only six test fills in 2015 where

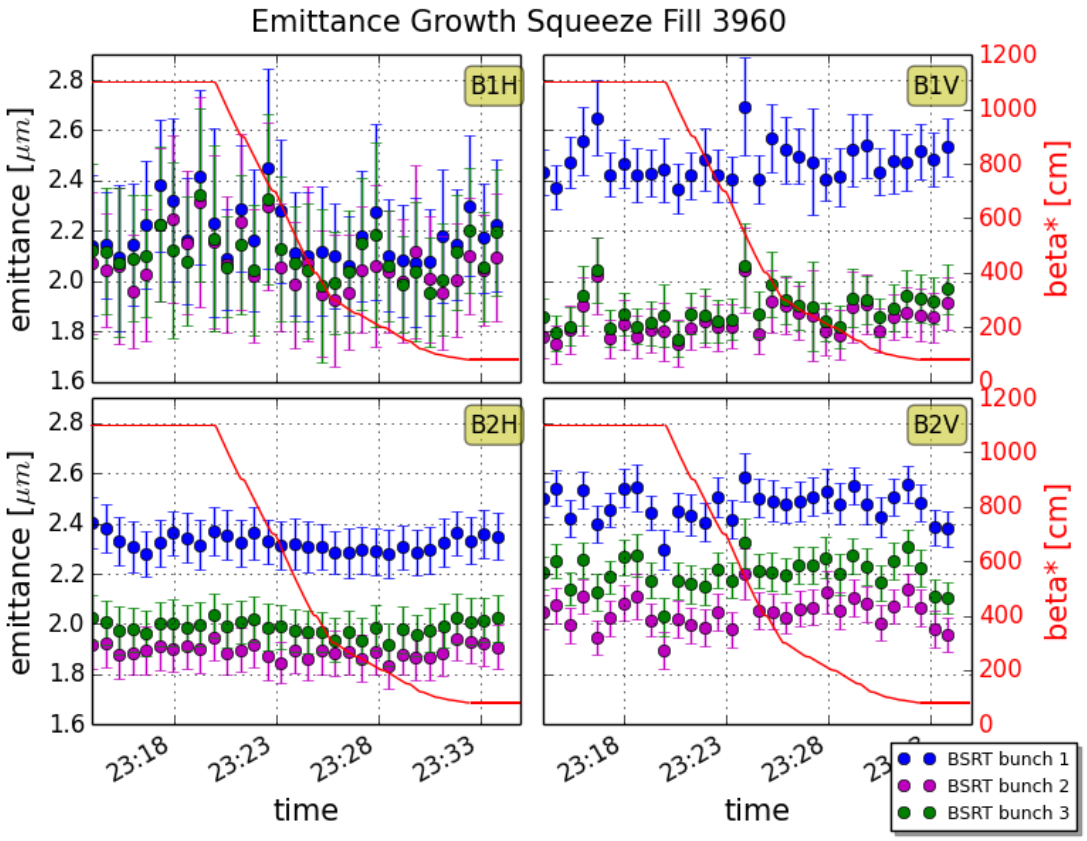

Figure 9.14.: Emittance evolution during the LHC squeeze. The β^* value (red) is displayed. It is squeezed to 80 cm in ATLAS and CMS. Emittances of three single bunches were measured with the BSRTs during Fill 3960 (4 July 2015).

emittances could be measured during the squeeze with wire scanners. During other fills the emittances are preserved during the squeeze.

9.6. Radiation Damping Observations at 6.5 TeV

At high energies protons circulating in the LHC emit enough synchrotron radiation (SR) to modify the beam parameters. This effect counteracts IBS and could be observed for the first time during LHC Run 2. Synchrotron radiation damping slowly reduces the vertical emittance at 6.5 TeV, see Fig. 9.16. BSRT measurements of beam 2 vertical during collisions of a physics fill with 296 bunches are shown. The average emittance of all bunches and several consecutive measurements is plotted.

The emittance evolution due to radiation damping was simulated with the MADX IBS module and also displayed in Fig. 9.16. The simulation predicts slightly faster vertical emittance decrease than measured due to emittance growth from proton collisions and other beam-beam effects not included in the simulation.

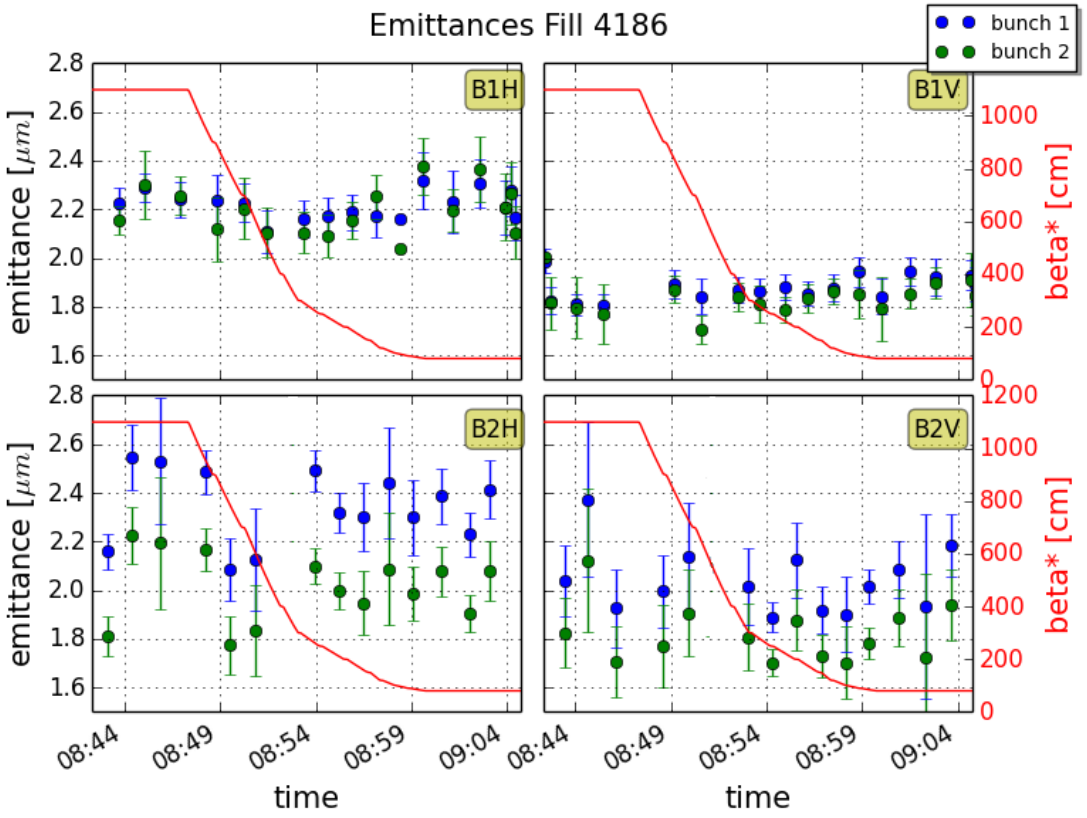

Figure 9.15.: Emittance evolution during the LHC squeeze. The β^* value (red) is displayed. It is squeezed to 80 cm in ATLAS and CMS. Emittances of two single bunches were measured with wire scanners during Fill 4186 (9 August 2015).

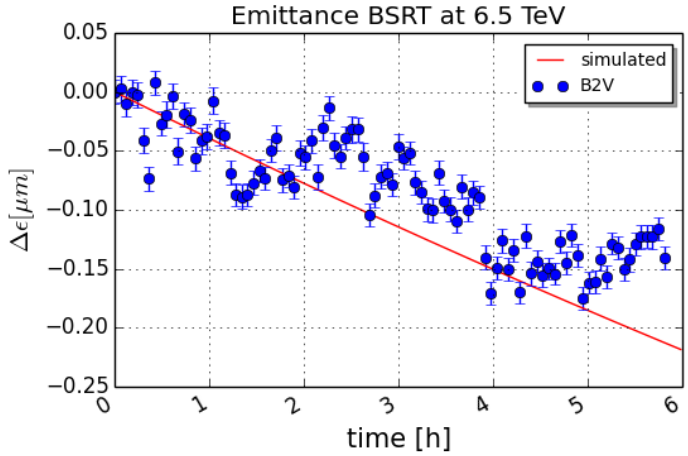

Figure 9.16.: Radiation damping observations at 6.5 TeV. BSRT measurements (blue) of beam 2 vertical emittance during collisions of Fill 3988 (12 July 2015) compared to simulations (red). The average emittance of 296 bunches and several consecutive measurements is displayed normalized to the emittance value at the start of collisions. Simulations were carried out with MADX.

9.7. Summary of Emittance Preservation Studies at the LHC

LHC Run 2 started in 2015 with a higher collision energy of 6.5 TeV. The beginning of the year was spent commissioning the machine with beams of reduced brightness and 50 ns bunch spacing. The overall emittance blow-up from LHC injection to start of collisions is slightly smaller than for the high brightness beams in LHC Run 1. Approximately 25 % ($\sim$ 0.4 µm) emittance growth from wire scans and ATLAS luminosity was measured on average. This growth rate is not consistent with IBS simulation results.

The performance of 25 ns LHC beams in 2015 was also degraded with similar emittance blow-up as in 2015 with 50 ns fills. ATLAS luminosity measurements of 25 ns beams in 2015 indicate about 25 % (0.6 µm) emittance growth through the LHC cycle.

Low intensity test fills were used to examine the emittance growth through the different phases of the LHC cycle in order to find the origin of the growth. For most fills, horizontal emittance growth during the entire LHC cycle can be matched with IBS simulations. Sometimes significant growth in the vertical planes and larger horizontal growth than expected from IBS was measured. The growth occurs at the injection plateau and is not correlated to machine settings such as tune, chromaticity and octupoles within the tested range of parameters. It decreases with energy and is independent of initial beam parameters, again within the tested range. The growth rate also does not change with time spent at the injection plateau.

Vertical dispersion and betatron coupling cannot solely explain the large growth. Emittance growth from wire scans can only explain a very small fraction of the growth. The evolution of bunch tails at 450 GeV does not indicate a perturbation of the Gaussian particle distribution. An extensive measurement campaign revealed that neither injection gap nor abort gap cleaning by the transverse damper cause emittance blow-up. Also the transverse damper itself has no influence on transverse emittance growth.

External noise might play a role for emittance growth at the LHC injection plateau. The growth is believed to originate from noise, possibly created by quadrupole vibrations through ground motion.

Measurements in 2015 showed that the emittances are mostly preserved during the LHC ramp and β^* squeeze within measurement accuracy. Seemingly increasing and decreasing emittances during the ramp and the squeeze are due to non-monotonically changing beta functions during these beam processes. The β knowledge at each point during the ramp and the squeeze is required to reduce emittance measurement fluctuations.

For the first time, synchrotron radiation damping of protons at 6.5 TeV was observed. The damping counteracts IBS and reduces the vertical emittance at high energies.

Part V.

Outlook, Summary and Conclusion

10. Outlook: LHC High Luminosity Era

10.1. High Brightness Beams

The remarkable achievements during the first LHC run were partly due to the choice of running with 50 ns beams, which could be produced with a brightness beyond LHC design values. LHC Run 2 started with a more conservative choice of beam and machine parameters to commission the accelerator for beams with 25 ns bunch spacing. Beams with a bunch intensity of approximately 1.1×10^{11} protons per bunch (ppb) and a normalized transverse emittance of 2.5 µm were injected. The brightness was about a factor 2 below the 2012 LHC physics beams.

The LHC injector team has been developing new types of high brightness beams (BCMS beams)[1] for the LHC to increase luminosity production [110]. Beams with very low emittance (approximately 1 µm) and bunch intensities of 1.0 to 1.5×10^{11} ppb can be produced for the LHC. The proposed parameters for the high brightness 25 ns BCMS beam result in similar brightness values as the 2012 50 ns physics beams. The emittance preservation studies during Run 1 and Run 2 indicate that the emittance growth through the LHC is almost independent of initial emittance and bunch intensities within the range of obtained parameters. A constant absolute emittance growth would compromise the potential improvement given by the proposed low emittance beams.

Figure 10.1 shows the emittance growth through the LHC cycle as function of bunch intensity for 2012 and 2015 physics fills. The emittance was measured with wire scanners at injection and derived from ATLAS peak luminosity at the start of collisions. The blow-up of the 2012 50 ns physics beams is plotted in blue and the 2015 25 ns physics beam emittance growth in green. The initial emittance (black) is displayed as well. High brightness BCMS beams were tested in four dedicated fills in the LHC (orange and red).

As can be seen in Fig. 10.1, for bunch intensities from 1.0 to 1.5×10^{11} ppb the emittance growth is indeed constant, about 0.4 - 0.5 µm. On this plateau the initial emittances vary between 1.7 µm (50 ns bunch spacing) and 2.7 µm (25 ns bunch spacing). For bunch intensities beyond 1.5×10^{11} ppb the blow-up increases with bunch intensity. Also the injected emittances are as small as 1.5 µm. It could not be investigated where in the cycle the additional growth for higher bunch intensities during physics fills occurs and if it is mainly due to instabilities. No LHC emittance measurement tool for high intensity beams was available.

Four test fills have been carried out in 2012 and 2015 with the high brightness

[1] The Batch Compression, Merging and Splitting (BCMS) scheme is a novel idea for RF bunch splitting and batch compression in the Proton Synchrotron (PS), an accelerator in the LHC injection chain. By reducing the total splitting factor in the PS and injecting 4 + 4 bunches from the Booster, beams with low emittances and high bunch intensity can be produced for the LHC.

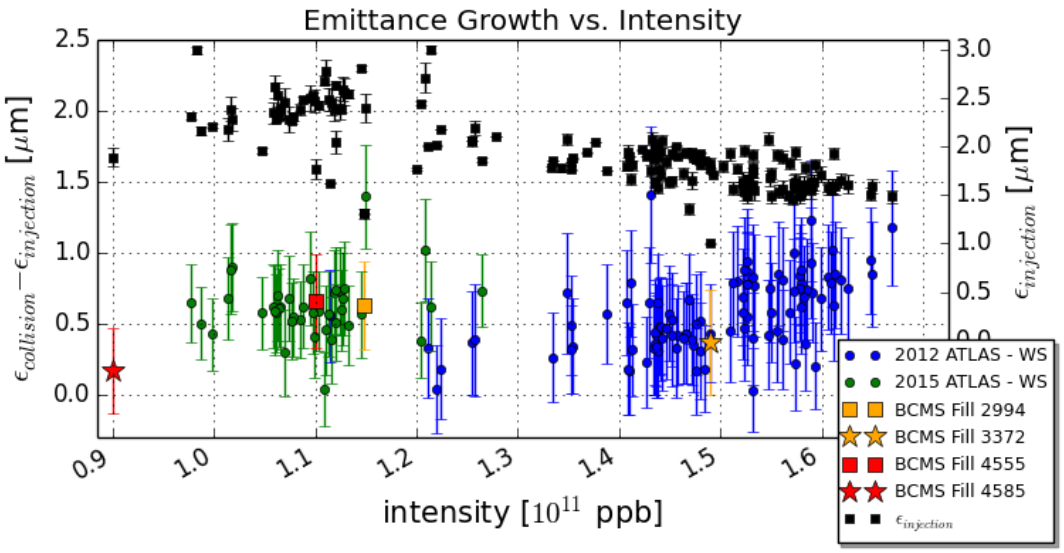

Figure 10.1.: Bunch intensity versus emittance growth in 2012 and 2015. The emittance growth from injection to start of collisions as a function of bunch intensity is plotted. $\epsilon_{collision}$ is calculated from ATLAS peak luminosity and $\epsilon_{injection}$ is the convoluted average emittance of the first 144 bunch batch measured with wire scanners at LHC injection. The intensity is measured with the Fast Beam Current Transformer (FBCT). Measurements of the 50 ns physics fills in 2012 are blue, the 25 ns physics fills in 2015 are green. The high brightness fills (BCMS) are highlighted. There were two high brightness test fills in 2012 (orange) and two BCMS fills in 2015 (red).

BCMS beams. For Fill 2994 during the 2012 LHC proton run, 32 high brightness bunches with a bunch intensity of 1.15×10^{11} ppb and an initial emittance of about 1.2 µm were produced. For Fill 3372 in 2012, 24 BCMS bunches with a bunch intensity of 1.5×10^{11} ppb and an initial emittance of about 1 µm were injected. Both fills had a bunch spacing of 50 ns. The blow-up through the cycle for these two fills is also indicated in Fig. 10.1 (orange). While for Fill 2994 the overall growth is similar as surrounding points in the plot (about 0.6 µm), the growth for Fill 3372 is below 0.5 µm.

For the high brightness Fill 4555 (30 October 2015) 589 bunches were injected in the LHC. Bunch trains of 48 bunches with 25 ns bunch spacing were produced. The high brightness bunches had an initial average emittance of about 1.8 µm and a bunch intensity of 1.1×10^{11} ppb. Fill 4585 (5 November 2015) was a medium brightness fill. 12 bunches with 25 ns bunch spacing produced with the BCMS scheme were injected in the LHC with a bunch intensity of 0.9×10^{11} ppb and 1.9 µm initial emittance. During Fill 4555 the emittances blew up by about 0.7 µm from LHC injection to start of collisions. Many bunch instabilities occurred at injection and start of squeeze during this fill. The lower brightness Fill 4585 shows an emittance growth below 0.2 µm.

10.2. Discussion

For the LHC proton runs from 2016 to 2018 the bunch intensities will not be higher than 1.3×10^{11} ppb due to limitations of the SPS RF system with beam loading and longitudinal instabilities [111]. The emittance blow-up for the standard 25 ns beams through the LHC cycle is expected to remain around 0.5 µm, as seen in Fig. 10.1. Only during the next long shutdown (LS2) the SPS 200 MHz RF system will be upgraded to allow higher bunch intensities for LHC beams through higher RF voltage and power [112].

For the high luminosity era following LS2 higher brightness beams will be produced for the LHC. The proposed parameters for the high brightness 25 ns batch compression beam [110] and the maximum parameters for the LHC Injector Upgrade after LS2 [113] give a similar brightness as the 2012 50 ns physics beams[2]. The intra-beam scattering (IBS) growth rates are therefore expected to be similar to what was observed in the LHC in 2012.

This thesis demonstrates that a good fraction of the observed growth (about 0.5 µm) is independent of initial emittance and bunch intensity. Emittance blow-up in the LHC occurs mainly at injection energy, due to IBS and noise. These effects, if not cured, could partially spoil the performance of the proposed 1 µm BCMS beams. At the moment there is no cure for IBS or noise effects in the LHC. The resulting emittance growth depends significantly on the time spent at the 450 GeV injection plateau, which is essentially the time required to fill the LHC. During the 2012 and 2015 LHC proton runs the injection time was about 30 minutes at best. With optimization of the injection process in the LHC (less failed injections) one could gain about 5 to 10 minutes. It is not foreseen to reduce this time further for future LHC runs.

Once the SPS 200 MHz RF system is upgraded, it would be advantageous to also match the RF in the LHC. Theoretically, a 200 MHz RF system in the LHC would allow larger RF buckets and consequently longer bunch lengths of up to 3 ns [115]. This could have a positive effect on IBS emittance growth rates. However, there are some draw backs such as slightly lower threshold for the onset of electron cloud in the quadrupoles and for the onset of the transverse mode coupling instability that would again reduce the maximum possible bunch intensity [114]. As an alternative or partial mitigation a batch-by-batch longitudinal RF blow-up of the bunch lengths at injection is possible. The RF blow-up was already tested in 2012, see chapter 5. It was successfull for low intensity test fills, but no effect on emittance growth for 50 ns physics fills could be observed [6] possibly due to bunch instabilities.

The above mentioned scenarios give different emittance growth rates at 450 GeV. For comparison IBS simulation results from MADX are presented in Fig. 10.2. Four simulations were launched with different beam parameters given in Table 10.1. A 25 ns bunch batch staying the average 15 minutes at the injection plateau was simulated. The nominal case (green) refers to the 25 ns beam for the 2016 proton run. The expected average emittance growth from IBS for this type of beam is 0.04 µm (< 2 %) in 15 minutes. An alternative beam for Run 2 is the BCMS beam (blue) with higher brightness and thus resulting in a higher emittance growth rate from IBS. About 0.06 µm (3 %) emittance blow-up in 15 minutes was simulated. For the high luminosity era of the LHC, beams with much higher brightness can be

[2]Beams with emittances of 2 µm and bunch intensities of 2.3×10^{11} ppb are foreseen for LHC injection after LS2 [114].

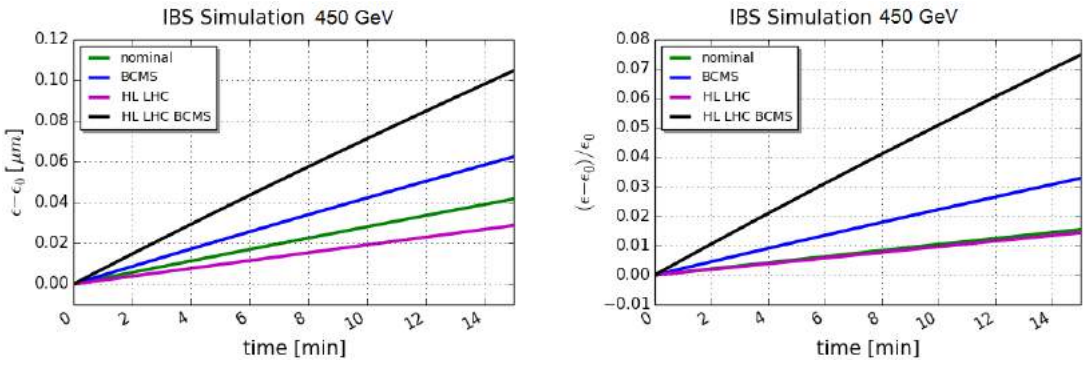

Figure 10.2.: IBS emittance growth at 450 GeV. MAX IBS simulation results for different beams staying 15 minutes at the 450 GeV LHC injection plateau. The beam parameters are presented in Table 10.1. The nominal 25 ns (green) physics beam parameters will be used in the 2016 LHC proton run. An alternative is the BCMS 25 ns physics beam (blue). One possible LHC beam foreseen for the high luminosity era following LS3 (purple) is also displayed along with its alternative the high luminosity BCMS beam (black). The absolute emittance growth is shown on the left, the relative growth on the right.

	bunch intensity [10^{11} ppb]	emittance [µm]	bunch length [ns]
Nominal	1.25	2.7	1.25
BCMS	1.25	1.9	1.25
HL LHC	2.3	2.0	3.0
HL LHC BCMS	2.0	1.4	1.5

Table 10.1.: Future LHC beam parameters for the nominal 25 ns physics beams and the BCMS 25 ns beams in Run 2. Possible parameters for the high luminosity era of the LHC (HL LHC) are also given. The values refer to the beam at injection into the LHC.

produced. One scenario foresees a bunch length of 3 ns for the high luminosity LHC beams after LS3 (purple). This would result in significantly less emittance growth from IBS than all other scenarios with a bunch length between 1 and 2 ns. The emittance would blow up by about 0.03 µm (< 2 %) in 15 minutes. Whereas the emittances of the BCMS high luminosity beams (black) are expected to grow by more than 0.1 µm (> 7 %). This demonstrates the importance of the utilization of longer bunch lengths for low emittance growth rates from IBS.

The total number of bunches per injected batch in the LHC was limited to 144 in the 2012 and 2015 LHC proton runs. In the future, nominal batches of 288 bunches will be injected in the LHC increasing electron cloud effects, which in turn could cause more bunch instabilities and emittance blow-up. Mitigation of intra-beam scattering and noise can only improve emittance growth rates if effects from electron cloud are kept to a minimum, which is achieved with sufficient scrubbing of the machine.

11. Summary and Conclusion

The performance of a collider is defined by its luminosity production, which is closely linked to the size of the transverse beam emittance. The transverse emittance is the phase space density of the beam. It should be conserved in proton accelerators, but numerous effects can lead to emittance increase or decrease. It is part of the commissioning and optimization of the operational settings of the accelerator to study these effects and keep them to a minimum. At the LHC design stage the total allowed emittance increase through the cycle was set to 7 %.

Measuring the emittance growth is a complex task with high intensity beams and changing energies. The machine optics, beta function, and the transverse beam size have to be measured as accurately as possible. This thesis presents beta function and beam size measurements, as well as emittance preservation studies during the 2012 and 2015 LHC cycle. Transverse profile monitors such as wire scanners and synchrotron light monitors are used in the LHC to measure the transverse beam size. The beta functions were measured with k-modulation.

K-modulation is an alternative method for measuring the beta functions at locations of individually powered quadrupoles. The method was used in 2015 to measure beta functions in LHC point 4 and in the interaction points to obtain β^*, the beta function at the interaction point. I developed a new and safe, dedicated online tool, which is operational since the start of LHC Run 2 to simplify and speed up the measurements. The obtained beta function measurement accuracy from k-modulation in the LHC is mainly limited by tune noise. Nevertheless, measurement errors smaller than 2 % could be achieved with sinusoidal excitation of quadrupoles. These are very promising results and pave the way for high precision beta function measurements at the interaction points and beam profile monitors to further decrease the emittance measurement uncertainty.

Wire scanners are an important tool for beam size measurements in the LHC. Even though they can only be used with low intensity beams, wire scanners are currently the only instrument that can measure useful transverse profiles during the entire LHC cycle. Wire scanners need to measure the beam size as accurately as possible because they are also used to calibrate other profile monitors such as the synchrotron light monitors (BSRT). During the long shutdown, LHC wire scanners were upgraded followed by an extensive calibration verification measurement campaign in 2015 to minimize the absolute beam size measurement uncertainty. The wire position measurement accuracy was determined and measurement reproducibility was studied. New fitting algorithms and averaging over several consecutive scans could reduce the beam size measurement accuracy to about 5 %. Wire scanner photomultiplier saturation was also investigated. Contrary to Run 1, no influence of wire scanner settings on the measured beam size could be detected for non-ADC-saturated profiles.

In addition, the transverse emittance can be derived from ATLAS and CMS luminosity with an overall uncertainty of about 10 % including measured bunch length, bunch intensity, β^* and crossing angle.

In 2015, the overall measured emittance blow-up for 50 ns beams from LHC injection to start of collisions was slightly smaller than for the high brightness beams in LHC Run 1. About 25 % emittance growth from wire scans and ATLAS luminosity was measured on average. The performance of 25 ns LHC beams in 2015 was also degraded. ATLAS luminosity measurements of 25 ns beams in 2015 indicate about 25 % emittance growth through the LHC cycle.

Low intensity test fills were used to examine the emittance growth through the different phases of the LHC cycle in order to find the origin of the growth. Horizontal emittance growth during the entire LHC cycle can be matched with intra-beam scattering (IBS) simulations in most cases. Sometimes significant growth in the vertical planes and larger horizontal growth than expected from IBS was measured. The growth occurs at the injection plateau and sometimes also at the start of the ramp. The emittance blow-up is believed to originate from noise, possibly created by quadrupole vibrations through ground motion.

Measurements in 2015 showed that the emittances are preserved during the LHC ramp and β^* squeeze. Seemingly increasing and decreasing emittances during the ramp and the squeeze are due to non-monotonically changing beta functions during these beam processes. The β knowledge at each point during the ramp and the squeeze is required in order to measure the emittance correctly.

For the first time, synchrotron radiation damping of protons at 6.5 TeV was observed; this damping counteracts IBS and reduces the vertical emittance at high energies.

If the beams are kept stable during the LHC cycle and no emittance blow-up from electron cloud effects is expected, the emittance growth in the LHC can be kept as small as 10 % from injection to start of collision. IBS and noise are causes of emittance blow-up in the horizontal and vertical plane at the 450 GeV injection plateau. A possible cure for these effects is reducing the time spent at injection. This is especially important when injecting higher brightness beams, as foreseen for future LHC upgrade scenarios, when emittance growth due to IBS will become more pronounced.

Glossary

ADC	Analogue to Digital Converter
ADT	LHC transverse damper
AGC	Abort Gab Cleaning
ALICE	A Large Ion Collider Experiment
ATLAS	A Toroidal LHC ApparatuS
BBQ	Base Band Tune System
BCMS	Batch Compression, Merging and Splitting
BPM	Beam Position Monitor
BGI	Beam-Gas Ionization Profile Monitor
BGV	Beam Gas Vertex Detector
BQM	Beam Quality Monitor
BSRT	Beam Synchrotron Radiation Telescope
CERN	European Center for Nuclear Research
CMS	Compact Muon Solenoid
DCCT	DC (Direct Current) Current Transformer
FBCT	Fast Beam Current Transformer
FFT	Fast Fourier Transformation
FODO	Linear optics scheme with focusing (F) and defocusing (D) quadrupoles, and drift spaces or dipoles (O) in between
FWHM	Full Width Half Maximum
Higgs Boson	Fundamental interaction particle responsible for the origin of mass
HL LHC	High Luminosity LHC
HOM	Higher Order Mode
IBS	Intra-Beam Scattering
IGC	Injection Gab Cleaning
IP	Interaction Point
IR	Insertion Region
LEP	Large Electron-Positron Collider
LHC	Large Hadron Collider
LHCb	Large Hadron Collider beauty
LS1	Long Shutdown 1

LUCID	LUminosity measurement using a Cherenkov Integrating Detector
MADX	Methodical Accelerator Design-X
NAFF	Numerical Analysis of Fundamental Frequencies
p	proton(s)
PLT	Pixel Luminosity Telescope
PM	PhotoMultiplier
ppb	protons per bunch
PS	Proton Synchrotron
PSD	Power Spectral Density
Q	Quadrupole
Q20	SPS working point
QPS	Quench Protection System
RF	Radio Frequency
rms	root mean square
Run 1	LHC running years 2010 - 2012
Run 2	LHC running years 2015 - 2018
SPS	Super Proton Synchrotron
SR	Synchrotron Radiation
Standard Model	General theory to describe fundamental particle interactions
TCP	Target Collimator Primary
TDI	Beam Absorber for Injection
TI	Transfer line
TMCI	Transverse Mode Coupling Instability
TS	Technical Stop
vdM	van der Meer
WS	Wire Scanner

Bibliography

[1] O. S. Brüning, P. Collier, P. Lebrun, *et al.*, *LHC Design Report - The LHC Main Ring*, vol. 1. CERN, 2004.

[2] "European organization for nuclear research." `http://home.web.cern.ch/`.

[3] M. Kuhn, "LHC Beam Operations: Past, Present and Future," in *Proceedings of the 48th Rencontres de Moriond, 2013 QCD and High Energy Interactions*, (La Thuile, Aosta Valley, Italy), pp. 55–60, March 2013.

[4] J. Incandela, F. Gianotti, and R. Heuer, "Latest Update in the Search for the Higgs." CERN Scientific Seminar, (Geneva, Switzerland), July 2012.

[5] Nobelprize.org, "The Nobel Prize in Physics 2013." `http://www.nobelprize.org/nobel_prizes/physics/laureates/2013/`, October 2013. Nobel Media AB.

[6] M. Kuhn, "Emittance Preservation at the LHC," Master's thesis, University of Hamburg/CERN, March 2013.

[7] T. A. Collaboration, "The ATLAS Experiment at the CERN Large Hadron Collider," *Journal of Instrumentation*, vol. 3, no. 08, p. S08003, 2008.

[8] T. C. Collaboration, "CMS Physics Technical Design Report, Volume II: Physics Performance," *Journal of Physics G: Nuclear and Particle Physics*, vol. 34, no. 6, p. 995, 2007.

[9] T. L. Collaboration, "LHCb, a Large Hadron Collider beauty experiment for precision measurements of CP-violation and rare decays," Technical Proposal LHCC-1998-004, CERN, Geneva, Switzerland, 1998.

[10] T. A. Collaboration, "ALICE: Physics Performance Report, Volume II," *Journal of Physics G: Nuclear and Particle Physics*, vol. 32, no. 10, p. 1295, 2006.

[11] B. Barish, "The LHC Performance and Prospects." `http://newsline.linearcollider.org/2011/10/06/the-lhc-performance-and-prospects/`, October 2011.

[12] A. M. Asner, Y. Baconnier, O. Barbalat, *et al.*, "Large hadron collider in the LEP tunnel: a feasibility study of possible options," Tech. Rep. CERN-DIR-TECH-84-01, CERN, Geneva, Switzerland, May 1984.

[13] P. Lebrun *et al.*, "Report of the Task Force on the Incident of 19th September 2008 at the LHC," Tech. Rep. LHC Project Report 1168, CERN, Geneva, Switzerland, March 2009.

[14] R. Aymar, "Status of CERN Activities." 84th Plenary European Committee for Future Accelerators (PECFA) Meeting, November 2008. CERN, Geneva, Switzerland.

[15] F. Bordry, S. Baird, K. Foraz, *et al.*, "The First Long Shutdown (LS1) for the LHC," in *Proceedings of the 4th International Particle Accelerator Conference, IPAC13*, (Shanghai, China), pp. 44–48, May 2013.

[16] O. Brüning, H. Burkhardt, and S. Myers, "The Large Hadron Collider," *Progress in Particle and Nuclear Physics 67*, vol. 67, no. 3, pp. 705–734, 2012.

[17] G. Arduini, H. Bartosik, G. Iadarola, *et al.*, "Electron Cloud and Scrubbing in the LHC," in *Proceedings of the 2012 Evian Workshop on LHC Beam Operation*, (Evian, France), December 2012.

[18] J. Uythoven, V. Kain, A. Lechner, *et al.*, "Operation with BCMS Beams for Run 2: Introduction and Machine Limits." Third LHC Injection and Beam Dump Meeting (LIBD) Meeting on BCMS Beams for Run 2, February 2015. CERN, Geneva, Switzerland.

[19] R. Alemany, M. Lamont, and S. Page, "Functional Specification LHC Modes," Tech. Rep. CERN-LHC-OP-ES-0005, CERN, Geneva, Switzerland, November 2007.

[20] G. Iadarola, H. Bartosik, K. Li, *et al.*, "Electron Cloud Effects," in *Proceedings of the 6th Evian Workshop on LHC Beam Operation*, (Evian, France), December 2015. (forthcoming).

[21] W. Herr and B. Muratori, "Concept of Luminosity," in *CAS - CERN Accelerator School: Intermediate Course on Accelerator Physics*, (Zeuthen, Germany), DESY, September 2003.

[22] K. Wille, *The Physics of Particle Accelerators - An Introduction*. Oxford University Press, 2000.

[23] H. Wiedemann, *Particle Accelerator Physics*. Springer-Verlag, 2007.

[24] J. Rossbach and P. Schmüser, "Basic Course on Accelerator Optics," in *CERN European Organisation for Nuclear Research-Reports*, (Geneva, Switzerland), CERN, 1994.

[25] D. A. Edwards and M. J. Syphers, *An Introduction to the Physics of High Energy Accelerators*. John Wiley & Sons, Inc., 1993.

[26] V. Kain, *Machine Protection and Beam Quality during the LHC Injection Process*. PhD thesis, Technische Universität Wien/CERN, Vienna, Austria, October 2005.

[27] K. Fuchsberger, *Novel Concepts for Optimization of the CERN Large Hadron Collider Injection Lines*. PhD thesis, Technische Universität Wien/CERN, Vienna, Austria, June 2011.

[28] L. Drosdal, *LHC Injection Beam Quality during LHC Run I*. PhD thesis, Oslo University/CERN, Oslo, Norway, August 2015.

[29] L. Vos, "Mismatch, Damping and Emittance Growth," in *9th LEP-SPS Performance Workshop*, (Chamonix, France), pp. 99–102, CERN, January 1999.

[30] V. Kain, W. Bartmann, C. Bracco, *et al.*, "Emittance Preservation at Injection into LHC," in *Proceedings of HB2010*, (Morschach, Switzerland), pp. 188–192, September 2010.

[31] W. Höfle, G. Kotzian, M. Schokker, *et al.*, "LHC Damper Beam Commissioning in 2010," in *Proceedings of the 2nd International Particle Accelerator Conference, IPAC11*, (San Sebastian, Spain), pp. 505–507, September 2011.

[32] W. Hofle, "Progress in Transverse Feedbacks and Related Diagnostics for Hadron Machines," in *Proceedings of the 4th International Particle Accelerator Conference, IPAC13*, (Shanghai, China), May 2013.

[33] D. Valuch, F. Dubouchet, W. Höfle, *et al.*, "What you get - Transverse Damper System," in *Proceedings of the 2012 Evian Workshop on LHC Beam Operation*, (Evian, France), December 2012.

[34] W. Hofle and D. Valuch, "Transverse feedback: high intensity operation, AGC, IGC, lessons for 2012," in *Proceedings of the 3rd Evian Workshop on LHC Beam Operation*, (Evian, France), pp. 97–100, December 2011.

[35] W. Hofle, "Margins to Increase ADT Gain at Injection." LHC Beam Operation Committe (LBOC) Meeting on 6 October 2015. CERN, Geneva, Switzerland.

[36] M. Meddahi, S. Bart Pedersen, A. Boccardi, *et al.*, "LHC Abort Gap Monitoring and Cleaning," in *Proceedings of the 1st International Particle Accelerator Conference, IPAC10*, (Kyoto, Japan), pp. 474–476, 2010.

[37] A. Piwinski, "Intra-Beam Scattering," in *9. International Conference on High Energy Accelerators*, (Stanford, California, USA), pp. 405–409, 1974.

[38] A. Dougan, "Lecture 18: Beam Loss and Beam Emittance Growth," in *USPAS 2002: Introduction to Accelerator Physics*, (Long Beach, California, USA), January 2002.

[39] A. Wolski, "Space Charge, Intrabeam Scattering and Touschek Effects," in *Fourth International Accelerator School for Linear Colliders*, (Beijing, China), September 2009.

[40] M. Sands, "The Physics of Electron Storage Rings - An Introduction," Tech. Rep. SLAC-121 UC-28, SLAC National Accelerator Laboratory, Standford, California, USA, November 1970.

[41] A. Wolski, *Beam dynamics in high energy particle accelerators*. London: Imperial College Press, 2014.

[42] "MAD - Methodical Accelerator Design." `http://madx.web.cern.ch//`.

[43] J. D. Bjorken and S. K. Mtingwa, "Intrabeam scattering," *Particle Accelerators*, vol. 13, no. FERMILAB-PUB-82-47-THY, pp. 115–143, 1983.

[44] M. Conte and M. Martini, "Intrabeam scattering in the cern antiproton accumulator," *Particle Accelerators*, vol. 17, no. FERMILAB-PUB-82-47-THY, pp. 1–10, 1985.

[45] T. Mastoridis, J. D. Fox, C. H. Rivetta, *et al.*, "Studies of RF Noise Induced Bunch Lengthening at the LHC," in *Proceedings of the 2011 Particle Accelerator Conference*, (New York City, NY, USA), pp. 91–93, March 2011.

[46] V. Lebedev, V. Shiltsev, G. Stupakov, *et al.*, "Emittance Growth Due to Noise and its Suppression with the Feedback System in Large Hadron Colliders," *Particle Accelerators*, vol. 44, no. SSCL-P-188, pp. 147–164, 1993.

[47] L. R. Carver, N. Biancacci, J. Wenninger, *et al.*, "First Observations with the ADT Observation Box." LHC Beam Operation Committe (LBOC) Meeting on 24 November 2015. CERN, Geneva, Switzerland.

[48] J. Laskar, C. Froeschle, and A. Celletti, "The measure of chaos by the numerical analysis of the fundamental frequencies. Application to the standard mapping," *Physica D: Nonlinear Phenomena*, vol. 56, no. 2, pp. 253 – 269, 1992.

[49] J. Wenninger, "Lessons Learned from the Civil Engineering Test Drilling and Earthquakes on LHC Vibration Tolerances," in *Chamonix 2016 workshop on LHC Performance*, (Chamonix, France), January 2016.

[50] C. Collette, K. Artoos, M. Guinchard, *et al.*, "Seismic Response of Linear Accelerators," *Phys. Rev. ST Accel. Beams*, vol. 13, p. 072801, July 2010.

[51] M. Kuhn, G. Arduini, B. Holzer, *et al.*, "Causes and Solutions for Emittance Blow-Up during the LHC Cycle," in *Proceedings of the 3rd International Particle Accelerator Conference, IPAC12*, (New Orleans, Louisiana, USA), pp. 160–162, May 2012.

[52] M. Kuhn, G. Arduini, J.-F. Comblin, *et al.*, "Brightness Evolution for LHC Beams during the 2012 Run," in *Proceedings of HB2012*, (Beijing, China), September 2012.

[53] M. Kuhn, G. Arduini, J. Emery, *et al.*, "LHC Emittance Preservation during the 2012 Run," in *Proceedings of the 2012 Evian Workshop on LHC Beam Operation*, (Evian, France), December 2012.

[54] M. Kuhn, G. Arduini, P. Baudrenghien, *et al.*, "Investigations of the LHC Emittance Blow-Up during the 2012 Proton Run," in *Proceedings of the 4th International Particle Accelerator Conference, IPAC13*, (Shanghai, China), pp. 1394–1396, May 2013.

[55] M. Kuhn, G. Arduini, V. Kain, *et al.*, "Origins of Transverse Emittance Blow-up during the LHC Energy Ramp," in *Proceedings of the 5th International Particle Accelerator Conference, IPAC14*, (Dresden, Germany), pp. 1021–1023, June 2014.

[56] G. Trad, *Development and Optimisation of the SPS and LHC Beam Diagnostics Based on Synchrotron Radiation Monitors*. PhD thesis, Laboratoire de

Physique Subatomique et de Cosmologie (LPSC)/CERN, Grenoble, France, May 2015.

[57] H. Bartosik, G. Arduini, and Y. Papaphilippou, "Optics Considerations for Lowering Transition Energy in the SPS," in *Proceedings of the 2nd International Particle Accelerator Conference, IPAC11*, (San Sebastian, Spain), pp. 619–621, September 2011.

[58] L. Drosdal, V. Kain, W. Bartmann, *et al.*, "Sources and Solutions for LHC Transfer Line Stability Issues," in *Proceedings of 3rd International Particle Accelerator Conference, IPAC12*, (New Orleans, Louisiana, USA), pp. 2047–2049, May 2012.

[59] V. Kain, G. Arduini, B. Goddard, *et al.*, "Emittance Preservation in the LHC," in *Proceedings of the Chamonix 2012 workshop on LHC Performance*, (Chamonix, France), pp. 81–88, February 2012.

[60] T. Mastoridis, P. Baudrenghien, A. Butterworth, *et al.*, "Batch By Batch Longitudinal Emittance Blowup MD," Tech. Rep. CERN ATS-Note-2012-050 MD, CERN, Geneva, Switzerland, June 2012.

[61] A. Langner *et al.*, "Improvements in the Optics Measurement Resolution for the LHC," in *Proceedings of the 5th International Particle Accelerator Conference, IPAC14*, (Dresden, Germany), June 2014.

[62] M. Kuhn, B. Dehning, V. Kain, *et al.*, "New Tools for K-Modulation in the LHC," in *Proceedings of the 5th International Particle Accelerator Conference, IPAC14*, (Dresden, Germany), pp. 1024–1026, June 2014.

[63] M. Kuhn, V. Kain, A. Langner, *et al.*, "Firsst K-Modulation Measurements in the LHC during Run 2," in *Proceedings of the International Beam Instrumentation Conference 2015, IBIC15*, (Melbourne, Victoria), September 2015.

[64] S. Fartoukh and O. Bruening, "Field Quality Specification for the LHC Main Dipole Magnets," Tech. Rep. LHC Project Report 501, CERN, Geneva, Switzerland, October 2001.

[65] A. Garcia-Tabares Valdivieso, F. Carlier, A. Langner, *et al.*, "LHC Optic Measurements at Injection," Tech. Rep. CERN-ATS-Note-2015-XX, CERN, Geneva, Switzerland, October 2015. (forthcoming).

[66] A. Langner, R. Calaga, R. Miyamoto, *et al.*, "Optics Measurement in the LHC Close to the Half Integer Tune Resonance," Tech. Rep. CERN-ATS-Note-2011-095 TECH, CERN, Geneva, Switzerland, December 2011.

[67] R. J. Steinhagen, A. Boccardi, E. Calvo Giraldo, *et al.*, "On the Continuous Measurement of the LHC Beta-Function - Prototype Studies at the SPS," in *Proceedings of the 23rd Particle Accelerator Conference, PAC09*, (Vancouver, Canada), pp. 3528–3530, May 2009.

[68] F. Tecker, *Methods of Improving the Orbit Determination and Stability at LEP*. PhD thesis, RWTH Aachen/CERN, Aachen, Germany, 1998.

[69] N. Aquilina, M. Giovannozzi, M. Lamont, *et al.*, "Tune Variations in the Large Hadron Collider," *Nuclear Instruments and Methods in Physics Research Section A: Accelerators, Spectrometers, Detectors and Associated Equipment*, vol. 778, pp. 6–13, April 2015.

[70] R. Steinhagen, "Real-Time Beam Control at the LHC," in *Proceedings of 2011 Particle Accelerator Conferences*, (New York, New York, USA), pp. 1399–1403, March 2011.

[71] D. Jacquet *et al.*, "LSA - the High Level Application Software of the LHC - and Its Performance during the First Three Years of Operation," in *Proceedings of the 14th International Conference on Accelerator And Large Experimental Physics Control Systems, ICALEPCS2013*, (San Francisco, California, USA), 2013.

[72] A. Vergara Fernandez and F. Rodriguez-Mateos, "Reliability of the quench protection system for the LHC superconducting elements ," *Nuclear Instruments and Methods in Physics Research Section A: Accelerators, Spectrometers, Detectors and Associated Equipment*, vol. 525, no. 3, pp. 439 – 446, 2004.

[73] J. Wenninger *et al.*, "BPM Offset Determination by Sinusoidal Quadrupole K-modulation," Tech. Rep. ATS-Note-2011-043 MD (LHC), CERN, Geneva, Switzerland, May 2011.

[74] C.-x. Wang, "Formulas for Tune Shift and β Beat due to Perturbations in Circular Accelerators," *Physical Review E*, vol. 71, no. 3, p. 036502, 2005.

[75] G. Valentino, "Performance of the Collimation System during 2015," in *Proceedings of the 6th Evian Workshop on LHC Beam Operation*, (Evian, France), December 2015. (forthcoming).

[76] L. Palumbo, V. G. Vaccaro, and M. Zobov, "Wake Fields and Impedance," in *CAS - CERN Accelerator School: 5th Advanced Accelerator Physics Course*, (Rhodes, Greece), CERN, September 1993.

[77] V. Granata, J. Billan, F. Bordry, *et al.*, "Tracking and k-modulation measurements in String II," Tech. Rep. LHC Project Note 319, CERN, Geneva, Switzerland, August 2003.

[78] F. S. Carlier and R. Tomas Garcia, *Beam Optics Studies in the Large Hadron Collider: Observations on an Anomalous Octupolar Resonance Line in the LHC and Accuracy and Feasibility of the β^* Measurement for LHC and HL-LHC Using K-Modulation*. PhD thesis, Delft University of Technology/CERN, Delft, Netherlands, August 2015.

[79] M. Schaumann, "Tune and Chromaticity: Decay and Snapback," in *Proceedings of the 6th Evian Workshop on LHC Beam Operation*, (Evian, France), December 2015. (forthcoming).

[80] A. Boccardi, M. Gasior, O. R. Jones, *et al.*, "First Results from the LHC BBQ Tune and Chromaticity Systems," Tech. Rep. LHC Performance Note 007, CERN, Geneva, Switzerland, January 2009.

[81] F. Roncarolo *et al.*, "BI MD Studies on April 22nd 2012," Tech. Rep. CERN-ATS-Note-2012-061 MD, CERN, Geneva, Switzerland, July 2012.

[82] R. Ostojic, R. Bossert, J. DiMarco, *et al.*, "The Construction of the Low-β Triplets for the LHC," in *Proceedings of 2005 Particle Accelerator Conference, PAC05*, (Knoxville, Tennessee), pp. 2798 – 2800, May 2005.

[83] T. Persson, "Corrections from Crossing, Tunes and Corrections." Talk at the Beta* and K-Modulation Meeting, October 2015.

[84] D. Trbojevic, J. Kewish, S. Peggs, *et al.*, "Measurements of the Betatron Functions and Phases in RHIC," in *Proceedings of the Sixth European Particle Accelerator Conference (EPAC98)*, (Stockholm, Sweden), pp. 1620 – 1622, June 1998.

[85] O. E. Berrig, C. Fischer, and H. Schmickler, "Measuring Beta-Functions with K-Modulation," Tech. Rep. CERN-SL-2001-021-BI, CERN, Geneva, Switzerland, May 2001.

[86] G. Vanbavinckhove, *Optics measurements and corrections for colliders and other storage rings*. PhD thesis, Amsterdam University/CERN, Amsterdam, Netherlands, January 2013.

[87] R. Calaga, R. Miyamoto, R. Tomas, and G. Vanbavinckhove, "Beta* Measurement in the LHC Based on K-modulation," Tech. Rep. CERN-ATS-2011-149, CERN, Geneva, Switzerland, September 2011.

[88] F. Roncarolo, T. Baer, E. Bravin, *et al.*, "BI MD studies on April 22nd 2012 (LHC MD1)," Tech. Rep. CERN-ATS-Note-2012-061 MD, CERN, Geneva, Switzerland, July 2012.

[89] M. Sapinski, "Beam Interaction with Thin Materials: Heat Deposition, Cooling Phenomena and Damage Limits," in *2012 Beam Instrumentation Workshop*, (Newport News, Virginia, USA), April 2012.

[90] G. Trad, "Status of the Beam Profile Measurements at the LHC," in *Proceedings of the 2015 Evian Workshop on LHC Beam Operation*, (Evian, France), December 2015. (forthcoming).

[91] P. Hopchev, V. Baglin, C. Barschel, *et al.*, "A Beam Gas Vertex Detector for Beam Size Measurement in the LHC," in *Proceedings of the 5th International Particle Accelerator Conference, IPAC14*, (Dresden, Germany), pp. 3680–3683, June 2014.

[92] S. Fartoukh, "Optics Change Requests for Run II and Possible Options for 2015." LMC Meeting 179, April 2014. CERN, Geneva, Switzerland.

[93] A. Nosych, "Geometrical Non-Linearity Correction Procedure of LHC Beam Position Monitors," EDMS Document 1342295, CERN, Geneva, Switzerland, 2014.

[94] E. Piselli, J. Emery, and L. Timeo, "LHC Photomultiplier Studies." Emittance Working Group Meeting, February 2015. CERN, Geneva, Switzerland.

[95] P. Grafstroem and W. Kozanecki, "Luminosity Determination at Proton Colliders," *Progress in Particle and Nuclear Physics*, vol. 81, pp. 97–148, March 2015.

[96] P. Lujan, "Update on the 13 TeV p-p CMS 2015 Offline Luminosity Uncertainty." LHC Luminosity Calibration and Monitoring Working Group Meeting, December 2015. CERN, Geneva, Switzerland.

[97] E. Bartz, J. Doroshenko, V. Halyo, *et al.*, "The PLT: A Luminosity Monitor for CMS Based on Single-Crystal Diamond Pixel Sensors ," *Nuclear Physics B - Proceedings Supplements*, vol. 197, no. 1, pp. 171 – 174, 2009.

[98] W. Kozanecki, "Update of the ATLAS Luminosity Calibration for the 2015 pp Run at 13 TeV." LHC Luminosity Calibration and Monitoring Working Group Meeting, December 2015. CERN, Geneva, Switzerland.

[99] A. Sbrizzi, "A Cherenkov Detector for Monitoring ATLAS Luminosity ," *Nuclear Physics B - Proceedings Supplements*, vol. 215, no. 1, pp. 232 – 234, 2011.

[100] D. Belohrad, L. Jensen, O. Jones, *et al.*, "The LHC Fast BCT system: A comparison of Design Parameters with Initial Performance," in *Proceedings of the 14th Beam Instrumentation Workshop*, (Santa Fe, New Mexico, USA), pp. 269 – 273, CERN, May 2010.

[101] P. Odier, M. Ludwig, and S. Thoulet, "The DCCT for the LHC Beam Intensity Measurement," Tech. Rep. CERN-BE-2009-019, CERN, Geneva, Switzerland, May 2009.

[102] K. Unser, "Beam Current Transformer with DC to 200MHz Range," *IEEE Trans.Nucl. SCI. NS-16*, pp. 934–938, June 1969.

[103] C. Barschel, M. Ferro-Luzzi, J.-J. Gras, *et al.*, "Results of the LHC DCCT Calibration Studies," Tech. Rep. CERN-ATS-Note-2012-026 PERF, CERN, Geneva, Switzerland, May 2012.

[104] G. Papotti, T. Bohl, F. Follin, *et al.*, "Longitudinal Beam Measurements at the LHC: The LHC Beam Quality Monitor," in *Proceedings of the 2nd International Particle Accelerator Conference, IPAC11*, (San Sebastian, Spain), pp. 1852 – 1854, September 2011.

[105] M. Hofstettler, "Observations from OP Extended Luminosity Scans." LHC Beam Operation Committe (LBOC) Meeting on 28 July 2015. CERN, Geneva, Switzerland.

[106] M. Kuhn, F. Antoniou, E. Bravin, *et al.*, "First LHC Emittance Measurements at 6.5 TeV," in *Proceedings of the International Beam Instrumentation Conference 2015, IBIC15*, (Melbourne, Victoria), September 2015.

[107] M. Kuhn, "LHC Emittance Growth Until Stable Beams," in *Proceedings of the 6th Evian Workshop on LHC Beam Operation*, (Evian, France), December 2015. (forthcoming).

[108] T. Camporesi, "Status of CMS - Progress Summary Report for October 2015 RRB41," Tech. Rep. CERN-RRB-2015-078, CERN, Geneva, Switzerland, October 2015. LHC Resource Review Board.

[109] F. Roncarolo, *Accuracy of the Transverse Emittance Measurements of the CERN Large Hadron Collider*. PhD thesis, Ecole Polytechnique Federale de Lausanne/CERN, Lausanne, Switzerland, 2005.

[110] H. Damerau, H. Bartosik, C. Carli, *et al.*, "Performance Potential of the Injectors after LS1," in *Proceedings of the Chamonix 2012 workshop on LHC Performance*, (Chamonix, France), pp. 268–275, February 2012.

[111] R. Bruce, G. Arduini, B. Goddard, *et al.*, "LHC Machine Configuration in the 2016 Proton Run," in *Chamonix 2016 workshop on LHC Performance*, (Chamonix, France), January 2016.

[112] H. Damerau, "LIU - RF Systems Along the Injector Chain and Outlook for Post-LS2 Performance," in *Chamonix 2016 workshop on LHC Performance*, (Chamonix, France), January 2016.

[113] B. Goddard, H. Bartosik, C. Bracco, *et al.*, "Can the Proton Injectors Meet the HL-LHC Requirements after LS2?," in *Proceedings of the Chamonix 2012 workshop on LHC Performance*, (Chamonix, France), pp. 325–331, February 2012.

[114] G. Arduini, "Performance Limitations in LHC after LIU Upgrade," in *Chamonix 2016 workshop on LHC Performance*, (Chamonix, France), January 2016.

[115] R. Tomas, O. Dominguez, and S. White, "HL-LHC Performance with a 200 MHz RF System," in *Proceedings of the 5th International Particle Accelerator Conference, IPAC14*, (Dresden, Germany), pp. 1043–1045, June 2014.

Appendix

A. Introduction to Basic Accelerator Physics and Concept of Emittance

This chapter has already been published in [6]. Parts are copied here as reference introducing the basic principles of high energy particle accelerators. The linear transverse motion in the accelerator and the concept of emittance are discussed.

A.1. Lorentz Forces

Charged particles gain energy by accelerating them in electromagnetic fields. The driving force is the Lorentz force [23]:

$$\vec{F} = e \cdot \left(\vec{E} + \vec{v} \times \vec{B} \right), \tag{A.1.1}$$

where e is the elementary charge, the vectors $\vec{E}$ and $\vec{B}$ are the electric and the magnetic field vectors, respectively, and $\vec{v}$ is the velocity vector of the particle. Only electric fields lead to an increased energy with $\mathcal{E} = \int \vec{F} \mathrm{d}\vec{r}$ [1] for a particle with charge e.

The construction of an accelerator determines the design orbit. To keep the particles on the reference path, which might be curved, bending and focusing magnets are needed. Both bending and focusing is accomplished by electromagnetic forces.

The particles in high energy accelerators have velocities $v \approx c$. In this case:

$$|\vec{E}| = c \cdot |\vec{B}|. \tag{A.1.2}$$

So that a magnetic field of 1 T corresponds to an electric field of 300 MV/m. Electric fields of this strength are technically not feasible. High energy accelerators therefore rely only on magnetic fields for bending and focusing.

Beam dynamics and optics describe the evolution of the particle orbit under the Lorentz forces. The main task in beam optics is to transport a charged particle from an arbitrary starting point to a final point along the beam line. The collection of bending and focusing magnets along the ideal path is called the magnet lattice.

[1] The particle's velocity $\vec{v}$ is parallel to $\vec{r}$, the vector of the longitudinal particle motion, thus $\vec{v} \times \vec{B}$ is perpendicular to $\vec{r}$. Therefore the magnetic term cancels out in the energy relation.

A.2. Betatron Oscillations

From Newton's second law the general equation of motion for a particle with charge e in a magnetic field without acceleration ($\vec{E} = 0$) is [22]

$$\vec{F} = \frac{\mathrm{d}\vec{p}}{\mathrm{d}t} = \frac{\mathrm{d}}{\mathrm{d}t}\left(m_0\gamma\vec{v}\right) = e\left(\vec{v}\times\vec{B}\right). \tag{A.2.1}$$

Assuming a planar circular accelerator with a curvature in the horizontal plane, the coordinate system only rotates around the y-axis. The deflection angle is φ and the path element of a curved trajectory with radius R is $\mathrm{d}s = R\mathrm{d}\varphi$.

If the magnetic field only has transverse components, $\vec{B} = (B_\mathrm{x}, B_\mathrm{y}, 0)$, the equation of motion can be written as

$$x'' = \frac{1}{R}\left(1+\frac{x}{R}\right) - \left(1+\frac{x}{R}\right)^2\frac{eB_\mathrm{y}}{p}, \tag{A.2.2}$$

$$y'' = \left(1+\frac{x}{R}\right)\frac{eB_\mathrm{x}}{p}. \tag{A.2.3}$$

The deduction can be found in [22]. With a small momentum deviation $\frac{\Delta p}{p}$ the evolution of the momentum to first order is

$$\frac{1}{p_\mathrm{d}} = \frac{1}{p}\left(1-\frac{\Delta p}{p}\right), \tag{A.2.4}$$

where p_d is the particle momentum which differs from the ideal momentum. Assuming only horizontal deflecting dipoles with a strength $\frac{1}{R}$ and quadrupoles with strength k the magnet field components can be written as

$$\frac{e}{p}B_\mathrm{y} = \frac{1}{R} - kx, \qquad \frac{e}{p}B_\mathrm{x} = -ky. \tag{A.2.5}$$

Then Eq. A.2.2 and Eq. A.2.3 transform to

$$x'' = \frac{1}{R}\left(1+\frac{x}{R}\right) - \left(1+\frac{x}{R}\right)^2\left(\frac{1}{R}-kx\right)\left(1-\frac{\Delta p}{p}\right) \tag{A.2.6}$$

$$y'' = -\left(1+\frac{x}{R}\right)^2 ky\left(1-\frac{\Delta p}{p}\right). \tag{A.2.7}$$

With $x \ll R$, $y \ll R$ and $\frac{\Delta p}{p} \ll 1$ the equations simplify to the linear equations of motion for a charged particle moving through the magnetic lattice depending on the longitudinal position s in the accelerator

$$x''(s) - x(s)\left(k(s) - \frac{1}{R^2(s)}\right) = \frac{1}{R(s)}\frac{\Delta p}{p} \tag{A.2.8}$$

$$y''(s) + k(s)y(s) = 0. \tag{A.2.9}$$

These are the basic equations to calculate the particle motion through linear beam optics [22].

In the special case where there is no bending of the beam, $\frac{1}{R} = 0$, and for a non-dispersive trajectory, $\frac{\Delta p}{p} = 0$, the linear equations of motion transforms to a

homogeneous differential equation [23]

$$u''(s) \mp k(s)u(s) = 0. \tag{A.2.10}$$

For any point s of the trajectory the solutions of Eq. A.2.10 are

$$\begin{aligned} u(s) &= C(s)u_0 + S(s)u_0', \\ u'(s) &= C'(s)u_0 + S'(s)u_0', \end{aligned} \tag{A.2.11}$$

which can be written in matrix notation:

$$\begin{pmatrix} u(s) \\ u'(s) \end{pmatrix} = \underbrace{\begin{pmatrix} C(s) & S(s) \\ C'(s) & S'(s) \end{pmatrix}}_{\text{transfer matrix}} \begin{pmatrix} u_0 \\ u_0' \end{pmatrix}, \tag{A.2.12}$$

where the index 0 describes the initial parameters at $s = s_0$.

Solution of Hill's Equation

As shown in chapter 3 the particle trajectory in the horizontal plane is described by the homogeneous differential Hill equation

$$x''(s) - k(s)x(s) = 0, \tag{A.2.13}$$

which is solved with the ansatz:

$$x(s) = a \cdot q(s)\cos(\psi(s) + \phi), \tag{A.2.14}$$

where a is the constant amplitude of the oscillation and ϕ is the constant initial phase. Inserting this solution into Hill's equation, Eq. A.2.13, yields

$$q''(s) - q(s)\psi'(s)^2 - k(s)q(s) = 0, \tag{A.2.15}$$

$$2q'(s)\psi'(s) + q(s)\psi''(s) = 0. \tag{A.2.16}$$

Integrating Eq. A.2.16 leads to

$$\psi(s) = \int_0^s \frac{\mathrm{d}\lambda}{q^2(\lambda)}. \tag{A.2.17}$$

Using this result for $\psi(s)$, Eq. A.2.15 can be written as

$$q''(s) - \frac{1}{q^3(s)} - k(s)q(s) = 0, \tag{A.2.18}$$

with the definition

$$\beta(s) \equiv q^2(s). \tag{A.2.19}$$

Thus the solution to Hill's equation $x(s)$ and its derivative $x'(s)$ with respect to s, as well as the phase $\psi(s)$ are

$$x(s) = a\sqrt{\beta(s)}\cos(\psi(s)+\phi), \tag{A.2.20}$$

$$x'(s) = -\frac{a}{\sqrt{\beta(s)}}\left(\alpha(s)\cos(\psi(s)+\phi)+\sin(\psi(s)+\phi)\right), \tag{A.2.21}$$

$$\psi(s) = \int_0^s \frac{\mathrm{d}\lambda}{\beta(\lambda)}, \tag{A.2.22}$$

where $\beta(s)$ is the well-known beta function. The definition of $\alpha(s)$ is:

$$\alpha(s) \equiv -\frac{\beta'(s)}{2}. \tag{A.2.23}$$

The derivative $\beta'(s)$ is taken with respect to s.

The number of betatron oscillations per revolution 2π is called the tune Q [22]:

$$Q = \frac{1}{2\pi}\int_0^L \frac{\mathrm{d}\lambda}{\beta(\lambda)}, \tag{A.2.24}$$

where L is the circumference of the accelerator.

In matrix notation the transfer from a starting point s_0 with optical functions α_0 and β_0 to the end of the structure where the optical functions are $\alpha(s)$ and $\beta(s)$ is

$$\boldsymbol{M} = \begin{pmatrix} \sqrt{\frac{\beta}{\beta_0}}(\cos\Delta\psi + \alpha_0\sin\Delta\psi) & \sqrt{\beta\beta_0}\sin\Delta\psi \\ \frac{(\alpha-\alpha_0)\cos\Delta\psi - (1+\alpha_0\alpha)\sin\Delta\psi}{\sqrt{\beta\beta_0}} & \sqrt{\frac{\beta}{\beta_0}}(\cos\Delta\psi - \alpha\sin\Delta\psi) \end{pmatrix}, \tag{A.2.25}$$

with the phase advance $\Delta\psi$ of the betatron oscillation between s and s_0. In this way any point of the particle trajectory in the accelerator can be calculated.

A.3. Dispersion

In the six-dimensional phase space a particle on the design orbit also has the ideal momentum p. Inside a bending magnet with homogeneous magnet field and no gradient, however, particles with momentum offset move on different trajectories. For a particle with a momentum offset $\frac{\Delta p}{p} \neq 0$ the equation of motion becomes

$$x'' + \frac{1}{R^2}x = \frac{1}{R}\frac{\Delta p}{p}, \tag{A.3.1}$$

where R is the radius of curvature of the particle trajectory. Introducing a dispersion function $D(s)$ for which $\frac{\Delta p}{p} = 1$ yields

$$D''(s) + \frac{1}{R^2}D(s) = \frac{1}{R}. \tag{A.3.2}$$

This is an inhomogeneous differential equation that can be solved with the already known solution of the homogeneous equation and any particular solution to the inhomogeneous equation. The deduction can be found in [22]. Finally the dispersion

function can be written as

$$D(s) = D_0 \cos\left(\frac{s}{R}\right) + D'_0 R \sin\left(\frac{s}{R}\right) + R\left(1 - \cos\left(\frac{s}{R}\right)\right), \quad \text{(A.3.3)}$$

$$D'(s) = -\frac{D_0}{R}\sin\left(\frac{s}{R}\right) + D'_0 \cos\left(\frac{s}{R}\right) + \sin\left(\frac{s}{R}\right). \quad \text{(A.3.4)}$$

In regions with non-zero dispersion the transverse position of the particle with momentum deviation $\frac{\Delta p}{p}$ changes to

$$x_{\mathrm{g}}(s) = x(s) + x_{\mathrm{D}}(s) = x(s) + D(s)\frac{\Delta p}{p}, \quad \text{(A.3.5)}$$

with an offset $x_{\mathrm{D}}(s)$ with respect to the position $x(s)$ of a particle with no dispersion. The dispersive trajectory is determined by $\frac{\Delta p}{p}$ [22].

A.4. Liouville's Theorem

The area of the ellipse containing always the same fraction of the beam, meaning the emittance, remains constant when the particle beam is transformed through the accelerator. This is the principle of Liouville's Theorem [24]. It postulates the conservation of a particle density in phase space for non-dissipative systems.

To prove this theorem, it has to be verified that the total time derivative, $\frac{d}{dt}$, of a particle phase space density vanishes, which means that the phase space density stays constant under the influence of conservative forces.

A conservative system with a general set of coordinates $(q_1(t), \ldots, q_n(t), p_1(t), \ldots, p_n(t))$ can be described by the Hamiltonian $H(q_1, \ldots, q_n, p_1, \ldots, p_n)$ and the Hamiltonian equations [23]:

$$\frac{\partial q_i}{\partial t} = \dot{q}_i = \frac{\partial H}{\partial p_i}, \qquad \frac{\partial p_i}{\partial t} = \dot{p}_i = -\frac{\partial H}{\partial q_i}. \quad \text{(A.4.1)}$$

First, the total derivative of the phase space density $\rho(q_1, \ldots, q_n, p_1, \ldots, p_n)$ is calculated:

$$\begin{aligned}\frac{\mathrm{d}\rho}{\mathrm{d}t} &= \frac{\partial\rho}{\partial t} + \sum_i \frac{\partial\rho}{\partial q_i}\frac{\partial q_i}{\partial t} + \sum_i \frac{\partial\rho}{\partial p_i}\frac{\partial p_i}{\partial t}, \\ &= \frac{\partial\rho}{\partial t} + \sum_i \frac{\partial\rho}{\partial q_i}\dot{q}_i + \sum_i \frac{\partial\rho}{\partial p_i}\dot{p}_i. \end{aligned} \quad \text{(A.4.2)}$$

To prove that $\dfrac{\mathrm{d}\rho}{\mathrm{d}t}$ vanishes, a phase space current $\vec{v}\cdot\rho$ is defined with $\vec{v}(\dot{q}_1, \ldots, \dot{q}_n, \dot{p}_1, \ldots, \dot{p}_n)$. The continuity equation for this current is

$$0 = \frac{\partial\rho}{\partial t} + \vec{\nabla}(\rho\vec{v}), \quad \text{(A.4.3)}$$

stating that the total number of particles in the beam is constant. Equation A.4.3

gives

$$0 = \frac{\partial \rho}{\partial t} + \sum_i \frac{\partial(\rho \dot{q}_i)}{\partial q_i} + \sum_i \frac{\partial(\rho \dot{p}_i)}{\partial p_i}, \tag{A.4.4}$$

$$0 = \frac{\partial \rho}{\partial t} + \sum_i \frac{\partial \rho}{\partial q_i}\dot{q}_i + \rho \sum_i \frac{\partial \dot{q}_i}{\partial q_i} + \sum_i \frac{\partial \rho}{\partial p_i}\dot{p}_i + \rho \sum_i \frac{\partial \dot{p}_i}{\partial p_i}. \tag{A.4.5}$$

Inserting Eq. A.4.2 yields

$$0 = \frac{\mathrm{d}\rho}{\mathrm{d}t} + \rho \sum_i \left(\frac{\partial \dot{q}_i}{\partial q_i} + \frac{\partial \dot{p}_i}{\partial p_i} \right), \tag{A.4.6}$$

$$0 = \frac{\mathrm{d}\rho}{\mathrm{d}t} + \rho \sum_i \underbrace{\left(\frac{\partial^2 H}{\partial q_i \partial p_i} - \frac{\partial^2 H}{\partial p_i \partial q_i} \right)}_{=0}, \tag{A.4.7}$$

$$0 = \frac{\mathrm{d}\rho}{\mathrm{d}t}, \tag{A.4.8}$$

which proves the invariance of the phase space density.

B. Emittance Preservation at the LHC in 2012

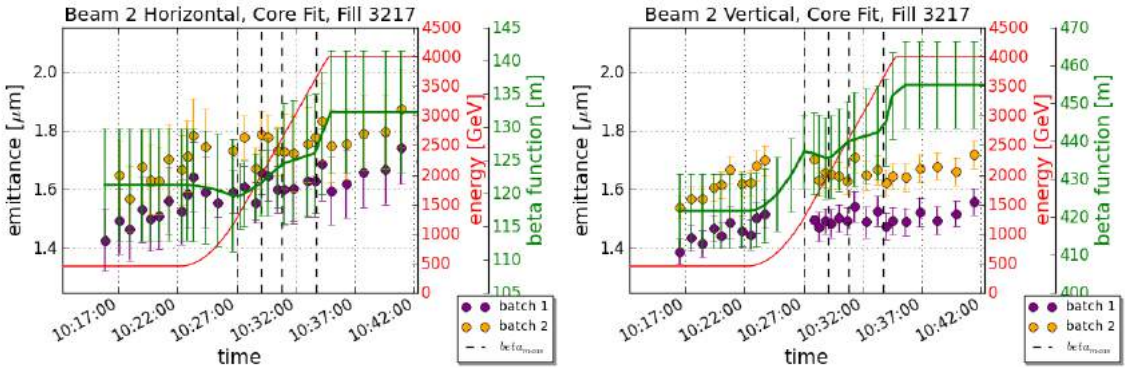

Figure B.1.: Emittance and beta function evolution during the LHC ramp. Average beam 2 horizontal and vertical emittances of 6 bunches per batch through the LHC ramp for Fill 3217 measured with wire scanner and compared to the beta function evolution (green). The core emittance is displayed. Vertical black dashed lines indicate a beta function measurement.

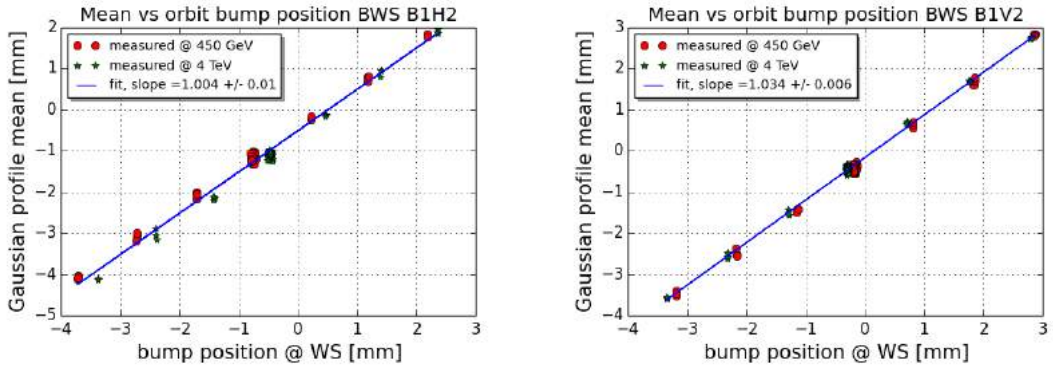

Figure B.2.: Wire scanner orbit bump calibration 2012. While the centre of the beam was shifted locally at the scanners, wire scans were triggered to determine the accuracy of the position measurement of the wire scanners. The beam position is measured with the surrounding Beam Position Monitors (BPMs) and extrapolated to the wire scanner location. The fitted orbit at the wire scanner is compared to the mean position obtained from a Gaussian fit to the measured wire scanner beam profile. Measurements were carried out at 450 GeV and 4 TeV for each operational scanner. The slope of the linear fit shows a 0.4 % calibration error for wire scanner B1H2 and 3.4 % error for wire scanner B1V2.

C. Measured Beta Beating and Beta Functions in the LHC

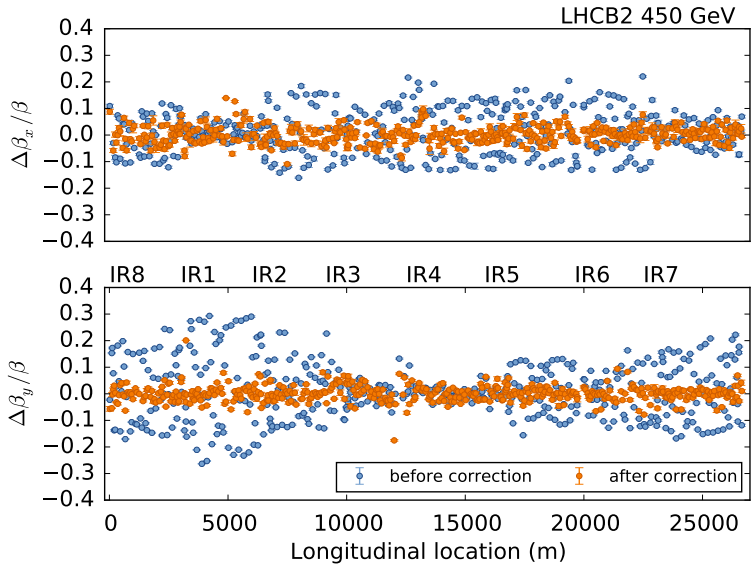

Figure C.1.: LHC beta beating measurements in 2015 for beam 2 horizontal (top) and vertical (bottom) at 450 GeV injection optics [65]. The beta beating around the ring is shown before correction (blue) and after global corrections have been implemented (orange).

Scanner	β_{inj} [m]	β_{top} [m]	β_{squeeze} [m]
B1H2	194.9 ± 2.1	196.8 ± 1.4	209.0 ± 5.0
B1V2	369.8 ± 4.4	369.0 ± 3.0	366.0 ± 4.0
B2H1	194.0 ± 2.3	193.8 ± 1.1	196.0 ± 3.0
B2V1	417.9 ± 4.5	396.0 ± 3.0	404.0 ± 5.0

Table C.1.: LHC Run 2 beta function measurement results in LHC point 4 at the wire scanner location. Results for all operational wire scanners in beam 1 (B1) and beam 2 (B2), horizontal (H) and vertical (V), in 2015 are shown. Beta functions at 450 GeV injection energy (inj) were measured with k-modulation. Results at 6.5 TeV flattop energy before (top) and after (squeeze) the squeeze were obtained from the turn-by-turn phase advance method with the AC dipole (*Courtesy A. Langner, CERN, Geneva Switzerland*).

D. Emittance Preservation at the LHC in 2015

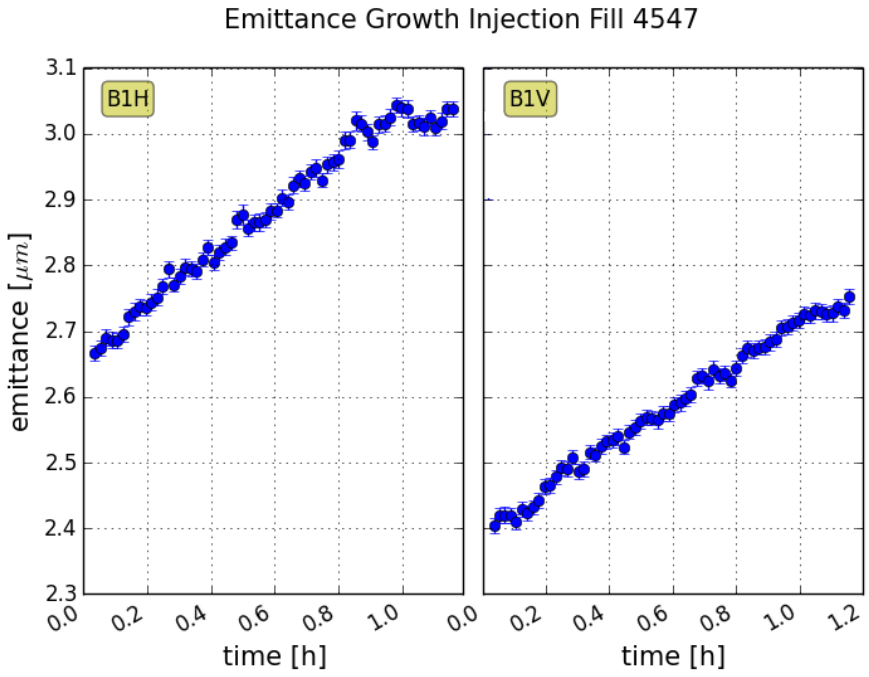

Figure D.1.: Emittance growth at 450 GeV LHC injection energy. Emittances of beam 1 horizontal and vertical were measured with the BSRT during Fill 4547 (29 October 2015). 12 bunches with 25 ns bunch spacing were injected into the LHC and stayed about 1 hour at the injection plateau. The average emittance of all bunches is plotted (blue). Mean bunch length is 1.05 ns and mean bunch intensity 1.1 10^{11} ppb.

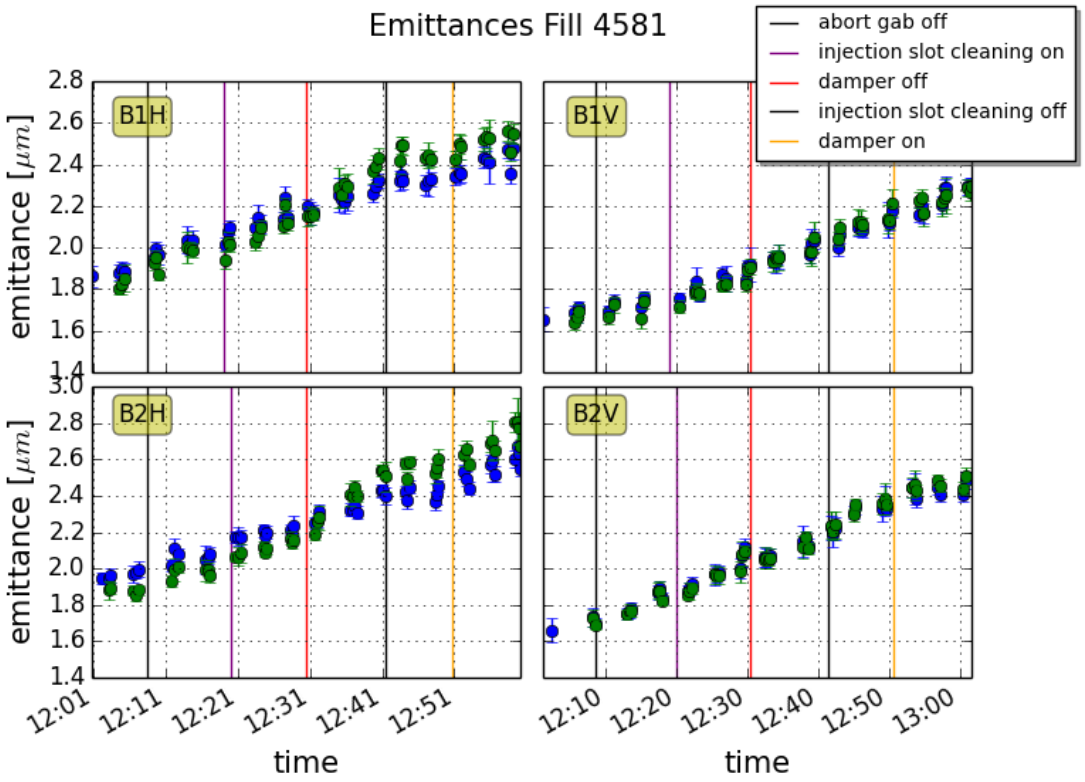

Figure D.2.: Effect of injection gab cleaning on emittance growth. Emittances in all planes are measured with wire scanners. Two single nominal bunches were injected. Bunch 1 (blue) is positioned next to the injection gab. Bunch 2 (green) is a witness bunch. Vertical lines indicate the activation or disabling of the IGC and the transverse damper. IGC has an effect on close-by bunches in the horizontal plane.

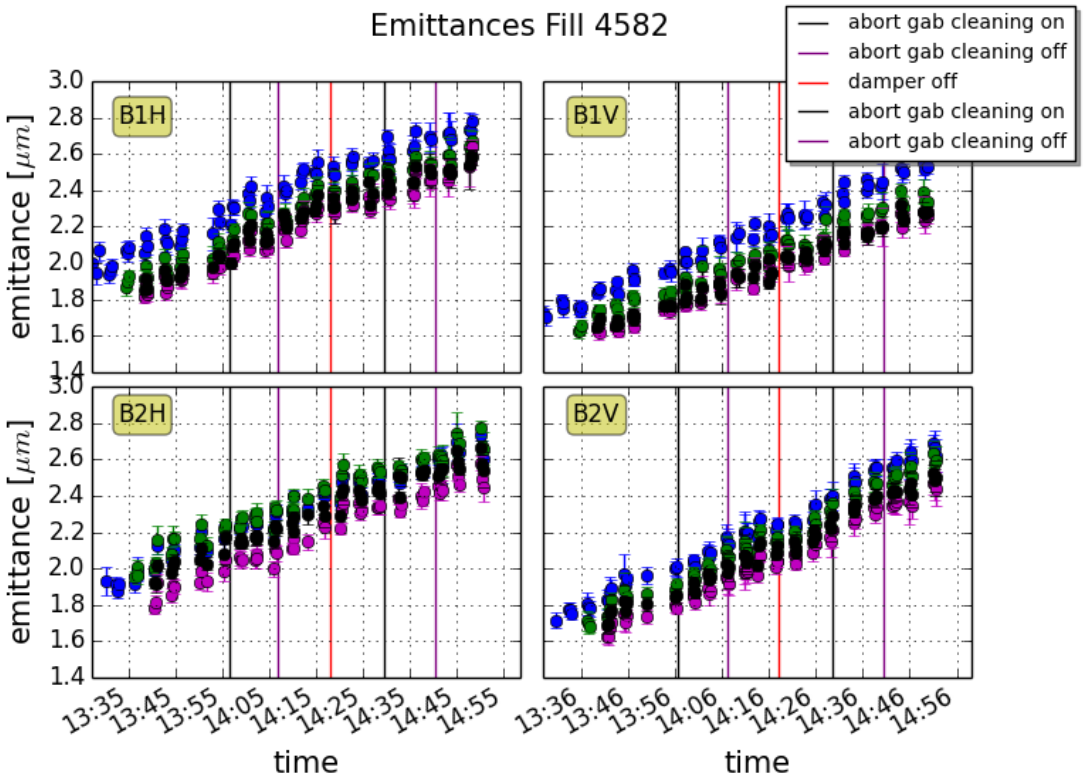

Figure D.3.: Effect of abort gab cleaning on emittance growth. Emittances in all planes are measured with wire scanners. Four single nominal bunches were injected. Bunch 1 (blue) and bunch 4 (black) are positioned left and right of the abort gab, respectively. Bunch 2 (green) and 3 (purple) are witness bunches. Vertical lines indicate the activation or disabling of the AGC and the transverse damper. No effect of AGC on emittance growth could be observed.

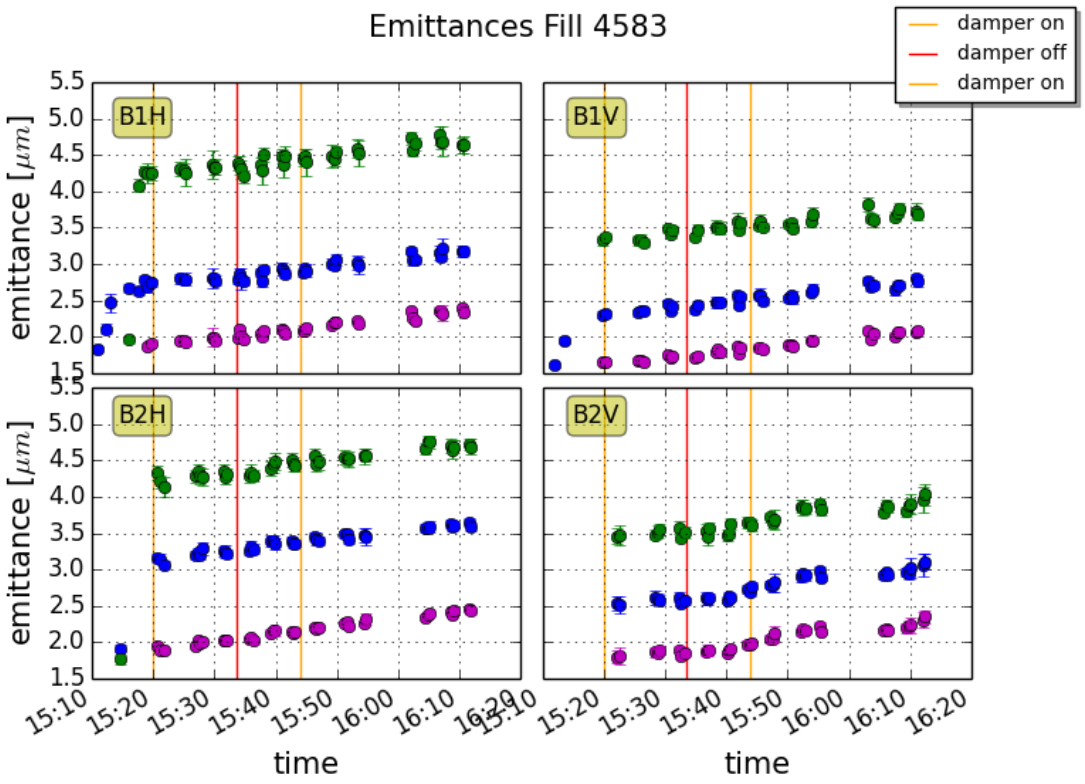

Figure D.4.: Effect of transverse damper on emittance growth. Emittances in all planes are measured with wire scanners. Three single nominal bunches with different emittances were injected. Vertical lines indicate the activation or disabling of the transverse damper. No effect of transverse damping on emittance growth could be observed.

Hiermit erkläre ich an Eides statt, dass ich die vorliegende Dissertationsschrift selbst verfasst und keine anderen als die angegebenen Quellen und Hilfsmittel benutzt habe.

Hamburg, den 18. Juli 2016